

DIFFERENTIAL INFRARED THERMOGRAPHY FOR ROTOR AERODYNAMICS

Von der Fakultät für Maschinenbau
der Gottfried Wilhelm Leibniz Universität Hannover
zur Erlangung der Lehrbefugnis (*venia legendi*)
für das Fachgebiet Strömungsmechanik
genehmigte Habilitationsschrift

von
Dr. Claus Christian Wolf

2022

Abstract

Understanding the flow around helicopter rotors is one of the greatest challenges in modern aerodynamics. The flow field plays a key role in the rotorcraft performance and operational safety, and it is characterized by highly unsteady and three-dimensional phenomena. State-of-the-art computational fluid dynamics (CFD) is applied during the design of future rotorcraft and offers remarkable capabilities, including the simulation of entire helicopter configurations in maneuvering flight.

Nevertheless, experiments are still essential for the understanding of complex flow regimes, and for the validation of numerical results. An ever-increasing level of detail in CFD studies motivates the development and refinement of experimental methods, and combined experimental-numerical efforts have been particularly rewarding in recent studies.

Starting with early rotorcraft-specific research topics, for example the systematic characterization of pitch-oscillating airfoils in the 1960s, experimental techniques have undergone continuous improvement. This particularly holds true for optical methods, which have developed from providing qualitative and “simple” snapshots of the flow into quantitative and time-resolving diagnostic tools. Optical methods require few modifications of the rotor or rotorcraft under investigation. They are particularly suitable for an application on multiple scales, ranging from small-scale laboratory studies to full-scale free-flying helicopters.

This thesis concentrates on the development, validation, and application of the differential infrared thermography (DIT). The DIT method is able to determine the moving position of the laminar-turbulent boundary layer transition, which is a relevant aerodynamic feature on rotor blades, accounting for the unsteadiness introduced by the different inflow conditions on the advancing and retreating sides of the trimmed rotor plane in forward flight. Additional helicopter-relevant applications include the study of pitch-oscillating airfoils or small-scaled rotors in laboratory or wind-tunnel environments. Furthermore, it will be shown that the DIT principle can be adapted to other rotor-relevant topics beyond transition research, such as dynamic stall investigations. DIT is a valuable addition to the larger family of optical measurement techniques for aerodynamic applications.

Zusammenfassung

Das Verständnis der Umströmung von Hubschrauberrotoren gehört zu den größten Herausforderungen in der modernen Aerodynamik. Dem Strömungsfeld kommt eine Schlüsselrolle in den Bereichen der Flugleistung und der operationellen Sicherheit von Drehflüglern zu, und es ist durch hochgradig instationäre und dreidimensionale Phänomene gekennzeichnet. Bei der Auslegung zukünftiger Hubschrauber werden moderne Methoden aus dem Bereich der numerischen Strömungssimulation (CFD - Computational Fluid Dynamics) eingesetzt und bieten bemerkenswerte Möglichkeiten, bis hin zur Simulation einer Gesamtkonfiguration im Manöverflug.

Dennoch sind experimentelle Untersuchungen weiterhin essenziell für das Verständnis komplexer Strömungssituationen. Der zunehmende Detailgrad in numerischen Vorhersagen bedingt die Entwicklung und Verbesserung von experimentellen Verfahren, und kombinierte experimentell-numerische Untersuchungen haben sich in aktuellen Studien als besonders erfolgsversprechend herausgestellt.

Seit dem Beginn der hubschrauberspezifischen Forschung, wie etwa der systematischen Charakterisierung von nickenden Rotorblattprofilen in den 1960er Jahren, wurden experimentelle Methoden kontinuierlich weiterentwickelt. Dies trifft in hohem Maße auch auf optische Verfahren zu, welche neben „einfachen“ qualitativen Momentaufnahmen der Strömung zunehmend quantitative und zeitauflösende Ergebnisse liefern können. Die Anwendung optischer Messtechniken benötigt oftmals nur wenige Modifikationen des zu untersuchenden Rotors. Sie sind daher besonders geeignet für die Anwendung auf verschiedenen Größenskalen, welche sich von kleinskaligen Laborversuchen bis hin zu vollskaligen, frei fliegenden Hubschraubern erstrecken.

Die vorliegende Arbeit beschäftigt sich mit der Entwicklung, Validierung und Anwendung der Differenzinfrarotthermographie (DIT - Differential Infrared Thermography). Die DIT-Methode bestimmt die aktuelle Position des laminar-turbulenten Grenzschichtumschlags bei instationärer Zuströmung, welche beispielsweise bei Rotorblättern im Vorwärtsflug durch den Wechsel zwischen vor- und rücklaufender Rotorseite auftritt. Weitere hubschrauberspezifische Anwendungsfälle sind die Untersuchung der Profilaerodynamik unter Anstellwinkelschwingungen oder Modellrotoren in Windkanälen. Neben der Bestimmung der Transitionslage kann das DIT-Prinzip auch an weitere Messaufgaben angepasst werden, wie beispielsweise die Untersuchung des dynamischen Strömungsabrisses. DIT ist somit eine wertvolle Ergänzung bestehender optischer Messmethoden für aerodynamische Anwendungsgebiete.

Foreword and Acknowledgements

This habilitation thesis is based on my work at the “helicopter aerodynamics” department of the Institute of Aerodynamics and Flow Technology at the German Aerospace Center (DLR) Göttingen between 2013 and 2021. A particular focus is set on the “differential infrared thermography” (DIT), a novel infrared-based approach for boundary layer transition measurements in unsteady inflow conditions. Parts of the work have already been released in several refereed and unrefereed publications, as indicated by corresponding citations in the text. A full publication list can be found in the bibliography under sections 5.1 to 5.4.

Teamwork is arguably the most important part of scientific achievements. I am very grateful for the pleasant, cooperative, and supportive work atmosphere at the DLR Göttingen. In particular, I would like to extend my deepest gratitude to

- Prof. Dr. habil. Markus Raffel, for his outstanding guidance and support, and for sharing his knowledge and ideas concerning experimental measurement techniques,
- Prof. Dr. Jörg Seume, for supporting this thesis at the Leibniz University Hannover, and for giving me the opportunity to teach “Fluid Mechanics” courses at his institute,
- Prof. Dr. Christian Kähler, for his support as a reviewer and member of the habilitation committee,
- Dr. habil. Tony Gardner, for sharing his profound knowledge of rotor aerodynamics in countless discussions, and for his contribution to the realization and analysis of aerodynamic studies,
- Dr. Kai Richter, for contributing his results acquired during measurement campaigns within the DLR project “STELAR”, and for sharing his deep insight into boundary layer flows,
- Dr. Johannes Braukmann and Dr. Till Schwermer, for designing and operating the rotor test stand Göttingen (RTG), and for their profound knowledge of experimental measurement techniques and aerodynamics,
- Dr. Armin Weiss, for his accurate and insightful analysis of a test campaign at the RTG, and for lots of fruitful discussions,
- James T. Heineck, for his support during the helicopter flight tests, and for sharing his deep insight concerning optical measurement systems,
- Dr. Kurt Kaufmann and Rohit Jain, for providing accurate and detailed numerical predictions complementing the experimental measurements,

- Dr. Andreas Goerttler and Dr. Stefan Koch, for the setup and data analysis of the hot-film measurement system used during tests in the transonic wind tunnel Göttingen,
- Dr. Clemens Schwarz, Dr. Benjamin Ewers, and Dr. Christoph Merz for their support during the establishment of optical measurement techniques, and for sharing their experience in aerodynamics,
- Austin Overmeyer, in appreciation of the excellent cooperation during a joint analysis of a large-scale rotor test,
- Christoph Mertens and Christian Eder, who contributed to the development of DIT in form of outstanding master's theses,
- the "helicopter flight experiments" team at DLR Braunschweig, for their professional and encouraging support during the helicopter test campaign,
- and Markus Krebs, for his skillful and enthusiastic help during the setup of virtually every measurement campaign.

Claus Christian Wolf, Göttingen, 2022.

Contents

	Page
Contents	ix
1 Introduction	1
2 State of research	9
2.1 Infrared thermography for steady boundary layer transition measurement . . .	9
2.2 Non-infrared methods for unsteady boundary layer transition measurement . .	12
2.2.1 Hot-film sensors	12
2.2.2 Fast-response pressure transducers and microphones	14
2.2.3 Temperature- and pressure-sensitive paints	16
2.2.4 Direct skin friction measurements	17
2.2.5 Comparison of methods	17
2.3 Additional experimental methods for full-scale rotors and free-flying helicopters	19
2.3.1 Blade deformation measurements	19
2.3.2 Wake aerodynamics	23
2.3.3 Dynamic stall measurements	34
3 Boundary layer measurements by differential infrared thermography (DIT)	37
3.1 Principle of DIT and method development	37
3.1.1 Test setup for airfoil measurements in the 1MG	37
3.1.2 Static pitch and comparison to standard infrared thermography	41
3.1.3 Introduction into unsteady test cases	45
3.1.4 Compensation of temperature drift	49
3.1.5 Influence and optimization of DIT separation	51
3.1.6 Discussion of pitch frequency and pitch amplitude effects	53
3.2 Validation of DIT for airfoil measurements	57
3.2.1 Test setup for airfoil measurements in the TWG	57

3.2.2	Processing of the TWG transition data	59
3.2.3	Influence of surface heating	64
3.2.4	Comparison of the different measurement techniques	66
3.3	Analysis of DIT using a coupled aerothermal simulation	69
3.3.1	Temperature computation in the surface layer	69
3.3.2	CFD solutions for the skin friction and pressure coefficients	71
3.3.3	Coupled computations	73
3.3.4	Review of the DIT principle and finite temperature delay	75
3.3.5	Reversal of the transition motion	79
3.3.6	Simulated effect of DIT image separation	79
3.3.7	Simulated effect of material selection	81
3.4	Application to small-scale rotor experiments	83
3.4.1	Rotor test stand Göttingen (RTG) and test cases	83
3.4.2	Infrared camera and image de-rotation	85
3.4.3	Numerical TAU-RBT simulation	88
3.4.4	Static pitch angle and intermittency	90
3.4.5	Pitch-oscillating test cases with cyclic input	92
3.5	Application to large-scale rotor experiments in forward flight conditions	96
3.5.1	Experimental setup	96
3.5.2	Periodic heating and cooling due to edgewise inflow	98
3.5.3	Measurements on the upper side of the rotor plane	102
3.5.4	Comparison to numerical simulations	105
3.6	Application to flight tests	112
3.6.1	Experimental setup and test procedure	112
3.6.2	Hover results outside of ground effect	115
3.6.3	Forward flight results	117
3.7	DIT applied to flow separation detection	121
3.7.1	Airfoil in static and dynamic stall	121
3.7.2	Small-scale rotor in dynamic stall	127
4	Conclusions and outlook	133
5	References	137
5.1	Reviewed journal publications (first authorship)	137
5.2	Conference publications (first authorship)	137
5.3	Reviewed journal publications (co-authorship)	138

5.4	Conference publications (co–authorship)	139
5.5	Publications by other authors	141
	Curriculum Vitae	157

Nomenclature

Latin symbols

c	(m)	Chord length
C_f	(-)	Skin friction coefficient
C_l	(-)	Lift coefficient
C_m	(-)	Moment coefficient
c_p	(J/kg/K)	Specific heat capacity at constant pressure
C_p	(-)	Pressure coefficient
C_T	(-)	Rotor thrust coefficient
D	(m)	Diameter
f	(Hz)	Frequency
$f_{\#}$	(-)	Relative optical aperture, f -number
h	(-)	Rotor hub height above ground, normalized with the rotor radius
k	(-)	Reduced frequency, airfoils: $k = \pi fc / V_{\infty}$, rotors: $k = c / (2r)$
M	(-)	Mach number
n	(-)	Load factor
N	(-)	Total number of samples or cycles
Q	(1/s ²)	Q-criterion (vortex identification)
\dot{q}	(W/m ²)	Heat flux
\dot{q}_{cond}	(W/m ²)	Conductive heat flux
\dot{q}_{conv}	(W/m ²)	Convective heat flux
\dot{q}_{rad}	(W/m ²)	Radiative heat flux
r	(m)	Radial coordinate in the rotor system
r_C	(-)	Recovery factor
R	(m)	Rotor radius
R_s	(J/kg/K)	Specific gas constant
R_z	(μm)	Ten-point surface roughness
Re	(-)	Reynolds number
s	(-)	Skewness
t	(s)	Time
T	(s)	Period of the pitch oscillation
T	(K)	Temperature
T_{eq}	(K)	Equilibrium temperature
T_r	(K)	Recovery temperature
T_w	(K)	Wall (surface) temperature
T_u	(-)	Turbulence level

u, v, w	(m/s)	Flow velocity components in x -, y -, and z -direction
U_{HF}	(V)	Hot-film voltage
V	(m/s)	Flow velocity
V_h	(m/s)	Hover-induced velocity
V_{tip}	(m/s)	Blade tip velocity
V_x	(m/s)	Horizontal (forward) flight velocity of the helicopter or rotor
x, y, z	(m)	Cartesian coordinates
x_{begin}	(m)	Begin of transition region
x_{end}	(m)	End of transition region
x_{tr}	(m)	Streamwise transition position (50% intermittence)
y^+	(-)	Dimensionless wall distance

Greek symbols

α	($^\circ$)	Angle of attack, pitch angle
β	($^\circ$)	Angle of sideslip, yaw angle
γ	(-)	Isentropic exponent
δ	(m)	Boundary layer thickness
Δ	(-)	Difference
$\Delta x_{50\%}$	(-)	Distance from transition begin to 50% intermittency
ϵ	(-)	Spectral emissivity
Θ	($^\circ$)	Blade pitch angle
λ	(W/m/K)	Thermal conductivity
μ	(-)	Advance ratio, $\mu = V_x / V_{tip}$
μ^*	(-)	Normalized advance ratio, $\mu = V_x / V_h$
σ	(-)	Standard deviation
σ_r	(-)	Rotor solidity
Ψ	($^\circ$)	Azimuth angle
Ω	(rad/s)	Angular velocity

Operators

∇	(1/m)	Nabla (gradient) operator
----------	-------	---------------------------

Subscripts, superscripts, and other symbols

75		Value at $r/R = 75\%$
e		Flow variables of the external flow
p		Peak
S		Surface layer properties
S_v		Surface layer properties in vertical direction
\uparrow		Upstroke

↓	Downstroke
^	Amplitude, sinusoidal motion
-	Mean value, sinusoidal motion
∞	Inflow or freestream conditions

Abbreviations

1D	One-dimensional
1MG	One-meter wind tunnel Göttingen
2D	Two-dimensional
3D	Three-dimensional
AFT	Amplification factor transport transition model
AHD	Arnal-Habiballah-Delcourt transition model
AHS	American Helicopter Society (1943-2018, now VFS)
AIAA	American Institute of Aeronautics and Astronautics
BL	Boundary layer
BOS	Background oriented schlieren-technique
BVI	Blade-vortex interaction
BYP	Bypass transition mechanism
CAMRAD	Comprehensive Analytical Model of Rotorcraft Aerodynamics and Dynamics
CF	Crossflow transition mechanism
CFD	Computational fluid dynamics
CFRP	Carbon fiber reinforced plastic
CSD	Computational structural dynamics
CTA	Constant temperature anemometry
(D)DES	(Delayed) detached-eddy simulation
DIT	Differential infrared thermography
DLR	Deutsches Zentrum für Luft- und Raumfahrt e.V. (German Aerospace Center)
DSA-9A	“Dynamic stall airfoil”-geometry with 9% relative thickness
ERF	European Rotorcraft Forum
GRC	Green Rotorcraft
GRMS	General Rotor Model System
HF	Hot-film (sensor)
IGE	In ground effect
IR	Infrared (imaging)
IRT	Infrared thermography
LED	Light-emitting diode
LM	Langtry-Menter transition model
LSB	Laminar separation bubble
LWIR	Long-wave infrared
MBB	Messerschmitt-Bölkow-Blohm
MCT	Mercury-Cadmium-Telluride (IR image sensor)

MWIR	Mid-wave infrared
NACA	National Advisory Committee for Aeronautics (1915-1958, now NASA)
NASA	National Aeronautics and Space Administration (up to 1958: NACA)
NETD	Noise-equivalent temperature difference
OGE	Out of ground effect
ONERA	Office national d'études et de recherches aérospatiales (The French Aerospace Lab)
PIV	Particle image velocimetry
PSP	Pressure sensitive paint
RANS	Reynolds-averaged Navier-Stokes
RBT	Rotor blade transition (toolbox)
RCAS	Rotorcraft Comprehensive Analysis System
rpm	Revolutions per minute
RTG	Rotor test stand Göttingen
SA	Spalart-Allmaras turbulence model
SST	Shear stress transport model
SLS	Strained layer superlattice (IR image sensor)
SPR	Stereo pattern recognition
STELAR	Stall and transition on elastic rotor blades (DLR Project)
TDT	Temperature decline thermography
TS	Tollmien-Schlichting transition mechanism
TSP	Temperature sensitive paint
URANS	Unsteady Reynolds-averaged Navier-Stokes
VFS	Vertical Flight Society (up to 2018: AHS)
VTOL	Vertical take-off and landing

1 Introduction

“It appeared most desirable to create an aircraft of a different type (...), with the possibility of rising or coming down along a vertical line, with the ability to hover over one spot for indefinite periods, to move forward or backward and to travel at any speed between zero and its maximum.”

Igor Ivanovitch Sikorsky (1889-1972), autobiography [204]

Helicopters carry out important tasks in the field of aerial passenger or material transport under difficult circumstances, due to their unique capabilities. The initial idea of helicopters is often attributed to Leonardo da Vinci’s “aerial screw machine” in 1483, but the scientific evaluation and technical implementation of rotorcraft can be dated to the early- and mid-twentieth century. Historical review chapters including a discussion of different rotorcraft concepts can be found in the books by Leishman [133] or van der Wall [228]. In recent years and fostered by innovations in flight control or electrical propulsion, the helicopter is challenged by novel approaches to vertical take-off and landing (VTOL), such as tilt-wing/tilt-rotor or multicopter designs. Figure 1.1 is a particularly interesting starting point for the current work, mainly for three different reasons.

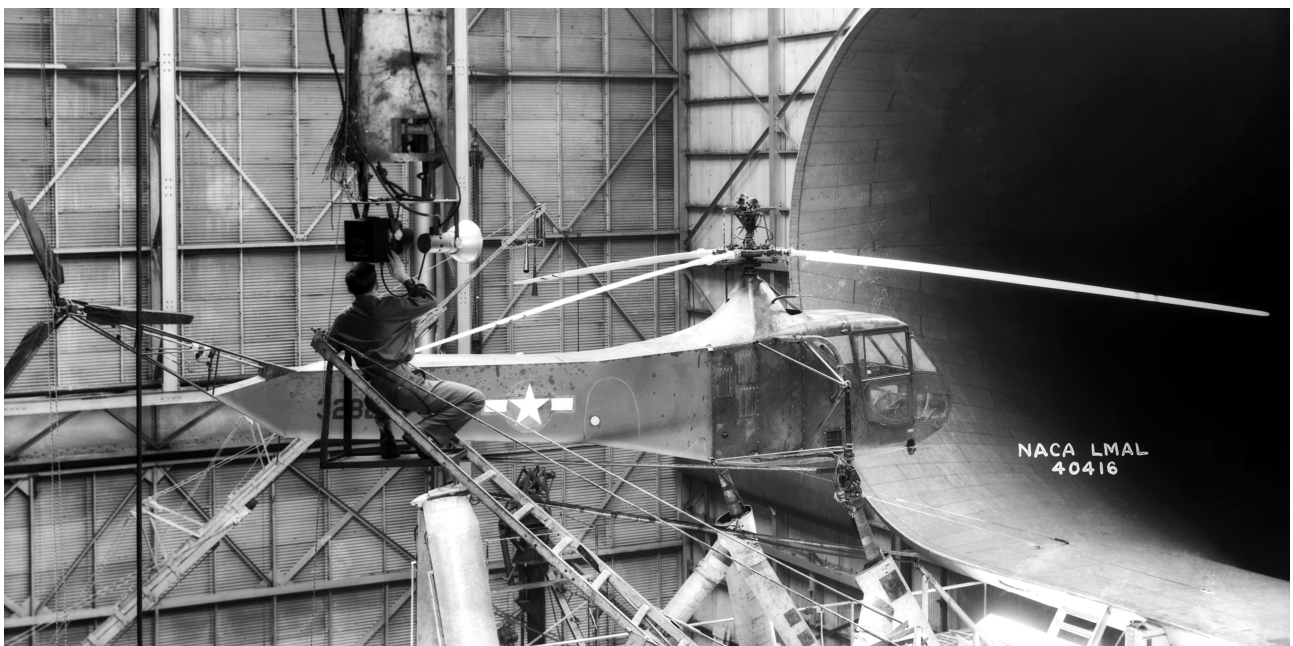


Figure 1.1: Tests with a Sikorsky R-4 helicopter in the NASA Langley 30 × 60 foot wind tunnel, October 1944 [152].

- First, the shown Sikorsky R-4 helicopter is the first mass-produced rotorcraft, with about 130 units built in total. It promoted Igor Sikorsky's design with a single main rotor, providing both lift and thrust, and a smaller tail rotor only used for anti-torque purposes. This setup is still the most relevant configuration for manned vertical flight vehicles today, and the large main rotor results in a number of specific aerodynamic features and problems.
- Second, the photograph shows a very early full-scale wind tunnel test conducted in the 30×60 foot-tunnel of the NACA/NASA Langley Research center. The facility was built in the 1930's and primarily served during drag reduction-studies of fixed-wing aircraft, but its width was also large enough for the 11.5 m-diameter of the R-4 main rotor, enabling systematic aerodynamic studies in forward flight conditions.
- Third, the image shows a very early application of fast-response optical measurement techniques to helicopters. The R-4 main rotor spins at 215 rpm in operating conditions, and the technician on the ladder prepares a fixed, ceiling-mounted camera-and-flashlamp imaging system with small exposure times to acquire stopped-action images of the rotor blades.

The Sikorsky R-4 had a cruise speed of only 105 km/h. This is slow in comparison to current helicopter generations, for example the Airbus EC135 with a cruise speed of 230 km/h, or in comparison to the world record holder for conventional rotor configurations, a Westland Lynx demonstrator with a top speed of 401 km/h flown in 1986. It is relatively easy to adapt the main rotor blades to hover conditions, but the superposition of rotational motion and edgewise velocity yields a complex and unsteady flow situation during forward flight. Figure 1.2 visualizes the local inflow magnitude and direction of the blades in the rotor plane. The sense of rotation is counterclockwise when viewed from above, which usually corresponds to German- or American-designed helicopter main rotors.

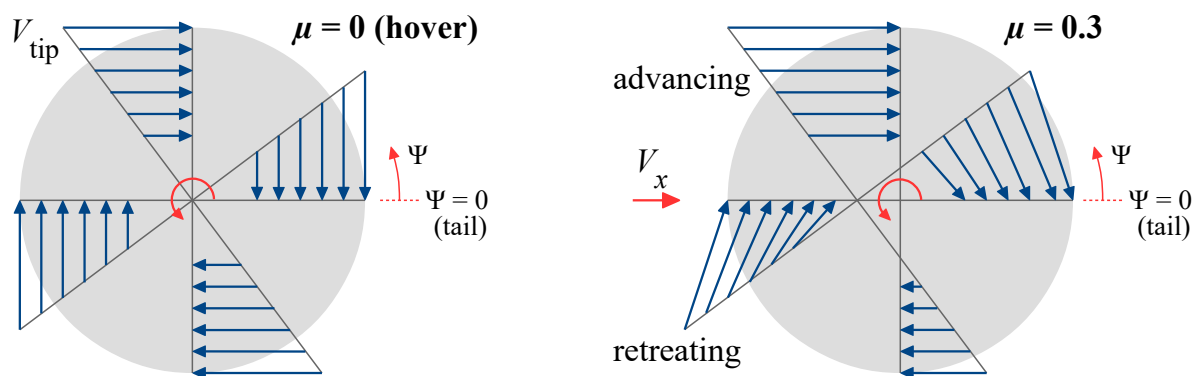


Figure 1.2: Influence of edgewise flight on the local inflow conditions in a rotor plane, advance ratios $\mu=0$ (left) and $\mu=0.3$ (right).

In hover, see the left side of Fig. 1.2, the velocity linearly increases with the radius but is constant over the azimuth. The rotor-induced velocity distribution can be tailored to a maximum hover efficiency [133], for example using a negative blade twist, or by varying the airfoil and blade planform. The right side of Fig. 1.2 corresponds to edgewise flight at an advance ratio of $\mu=0.3$, which is the flight velocity, V_x , normalized with the rotational velocity

at the blade tip, V_{tip} . For example considering the EC135 main rotor, $\mu = 0.3$ approximately corresponds to the cruise speed of $V_x = 230$ km/h. By common definition, the azimuth angle, Ψ , is zero when a rotor blade points in the aft direction over the tail. The inflow magnitude is increased on the advancing side, $\Psi = 90^\circ$, but decreased on the retreating side, $\Psi = 270^\circ$, including reverse flow in the vicinity of the rotor hub. Crossflow components in rotor-radial direction are encountered over the tail and nose, $\Psi = 0$ and $\Psi = 180^\circ$.

The integral pitch and roll moments at the main rotor hub must be trimmed to zero in steady forward flight and for a given lift and thrust requirement using the cyclic swashplate settings. Tilting the swashplate acts on the blades via the pitch links, resulting in a phase-shifted sinusoidal pitch motion as a function of the azimuth angle. As a result, the flow condition at a given blade section is unsteady over the course of a single rotor revolution. The level of the flow's unsteadiness can be expressed as a reduced frequency, k . For example, the EC135 main rotor at 75% of the tip radius results in $k_{75} = c / (2r_{75}) = 0.0376$, meaning that it takes $0.0376 / \pi$ or 1.2% of the rotor's pitch cycle for a fluid element to cover the chord length from leading edge to trailing edge. Even though the variation of many flow variables over the rotor cycle will be sinusoidal, additional complexity is added by the elastic motion and coning of the blades, and by the interaction with the rotor's own wake.

The requirements of a trimmed rotor are altered when deviating from a traditional main rotor-tail rotor configuration, as shown by the examples in Fig. 1.3. The recent Airbus X³ compound design (left) features additional auxiliary wings and propulsive rotors to unload the main rotor in forward flight. The Kamov Ka-32 (right) is an older design from the 1980s. Moment trim must be achieved for the sum of the two coaxial, counter-rotating main rotors. Hence, each rotor can be unloaded on its retreating side. Despite the relaxed requirements for the main rotor blades, the unsteady inflow into the rotor plane is still present.



Figure 1.3: Airbus X³ technology demonstrator, note the auxiliary wings and propulsive rotors (left, adapted from [56]), Kamov Ka-32 “Helix” helicopter, note the two coaxial main rotors (right, adapted from [155]).

The DLR currently operates two helicopters with conventional main rotor/tail rotor designs for flight test purposes, modified versions of the MBB/Eurocopter Bo105 and Airbus EC135. The latter is shown in Fig. 1.4. Both rotorcraft are light twin-engined transport helicopters with four-bladed main rotors. The corresponding base models have been mass-produced with more than 1000 units each, built in different versions. Figure 1.4 also illustrates common unsteady flow phenomena occurring during forward flight and relevant for the

performance, efficiency, and safety of the rotorcraft operation. State-of-the-art computational fluid dynamics (CFD), for example see Fig. 1.5, offer the potential to capture an amazing level of detail, including the simulation of entire helicopters in level flight or even during maneuvers. Therefore, CFD is applied during the development and optimization of new rotorcraft.

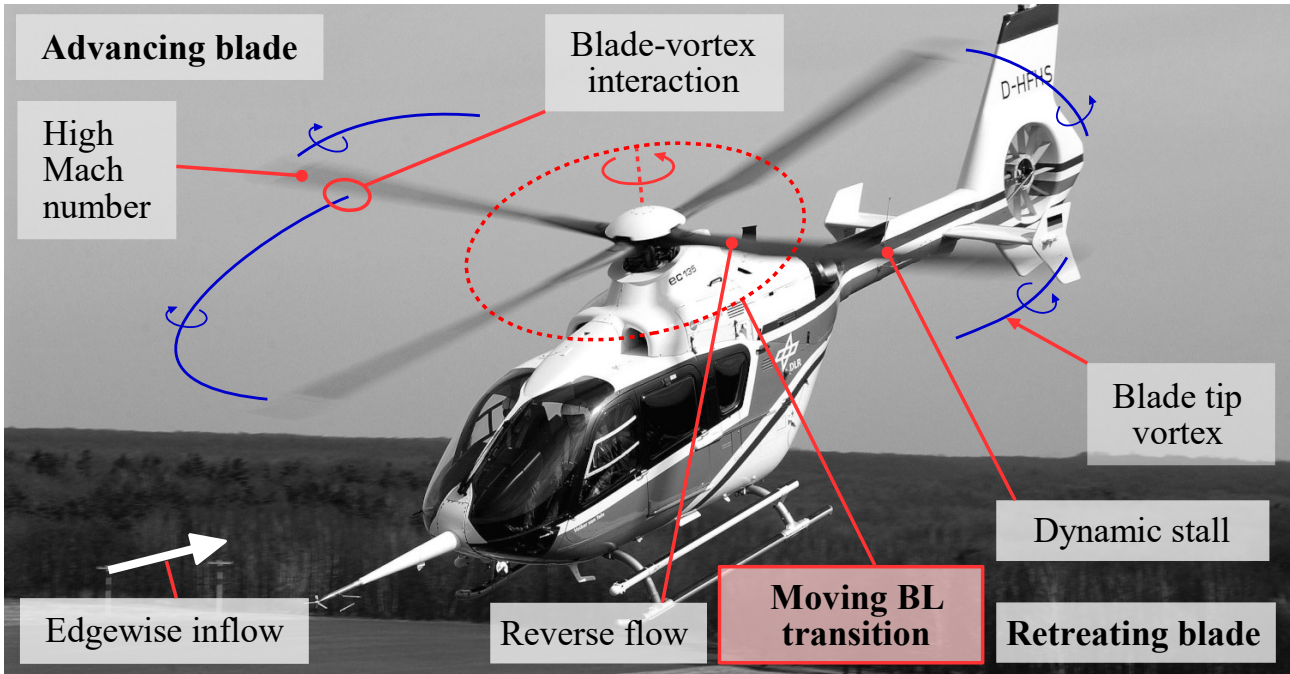


Figure 1.4: Flow phenomena in the flow field of a helicopter main rotor in forward flight.

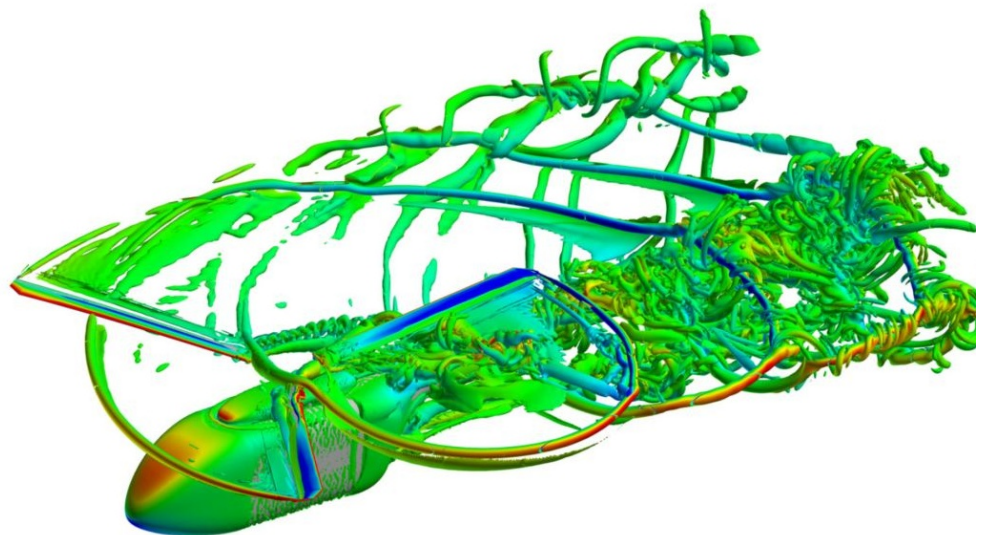


Figure 1.5: CFD simulation of a large-scale helicopter configuration in forward flight, adapted from Jain [109]. More details will be discussed in Sec. 3.5.4.

Nevertheless, experimental studies are still an essential part of modern helicopter aerodynamics. High-quality experimental data is mandatory to validate innovative CFD methods. Moreover, a multitude of combined experimental-numerical efforts discovered relevant “true” flow phenomena and separated them from CFD- and measurement-related artifacts. Optical measurement systems are particularly rewarding due to a favorable balance between result

quality and experimental effort. Innovative evaluation solutions and advancing image sensor technologies provide a much deeper insight into the flow than early stopped-action images as in Fig. 1.1.

The current work contributes to this process with the development, validation, and application of the “differential infrared thermography” (DIT). This method is suitable to detect the unsteady, moving position of the laminar-turbulent boundary layer (BL) transition as seen on rotors in edgewise flight. The concept was proposed in 2014/2015 by Raffel et. al [168], it is the newest member in the family of boundary layer-diagnostics via infrared imaging, with earlier techniques for steady-state aerodynamics originating in the 1980’s and before. DIT can be used on multiple scales, ranging from small-scale laboratory experiments with pitching airfoils up to large-scale rotors in wind tunnels, and the first-ever flight experiments for unsteady BL transition using the DLR test helicopters. The DIT method is a valuable addition to the portfolio of other optical techniques suitable for full-scale helicopter applications, such as schlieren imaging, particle image velocimetry, or blade deformation measurements.

The laminar-turbulent transition of the BL is one of the key factors when optimizing the aerodynamic performance of vehicles, altering the skin friction coefficient and the corresponding drag, or affecting the stall resistance. The measurement, prediction, and manipulation of the BL was tackled in numerous studies concentrating on steady aerodynamics with a stationary transition position, as found on fixed-wing aircraft, road vehicles, trains, etc.

It is known from helicopter-related simulations in hover conditions that modeling the BL transition is crucial for a correct prediction of the rotor power requirement, for example seen in studies by Egolf et al. [78] or Sheng [202] in the framework of the “AIAA hover prediction workshops”. For forward flight conditions, Dietz and Dieterich [72] showed that industry-driven rotor simulations with fully turbulent BLs overestimate the power requirement by about 8% in comparison to flight tests, and that this discrepancy can be lowered by modeling the BL transition. Therefore, several contributions were made to integrate transition prediction into rotor-specific CFD frameworks over the last decades (Beaumier and Houdeville [45], Beaumier et al. [46], Zografakis et al. [244], Coder [64]).

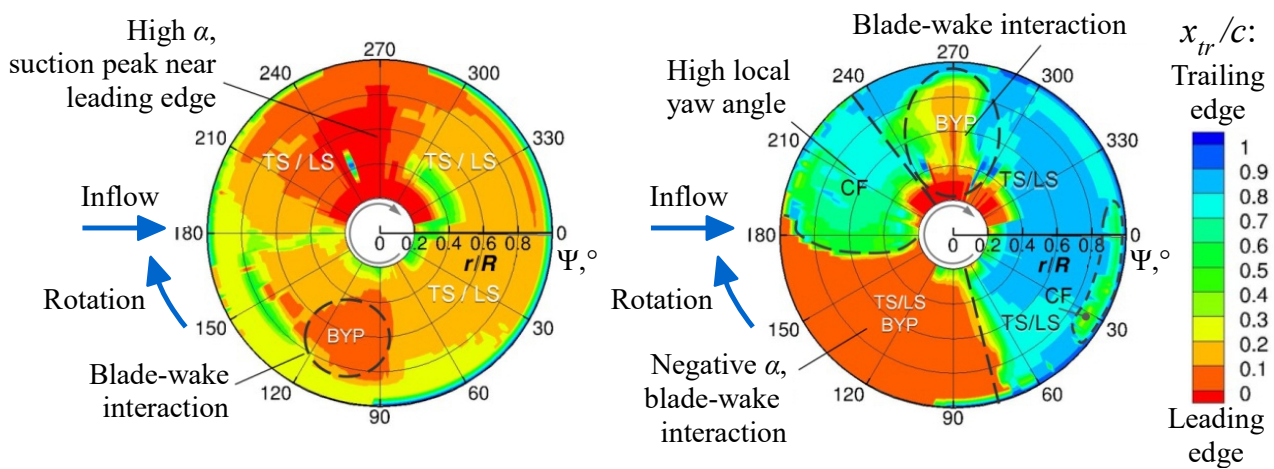


Figure 1.6: Prediction of the transition location x_{tr} on the upper (left) and lower (right) side of a trimmed rotor in forward flight, reproduced from Heister [101].

More recently, Heister [101] implemented the “rotor blade transition” (RBT) toolbox featuring several empirical criteria. The RBT approach was integrated into the URANS framework provided by the DLR TAU Code. A similar approach was chosen by Richez et al. [176] for the ONERA elsA code. Both studies performed successful comparisons to experimental data of the 7A/7AD rotor taken from integral torque measurements or sparse hot-film sensors applied within the GOAHEAD project [196]. However, a conclusive validation of numerical tools benefits from spatially well-resolved experimental data including three-dimensional effects, which is apparent from the predicted transition map shown in Fig. 1.6 for a trimmed, large-scale rotor at an advance ratio of $\mu=0.33$ and a tip Reynolds number of $2 \cdot 10^6$. The idea of providing a similar experimental transition map triggered the development of DIT at the DLR Göttingen.

The transition onset in Fig. 1.6 is governed by different criteria, which represent different relevant BL transition mechanisms. The following overview uses the same abbreviations as in Fig. 1.6, and Heister’s criteria selection [101] is very similar to other studies, for example, see Jain [109].

- **Tollmien-Schlichting (TS)** refers to the low Mach-number frequency amplification process in five stages [187]: Growth of TS instability waves (1) into spanwise vortical structures (2), three-dimensional breakdown (3), individual turbulent spots (4), and fully turbulent boundary layer (5). The TS mechanism is favored by high Reynolds numbers and low freestream turbulence levels, and it is visualized in Fig. 1.7.

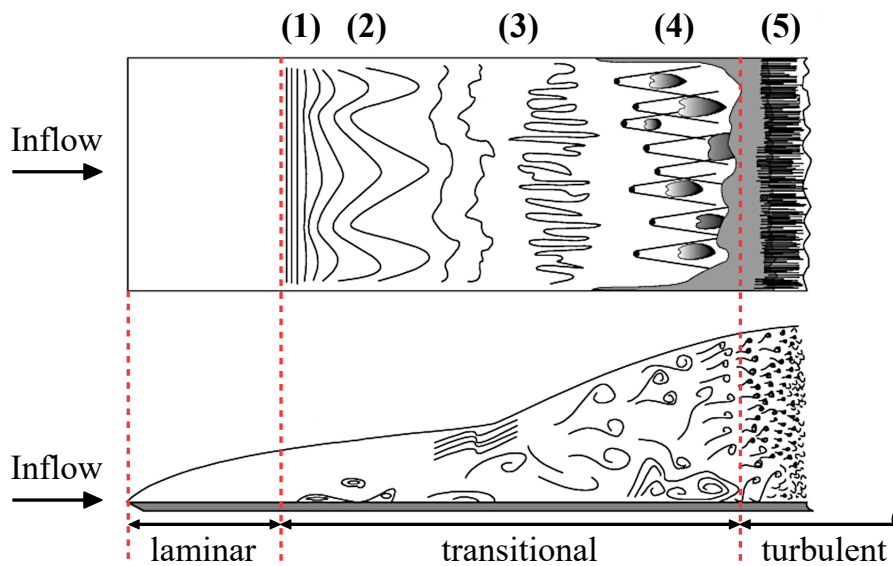


Figure 1.7: Tollmien-Schlichting boundary layer transition mechanism on a flat plate, adapted from Ref. [187].

- **Laminar separation bubble (LSB)** with turbulent reattachment results from a strong flow deceleration at low Reynolds numbers, or a shock. The occurrence of an LSB in rotor flows was first reported in the experiments by Velkoff et al. [222] in 1971, who analyzed surface traces of ammonia injected at the leading edge.
- **Bypass transition (BYP):** A high inflow turbulence level can result in a reduced laminar flow length over a blade surface, since the first stages of the natural transition process

are “bypassed”. This mode is particularly relevant in gas turbine aerodynamics [145]. Relevance for helicopter rotors is given in case of blade-vortex interactions (see Figs. 1.4 and 1.5) or wake ingestion, which also increase the effective inflow turbulence of the subsequent rotor blade.

- **Crossflow instabilities (CF):** The trajectory of a fluid element in the external flow around a rotor blade is governed by the equilibrium of centripetal pressure-driven forces and centrifugal velocity-driven forces. This balance is offset within the BL due to the decelerated flow, resulting in a radial crossflow velocity profile, see Fig. 1.8. The related instability mechanism is also relevant for swept wings, see Saric et al. [183] for a detailed overview.
- **Forced transition/BL tripping/surface roughness elements:** Surface protuberances added to the smooth aerodynamic surface can trigger BL transition. A forced transition can be intentional, by applying trip dots, trip wires, or profile steps, or unintentional, for example due to surface damage (see Fig. 1.9) or manufacturing defects.

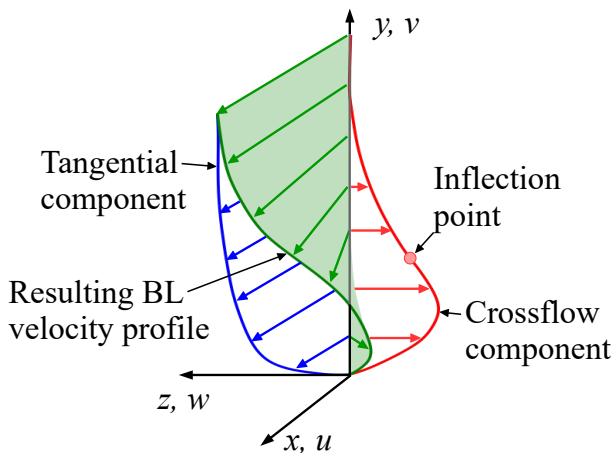


Figure 1.8: BL velocity profile with CF instability, adapted from Ref. [183].

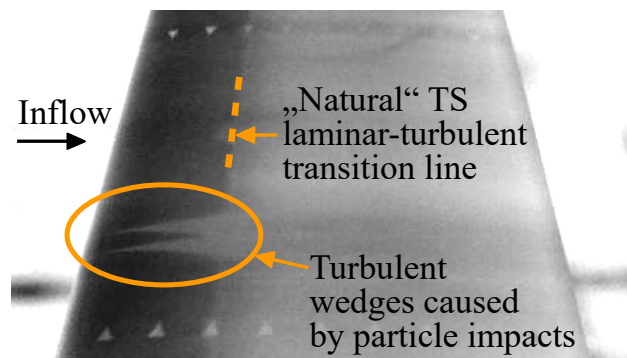


Figure 1.9: Steady infrared analysis of a wetted surface in a wind tunnel experiment.

It is noted that each mechanism refers to a phenomenon in flow physics, even though the RBT implementation is based on empirical correlations. Other implementations can be based on semi-empirical ideas (such as the e^N -method [108]), transport equations, or even solving the Navier-Stokes equations. A validation on the basis of experimental results is always advisable, and an increasing demand for computational resources makes high-fidelity approaches less suitable in industrial environments, see Ref. [102] for further discussions.

As closing remarks, the experimental determination of a moving BL transition position is helpful in several other applications beyond helicopter rotors in forward flight. An example is given by turbomachinery aerodynamics, where an unsteady inflow of the compressor or turbine blades in a rotor-stator layout is caused by the periodic wake of preceding stages, which also results in moving BL transition [70, 156]. The transition not only affects the friction drag, but also the thermal loads of the blades. It is particularly difficult to access this type of flow with sensors and measurement equipment, hence, many studies simplified the setup by

investigating the influence of periodic inflow perturbations on flat plates [139, 159], curved surfaces [189], or stationary blade cascades [158].

In addition, early fundamental research of moving BL transition on flat plates [149, 157] has currently been reviewed for fixed-wing aircraft applications [182], assuming that low-frequency atmospheric turbulence may affect the performance of natural laminar-flow airfoils.

The blades of horizontal-axis wind turbines can easily be subject to unsteady aerodynamics due to wind shear effects, yaw angles, interactions with the tower, or aeroelasticity [136, 242]. It can be expected that these unsteady effects become increasingly important in the future, given that the laminar flow length is a crucial parameter of wind turbine airfoil design [115]. Another recent publication by Thiessen and Schülein [218] concentrated on moving transition positions due to the effect of forward flight velocity on a fixed-pitch propeller for unmanned aerial vehicles.

2 State of research

The state of research is presented in three parts. The first part covers “standard” infrared thermography (IRT) measurements of the steady boundary layer transition position, which serve as a basis for the development of differential infrared thermography (DIT). A focus is set on the application to moving surfaces, particularly large rotors.

The second part addresses non-infrared methods suitable to detect a moving boundary layer transition position in unsteady inflow conditions. These methods must be seen as an alternative to DIT, and a discussion of individual advantages and disadvantages is included.

The third part gives an overview of experimental measurements for full-scale rotor aeromechanics other than (but related to) the boundary layer conditions. It is noted that due to strong couplings, an understanding of e.g. the blade elasticity or the wake structure is mandatory to understand or predict the BL transition process. A focus is set on optical techniques and recent activities of the helicopter aerodynamics-group at the DLR Göttingen, and on experimental restrictions connected to free-flying helicopter tests.

2.1 Infrared thermography for steady boundary layer transition measurement

Over the last decades, infrared thermography (IRT) has become one of most popular and most convenient techniques in experimental boundary layer transition research. The application to subsonic flows was pioneered by Quast [165]¹ as an alternative to oil-flow pictures. Other early publications include the work of Carlomagno et al. [58] or de Luca and Carlomagno [141], who investigated rectangular wing sections with established NACA- or Göttingen-type airfoils in a low-speed wind tunnel. Recent IRT applications cover wind tunnel testing of modern airfoils [47, 111] or fixed-wing aircraft models [240], supersonic applications [95, 245], and in-flight measurements on general aviation aircraft [67, 68]. IRT can be applied in many situations, but with a view to the current focus on rotor aerodynamics, the rest of this section will concentrate on applications with rotating surfaces.

In its basic form and for steady inflow conditions, IRT uses an infrared camera to visualize the non-moving BL transition region as a surface temperature step, which is connected to the Reynolds analogy between skin friction and convective heat transfer. This analogy will be evaluated in Sec. 3.1.2, and a comprehensive summary of the measurement technique can be found in standard textbooks [40]. IRT is non-intrusive and produces spatially resolved results in a two-dimensional measurement domain. No model instrumentation is required,

¹The cited journal article was published in 2006, but it is based on a presentation at the “XX OSTIV congress” in Benalla, Australia, in 1987.

but in some cases, an insulating surface coating or a heating foil can be beneficial, depending on the surface material and the experimental setup.

Figure 2.1 (left) is an IRT image of the DLR test rotorcraft Airbus EC135 placed on the apron of the Braunschweig regional airport, with the IR camera “IRCAM Equus 327k L” mounted obliquely above the rotor plane. The grayscale intensity corresponds to the long-wave infrared emission. The rotor turns at 75% of the nominal rpm, or $f = 5$ Hz. Parts of the fuselage and one of the four rotor blades is within the field of view, and the blade motion is frozen due to the small image integration time of $20 \mu\text{s}$.

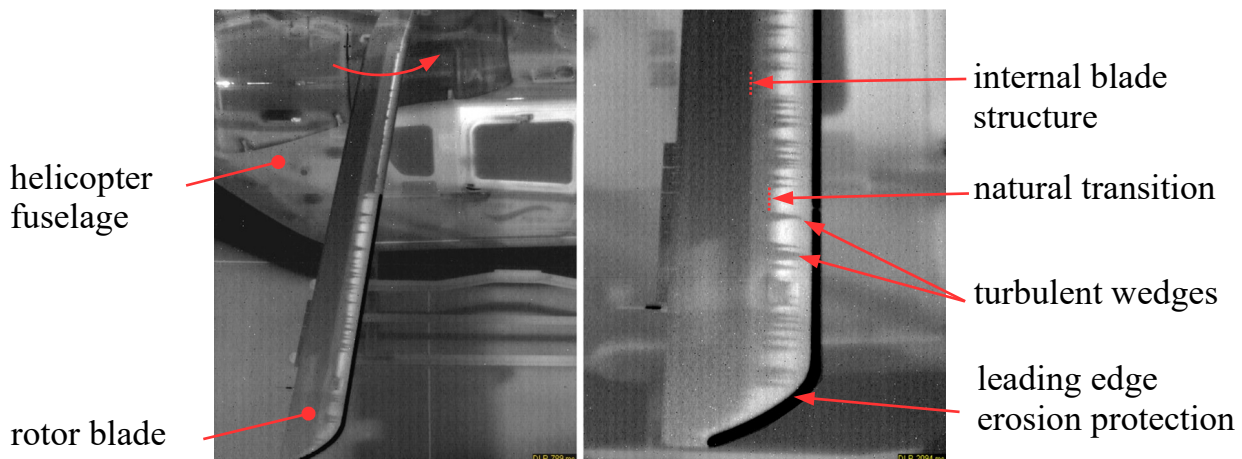


Figure 2.1: IRT measurement during an Airbus EC135 ground test run (left) and detail of the blade tip region (right), adapted from Richter and Schülein [179].

The detail in Figure 2.1 (right) reveals the footprint of the flow over the blade’s suction side. The natural laminar-turbulent BL transition is visible as an intensity gradient from light gray to dark gray, located at about 0.3 chord lengths downstream of the leading edge. Multiple turbulent wedges indicate premature transition due to surface contamination, mostly caused by insect impacts. The leading edge itself is covered by a titanium erosion protection appearing in black color. In comparison to the glass fiber composite surface of the rest of the blade, the metallic surface has a much lower emissivity ($\epsilon \approx 0.5$ versus $\epsilon \approx 0.85$) and a higher reflectivity. Thus, the erosion protection not only appears to be colder at the same or similar temperature, but it is also less suitable for IRT investigations and requires a high-emission insulation coating.

There is a “natural” wall temperature difference, ΔT_w , between the laminar and turbulent regions of a boundary layer, connected to the flow’s varying recovery temperature. Details and equations will be given in Sec. 3.3.1, but the temperature step can be roughly estimated [220] using the flow’s temperature, T_∞ , and Mach number, M_∞ , using

$$\Delta T_w \approx 0.012 \cdot T_\infty M_\infty^2. \quad (2.1)$$

This difference is smaller than 1 K for the current blade tip Mach number, $M_\infty = 0.46$ at 75% rpm. The signal-to-noise ratio can be improved by heating or cooling the blade surface relative to the flow temperature, which amplifies the laminar-to-turbulent contrast due to a varying convective heat transfer. In Fig. 2.1, the blades were pre-heated by sunshine. Shortly after rotor spin-up, the flow cools the turbulent regions more effectively than the laminar

regions, resulting in a lower thermal emission and a darker coloring. Thermal equilibrium is reached several minutes after spin-up, and the turbulent regions will then appear slightly brighter due to the larger skin friction, but the contrast will be much smaller as in Fig. 2.1.

Several methods to artificially establish a flow-to-surface temperature difference have been successfully demonstrated:

- surface heating by external radiation flux sources: general purpose spotlights [30, 4], infrared emitter [206], infrared laser [218], or sunlight [172, 179]
- surface heating by internal resistance heating: electrically conductive paint [160], carbon nano tube materials [119], heat foils [206], etc.
- surface pre-heating [94, 180] or pre-cooling [179] for short-term tests
- varying inflow temperature in laboratory environments or wind tunnels, altitude changes during atmospheric flight [68], etc.

The required temperature difference is on the order of several Kelvin, for example, 2.5 K as reported by Ikami et al. [106] or 5 K – 6 K as reported by Wolf et al. [4]. This number will depend on the camera setup and the resulting signal-to-noise ratio, and no general recommendations can be made. The transition position itself may be affected if the heating is too strong, see Joseph et al. [111] or Costantini et al. [66] for further discussions.

An insulating and dull coating can be applied to the surface in order to reduce thermal conductivity and infrared reflectivity, and to maximize infrared emissivity [40]. This is mandatory for metallic surfaces but optional for CFRP materials. Fiducial markers with differing radiation properties, for example silver conductive paint, can be applied to the surface for image registration and dewarping purposes.

Current infrared cameras are based on either thermal detectors, which sense the temperature rise due to an incoming energy flux, or quantum detectors, which convert the incoming photons to electrical charge [40, 59]. The former principle can, for example, be realized using microbolometer arrays, which is the cost-effective standard choice for many cameras applied to steady-state BL measurements. The required image exposure times are in the range of several milliseconds [226] and, therefore, unsuitable to “freeze” the motion of rotor blades. Quantum detectors are used in high-speed infrared cameras, featuring both a high repetition rate ($f > 100$ Hz) and small image exposure times ($\Delta t < 100$ μ s). The sensor resolution is currently between about 0.3 Mpixel and 1.3 Mpixel, which is at least one order of magnitude smaller than today’s visible-light cameras. The signal-to-noise ratio of the infrared images depends on the surface emissions, the camera exposure time, and its noise-equivalent temperature difference (NETD), which is typically below 50 mK. The studies discussed in the current work were conducted using either mercury cadmium telluride (MCT) or strained layer superlattice (SLS) sensors, both sensitive in the long-wave infrared band (LWIR) covering a wavelength of about 8 μ m to 14 μ m. In contrast, indium antimonide (InSb) sensors are sensitive in the mid-wave infrared band (MWIR) with a wavelength of about 3 μ m to 8 μ m. The LWIR band can be advantageous since carbon fiber surfaces are opaque in the long-wave regime and require no additional surface treatment. In contrast, the thermal information in MWIR images is not restricted to the partly translucent aerodynamic surface itself. Moreover, the images can be used to detect subsurface defects in the carbon fiber material [80].

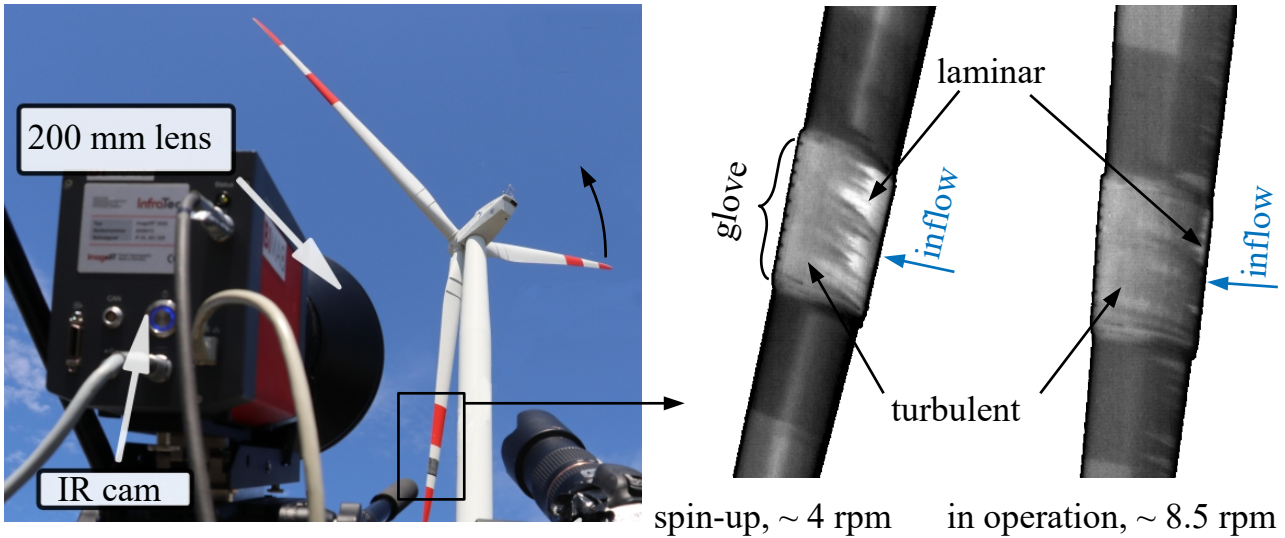


Figure 2.2: IRT measurement on a large 2 MW-wind turbine, experimental setup (left) and result images for different rotor speeds (right), adapted from Reichstein [172].

In addition to helicopters, the IRT technique was also applied to other full-scale rotor applications such as large wind turbines. Figure 2.2 shows a test campaign by Reichstein et al. [172] on a “Senvion MM92”-turbine with a nominal power output of 2 MW and rotor radius of 46 m. The IR images were taken with the same high-speed camera as used in Fig 2.1, but the focal length was increased from 50 mm to 200 mm due to the large viewing distance of about 140 m. A conformal CFRP glove equipped with microphones and pressure sensors was attached at $r/R=0.76$ ($r=35$ m), providing an IRT-suitable surface on the suction side of the blade. The local chord length, c , is 1.5 m. The rotor was spun up after being heated by sunlight, and the characteristic laminar-turbulent flow pattern was observed at a rotor speed of about 4 rpm (left IRT image in Fig. 2.2) corresponding to a local chord-based Reynolds number of $Re \approx 1.4 \cdot 10^6$. The image was dewarped and scaled in an additional post-processing step, and the natural transition position was determined at about 37% c from the leading edge. Similar to the helicopter test, multiple turbulent wedges due to surface contamination or surface defects were found. When reaching 8.5 rpm or $Re \approx 3.0 \cdot 10^6$ (right IRT image in Fig. 2.2, the turbine’s speed limit is 15 rpm), the laminar region only covers 8% c from the leading edge. The IRT results were found to be in good agreement with the subsurface microphones installed in the glove.

2.2 Non-infrared methods for unsteady boundary layer transition measurement

2.2.1 Hot-film sensors

The hot-film is a flush-mounted surface sensor that uses the principle of constant temperature anemometry similar to the well-known hot-wires [57]. It is a standard method for measuring the skin friction coefficient, C_f , in a boundary layer via the Reynolds analogy for heat transfer [48, 137]. This analogy will be further discussed in Sec. 3.1.2.

Hot-films can be used to detect a dynamically moving boundary layer transition [55], and they can also distinguish between transition, stagnation point motion, flow separation, and shock formation [177]. The state of the literature for transition measurements on static airfoils with non-moving transition is particularly good, see for example [181]. It should be noted that much of this literature refers to the unsteady turbulent structures within the BL, see for example [213], rather than a dynamically moving boundary layer position as experienced by the pitching airfoil or the helicopter rotor in forward flight.

The pitching airfoil has been investigated for low-Mach number airfoils [131, 132, 192] and for helicopter-relevant airfoils at Mach with compressible flow [61, 177, 34]. The investigations of Richter et al. involve 50 sensors on each airfoil, and are suitable for CFD calibration, see the comparisons in Ref. [35]. Hot-film sensors have also been extensively used for the investigation of dynamically moving BL transition on laminar airfoils [98, 144], particularly in relation to aeroelastic flutter. Lorber and Carta [140] did extensive investigations of the BL transition and flow separation on a pitching airfoil, but the transition investigations involved only two sensors due to the low chordwise resolution. For the rotating system, Sémézis and Beaumier [201] performed a hot-film investigation on the 7AD rotor and investigations within the GOAHEAD project [196]. The data was also used for CFD validation [101]. A similar BL transition measurement using hot-films on an instrumented full-scale wind turbine blade was done by Schaffarczyk et al. [185].

The evaluation of hot-film data presents several difficulties, which have increasingly been identified and at least partially solved in recent years. The first major problem is that for a dynamically moving BL transition, the transition intermittency is no longer seen as a transient stepping function. For a stationary BL transition region, a series of turbulent spots is generated and propagates past each sensor, and the fraction of time in which the sensor is in the laminar or turbulent state is the experimentally defined intermittency. For the moving boundary layer, an increased RMS signal is present, but the intermittency signal never appears, leaving the transition position to be assessed through the soft step attained between laminar and turbulent flow [92]. The step assessment also lends itself to fully automated data processing through “data skew”, which solves the second problem of dealing with the large amount of data required to include the sensor cut-off frequencies of around 60 kHz [55, 92]. More details on hot-film data processing will be given in Sec. 3.2.2, in which this measurement technique is used as a reference for the infrared-based DIT method.

An additional problem of hot-film sensors is that they involve an intrusion into the flow. Even if the sensor carrier foil is carefully kept to the same contour as the airfoil, the different surface roughness can result in a difference in the transition position, see Fig. 2.3. For the same reason, the edges of the foil and the localized heating spots of the sensors may cause disturbances. These influences can be reduced through good design and careful construction, but they can never be completely avoided. Similarly, Mertens et al. [24], noted that the regions of a pitching airfoil with pressure sensors had measurably different boundary layer transition for some test cases, either due to the local surface heating, or the pressure taps.

For impulsive, particularly hypersonic test facilities, the hot-film gauges can be operated in an unheated mode, and are called thin-film gauges, see for example [147]. In this case the “cold” resistance of the sensor is related to the heat transfer from the wall. The gauges have reaction times of the order of microseconds, but to the author’s knowledge were not yet used for dynamically moving boundary layer transition.

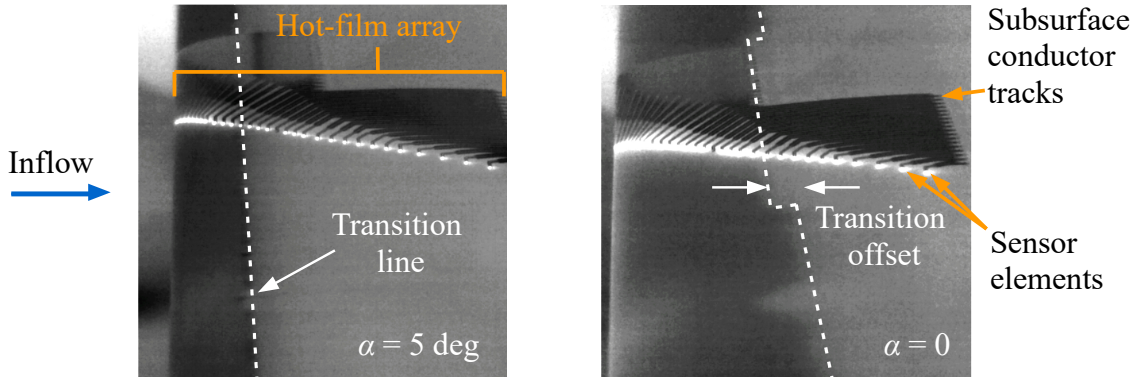


Figure 2.3: Infrared images showing a pitch angle-dependent difference of the BL transition position on an airfoil due to the presence of a hot-film foil, adapted from Richter et al. [35].

An alternative to hot-films is to place hot-wires in the boundary layer, which usually offer a better insight into the flow properties, such as a detailed characterization of the transition mechanism. A common approach for fixed model surfaces is to use sensor traverse mechanisms, for example see Refs. [53, 238], but the integration of hot-wires to moving model surfaces with unsteady inflow conditions is even more challenging compared to hot-films.

2.2.2 Fast-response pressure transducers and microphones

The laminar-turbulent transition of a boundary layer not only increases the skin friction coefficient, C_f , but also the boundary layer thickness, δ , as sketched in Fig. 2.4. The resulting displacement of the external flow affects the pressure distribution, C_p , along the surface in streamwise direction.

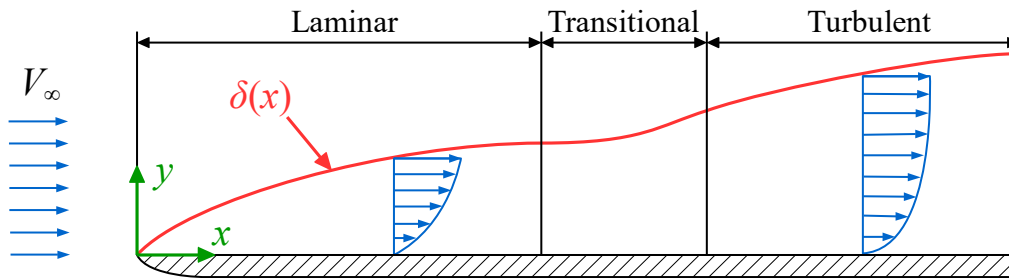


Figure 2.4: Sketch of a flat-plate boundary layer with laminar-turbulent transition, after Schlichting and Gersten [187].

Wind-tunnel models are often equipped with pressure taps connected to subsurface pressure transducers, commonly known under the brand name “Kulite[®]”. The transducers have a frequency limit in the kilohertz range, mainly limited by the air volume of the taps and its damping effect. The data can be used to investigate unsteady flow phenomena, or to calculate integral forces such as lift or pressure drag.

Several concepts have been proposed to use the unsteady pressure information for BL transition detection. For example, Popov et al. [163] defined a BL transition criterion based on the pressure’s inflection point as seen by the second derivative in streamwise direction, $\partial^2 C_p / \partial x^2$. The method was demonstrated for well-resolved numerical data, but it suffers

from a limited number of surface pressure transducers in experimental data.

The σC_p -concept by Gardner and Richter [86, 87] was developed with a particular view to pitch-oscillating test cases or quasi-steady pitch ramp motions. If the pressure sensor signals are evaluated for an airfoil's periodic pitch motion, then the differences between different cycles will be low in the laminar flow regions, medium in turbulent regions, and a maximum near the transition position. This is because slight differences in the wind tunnel's operating conditions or the pitch mechanism result in small cycle-to-cycle variations of the moving transition position. Hence, in a certain phase of the cycle, the transition position is in front of a given pressure sensor for some cycles but behind the sensor for the other cycles. This increases the cycle-to-cycle standard deviation of the pressure, σC_p , since the transition affects the BL displacement thickness. A sample analysis of a pressure transducer mounted to the suction surface of a rotor blade at 19% chord is shown in Fig. 2.5. Due to the chosen cyclic pitch amplitude, both the BL transition and the BL separation inducing dynamic stall leave a footprint in the standard deviation of C_p . The current work applies the σC_p -method to acquire reference data for DIT infrared measurements, for example see Secs. 3.1.3, 3.2.2, and 3.4.1.

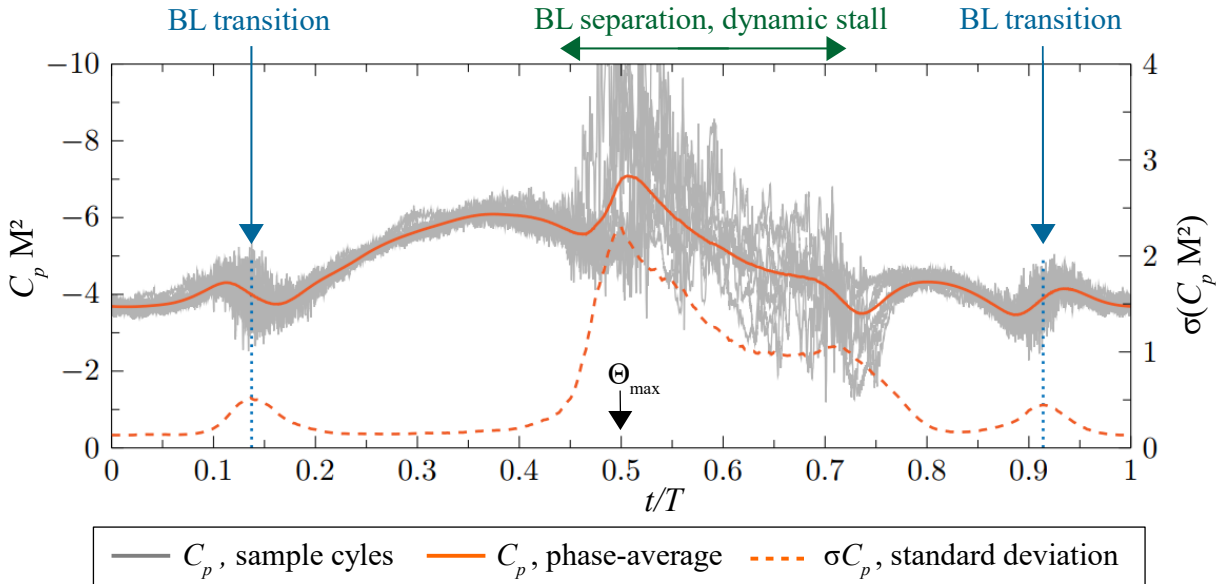


Figure 2.5: σC_p -analysis for a rotor blade with cyclic pitch input, $f = 23.6$ Hz, pitch amplitude $\hat{\Theta} = 6^\circ$, adapted from Schwermer [197].

The σC_p -technique does not require a very high temporal resolution of the pressure sensor as long as the overall aerodynamics is properly captured. This is due to the fact that no boundary layer modes are identified, but only the motion of the transition position which is a broadband signal. The method has been demonstrated for pitching airfoils at both high and low inflow velocities [86, 20], and for pitching finite wings in both swept and unswept configurations [15, 25]. An application to a rotor with cyclic pitch is also possible [198, 30] but the sensor integration requires additional effort, for example by means of a telemetry system.

Gao et al. [84] and Wei et al. [230] proposed an approach which is similar to the σC_p -idea but was developed independently. In their case, it was shown that using a sliding window analysis rather than the cycle-to-cycle deviation yields transition results with a comparable quality. This concept avoids the need for a precisely phase-locked data acquisition.

Another evaluation strategy in literature is the M-TERA intermittency approach. It was originally formulated for velocity fluctuations [243], but recently adapted to surface pressure fluctuations and transient inflow conditions [182]. The method must be seen as requiring additional validation.

Microphones with a much broader frequency response than the subsurface pressure sensors can also be used to detect BL transition, see Refs. [161, 172]. Microphones allow an analysis of boundary layer frequencies or modes of interest in addition to the mere transition location, but with additional difficulties in analyzing the acoustics.

2.2.3 Temperature- and pressure-sensitive paints

Temperature-sensitive paint (TSP) is an alternative to infrared thermography and can often be applied in similar situations [138]. TSP also optically measures the temperature distribution of a surface, but it is based on the luminescence of temperature-sensitive molecules (“luminophores”) in a surface coating rather than the thermal radiation of the base material. The luminescence is excited by an additional light source such as an LED or a laser. The surface preparation with the delicate paint layer requires experience and additional effort, and it offers the disadvantage that the surface contour may be altered. The surface roughness of the TSP can be very low if polished [81]. The luminescent response of the paint is in the visible spectrum, hence, “standard” cameras with lower costs and a much higher optical resolution compared to IR cameras can be used. The higher resolution not only helps to identify small-scale flow features, but also enables a precise image dewarping.

Under cryogenic conditions, TSP proved to be beneficial in contrast to infrared thermography [38] due to the challenges of capturing the reduced radiated energy in the infrared spectrum [89]. TSP can be used for very short time exposures, see Refs. [127, 232]. Figure 2.6 shows Weiss et al.’s [232] TSP results from a measurement at the rotor test stand Göttingen (RTG), which will also be used for DIT development in Sec. 3.4. The rotor frequency is 23.6 Hz, the rotor diameter is 1.3 m, and the light-to-dark gradient marks the non-moving BL transition position on the blade’s suction side for three constant-pitch test cases. The contrast is very good, despite small image exposure time of only 11 μ s.

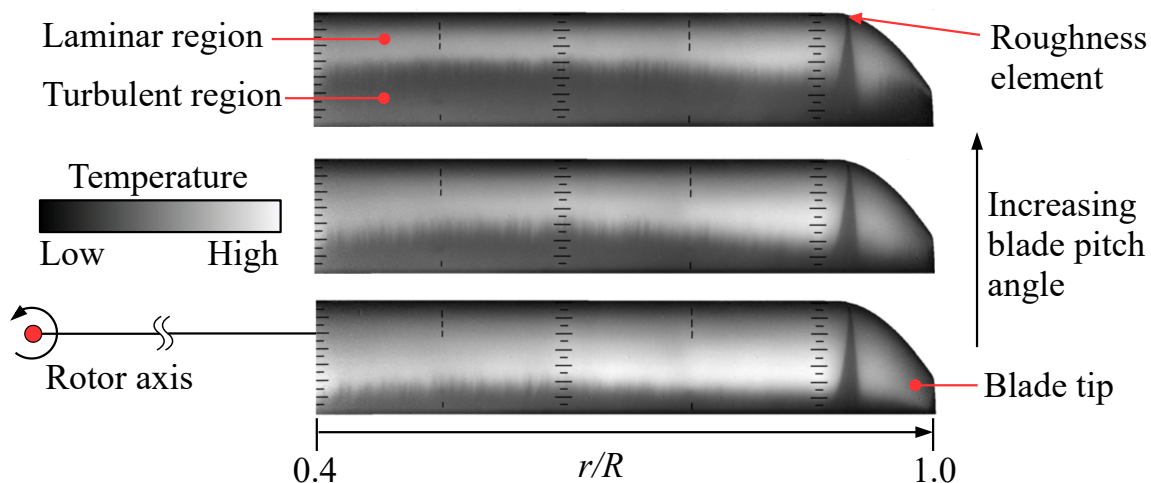


Figure 2.6: BL transition measurements using TSP at the rotor test stand Göttingen, collective blade pitch angles $\Theta = 11.0^\circ, 12.0^\circ, 13.1^\circ$ (bottom to top), adapted from Weiss et al. [232].

The TSP images are qualitatively very similar to infrared images as in Figs. 2.1 and 2.2, but the higher optical resolution of the 10.7 Mpixel-camera allows to identify very fine-scaled flow structures. The luminescent coating used ruthenium phenanthroline in a polyurethane binder matrix, it was applied to a white foil covering the CFRP blades as a protective and contrast-enhancing layer. The paint was carefully polished, and the entire coating process required extensive preparation in comparison to DIT measurements using the bare CFRP surface.

The application of difference-image techniques and the resulting heat flux estimate allows the use of TSP for the detection of dynamically moving BL transition. This concept was initially proposed by Yorita et al. [241] to increase the productivity of quasi-steady airfoil tests through a slow pitch motion with a rate of $0.25^\circ/\text{s}$. Ikami et al. investigated the response time of TSP [107] and applied the idea to a pitch-oscillating airfoil with a frequency of 0.42 Hz to 4.2 Hz ($k=0.01-0.10$). It is noted that fast-response TSP and infrared-based DIT methods have been developed recently and independently. Both techniques are based on similar concepts but require further validation for test cases with highly unsteady inflow.

Pressure sensitive paint (PSP) is similar to TSP, but the surface coating is modified to reflect the pressure distribution via the “oxygen quenching”-mechanism. Residual and parasitic temperature effects are compensated. Similar to pressure taps, the transition position can partly be detected as a by-product, e.g. see Weiss et al. [234] for a rotor test with steady transition positions.

2.2.4 Direct skin friction measurements

Direct skin friction measurements provide the most desirable data for any boundary layer problem. A possible approach is using sunk piezoelectric balances on which a small surface (“movable wall element”) is mounted. The acquisition of a moving boundary layer transition seems feasible, since small-floating mass, fast-response gauges are possible [93]. However the practical difficulty of achieving the precise tolerances and low noise for this measurement mean that not much data is available [186], and has not yet been used for moving boundary layer transition. The sensors also have a temperature and acceleration sensitivity which must be compensated. Another method of skin friction measurement is given by shear-sensitive liquid crystals [63], but these have also not yet been used for dynamically moving boundary layer transition.

2.2.5 Comparison of methods

Table 2.1 provides a short comparison of the most important measurement techniques for unsteady BL transition positions applicable to rotor flows, listing their main advantages (+) and disadvantages (–), and providing guidelines for future experiments. It is noted that the last section includes fast-response DIT infrared methods, which are the main topic of the current work to be discussed in Sec. 3.1.3, and which are included here for the sake of completeness.

hot-films

- + well-established and well-understood principle
 - + very high frequency range provides deeper insight into the flow beyond transition position
 - + suitable as reference for optical measurement techniques
 - + automated data analysis techniques available, but different from steady analysis
 - extensive model instrumentation, application to rotors requires telemetry or on-board data acquisition systems
 - low spatial resolution, limited number of sensors
 - surface roughness and sensor heating probably affect flow
-

pressure sensor-based techniques (σC_p)

- + transition detection as a by-product of measuring pressure or lift distributions
 - + suitable as a fast-response reference for optical measurement techniques
 - + data post-processing is simple and can be automated
 - + broadbanded response, results are robust to filtering effects
 - extensive model preparation with careful sensor layout
 - subscale models require miniaturized pressure sensors, no or limited possibilities for sensor repair during the tests
 - low spatial resolution, limited number of sensors
 - pressure tap can affect BL transition
-

temperature-sensitive paint (TSP)

- + 2D measurements with very high spatial resolutions possible
 - + camera and optics equipment less costly than IR cameras
 - + surface coating can be polished for a very low surface roughness
 - delicate surface coating, partly including additional base/insulation layers, total thickness $\sim 50 \mu\text{m}$ to $100 \mu\text{m}$
 - methods for unsteady measurements under development, may require validation with a reference technique
-

unsteady infrared techniques (DIT)

- + comparably low effort for experimental setup and model preparation
 - + particularly suitable for large- and full-scale testing
 - + non-intrusive technique
 - + 2D measurements with high spatial resolution (but lower than TSP)
 - additional thermal measurement lag
 - requires temperature difference between surface and flow, i.e. heating
 - IR spectrum susceptible to reflections from the measurement environment
 - comparably new technique, may benefit from comparison to reference sensors
-

Table 2.1: Main advantages (+) and disadvantages (–) of measurement techniques for unsteady BL transition.

2.3 Additional experimental methods for full-scale rotors and free-flying helicopters

2.3.1 Blade deformation measurements

Helicopter rotor blades are subject to significant elastic deformations, which are dominated by the interrelation between elasticity, aerodynamic loads, and inertia. A detailed understanding of the blade deformations is crucial to the blade design and the resulting performance, acoustics, and operational safety of a main rotor system. Amongst others, the blade dynamics also affect the prediction of the boundary layer transition, for example, requiring aeroelastic blade models in “comprehensive codes” as used later in Secs. 3.5 and 3.6.

An optical deformation measurement of the five-bladed prototype rotor “GRC1” was conducted by Wolf et al. [9] as part of the LuFo V-2 project “CHARME”. The rotor was flown on the Airbus Bluecopter™ test bed, but the deformation tests were conducted at a whirl tower facility of the Airbus Donauwörth site in 2016, see Fig. 2.7. The GRC1 design was later adopted in the “D-3” version of the Airbus H145 approved in 2020.



Figure 2.7: GRC1 prototype rotor on the Bluecopter™ demonstrator (left) and whirl tower (right), Kus et al. [124].

The blade deformations during whirl tower operation were measured with stereo pattern recognition (SPR), which is based on a stereo-optical triangulation of the three-dimensional position of fiducial marker on the blade surface. Similar approaches have been applied in wind tunnel tests of large-scale rotors, for example during the HART II campaign [188] or the UH-60A airloads campaign [36].

The GRC1 SPR setup, see Fig. 2.8, consisted of two “pco.dimax S4” high-speed cameras and two LED light arrays with a luminous flux of 72 000 lm, placed about 7 m below the rotor plane. Image bursts were triggered in each rotor revolution, tracking a reference blade at 1250 Hz over an azimuthal range of $\Delta\Psi \approx 20^\circ$.

Fig. 2.9(a) is an overlay of two sample images from camera 1 for low and high thrust settings. The different flap displacement at the blade tip is clearly visible. The rotor tip radius is 5.4 m, and the blade spins at 6.3 Hz.

Circular fiducial markers were applied to the lower side of the blade, arranged in 12 rows at different radii, with four markers per row arranged in chordwise direction. The samples point out several advantages of visible spectrum-imaging compared to infrared imaging,

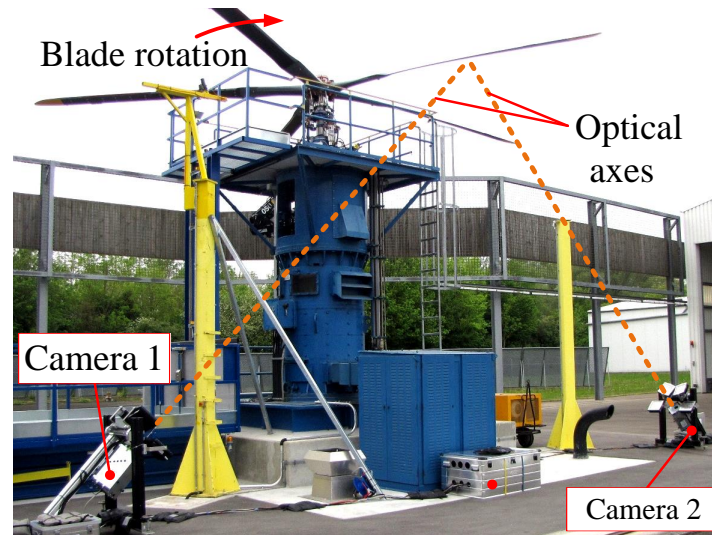
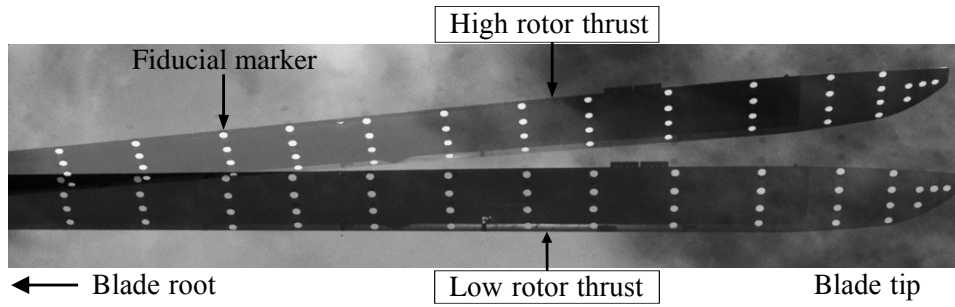


Figure 2.8: Stereo pattern recognition (SPR) setup with a dual high-speed camera system at the whirl tower, Wolf et al. [9].

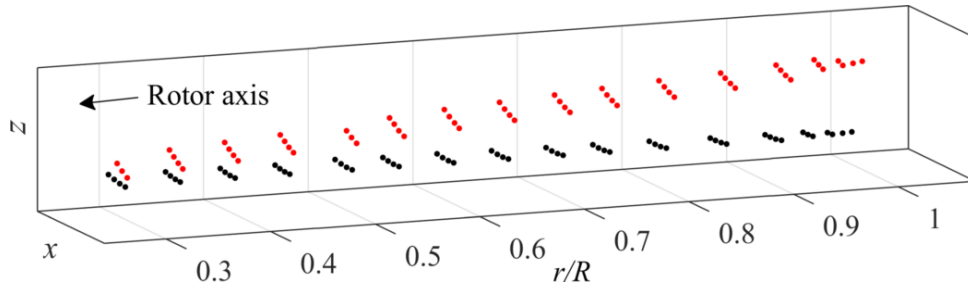
which are mainly connected to the maturity of the image sensor technology. First, the SPR images have a very good contrast despite a very low exposure time of only $4.35 \mu\text{s}$, which is about 10 to 50 times smaller compared to IR images used in this work. Consequently, the motion blur in the tip region is smaller than 1 mm or 3.5% of the marker diameter, $D = 28 \text{ mm}$. The markers are made from retro-reflective adhesive foil with a thickness of $110 \mu\text{m}$, and an effect on the BL transition was tolerated for this test. This can be avoided by embedding the markers into the outer CFRP layer, or by using a thinner foil at the cost of less optical contrast. Second, the image resolution and acquisition frequency in the visible spectrum is superior, enabling to visualize larger fields of view and finer details. The SPR image size is 4 Mpixel at 1250 Hz, compared to 0.3 – 1.3 Mpixel at 100 – 180 Hz for the high-speed IR cameras used in later sections of the current work. Both visible-spectrum and IR sensor technology was significantly improved over the last decades, but the comparably lower performance of IR cameras was more or less constant.

The 3D position of each marker and in each image pair was determined by a stereoscopic reconstruction of the calibrated camera system, see Fig. 2.9(b), and averaged over at least 20 successive rotor revolutions. In a next step, solid-body transformations were determined for the four markers in each blade section, and referenced to the local quarter chord position. The result is the flap (out-of-plane displacement), the lead/lag (in-plane displacement), and the pitch angle of the blade under loads. The measurement uncertainty was estimated using repetitive camera calibrations and precisely executed blade motions at zero rotor speed. When comparing different test conditions, the uncertainty is less than $\pm 1 \text{ mm}$ ($\pm 0.02\% R$) for flap and lead/lag, and $\pm 0.11^\circ$ for the pitch angle.

Figure 2.10 shows the SPR results of a GRC1 thrust polar using the collective setting of the swashplate, increasing the pitch input by a total of $\Delta\Psi = 14^\circ$. The blade expectedly bends in upward direction with an increasing thrust loading, Fig. 2.10(a), revealing the elastic deflection curve of the quarter chord. The maximum flap is in the range of $8\% R$. The lead/lag-deflection points in lag (aft) direction with increasing thrust, due to the increasing aerodynamic drag of the blades overcoming the centrifugal forces. The lead/lag-curves are



(a) Overlay of two images from camera 1.



(b) 3D view of the marker positions for low thrust (●) and high thrust (●).

Figure 2.9: Comparison of low and high rotor thrust settings, rotor frequency of $f = 6.3$ Hz.

almost linear for $0.3 \leq r/R \leq 1.0$, since the blade is stiff in the in-plane direction, and the largest part of the lag originates in the equivalent flexure lead/lag-hinge of the bearingless main rotor system. Figure 2.10(c) shows the elastic twist angle of the blade, defined as the local pitch angle minus the nominal geometric pitch angle commanded at the swashplate. The blades de-twist for larger thrust setting and with increasing radii due to a nose-down pitching moment. Amongst others, the shown experimental results were incorporated into the development and validation of aeroelastic blade models, with some examples given by Dieterich et al. [71].

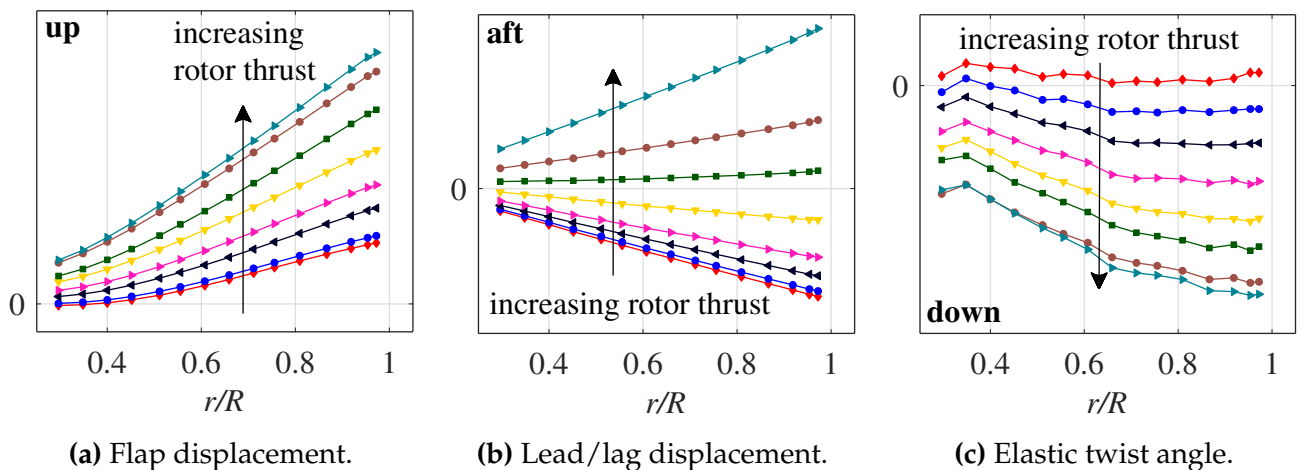


Figure 2.10: SPR results for a thrust polar of the GRC1 rotor, adapted from Wolf et al. [9].

The SPR flap results are partly affected by a low repeatability, which is a common problem for outdoor measurements also observed in other campaigns, and which predominantly originates in the atmospheric wind conditions. For a high-thrust long-term measurement

covering 300 rotor revolutions or about 50 s on a windy day, the dispersion of instantaneous flap displacement at $r/R=0.95$ is bounded by about ± 24 mm. The dispersion in both lead/lag displacement and pitch angle is much smaller, ± 0.7 mm and $\pm 0.09^\circ$. Figure 2.11 shows the flap signal (—) in normalized units, together with the root bending moment of the blade as acquired by strain gauges (—). Both signals are not expected to be identical, but a qualitative agreement is apparent, with a statistical coherence of about 86%. This example shows that even in the presence of adverse environmental conditions, the quality of the results can still be ensured by time-resolved and synchronized data acquisition. Unfortunately for the current case, instantaneous wind information was not available.

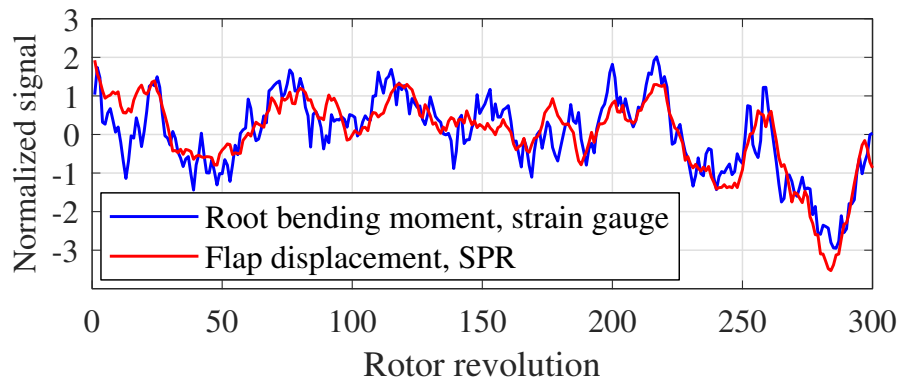


Figure 2.11: Correlation between SPR flap result and root bending moment.

Optical blade deformation measurements on free-flying helicopters are even more challenging than on full-scale whirl tower tests, due to the limited options for camera integration. A possible solution is a rotating camera system mounted at the rotor hub. A prototype system developed by Boden et al. [49] was also tested during the GRC1 whirl tower campaign, see Fig. 2.12.

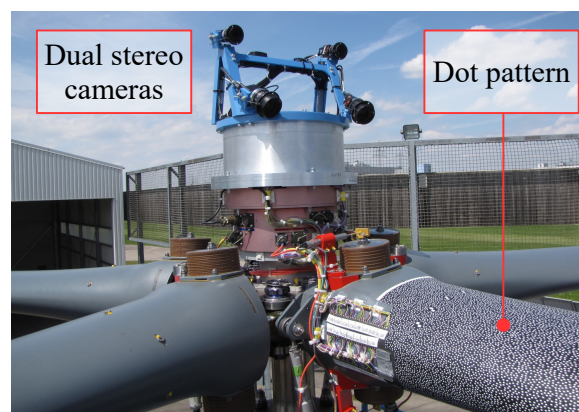


Figure 2.12: Prototype of a hub-mounted camera system for blade deformation measurement, Ref. [49].

The setup features two sets of stereoscopic cameras for the root region and the outboard region of the blade, respectively. The cameras observe a dot pattern on the reference blade's upper surface. In comparison to the ground-based SPR setup, the viewing angles of the hub cameras are very oblique, and the stereo camera axes are almost collinear. Miniaturized cameras and data recorders are available, but the entire structure must withstand strong

rotational forces. The results of this system are promising, but the setup and image post-processing is still under development. For a possible application in flight tests, additional regulatory and safety concerns must be considered.

A few additional publications used single-camera systems for in-flight measurements, only focusing on a reduced subset of the entire blade deformation data. For example, Bauknecht et al. [44] externally mounted a miniaturized camera system to the fuselage of an ultralight coaxial helicopter. The system evaluated the minimum separation distance between the upper and lower rotor planes in the tip region during forward flight and maneuver flight. Voigt et al. [224] applied a similar idea to the intermeshing rotors of an unmanned helicopter with a maximum take-off weight of 85 kg. In this case, a rotating camera was attached to a blade root, enabling data acquisition over the entire rotor azimuth.

2.3.2 Wake aerodynamics

The availability of experimental data for rotor wake aerodynamics of free-flying helicopters is comparably good, due to its relevance for the performance and operational safety of rotorcraft. The involved flow physics are summarized by topical reviews, for example see Komerath et al. [120]. The overall wake layout will depend on whether the helicopter is in hover or forward flight, and on its height above ground:

- **In ground effect (IGE)²:** The wake is affected by the presence of a ground surface, which deflects the vertical rotor flow into the horizontal direction. Flying in ground effect results in a strong reduction of the power requirement, but also in detrimental effects such as vibrations, a reduced visibility due to sediment pickup (“brownout”), or hazards for nearby ground personnel. IGE also significantly reduces the complexity of experimental setups.
- **Out of ground effect (OGE):** Larger distances to the ground are relevant for cruise flight or maneuvering flight. OGE experiments usually require the integration of on-board sensors, ground-based camera systems with long-range optics, or chase aircraft.

Several measurement techniques known from laboratory or wind tunnel environments have been successfully adapted to flight experiments, which favor “simple” methods reducing the interference with flight operations. Wadcock et al. [225] applied acrylic yarn tufts to the fuselage and ground surfaces during IGE flight tests with a Sikorsky UH-60 helicopter. The surface flow pattern was analyzed with a view to brownout conditions. Silva and Riser [205] measured the outwash flow field of a hovering Boeing CH-47D helicopter with an array of eight ultrasonic anemometers installed on a remote-controlled cart, focusing on the identification of hazardous regions for approaching ground personnel.

A very common technique for flow diagnostics is to optically track the motion of tracer particles (“seeding”) added to the flow. For example, Wong and Tanner [236] demonstrated a photogrammetric reconstruction of the dust cloud developing during the landing approach of an Sikorsky EH-60L in brownout conditions, adding colored chalk to the natural dust

²The Federal Aviation Administration defines IGE for a main rotor hub height of one rotor diameter and below [79]. However, this definition is somewhat arbitrary, and experiments with multiple helicopters showed that a reduction of the engine power can be measured up to at least two diameters above ground [97].

in a desert environment. A similar approach by Sugiura et al. [212] analyzed the wake development of an Airbus EC145 helicopter in IGE forward flight by means of smoke visualization. The results were combined to ultrasonic anemometer data and compared to numerical simulations. Artificial smoke was also used by Kutz et al. [125] to track the blade tip vortices of a Hughes 300C hovering in ground effect. An extensive study by Teagar et al. [216] used on-board smoke generators on five different helicopters with maximum takeoff masses between 3500 kg and 31 500 kg, visualizing the far-field wake vortices developing in OGE forward flight. The smoke trails were analyzed both qualitatively, via photographs as in Fig. 2.13, and quantitatively, via ground-based long-range laser doppler velocimetry. The report analyzes the hazards of wake vortex encounters and suggests separation distances for following aircraft.

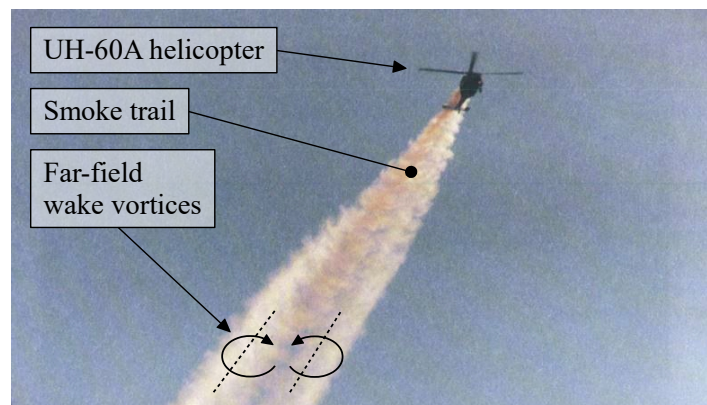


Figure 2.13: Wake visualization of a UH-60A helicopter in forward flight, adapted from Teagar et al. [216].

A quantitative evaluation of seeding patterns is also the basis of particle image velocimetry (PIV). The application of PIV to full-scale helicopters was pioneered by Raffel et al. [169], and later refined by Kindler et al. [117] and Schwarz et al. [27]. The three studies concentrated on the development and structure of blade tip vortices, and the valuable and high-quality PIV data came at the cost of a large experimental effort and comparably small measurement areas.

An effective and efficient measurement technique for blade tip vortices is the background oriented schlieren-technique (BOS). BOS visualizes inhomogeneities in the air's optical refractive index, resulting from density gradients within the vortex core via the Gladstone-Dale relation, by means of apparent distortions of a background pattern. The method was developed and applied to free-flying helicopters by Raffel et al. [170] and Richard and Raffel [175]. Since then, several extensions and improvements have been proposed for full-scale helicopter aerodynamics, including

- the use of cameras with color image sensors and adapted evaluation algorithms to increase the measurement resolution and precision, see Leopold [134],
- in-flight OGE measurements using natural background structures and on-board cameras or chase aircraft, see Kindler et al. [116] or Bauknecht et al. [42, 44],
- the application of high-speed camera systems and retro-reflective artificial backgrounds for time-resolved measurements, see Schwarz et al. [27],

2.3. Additional experimental methods for full-scale rotors and free-flying helicopters

- and a 3D reconstruction of the vortex system using the projections in multiple directions, see Bauknecht et al. [10].

In addition to helicopter aerodynamics, BOS has made its way into other aerospace applications, such as visualizing the shock system in supersonic flight [99], or jet engine diagnostics via an analysis of the thrust flow [96].

The following section summarizes important key aspects of an IGE measurement campaign conducted in 2019 with DLR’s research rotorcraft, the MBB/Eurocopter Bo105 and the Airbus EC135, at the apron of the Braunschweig regional airport. Important specifications of both helicopters, which will also be used in the DIT flight tests in Sec. 3.6, are given in Tab. 2.2. Wake velocities are normalized with the hover-induced velocity, $V_h = V_{tip} \sqrt{C_T/2}$, which was estimated assuming that the rotor thrust equals the helicopters’ gross weight. The weight was interpolated via the known fuel loads at take-off and landing. The focus will be set on the performance of the schlieren imaging system, and on the visualization of blade-vortex interactions in forward flight, which may play a role in the boundary layer transition process. Additional details unrelated to the current work can be found in Wolf et al. [1].

rotorcraft	EC135	Bo105
main rotor radius, R , m	5.10	4.91
rotor frequency, f , rad/s	$2\pi \cdot 6.58$	$2\pi \cdot 7.07$
number of rotor blades	4	4
airfoil	DMH3/4	NACA 23012
chord length, m	0.288	0.270
blade tip planform	parabolic	square
blade twist, $^\circ/R$	-10	-8
gross mass, kg	2760-2910	2070-2230
hover-ind. vel., V_h , m/s	11.8-12.1	10.6-11.1



EC135



Bo105

Table 2.2: Specifications of DLR’s test rotorcraft, see also Refs. [112, 228].

Figure 2.14(a) shows the EC135 hovering in the test region, and the details in the lower part illustrate the three measurement techniques applied in this study. The helicopter’s position is acquired by stereo pattern recognition (SPR) using fiducial markers on the fuselage. The SPR principle is the same as described in Sec. 2.3.1, and the stereo camera system tracks the helicopter’s position and attitude angles in a viewing field sized $10\text{ m} \times 10\text{ m}$ with a frequency of 10 Hz. An array of up to 17 fiber film velocity probes of type “TSI 1201” was set up in front of the helicopter. The probes operate after the principle of constant temperature anemometry (CTA). Each probe features a platinum film sensor wrapped around a quartz cylinder, with a diameter of $50.8\ \mu\text{m}$, and a sensing width of 1.27 mm. The sensor surface is resistively heated to approximately 560 K, and the required electrical power is related to the

convective heat transfer and, thus, the flow velocity. The sensors were set up to measure the instantaneous velocity value in the x, y -plane, $V = \sqrt{u^2 + v^2}$, with a frequency limit of 10 kHz. Additional technical details, such as the sensor calibration or the compensation of ambient temperature drift, are described in Ref. [1]. It is noted that CTA fiber films are similar to the better-known but much thinner hot wires. In comparison, the film sensors are less sensitive to particle impacts in contaminated flows, with no sensor defects occurring over a two-week test campaign.

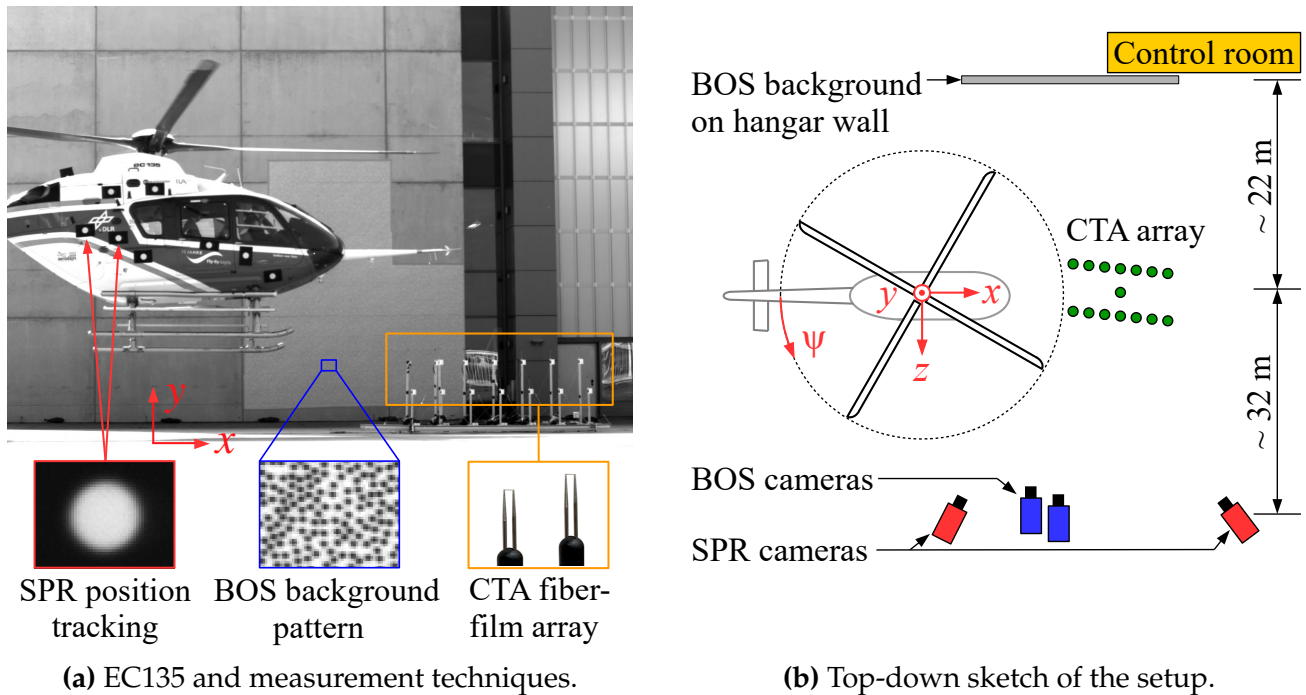


Figure 2.14: Experimental setup of the rotor wake study, Wolf et al. [1].

The third measurement technique used a high-speed BOS system to visualize density objects within the rotor wake, particularly the blade tip vortices. Two cameras of type “Phantom VEO 640” were mounted side-by-side, pointing through the rotor wake at an artificial background with a random dot pattern affixed to a hangar wall on the opposite side of the test section in a distance of about 54 m, also see the top-down sketch in Fig. 2.14(b). Images with a size of 2560×1600 pixel per camera were acquired at 420 Hz. The exposure time of $50 \mu\text{s}$ is about 11.5 times larger than the SPR blade deformation exposure in Sec 2.3.1, which is acceptable since flow structures within the wake move slower than the rotor blades. Apparent x - and y -shifts of the background pattern caused by schlieren were detected by cross-correlating a measurement image to an undisturbed reference image using the PIV software “LaVision DaVis 8.4”. An iterative multipass approach resulted in a final grid spacing of 3.4 mm at the helicopter reference position. A high resolution was possible since the background pattern was specifically adapted to the viewing geometry. The dots are tightly spaced and have a diameter of 3 – 4 pixel in the camera images, as required by the correlation algorithm. The pattern was printed on a retro-reflective carrier foil illuminated by LED spots to increase the contrast and, thus, to minimize random correlation errors defining the schlieren detection limit.

Instantaneous BOS samples for the EC135 and Bo105 in hover conditions are shown in Figs. 2.15(a) and 2.15(b). The rotor hub heights normalized with the rotor radius are similar

in both samples, $h = 0.78$ and $h = 0.83$. The fields of view from both cameras are slightly overlapping, with a vertical orientation of the upper camera and a horizontal orientation of the lower camera. The combination yields an “L”-shaped measurement region designed to follow the curved trajectory of the tip vortices. The background displacement data after cross-correlation relates to the integral of the spatial density gradients, $\partial\rho/\partial x$ and $\partial\rho/\partial y$, along the lines of sight. The blade tip vortices have a density minimum in the center, with the steepest density gradients located in a distance of about 0.7 core radii to the center (see Braukmann et al. [12] for further discussions). Hence, the divergence operator is applied to the 2D displacement field. The result represents the Laplace-transformed density field,

$$\nabla \cdot (\nabla\rho) = \frac{\partial^2\rho}{\partial x^2} + \frac{\partial^2\rho}{\partial y^2}, \quad (2.2)$$

which is shown in Fig. 2.15 in arbitrary units. Local minima of this scalar quantity mark the vortex center region, as seen by black filaments. Both BOS results were chosen so that one of the rotor blades points in forward direction. The blade is trailed by a tip vortex with a wake age of 0° right after its formation, labeled as “I”. The vortex of each blade passage convects downstream along the wake’s slipstream boundary, resulting in local wake ages of about $90^\circ, 180^\circ, 270^\circ, \dots$ (II,III,IV,...) in the BOS field of view due to the four-bladed rotors. Due to the cameras looking slightly upwards, and due to the rotors turning counterclockwise when viewed from above, the upper branch of each vortex lobe belongs to the advancing side of the rotor plane.

The EC135’s wake, Fig. 2.15(a), maintains an almost equidistant tip vortex spacing, but the tip vortices develop individual instabilities as seen by increasing wave-like deflections of the vortex core. The maximum detectable wake age in instantaneous BOS samples is between about 450° (VI) and 540° , before break-down effects reduce the tip vortex strength below the BOS detection limit.

The Bo105 hover sample, Fig. 2.15(b), is qualitatively similar to the EC135 result. This was expected since the helicopter characteristics are similar, for example, in terms of total mass and number of rotor blades. However, the Bo105 tip vortices were predominantly affected by cooperative instabilities, which is revealed in a high-speed BOS time series. The details on the right side of Fig. 2.15(b) show the “vortex pairing” or “leapfrogging” of vortices IV and V over a quarter revolution, $\Delta t = 35.7$ ms. Vortex pairing was found on smaller-scaled rotors before. The mechanism is relevant for both helicopters and wind turbines, and was investigated in laboratory experiments by Bolnot et al. [52]. Small irregularities of the initial vortex spacing are amplified until pairs of vortices start an orbital motion around each other, which may lead to a reversed order, merging, or break-down. In the current case, the systematic vortex pairing of the Bo105 helicopter is assumed to originate from an imperfect blade tracking, which is supported by the helicopters’ maintenance protocols.

The CTA velocity signals provide further details regarding the role of tip vortices in the wake flow. Figure 2.16 shows three selected CTA velocity spectra calculated from the same hover test points as in Fig. 2.15, accounting for a large time interval of 60 s. All sensors are located within the rotor wake, and at $y/R = 0.3$ or below. The spectra show a very flat and broad-banded distribution, which almost perfectly matches Kolmogorov’s well-known $-5/3$ -law (– –) for frequencies between about 5 Hz and 5000 Hz, indicating well-developed

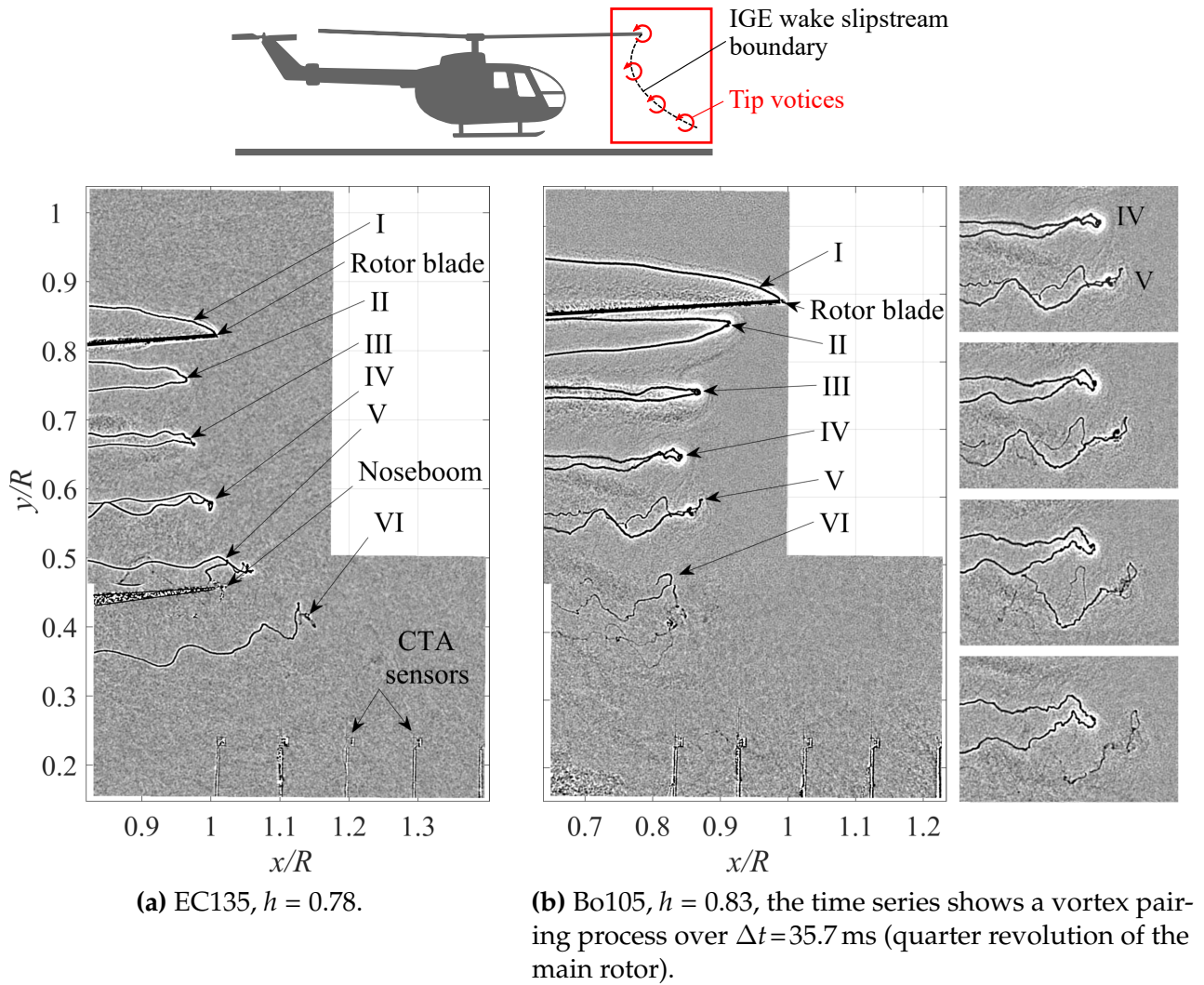


Figure 2.15: Instantaneous BOS visualizations of the rotor wake in hover [1], the tip vortices are labeled (I,II,III...) according to the wake ages of ($0^\circ, 90^\circ, 180^\circ \dots$) [1].

turbulence. It was checked that all values are above the CTA system's noise floor, which is at about 10^{-10} 1/Hz in the shown normalized unit.

One of the Bo105-signals (—) in Fig. 2.16 was chosen due to its location in the wake's slipstream boundary, along the projected path of the tip vortices. Even though the tip vortex-pairs dissolve below the BOS detection limit before reaching the CTA sensors, their remnants can still be tracked further downstream by means of a spectral peak with a 2/rev-periodicity. In contrast, the corresponding EC135-signal in the wake's slipstream (—) is very similar, but the tip vortex-related peak is at a 4/rev-periodicity indicating the passage of individual tip vortices of the four-bladed main rotor. The third signal (—) is located within the Bo105 wake flow and inboard of the slipstream boundary. The overall spectral content is similar to the other two signals, including the correspondence to the Kolmogorov-law, but it lacks distinct spectral peaks connected to the passage of tip-vortex structures.

Additional insight into the spectral 2/rev-peak within the slipstream boundary of the hovering Bo105 is given in Fig. 2.17. The figure shows two segments of the raw velocity signal (—), each sample covering two rotor revolutions ($\Delta t = 0.28$ s). The 2/rev-periodicity is clearly visible in the left sample 1, with four individual wave packages corresponding to the

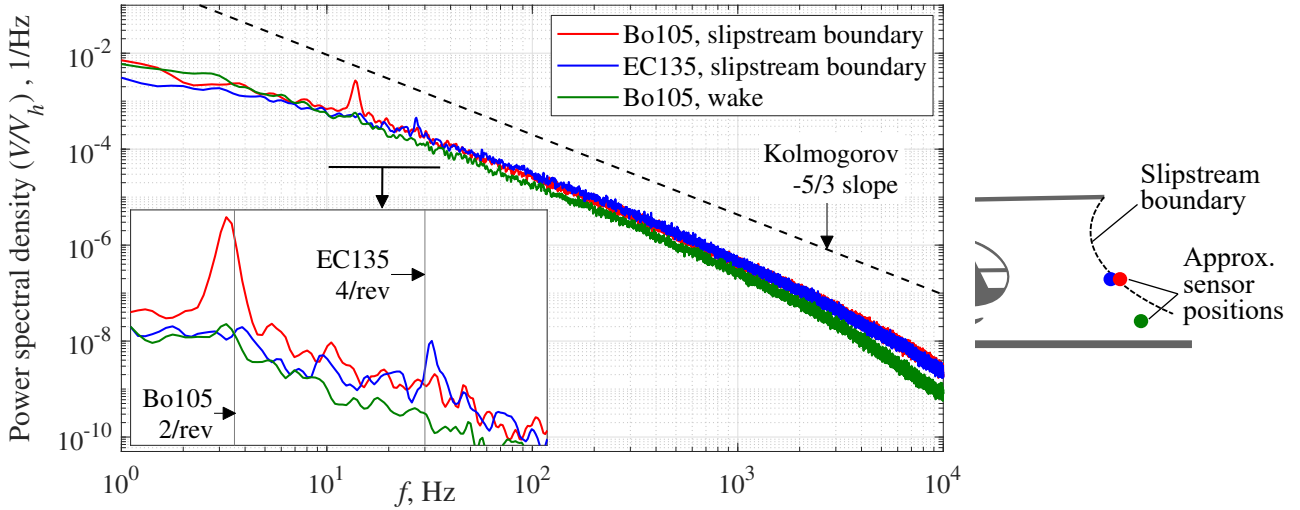


Figure 2.16: Fiber-film velocity spectra for the EC135 and Bo105 hover test cases in Fig. 2.15.

extrapolated trajectories of tip vortex-pairs seen in the synchronized BOS sequence. During each passage, both velocity levels and velocity fluctuations are increased. The two other signals in Fig. 2.17 correspond to additional CTA sensors staggered in rotor-circumferential direction, $\Delta z/R=0.007$ (—) and $\Delta z/R=0.126$ (—). The coherence of the three sensor signals underlines the circumferential alignment of the tip vortex-structures. Since the hovering helicopter’s position, the slipstream boundary, and the vortex pairing are not perfectly stationary, the phenomenon is not continuously observed at a fixed CTA position. This is shown by the right sample 2, which was taken by the same sensors within the same test run.

Additional CTA evaluations, including a discussion of time-averaged velocity profiles, the cross-spectral coherence at multiple sensor locations, and an analysis of the wind influence in hover test cases can be found in Ref. [1].

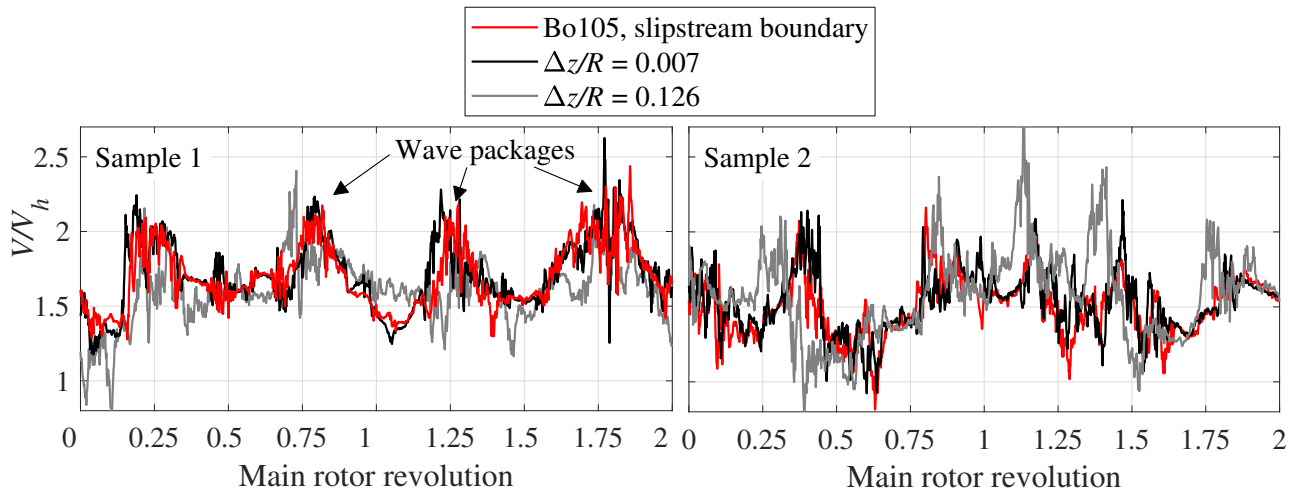


Figure 2.17: Samples of the CTA velocity signal in the Bo105 slipstream boundary for hover conditions, $y/R=0.3$, corresponding to the spectral density (—) shown in Fig. 2.15.

Level flight test cases were conducted with forward velocities, V_x , between 3 m/s and 11 m/s. Both rotorcraft were piloted manually according to target velocities and ground clearances, and each run was assessed in a posteriori analyses of the SPR trajectory data. The

helicopters traverse the static measurement region quickly, but the high image rate of the BOS system allows the collection of sufficient data. Examples are given in the schlieren overviews in Fig. 2.18, which were compiled by merging ten individual, successive BOS images with the same azimuth angle of the main rotor. The result shows the interleaving helices of the main rotor tip vortices, along with the tail rotor tip vortices in case of the Bo105, and the engines' exhaust plumes. The helicopter structures block the background pattern, yielding a random but non-zero noise signal when correlated with the reference image. Due to the small interrogation windows and grid size, this effectively masks even fine structural details such as the skid struts or antennas without further post-processing.

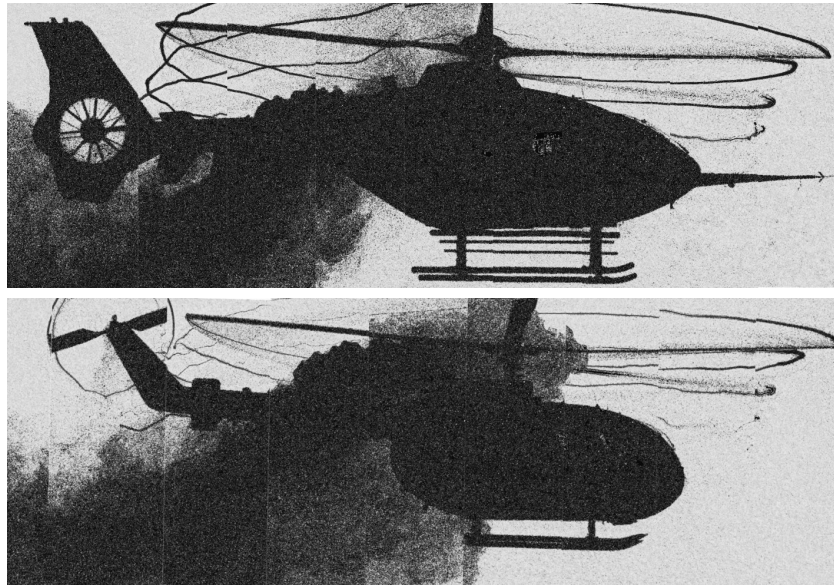


Figure 2.18: Contrast-enhanced BOS image compilations of the EC135 (top, $h = 0.87$, $V_x = 9.1$ m/s) and Bo105 (bottom, $h = 0.89$, $V_x = 5.1$ m/s) in edgewise flight [1].

The transition from hover into forward flight changes the layout of the main rotor wake and introduces a wake skew angle. The presence of a ground surface for IGE conditions adds further complexity depending on the normalized advance ratio, $\mu^* = V_x/V_h$. Figure 2.19 (left column) sketches four different wake layouts as defined by Sheridan and Wiesner [203] or Curtiss et al. [69].

Small advance ratios result in a hover-like radial outwash, $\mu^* \leq 0.4$ in Fig. 2.19(a). A large-scale recirculation area emerges ahead of the helicopter for increasing forward flight velocities. Its center can be either in front of the rotor plane, “recirculation” for $0.4 < \mu^* \leq 0.7$ in Fig. 2.19(b), or beneath the rotor plane, “ground vortex” for $0.7 < \mu^* \leq 0.9$ in Fig. 2.19(c). The momentum fluxes associated with these flow patterns are assumed to cause sediment pick-up in brownout conditions, also see the model- and full-scale investigations by Schwarz et al. [195, 27]. The ground vortex disappears for $\mu^* > 0.9$, see Fig. 2.19(d), and is replaced by a flow field similar to OGE forward flight, indicating a reduced influence of the ground surface on the flow pattern ahead of the helicopter.

The different flow regimes agree with the CTA velocity levels, as shown in the right column of Fig. 2.19 for the Bo105. The rotor hub height is between $h = 0.96$ and $h = 1.02$ for all cases, slightly adding ground clearance in comparison to the hover tests for safety considerations. Each case comprises the signals of seven fiber film-sensors (—), placed in a

2.3. Additional experimental methods for full-scale rotors and free-flying helicopters

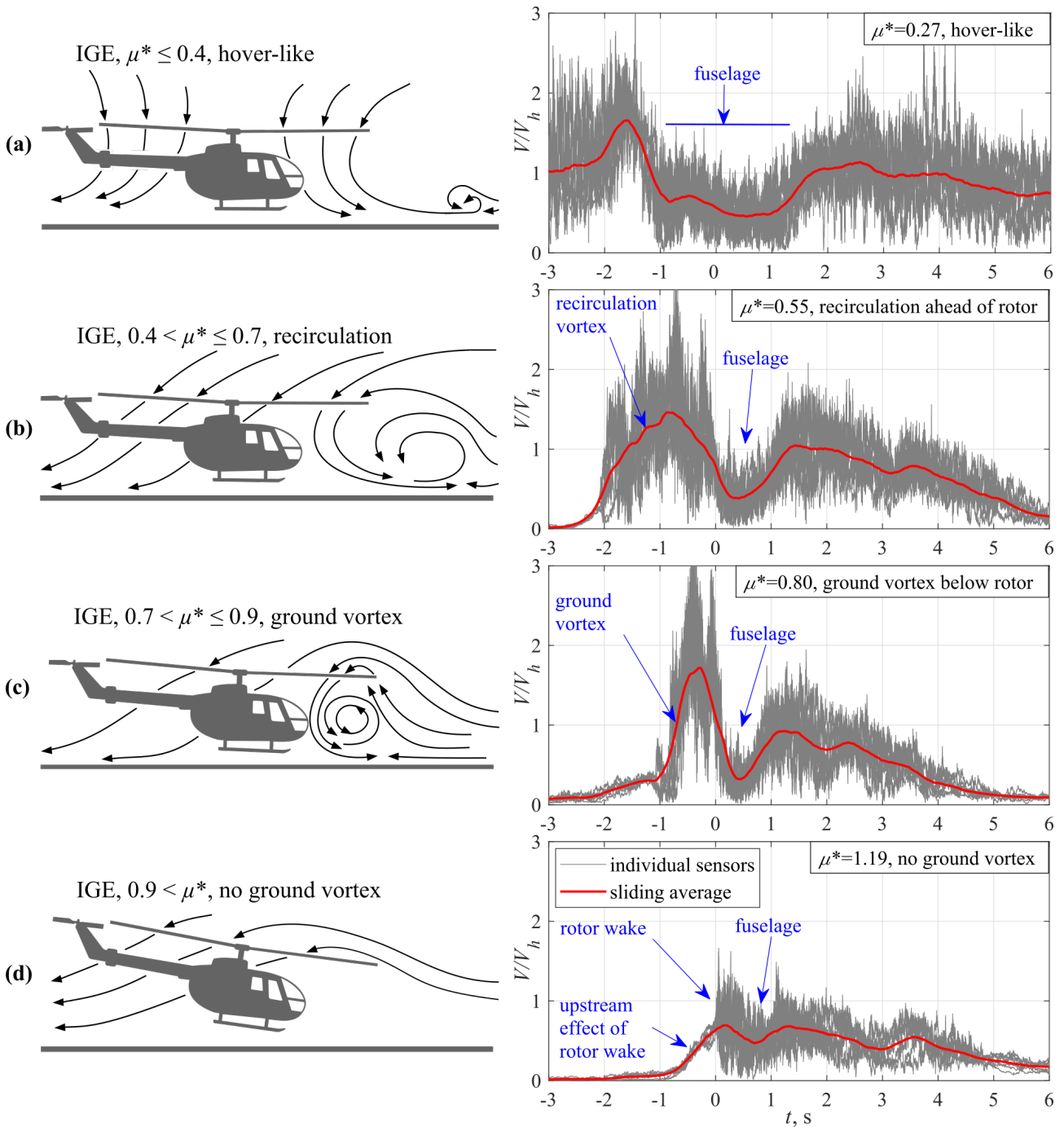


Figure 2.19: Layout of the IGE rotor wake as function of the normalized advance ratio after Sheridan and Wieser [203] (left column), and velocity signal $h = 0.19$ above ground, CTA sensor data adapted from Wolf et al. [1] (right column).

horizontal line along the flight path at $y = 0.19 R$ above ground. The signals were time-shifted so that $t = 0$ is when the rotor hub passes each sensor. The average of all sensors (—) was additionally filtered with a sliding average window sized $\Delta t = 0.5$ s.

The hover-like case, $\mu^* = 0.27$ in Fig. 2.19(a), results in a radial outwash profile ahead and behind of the helicopter. The entire velocity footprint is larger than the shown time interval and gradually trails off after about 15 s. The fluctuation level is high in comparison to the other cases, and there is a small velocity overshoot ahead of the rotor. The fuselage then shields the CTA sensors from the wake at $-1 \text{ s} < t \leq 1 \text{ s}$, resulting in a low-velocity plateau. The formation

of a recirculation vortex is noted at $\mu^* = 0.55$ in Fig. 2.19(b) by means of a distinct velocity peak of $V/V_h \approx 1.5$ at $t = -0.87$ s. Considering the helicopter's flight velocity of $V_x = 6.04$ m/s, this peak is $1.07 R$ ahead of the hub and, hence, slightly outside the rotor plane. The flow for $\mu^* = 0.80$ in Fig. 2.19(c) is qualitatively similar to $\mu^* = 0.55$ but squeezed into a shorter time frame. The velocity peak of $V/V_h \approx 1.75$ is now at $t = -0.28$ s. This is $0.49 R$ ahead of the hub when considering the flight velocity of $V_x = 8.65$ m/s, indicating that the ground vortex is indeed under the rotor plane. The highest flight speed, $\mu^* = 1.19$ in Fig. 2.19(d), significantly alters the CTA footprint by means of lower average velocities, lower fluctuation levels, and the absence of a large-scale recirculation area in front of the helicopter. The rotor wake hits the sensors at about $t = 0.1$ s, as seen by a sudden increase of the velocity fluctuations. This means that due to the wake skew, the rotor flow reaches the sensor positions slightly after the hub has passed. The flow is accelerated ahead of the wake boundary and with low velocity fluctuations, $-1 \text{ s} < t \leq 0.1 \text{ s}$, due to entrainment effects, which is a unique feature of this flight state. The shown CTA results were repeated in multiple test runs with good agreement [1].

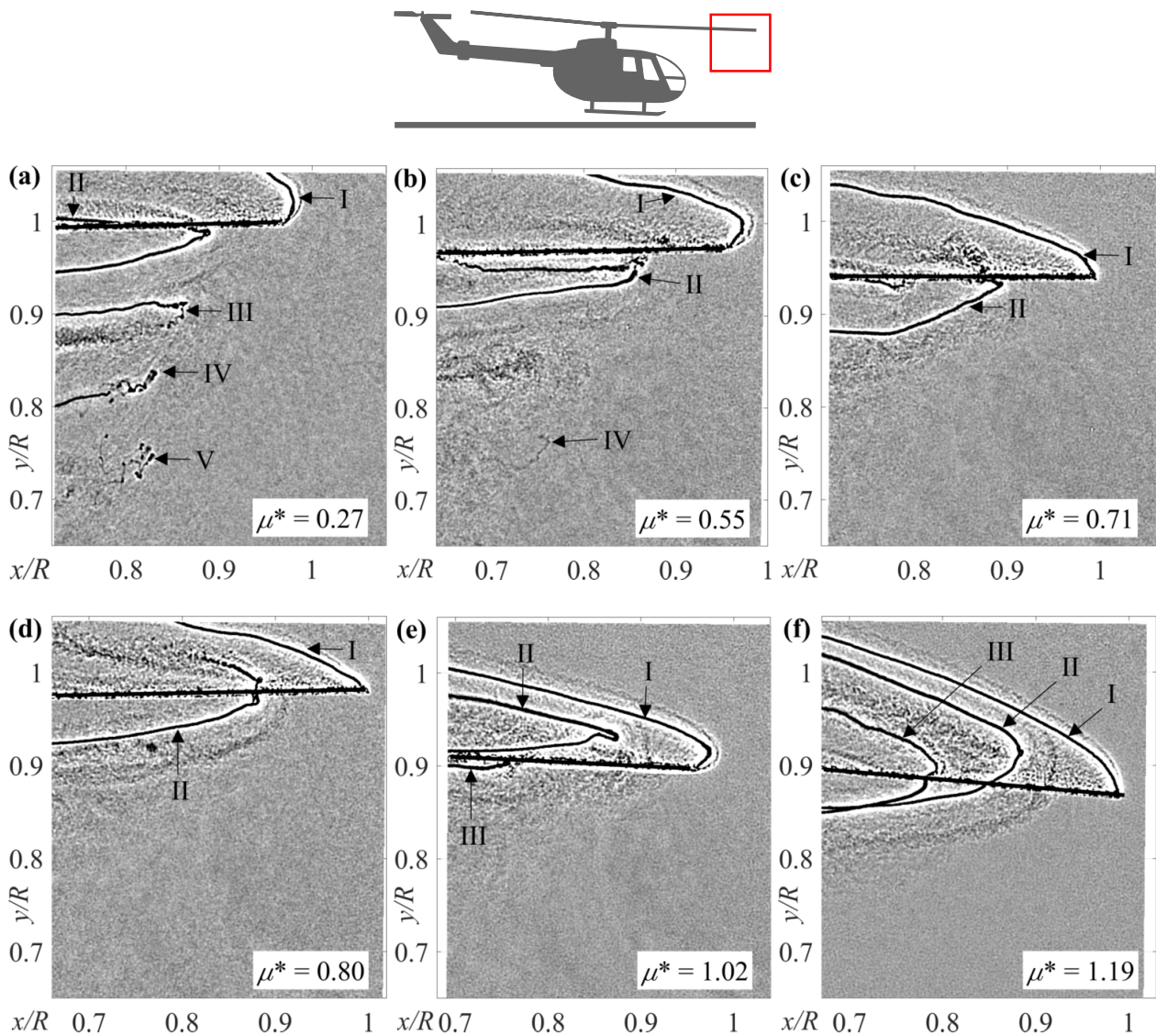


Figure 2.20: BOS visualizations in the frontal part of the rotor plane, blade-vortex interactions depending on the normalized advance ratio, adapted from Wolf et al. [1].

The different wake flow layouts affect the velocity distribution in the rotor plane. Edge-wise OGE flight is covered by inflow models, for example see Chen [62]. A cosine term in longitudinal direction predicts an upwash component over the bow, at a azimuth angle of $\Psi = 180^\circ$. Depending on the wake skew and the advance ratio, this upwash term can be large enough that the flow direction in the tip area is reversed and points bottom to top. For IGE, the flow field of the ground vortex further intensifies the upwash effect, also see the sketch on the left side of Fig. 2.19(c). The altered velocity distribution in the tip area affects the trajectory of the blade tip vortices, as shown in Fig. 2.20 via BOS details for normalized advance ratios between $\mu^* = 0.27$ and $\mu^* = 1.19$. It is noted that four of the six μ^* -values correspond to the CTA results shown in the preceding Fig. 2.19.

For a small advance ratio of $\mu^* = 0.27$, see Figure 2.20(a), the wake system is hover-like with a detectable vortex age up to 360° at label V, but the helicopter's forward motion increases the wake skew. In particular, the tip vortex II at an age of 90° is closer to the rotor plane but further inboard in comparison to the hover results, see Fig. 2.15(b). This trend intensifies when increasing μ^* to 0.55, see Fig. 2.20(b). Vortex II now almost touches the rotor plane, and the beginning blade-vortex interaction (BVI) leads to faster breakdown of the subsequent vortex system. Vortex III is already dissipated, but some scattered and incoherent vortex filaments are visible at an age of about 270° , label IV. The blade exactly hits the preceding tip vortex when $\mu^* = 0.71$, as shown in Fig. 2.20(c), and the advancing-sided (upper) branch of vortex filament II was erased due to BVI. A further increase of the forward velocity and the connected upwash velocity lifts the tip vortex sheet above the rotor plane, see Figs. 2.20(d) to 2.20(f). At $\mu^* = 1.02$, vortex II is above the rotor plane and the rotor blade hits the vortex filament III at an age of 180° . At $\mu^* = 1.19$, both vortices II and III are located above the rotor plane. Even though BVI is not visible in this image, an analysis of the schlieren image time series shows that the small miss distance between rotor blades and tip vortices induces disturbances, which cause vortex III to dissolve shortly after the shown time instant.

Similar BVI flow patterns were also found in frontal part of the EC135 rotor plane. Additionally in the range of $0.2 < \mu^* \leq 0.7$, a tip vortex-vortex interaction was found close to the Bo105 tail rotor, as shown in Fig. 2.21. The retreating (lower) branch of the main rotor vortex interacts with the upper branch of the tail rotor vortex creating a double-helix "corkscrew" pattern, and both co-rotating vortices merge for several milliseconds. This phenomenon is not seen at the EC135 due to the shrouded "Fenestron" tail rotor.

As concluding remarks, the current wake study demonstrates the suitability of BOS to gain detailed insight into full-scale free-flying rotor aerodynamics. Recent optimizations of the method itself, and improvements in high-speed imaging enabled the first systematic BVI study via BOS in forward flight. However, the ground-based camera system limited the test cases to IGE conditions and slow flight velocities. For example, BVI events in fast forward flight are expected in the rearward part of the rotor plane rather than in the frontal part. BVI has also been reported in BOS studies with natural backgrounds and airborne camera systems by Bauknecht et al. [42–44], but the results must be seen as individual "snapshots". This suggests further developments and improvements of airborne measurement techniques, with NASA's recent BOS systems for supersonic fixed-wing aircraft [99] being a step in this direction.

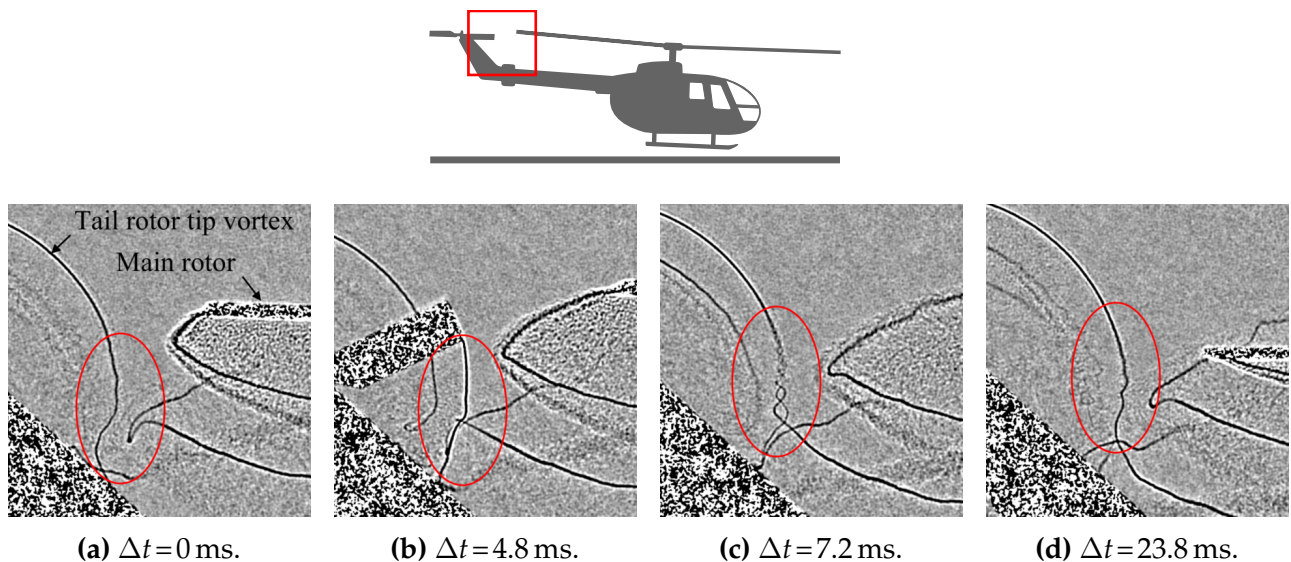


Figure 2.21: BOS time series showing a Bo105 vortex-vortex interaction, $\mu^* = 0.43$, see Ref. [1] for a detailed characterization of this process.

2.3.3 Dynamic stall measurements

The differences between the advancing and retreating sides of a trimmed rotor in edgewise flight, and the resulting periodic changes of the blade inflow conditions, not only affect the boundary layer transition. High local angles of attack can trigger dynamic stall, particularly for a highly loaded rotor. An example is given by the surface pressure analysis of a rotor blade, shown in Fig. 2.5, illustrating both laminar-turbulent BL transition and dynamic stall during a single revolution.

Early studies on 2D pitching airfoils in dynamic stall conditions, for example by McCroskey et al. [146], indicate a large hysteresis between up- and downstroke, a lift overshoot beyond static stall limits, and a strong nose-down pitching moment peak. The two latter aspects are connected to large-scale coherent dynamic stall vortices dominating the early stages of flow separation. A summary of the vast number of numerical or experimental work conducted over the last decades, including contributions by DLR’s helicopter aerodynamics group [16, 88, 20, 21, 25, 178, 198, 3, 6, 7], is far beyond the scope of the current work. An extensive topical review was provided by Smith et al. [207, 208] in the framework of the 2019 dynamic stall workshop at the Georgia Institute of Technology.

Flight test data for dynamic stall conditions is very scarce. This not only results from a difficult integration of measurement systems, such as pressure transducers, strain gauges, or accelerometers, but also from the fact that dynamic stall should be avoided in the helicopter’s flight envelope, particularly due to high pitch link loads. However, the laboratory rotor tests in Sec. 3.7 will show that differential infrared thermography (DIT) can be modified to detect dynamic stall on rotors, as a by-product of BL transition experiments.

Extensive research was conducted within the “UH-60A Airloads Program” at NASA Ames Research Center. An instrumented blade of the test helicopter, see Fig. 2.22, was equipped with 242 pressure transducers allowing to calculate the lift and pitching moment at nine radial stations. The research topics covered an analysis of the dynamic stall process as reported by Bousman [54]. Figure 2.23 shows dynamic stall-maps of the rotor plane for

two different flight states, indicating areas of separated flow in red coloring. The separation spreads from the retreating side with increasing load factor, n , and increasing advance ratio, $\mu = V_x/V_{tip}$. Note that the pattern is complex and consists of multiple separated areas, partly also on the advancing side in Fig. 2.23(b). The NASA tests were later revisited by Chaderjian [60], who evaluated the complex 3D flow field around the rotor blades with a high-fidelity coupled CFD/CSD simulation. Chaderjian suggests that the dynamic stall is partly triggered by local blade-wake or blade-vortex interactions (BVI), which agrees with other recent numerical studies.



Figure 2.22: Test helicopter of the UH-60A Airloads Program flying with an instrumented rotor blade, note the telemetry system on top of the rotor hub, Ref. [123].

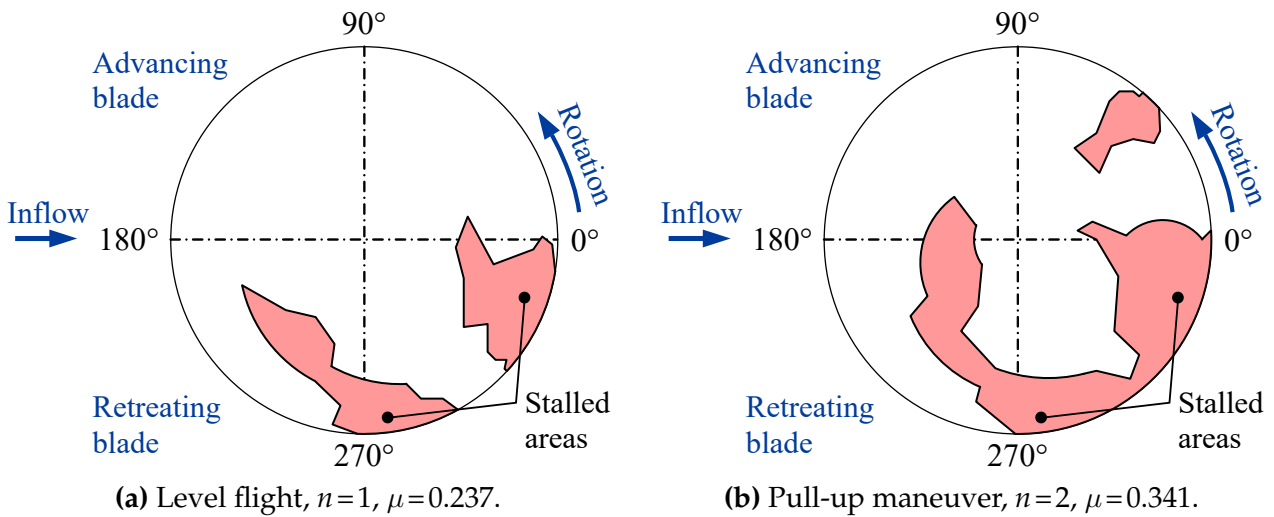


Figure 2.23: UH-60A dynamic stall maps indicating separated flow for different load factors, n , and advance ratios, μ , reproduced with data from Bousman [54].

A similar CFD/CSD simulation was also conducted by Letzgus et al. [135], who investigated a highly-loaded, high-speed turn flight of the Airbus Bluecopter™ demonstrator (see Fig. 2.7) equipped with an innovative five-bladed main rotor. The numerical predictions during dynamic stall were successfully compared to the pitch link loads acquired during a flight test campaign.

3 Boundary layer measurements by differential infrared thermography (DIT)

3.1 Principle of DIT and method development

The basic idea of the differential infrared thermography was developed and validated during investigations of two-dimensional pitching airfoils, conducted in the subsonic “one-meter wind tunnel Göttingen” (1MG). This approach is cost-efficient and allows the study of relevant fundamental effects while partly neglecting difficulties of later large-scale rotor tests, such as the fast relative motion between the blade surfaces and the IR camera. Similar test campaigns were conducted by Raffel and Merz [167], Gardner et al. [20], and Wolf et al. [4]. The latter publication serves as a basis for the following sections, and the corresponding experimental setup can be taken as a blueprint for wind tunnel test measurements applying IR techniques.

3.1.1 Test setup for airfoil measurements in the 1MG

An instrumented wind-tunnel model [34, 35] with the “DSA-9A” helicopter airfoil geometry, see Fig. 3.1, was installed into the open test section of the closed-return one-meter wind tunnel Göttingen (1MG), see Figs. 3.2 and 3.3.

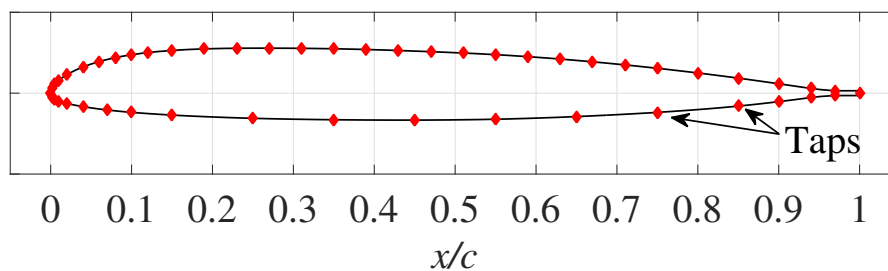


Figure 3.1: DSA-9A airfoil geometry and pressure tap distribution, adapted from Ref. [35].

The airfoil has a chord length of $c = 0.3$ m, a maximum relative thickness of 9%, and a span of 0.997 m. The surface is made from carbon fiber reinforced plastic (CFRP). The model was equipped with end plates to improve the two-dimensionality of the flow. The freestream velocity was set to $V_\infty = 50$ m/s ($M = 0.14$, $Re = 1.0 \cdot 10^6$). The 1MG’s freestream turbulence level at this V_∞ is in the range between 0.15% and 0.20%. An electric actuation mechanism developed in Ref. [25] rotates the airfoil around its quarter chord to adjust the pitch angle for static tests, or to enable pitch oscillation for dynamic tests. In the latter case, the time-varying pitch angle is given by

$$\alpha(t) = \bar{\alpha} - \hat{\alpha} \cdot \cos(2\pi tf). \quad (3.1)$$



Figure 3.2: One-meter wind tunnel Göttingen (1MG) after its refurbishment in 2014/15, configured with an open test section.

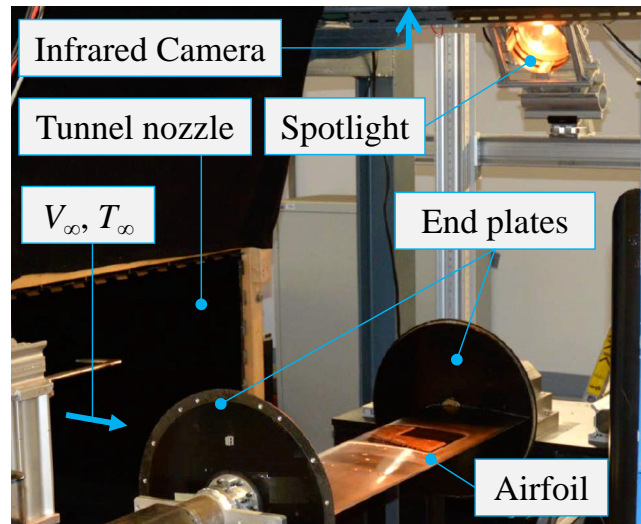


Figure 3.3: Picture of the setup in the wind tunnel's open test section.

It is noted that the pitch angle, α , is defined as the chord's geometric angle of attack. The aerodynamic angle of attack will differ due to wind tunnel wall effects, which were not determined quantitatively. By definition, the minimum α is at phases of $tf = 0$ and $tf = 1$, whereas the maximum α is at $tf = 0.5$. The notation will be abbreviated in the following sections. For example, " $\alpha = 4^\circ \pm 7^\circ$ " refers to a pitch motion with a mean of $\bar{\alpha} = 4^\circ$ and an amplitude of $\hat{\alpha} = 7^\circ$. A summary of the parameter range considered in this study is given in Tab. 3.1. The geometric blockage of the open test section is between 4% and 9% depending on the airfoil's pitch angle.

The airfoil was equipped with 50 Kulite[®] pressure transducers whose tap positions were optimized with a view to the lift coefficient discretization error [35], see the red markers (♦) in Fig. 3.1. The signals of the pressure transducers were acquired through a data recorder at a sample rate of 200 kHz. For each test condition the pressure data was recorded for 10 s (static cases) or 50 s (dynamic cases). The airfoil's geometric angle of attack as measured by laser triangulators and the status signals of the infrared system were stored simultane-

3.1. Principle of DIT and method development

parameter	unit	value or range
freestream Mach number, M_∞	-	0.14
chord-based Reynolds number, Re	-	$\sim 1.0 \cdot 10^6$
mean pitch angle, $\bar{\alpha}$	deg	static: -4 . . . 12.5, dynamic: 4
pitch amplitude, $\hat{\alpha}$	deg	1, 2, 3, 4, 5, 6, 7, 8
pitch frequency, f	Hz	0.25, 0.5, 1, 2, 4, 8
reduced frequency, $k = \pi fc / V_\infty$	-	0.005, 0.009, 0.019, 0.038, 0.075 , 0.151
number of IR images per test point	-	static: 1000, dynamic: 5000
surface heating $T_w - T_\infty$	K	static: $\sim 5 - 6$, dynamic: $\sim 10 - 12$

Table 3.1: Variation of 1MG experimental parameters, default values printed in bold letters.

ously to synchronize the different measurement systems. The high-speed infrared camera FLIR[®] SC7750-L [82], see Fig. 3.4, features a Cadmium-Mercury-Telluride (MCT) sensor with a spectral range between $8.0 \mu\text{m}$ and $9.4 \mu\text{m}$ (“long-wave infrared”, LWIR) and a size of 640×512 pixel. The thermal sensitivity is limited by a noise-equivalent temperature difference of 30 mK [82]. The camera was mounted 2 m above the airfoil, see Fig. 3.5, using a lens with a focal length of 50 mm and an aperture of $f_\# = 2.0$. The area around the camera was covered with black cloth to prevent reflections on the airfoil’s surface. The image integration time was set to $190 \mu\text{s}$, which is small enough to freeze the airfoil’s motion for the studied pitch parameters. The odd image acquisition frequency of the IR camera, 99.98 Hz , is slightly de-tuned to integral multiples of the airfoil’s pitching frequencies. The infrared images are therefore not phase-locked but slowly sweep through the airfoil’s pitch cycle. Assuring that a sufficient number of pitch cycles per test point is recorded and that cycle-to-cycle differences are negligible, this results in a high resolution of the pitch phase with $\Delta t f = 2 \cdot 10^{-4}$, and allows for a systematic study of the influence of the DIT image separation distance.



Figure 3.4: FLIR[®] SC7750-L high-speed IR camera [82].

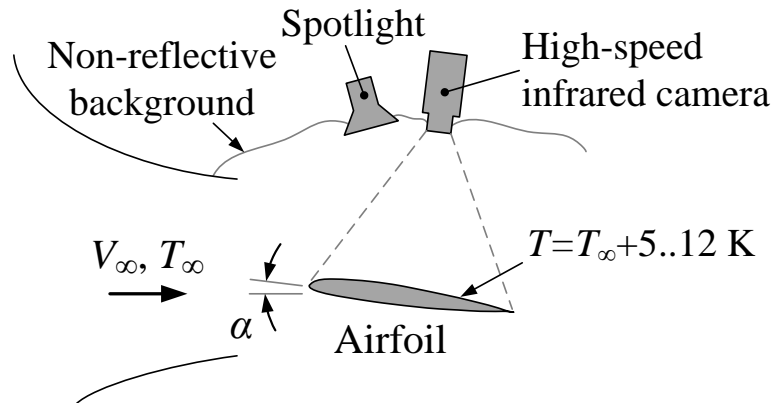


Figure 3.5: Sketch of the wind tunnel setup, not to scale.

The image sensor was calibrated after each camera start-up with a two-point non-uniformity correction to remove random pixel-to-pixel detuning, which is particularly ad-

visible for MCT sensors. Therefore, hollow hemispheres with a dull black coating and two different temperatures, $T \approx 293$ K and $T \approx 323$ K, were placed in front of the lens to simulate unidirectional black-body radiation. As a result, the camera measures surface temperatures in the arbitrary and camera-dependent unit “counts”. A conversion into absolute temperature readings requires an additional calibration of the specific emissivity of the airfoil surface, and regular zero-offset drift corrections. Since the current evaluation methods do not depend on absolute temperatures, this conversion was disregarded to reduce experimental effort.

Tests showed that the relation between the measured camera signal and the temperature of the hollow hemispheres is almost perfectly linear in the relevant range, with a sensitivity of about 10 mK/count, see Fig. 3.6 (left). This result is important in the light of the Stefan-Boltzmann law, which predicts that the radiated power of a black body scales with the fourth power of its temperature. Furthermore, a flat CFRP plate similar to the DSA-9A airfoil’s surface was viewed from multiple angles, and the average temperature signal in a rectangular region (50×100 pixel) of the image was acquired, see Fig. 3.6 (right). The measured temperature is constant within ± 1 counts if the angle between the viewing axis and the surface normal is within $\pm 60^\circ$. More oblique angles result in apparent temperature deviations, probably caused by an increasing reflection of the surrounding background, which is warmer in the shown case. A smaller deviation is also caused by diffuse reflections of the IR lens itself if the viewing axis is collinear with the face normal, which can be avoided during the experimental setup. In summary, the following sections treat the camera signal in the unit “counts” as a synonym for the “true” surface temperature.

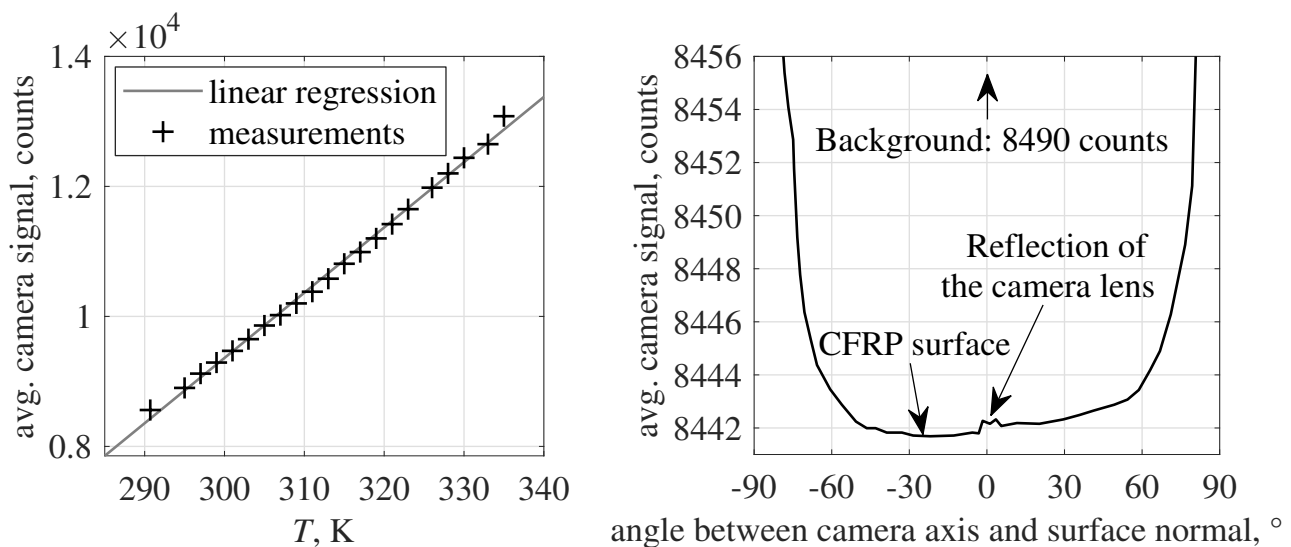


Figure 3.6: IR camera test, linear calibration curve (left), and angular sensitivity of the measured temperature signal of a constant-temperature CFRP surface (right).

A spotlight with a power output of up to 1500 W was mounted next to the infrared camera. The radiative heat flux was measured with a power meter and is roughly 1500 W/m^2 over $0 \leq x/c \leq 0.5$ reducing to 420 W/m^2 at the trailing edge. This results in a temperature difference of 10 K to 12 K between the airfoil’s upper surface and the freestream temperature for dynamic test cases. In constant-pitch test cases the electrical power supply to the spotlight was reduced, yielding a temperature difference between 5 K and 6 K.

An instantaneous IR image for a static test case with $\alpha = 1.5^\circ$ is shown in Fig. 3.7, the

flow direction is from left to right. The infrared intensity of the airfoil's surface is in the range of 9.000 to 10.000 counts. Both leading and trailing edges can be identified as vertical lines against the dark background. An automated detection of the edges is used to map the chordwise coordinate x in instantaneous images. The transition region is marked by the blue rectangle, in which the intensity gradually decreases due to the increasing convective heat transfer in the turbulent boundary layer. The transition is slightly closer to the leading edge in three small spanwise regions marked by orange triangles, this results from an increased surface roughness due to pressure taps (central region) or silver-paint fiducial markers (upper/lower region). The area used for DIT evaluation is marked by red horizontal lines, it covers 70 pixel (about 0.037 m) in the spanwise direction. The transition was found to be two-dimensional in this area, and the infrared signal will later be averaged along this direction to reduce the camera noise.

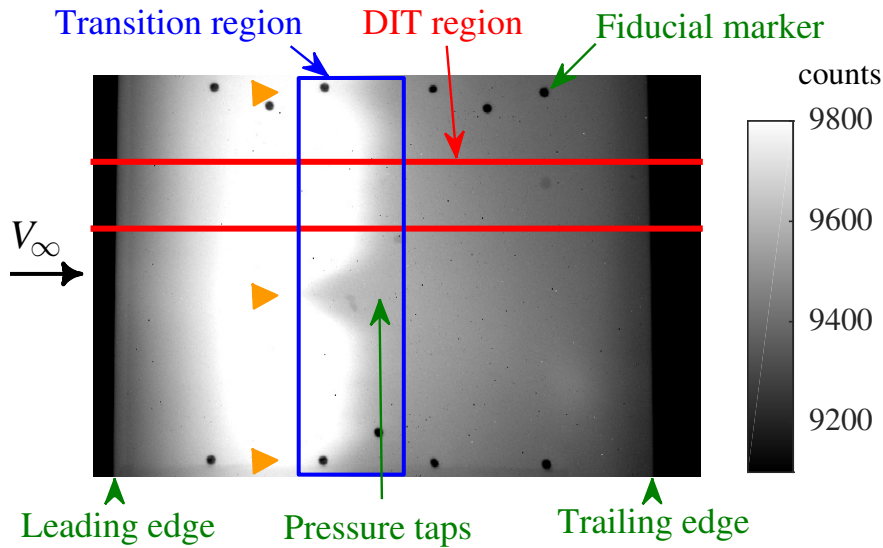


Figure 3.7: Infrared image for a static test case, $\alpha = 1.5^\circ$.

3.1.2 Static pitch and comparison to standard infrared thermography

Static-pitch test cases serve as a reference for the unsteady cases and demonstrate both the general idea of DIT and its validity under steady conditions. It is expected that the surface temperature T_w of the heated airfoil is predominantly governed by the forced convective heat transfer within the boundary layer. The Reynolds analogy establishes a relation between the skin friction coefficient, C_f , and the convective heat flux at the surface-to-fluid boundary, \dot{q}_{conv} . The analogy states, see Truckenbrodt [221]:

$$\dot{q}_{\text{conv}} = \frac{1}{2} C_f c_p \rho_\infty V_\infty (T_w - T_r), \quad (3.2)$$

with the fluid's heat capacity, c_p , and density, ρ_∞ , and with the flow velocity, V_∞ . The flux is driven by surface-to-fluid temperature difference, represented by the actual diabatic temperature of the wall, T_w , minus the adiabatic recovery temperature of the flow, T_r . The latter temperature is close to the flow's stagnation temperature but a weak function of the state of the boundary layer, details will be given in Sec. 3.3.1. Assuming that in thermal

equilibrium \dot{q}_{conv} equals the constant incoming radiative heat flux of the spotlight, and that other mechanisms of heat transfer have a minor influence, the local surface wall temperature T_w is inversely proportional to C_f .

The coefficient C_f was estimated using viscous boundary-layer solutions provided by the 2D Euler solver ‘‘MSES’’ [74], since the skin friction could not be directly measured in the current experiments. MSES predicts the BL transition using the enveloped e^N -method. The square symbols (■, ■) in Fig. 3.8 (top) correspond to the measured distributions of the pressure coefficient C_p for two different static angles of attack. The lift coefficient C_l was determined using the DLR in-house tool ‘‘cp2cl’’, which performs a first-order direct integration along the airfoil surface, accounting for the pressure taps shown in Fig. 3.1. This yields $C_l = 0.22$ for $\alpha = 4^\circ$ and $C_l = 0.36$ for $\alpha = 7^\circ$. The MSES solutions were calculated for the same C_l -values, see the solid lines (—, —) in Fig. 3.8 (top). They are in reasonable agreement with the experimental results. It is noted that the corresponding MSES angles of attack are smaller than the experimental values due to 3D- and wind-tunnel wall interference or blockage effects.

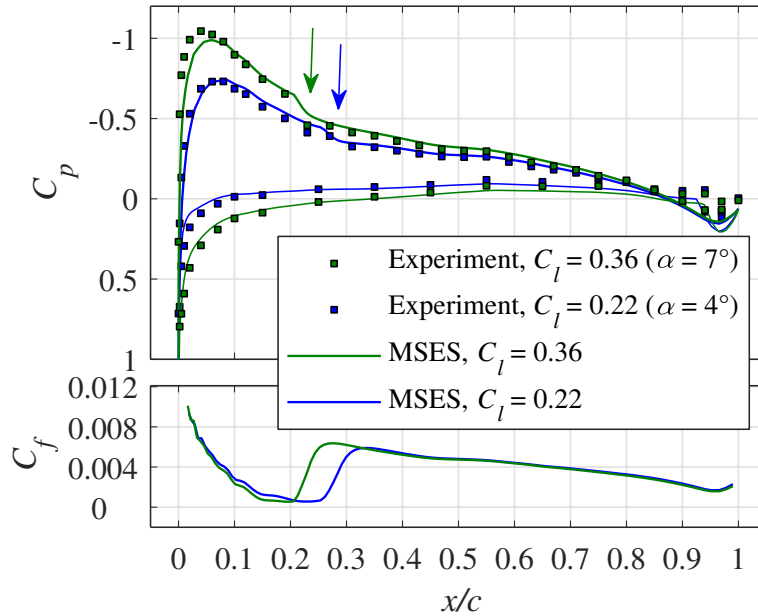


Figure 3.8: Pressure coefficient C_p (top) and skin friction coefficient C_f (bottom, suction side only) for two static angles of attack.

The boundary layer transition on the airfoil’s upper surface can be seen by the small kinks in the pressure distribution, see the blue and green arrow markers, whereas the lower surface is almost fully laminar. The MSES results for C_f are shown in Fig. 3.8 (bottom). The skin friction coefficient generally decreases from leading edge to trailing edge, except for a sharp increase in the transitional region between about $0.20 < x/c < 0.34$, depending on α . The C_f -distributions for $\alpha = 4^\circ$ and $\alpha = 7^\circ$ are very similar except for the upstream motion of the transition. This illustrates the basic idea of DIT, see Refs. [167, 168], which assumes that the transition motion is the dominant source of temperature changes in the infrared images.

The time- and spanwise-averaged surface temperature distribution as measured in the DIT region for $\alpha = 4^\circ$, see Fig. 3.9, has an inverse trend to the corresponding C_f -distribution. This underlines the applicability of Eq. 3.2. The temperature strongly increases in the laminar region, $x/c < 0.26$, but then sharply drops in the transitional region, $0.26 \leq x/c \leq 0.34$.

3.1. Principle of DIT and method development

Further downstream the temperature is nearly constant up to about $x/c = 0.5$ and then slowly decreases towards the trailing edge. The last part contrasts with the slightly decreasing C_f in the fully turbulent boundary layer. This is caused by an inhomogeneous radiative heating, and by an increasing heat conduction towards the lower side due to a decreasing thickness of the airfoil. Nevertheless, the tangents in the laminar, transitional, and turbulent regime can be determined, see the gray lines in Fig. 3.9. Using the method of Schülein [193], the intersections of these lines correspond to the start and end of the transition region, with a 50% intermittency in its geometric center. For the current data this point is also in very good agreement with the location of the steepest temperature gradient, $\partial T/\partial x$. This agrees with the criterion proposed by Ashill et al. [39], who additionally identify the peaks of the temperature's curvature, $\partial^2 T/\partial x^2$, as start and end of the transition. The results are very similar to Schülein's method. The procedure of static transition detection for an individual pitch angle is termed "infrared thermography" (IRT) in the following.

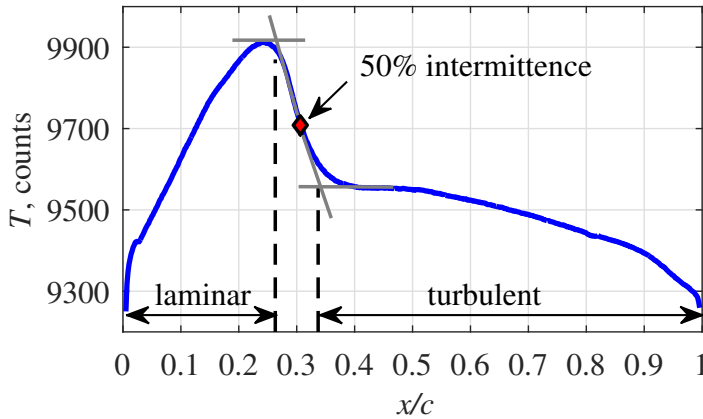


Figure 3.9: Temperature distribution, $\alpha = 4^\circ$.

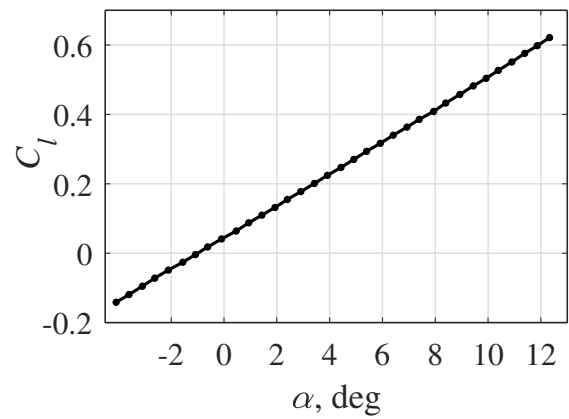


Figure 3.10: Lift coefficient for static α .

Static polar data was acquired with a stepping of $\Delta\alpha = 0.5^\circ$, and the resulting lift coefficient C_l is given in Fig. 3.10 as a function of the angle of attack α . Fig. 3.11 (top) shows four pairs of temperature distributions between $\alpha = -2^\circ$ and $\alpha = 7.5^\circ$ with the transition moving upstream for an increasing angle of attack. Note that for $\alpha = -2.0^\circ$ (—) and $\alpha = -1.5^\circ$ (---), an exact localization of the transition region using IRT is somewhat ambiguous due to its large streamwise extent and its proximity to the trailing edge.

The IRT results for the entire α -polar are shown in Fig. 3.12. The 50% intermittency point is represented by a green line (—). Its motion towards the leading edge is fast in the region of about $-1^\circ \leq \alpha \leq 2.5^\circ$ or $0.75 \geq x/c \geq 0.4$. This results from the flat pressure distribution and the small pressure gradients $\partial C_p/\partial x$ in this chordwise area, for example see Fig. 3.8 (top). The blue symbols (■) in Fig. 3.12 correspond to the identified transition locations as seen by the σC_p -method, which evaluates the standard deviation of the dynamic pressure transducers [87]. The method is based on a transition-induced change in the BL's displacement thickness, which affects the pressure distribution. A more detailed description is given in Sec. 3.2.2. The σC_p -results are mostly within the IRT transition region (gray lines) but slightly upstream of the 50% intermittency point, with a deviation between about 1% and 4% of the chord length.

Applying the idea of DIT to static data, the temperature difference ΔT of two measurements with a separation of $\Delta\alpha = \alpha_2 - \alpha_1 = 0.5^\circ$ is calculated, as shown in Fig. 3.11 (bottom).

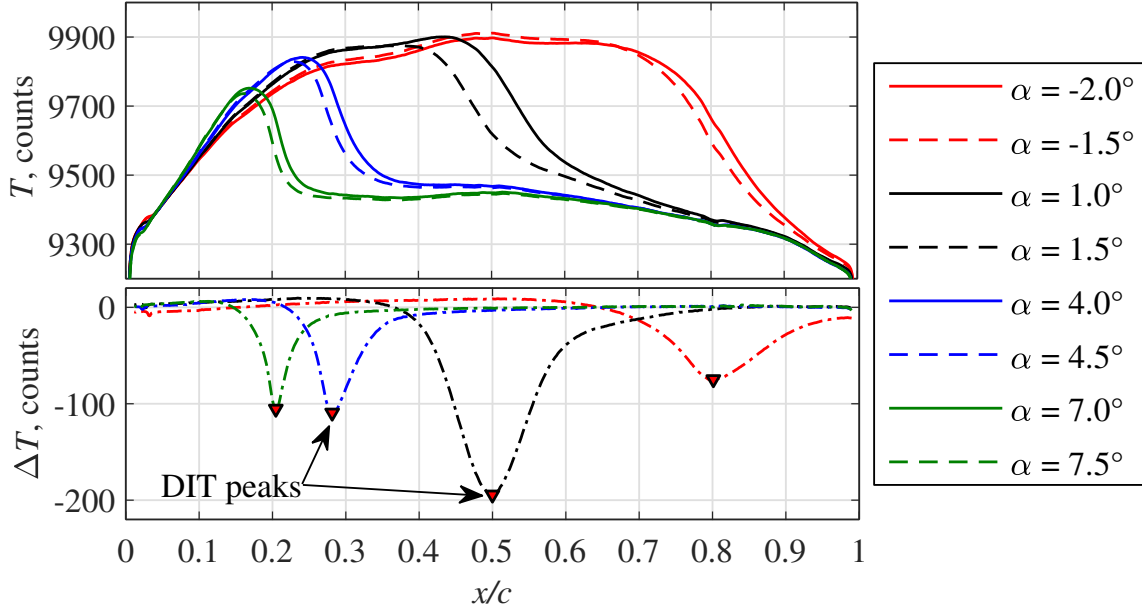


Figure 3.11: Intensity profiles (top) and DIT (bottom) for static pitch angles α .

The static data is assumed to be void of both aerodynamic and thermal hysteresis effects. The distributions have negative peaks since α_2 is larger than α_1 , that is, the larger heat convection of the turbulent boundary layer moves towards the leading edge. Following the argumentation of Richter et al. [35] and Gardner et al. [14], the peak position (\blacktriangledown) relates to the transition position, x_{tr} , at the average angle

$$\alpha = \frac{\alpha_1 + \alpha_2}{2}. \quad (3.3)$$

This is verified in Fig. 3.12, in which the 50% intermittency position for IRT (---) and the transition position for DIT (\blacklozenge) agree within 1% of the chord length. The negative DIT peak value of ΔT is shown in Fig. 3.13 as a function of the angle of attack after Eq. 3.3 for the static polar. The peak height is not analyzed quantitatively during DIT processing, but it determines the signal-to-noise ratio of the peak position detection, which will be crucial in later dynamic test cases.

For a linearization of steady-state DIT, it can be shown that the peak value of ΔT linearly scales with distance covered by the transition motion, Δx_{tr} , and with the steepness of the temperature distribution at the transition location, $\partial T / \partial x|_{x_{tr}}$. Consequently, DIT peaks exceeding -200 counts are observed between $\alpha = -0.5^\circ$ and $\alpha = 2^\circ$, where the transition moves quickly in the upstream direction. At larger angles of attack, $\alpha > 2^\circ$, the transition motion is smaller and decreases towards the leading edge, which in combination with a slightly increasing steepness of the temperature distribution results in an almost constant peak level around $\Delta T = -100$ counts. For $\alpha < -1^\circ$ both the transition motion and the steepness of the temperature distribution decrease, which yields a diminishing DIT peak signal towards the trailing edge.

At this point, it is noted that the DIT method shares the basic idea of differential temperature distributions with similar approaches developed independently. Calculating the tare signal between “wind-on” and “wind-off” images is a well-known strategy to eliminate

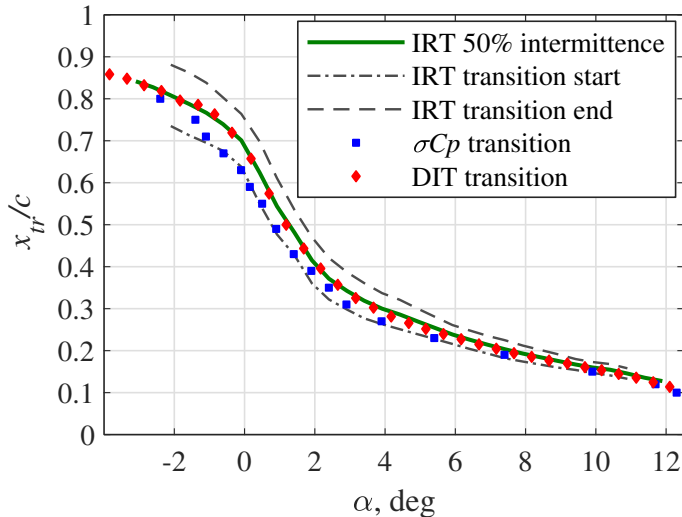


Figure 3.12: BL transition positions versus α for IRT, σC_p , and DIT.

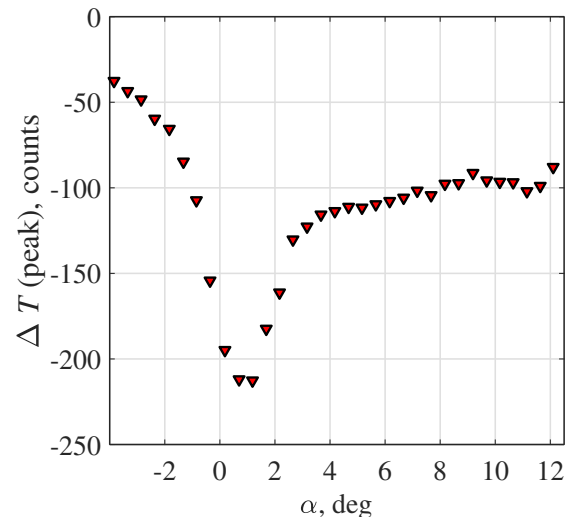


Figure 3.13: DIT peak height for static tests, $\Delta\alpha = 0.5^\circ$.

non-aerodynamic surface inhomogeneities. Hoesslin et al. introduced the “temperature decline thermography” (TDT), in which the thermal response of a surface after a heat pulse, generated by a flashlamp or a laser, is investigated by means of the temporal temperature gradient, $\Delta T / \Delta t$. TDT was developed with a view to transition detection in turbomachinery applications, and tested for steady inflow conditions on a NACA 0018 airfoil [104] and the blades of a turbine rig [103] using custom borescope IR optics. The temperature decline seen in an IR image time series is also used in a BL transition study by Boiko et al. [51], in which the heat pulse is replaced by a pre-heated wing model tested in a low-turbulence wind tunnel.

3.1.3 Introduction into unsteady test cases

A thermal equilibrium is hard to achieve during experiments in unsteady or even (quasi-) steady aerodynamics. On the one hand, the wetted surface and the structure beneath require large timespans for adapting to the instantaneous thermal environment. For example, Simon et al. [206] discuss the frequency response of infrared transition measurements for several surface materials and heat sources, with response times reported in the range of several seconds to minutes. On the other hand, a temperature drift in the inflow conditions is frequently observed, for example due to wind tunnel heating, or due to atmospheric changes during free-flight tests.

When the aerodynamic or thermal unsteadiness is sufficiently slow compared to the thermal responsiveness, steady-state evaluation methods can still be applied and yield unambiguous results. This was shown by Szewczyk et al. [214], observing the BL transition on a glider wing during a stall-and-recovery maneuver lasting about eight seconds. However, rotor aerodynamics or short-term facilities such as shock tubes produce a much higher unsteadiness, which is beyond the limits of steady-state evaluation.

A first example is given by the short-exposure IR image in Fig. 3.14, taken during a joint NASA-DLR wind tunnel-experiment. It shows the blade tip’s suction side of a large rotor operated in trimmed forward flight conditions, hence, the pitch angle undergoes

cyclic oscillations. Detailed results of this experiment will be discussed in Sec. 3.5. The IR camera is operated close to its signal-to-noise limit, but a clear split between dark and bright areas implies a transition line at about 75% chord when applying steady-state ideas. This impression is supported by several triangular-shaped structures indicating turbulent wedges due to surface defects close to the leading edge. A closer analysis of the IR time series shows that these structures were etched into the “thermal memory” of the surface during an earlier stage of the pitch cycle. The DIT analysis shows that the actual transition position (— —) is located much closer to the leading edge, underlining the need for advanced evaluation methods.

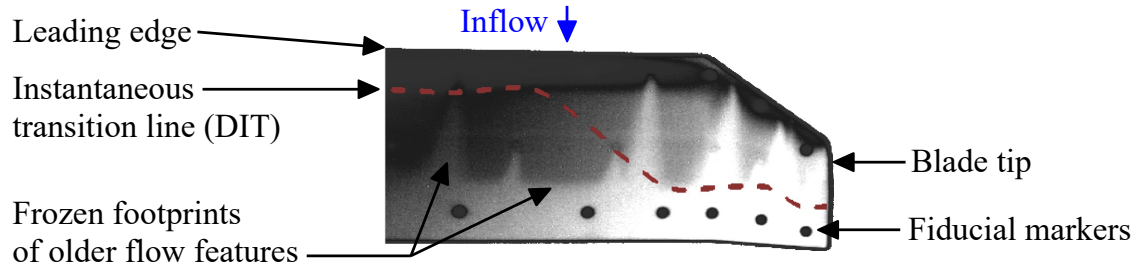


Figure 3.14: Blade tip of a large-scale rotor in the NASA Langley 14- by 22-Foot Subsonic Tunnel in forward flight conditions, IR image adapted from Ref. [18].

The effects of unsteady inflow conditions on infrared BL transition measurements of a wetted surface can be divided into three categories, see Tab. 3.2.

(i)	Inviscid effects: Inviscid aerodynamics in the external flow govern the time-dependency between the inflow conditions and the surface pressure distribution. For example considering pitch-oscillating airfoils, Theodorsen’s theory [217] predicts a hysteresis between the pitch angle and the lift force due to differential velocities induced by shed vorticity in the wake.
(ii)	Viscous effects: The time-history of the boundary layer may introduce an additional lag (i.e., a decoupling) between an airfoil’s pressure distribution and the boundary layer’s transition position. This effect was shown by Richter et al. [34] for a pitching airfoil, and confirmed by Gardner et al. [15].
(iii)	The thermal responsiveness, comprising the thermal diffusivity and the specific heat, connects the boundary layer’s instantaneous convective heat transfer with the surface temperature as acquired by an infrared camera.

Table 3.2: Time lag-effects of IR measurements under unsteady aerodynamic conditions.

The “true” aerodynamic transition position only includes effects (i) and (ii), whereas effect (iii) is an error which must be eliminated or reduced by the infrared measurement technique. Returning to the pitching-airfoil experiment, see Sec. 3.1.1, and the differential evaluation, see Sec. 3.1.2, it will be shown that DIT is a possible strategy.

Fig. 3.15 shows the instantaneous temperature distributions at the minimum and maximum pitch angles for sinusoidal motions with $\alpha = 4^\circ \pm 3^\circ$, $V_\infty = 50$ m/s, and three different reduced frequencies $k = 0.005, 0.009, 0.038$ (0.25 Hz, 0.5 Hz, 2 Hz). Offsets were added to the

graphs to improve the readability of the figure, with the frequency increasing towards the top. For reference, also the static case $k = 0$ is repeated from Fig. 3.11. It is noted that the radiative heating was halved in the static case (see Table 3.1), which can be seen by a reduced temperature gradient $\partial T/\partial x$ in the area of the leading edge.

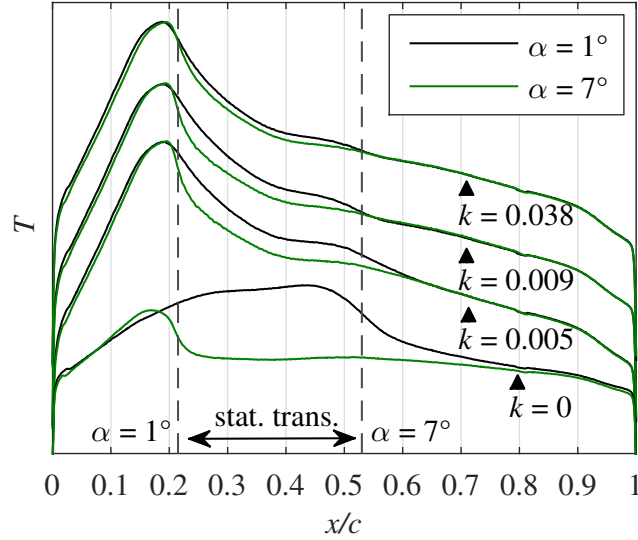


Figure 3.15: Intensity profiles for $\alpha = 4^\circ \pm 3^\circ$, pitching frequencies $k = 0, 0.005, 0.009, 0.038$.

In the expected region of the transition movement between both pitch angles, circa $x/c = 0.22$ to $x/c = 0.53$ (dashed vertical lines), the temperatures for $\alpha = 7^\circ$ (—) differ from the temperatures for $\alpha = 1^\circ$ (—). However even for the lowest frequency of $k = 0.005$ (0.25 Hz) this difference is much smaller than in the static case despite the higher heating. With increasing frequency k the temperature differences further decrease, meaning that the temperature at a given chordwise position approaches a constant level between the laminar and turbulent temperatures due to the limited thermal responsiveness of the model surface. Therefore, the instantaneous transition position and the overall temperature distribution are decoupled, and steady-state transition detection methods relying on the spatial temperature gradient (for example as shown in Fig. 3.9) fail. Nevertheless, Refs. [14, 167, 168, 35] prove that the transition still results in meaningful temporal temperature gradients, which motivates the application of DIT.

Fig. 3.16(a) (top) shows the instantaneous temperature profiles for the $k = 0.038$ -case (2 Hz) at $\alpha = 4^\circ \uparrow$ (—) and $\alpha = 4.5^\circ \uparrow$ (—) during the upstroke, but the difference is barely visible in this scaling. Nevertheless, a subtraction reveals the negative DIT peak (▼) which is clearly discernible against the background noise level, see Fig. 3.16(a) (bottom). The dynamic results can be compared to the respective static data at the same pitch angles, see Fig. 3.16(b). In static conditions, the temperature profiles are different and have a steeper gradient in the transition region. This results in a much larger differential peak value, about 110 counts versus 20 counts.

The next step evaluates a pitch motion with $\alpha = 4^\circ \pm 7^\circ$, in which the transition motion covers large parts of the airfoil. Both the aerodynamic and thermal hysteresis are considerable when choosing $k = 0.075$ (4 Hz). Up to this point the DIT was always calculated for an angle of attack-difference of $\Delta\alpha = 0.5^\circ$. This value cannot be kept constant for sinusoidal motions since the pitching velocity varies as a function of the phase tf and approaches zero at the

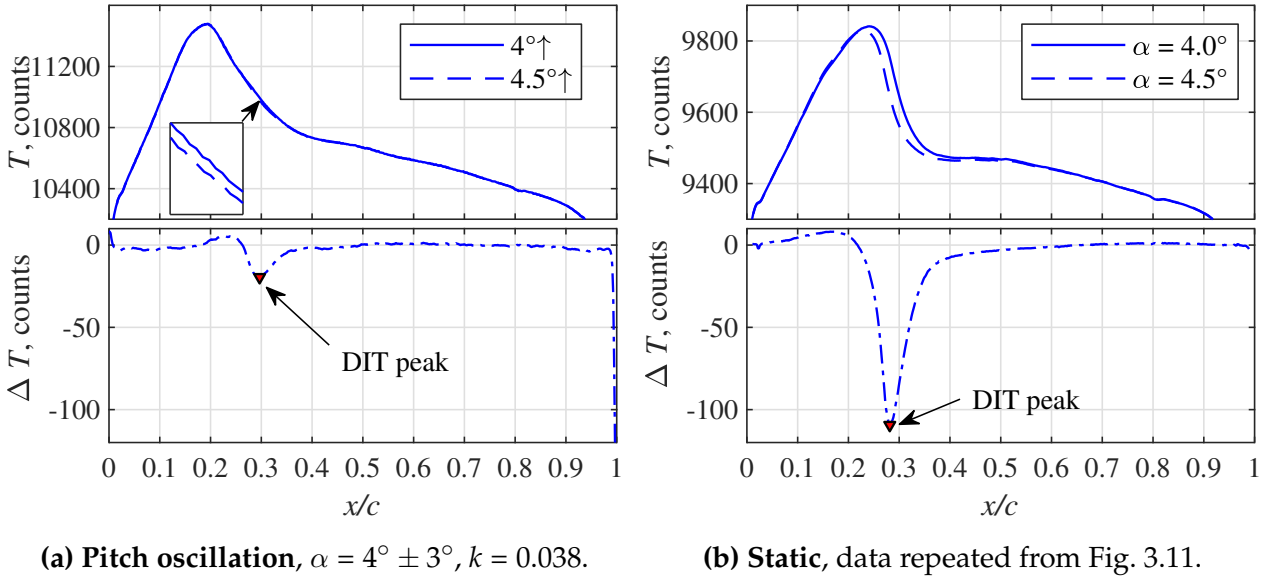


Figure 3.16: Instantaneous temperature distributions (top) and DIT signal (bottom).

upper and lower reversal points. Therefore and in agreement with Refs. [167, 168, 35], a constant phase difference was chosen for DIT processing. The current example uses a separation of $\Delta tf = 0.01$ resulting in angle of attack-differences $\Delta\alpha$ with a maximum of 0.5° (upstroke) and a minimum of -0.5° (downstroke). The 5000 infrared images of the test case were sorted in ascending phase, and for each image pair with t and $t + \Delta t$ the DIT peak was detected as shown in Fig. 3.16(a). It is noted that the peak is negative for a transition motion towards the leading edge, and positive for a motion towards the trailing edge. The peak search region was restricted to ± 0.25 chord lengths around the corresponding static transition position, this choice includes hysteresis effects but removes some outliers.

Fig. 3.17 shows the raw DIT data versus the pitch phase tf as black dots (\bullet), together with the angle of attack scaled between 0 and 1 as a dashed line ($- -$). The transition position, x_{tr} , can be unambiguously identified during large parts of the up- and downstroke. Towards the reversal points unreliable data is expected since the DIT separation $\Delta\alpha$ and the transition motion approach zero. This can be seen by means of moderate data scatter around $tf = 0.5$, at the upstream reversal of the transition motion. For $tf < 0.16$ and $tf > 0.90$, corresponding to the downstream reversal, a large data scatter outweighs the valid DIT transition results. In this area the decreasing DIT separation combines with the decreasing temperature differences towards the trailing edge, which was already shown in the static data of Fig. 3.13, effectively preventing the DIT evaluation.

The raw transition data was filtered using a similar approach as in Richter et al. [35]. The data points were sorted in 100 equidistant bins along the phase tf , and the median of x_{tr} was calculated for each bin, see the red line ($-$) in Fig. 3.17. The standard deviation of the bins represents the local magnitude of data scatter. This value can be taken as a criterion to identify invalid data. An arbitrary threshold of 5% was used in the current case, which excludes unreliable data at the lower pitch reversal from further evaluation.

In Fig. 3.18 the filtered DIT result ($-$) is plotted versus the angle of attack, α , revealing a hysteresis between the up- and downstroke of the motion which is approximately symmetric to the static transition position ($-$).

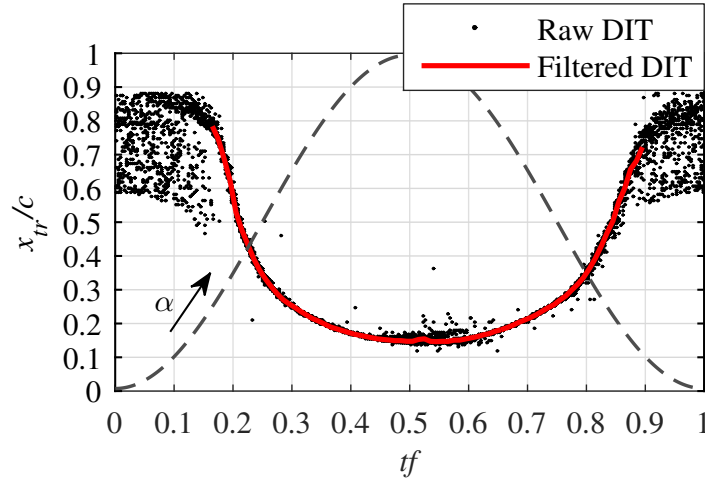


Figure 3.17: DIT transition results versus phase tf , $\alpha = 4^\circ \pm 7^\circ$, $k = 0.075$.

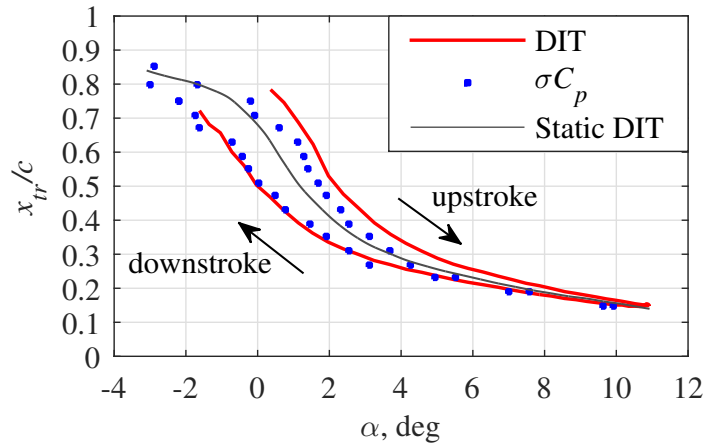


Figure 3.18: Transition position x_{tr} versus α , $\alpha = 4^\circ \pm 7^\circ$, $k = 0.075$.

The σC_p -procedure (■) has a smaller hysteresis. This indicates that DIT introduces a measurement-related lag in addition to the aerodynamic hysteresis. A detailed analysis of this effect will be presented in Sec. 3.1.5. On the average, the transition locations measured by σC_p are further upstream in comparison to DIT. This corresponds to the static results in Fig. 3.12, and it is most probably caused by the surface disturbances of the pressure taps.

3.1.4 Compensation of temperature drift

The de-tuning of the camera acquisition frequency and pitching frequencies, see Sec. 3.1.1, means that the DIT image separation can be chosen as integral multiples of the minimum value $\Delta tf = 2 \cdot 10^{-4}$, corresponding to 0.02% of the pitch cycle. On the downside, two images with a small phase difference may have a large wall-clock time difference with multiple pitch cycles in between. Cycle-to-cycle differences of the transition position are considered to be small, but a temperature drift cannot be neglected. This is demonstrated for the test point of the previous section, $\alpha = 4^\circ \pm 7^\circ$ at $k = 0.075$. Fig. 3.19 shows the temperature drift as function of the chordwise position x/c and the test time with a total duration of about 50 s. The drift was determined using a temporal low-pass filter which applies a sliding average window twice as large as the pitching period. By tendency, the area between $x/c = 0.1$ and $x/c = 0.2$

cools down, whereas the area between $x/c=0.3$ and $x/c=0.9$ heats up. This non-uniform evolution is unlikely to be caused by a drift of the freestream flow temperature or the heating intensity. It is more likely that the surface of the airfoil was not in a thermal equilibrium at the start of the test point, even though the pitch motion was turned on prior to the first infrared image for about 20 s to 30 s required for a fine-tuning of the motion controller. A similar drift is found in the majority of the current test points, indicating that it is a general problem, and that the thermal inertia of the model surface is too large to wait for equilibrium under the constraints of limited wind-tunnel time. A drift of 10 counts corresponds to approximately 0.5 K over 50 s of test time. Gardner et al. [14] suggest that roughly 10 min of waiting time after setting the pitch motion would reduce this drift by a factor of 10.

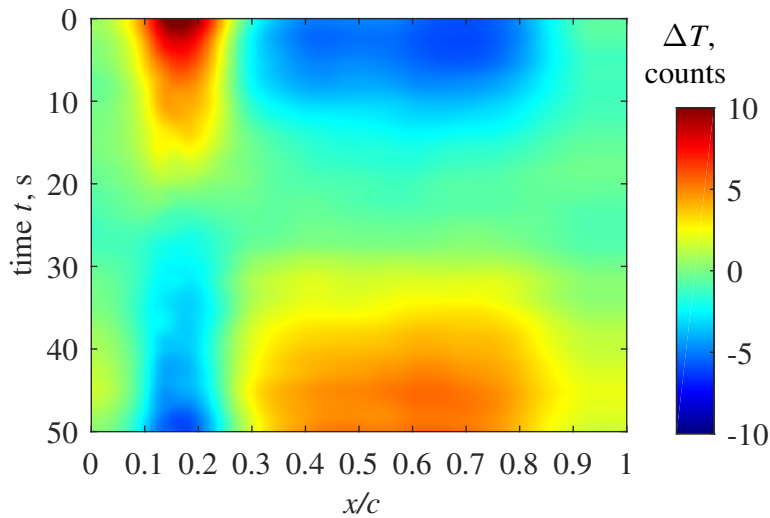


Figure 3.19: Sample drift of the airfoil's infrared temperature signal.

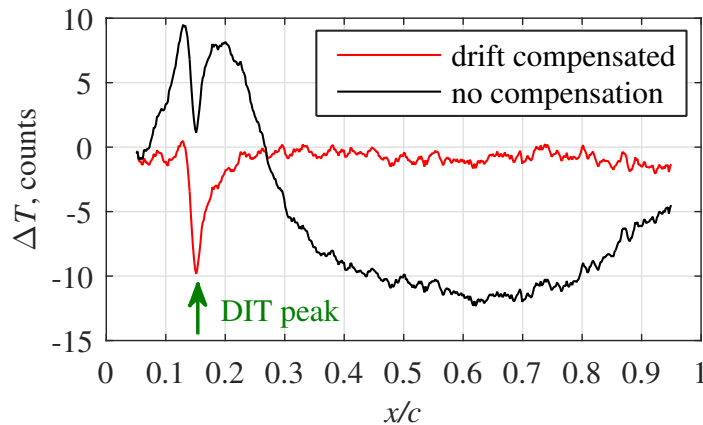


Figure 3.20: Example for DIT temperature compensation.

The temperature drift can be compensated through a subtraction of the low-pass filtered signal. Fig. 3.20 shows the DIT differential temperature distribution at a phase of $tf=0.47$ ($\alpha=10.9^\circ \uparrow$). The chosen phase separation $\Delta tf=0.01$ of the two underlying infrared images is small, but the wall-clock time separation is large, about 39 s. In the temperature-compensated DIT (—) a single negative DIT peak at $x/c=0.15$ clearly marks the transition motion. In the non-compensated DIT (—) the same transition peak is superimposed with a strong

temperature drift. The DIT peak is distorted and hardly detectable by automated algorithms, and its position is slightly biased. Therefore, DIT results discussed in the previous and next sections are corrected for possible temperature drifts, without further notice.

3.1.5 Influence and optimization of DIT separation

The separation distance Δtf between two temperature distributions processed by DIT has a decisive influence on the quality of the results. It will be shown that smaller separations result in smaller lags between the measured and the true transition positions, since the influence of the airfoil's thermal inertia is reduced. On the other hand, also the DIT peak height and therefore the signal-to-noise ratio is reduced. The effects will be studied in more detail by revisiting the reference test case of Sec. 3.1.3, $\alpha = 4^\circ \pm 7^\circ$ at $k = 0.075$.

Fig. 3.21 shows the unfiltered DIT results for the separations $\Delta tf = 0.005$ (top, ●) and $\Delta tf = 0.05$ (bottom, ●). The results are generally similar, but the smaller separation yields a larger scatter. This can be explained by the corresponding ΔT peak heights shown in Fig. 3.22. As expected from the larger convective heat transfer in the turbulent boundary layer, the peaks have a negative sign (cooling) when the transition moves forward and a positive sign (heating) when the transition moves backward. The larger separation (●) results in distinct DIT peaks of up to about ± 50 counts, whereas the peaks of the smaller separation (●) are at the edge of the noise limit, which is about ± 5 counts for the current infrared imaging setup.

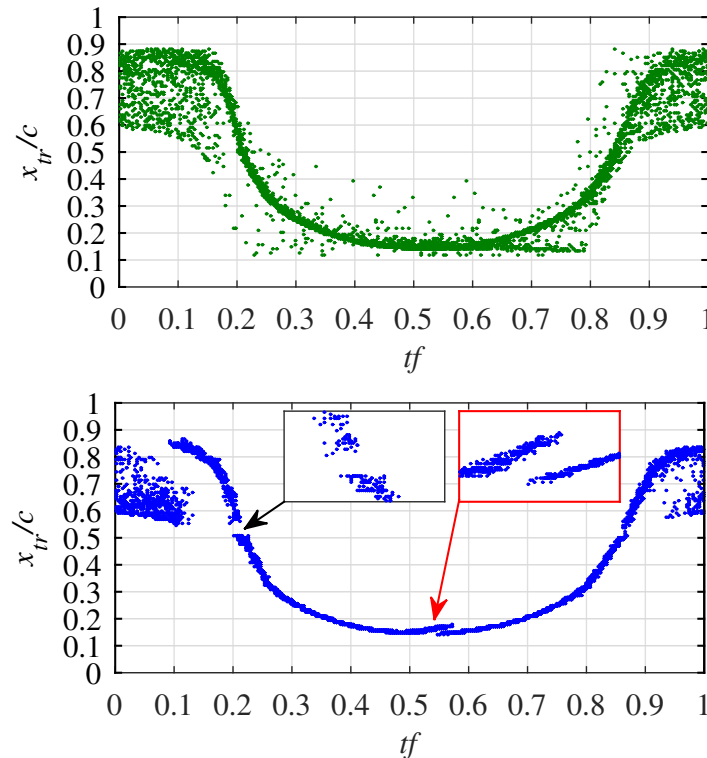


Figure 3.21: DIT transition results for $\alpha = 4^\circ \pm 7^\circ$, $k = 0.075$, DIT separations $\Delta tf = 0.005$ (top) and $\Delta tf = 0.05$ (bottom).

Apart from the higher signal-to-noise ratio the DIT transition position of the large Δtf , see Fig. 3.21 (bottom), has three discontinuities which do not occur for the small Δtf . Two voids are formed during the up- and downstroke at about $tf = 0.21$ and $tf = 0.86$, the former region

is shown in the black-framed detail. At this point the choice of $\Delta tf = 0.05$ results in a large pitch difference of $\Delta\alpha = 2.4^\circ$ and a large transition motion Δx_{tr} of more than 0.3 chord lengths. The corresponding differential temperature distribution is shown as the black line (—) in Fig. 3.23. The DIT peak is not only very broad due to the large transition motion, but it begins to split up into two separate peaks with a valley in between. This violates the single-peak assumption of the DIT method. The detected peak positions randomly switch between both double-peaks, forming a void in the result data between $x_{tr}/c = 0.52$ and $x_{tr}/c = 0.53$. It is noted that the same effect can also be observed when increasing the pitch difference of the static DIT evaluation from $\Delta\alpha = 0.5^\circ$ to values larger than $\Delta\alpha = 2^\circ$, even though this was not discussed in Sec. 3.1.2.

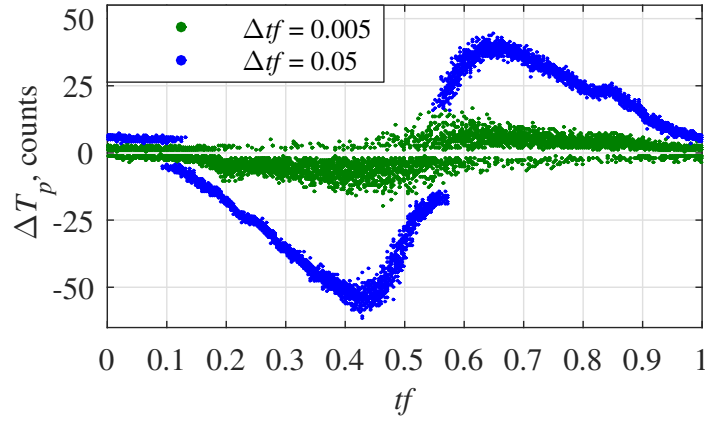


Figure 3.22: DIT peak height, $\Delta tf = 0.005$ and $\Delta tf = 0.05$.

The third gap in the results for $\Delta tf = 0.05$ occurs at the upstream reversal point of the transition, about $tf = 0.56$. It is shown by the red-framed detail in Fig. 3.21 (bottom). This phenomenon was first discovered by Ref. [35] and studied in more detail by Ref. [14]. The sign of the DIT peak switches from negative to positive at the reversal point. Both states are coexistent due to the thermal hysteresis particularly for large DIT separations, and again the double-peak structure in the temperature difference yields erroneous results. This is shown by the red line (—) in Fig. 3.23. The current evaluation detects the temperature peak regardless of its sign, that is, as the maximum value of ΔT . Therefore, the peak position randomly switches between the positive and negative peaks. Gardner et al. [14] suggest that the peak search algorithm should be modified to differentiate between forward motion (negative peak) and backward motion (positive peak). This requires a priori knowledge of the exact transition reversal point, which lags behind the pitch reversal. The current work shows that instead the DIT separation can be reduced up to a point where this double-peak effect merges into the general noise level, see Fig. 3.17 and Fig. 3.21 (top). It is noted that the same problems are also expected at the rearward motion reversal, Ref. [14]. This cannot be observed in the current pitch motion, since the signal-to-noise ratio towards the trailing edge is too low even for very large DIT separations.

Finally, the effect of the DIT separation Δtf on the measured hysteresis is studied. The angle of attack in which the transition crosses a certain location x/c is determined for both up- and downstroke of the pitch motion. The deviation between both values, $\Delta\alpha = \alpha_{\uparrow} - \alpha_{\downarrow}$, is taken as a measure for the hysteresis, corresponding to the horizontal distance between up- and downstroke in Fig. 3.18. In addition, the hysteresis calculated by σC_p is subtracted

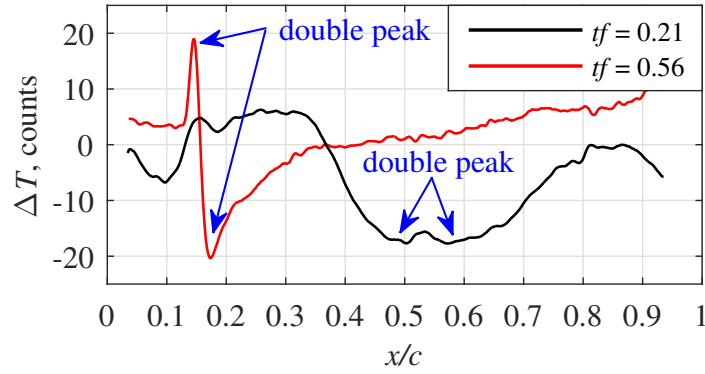


Figure 3.23: Erroneous DIT results, $\Delta tf = 0.05$.

from the respective DIT result, assuming that the fast-response σC_p -method is close to the true aerodynamic hysteresis. The difference therefore represents the additional measurement hysteresis or thermal lag which is introduced by DIT. This additional measurement hysteresis is shown in Fig. 3.24 for three transition locations $x/c = 0.19, 0.31, 0.43$ and multiple separation distances up to $\Delta tf = 0.075$ of the pitch period. All three graphs decrease approximately linearly from about $\Delta tf = 0.075$ to $\Delta tf = 0.03$. The extrapolation of this trend is shown as a dashed gray line (– –) which crosses the origin.

This behavior was predicted in the DIT simulations by Gardner et al. [14], which imply that the measurement-related delay approaches zero when the separation distance is reduced. In contrast to this prediction, the measured lags in Fig. 3.24 successively level out for separations smaller than $\Delta tf = 0.03$, and assume an almost constant DIT-to- σC_p -offset between 0.5° and 1° for $\Delta tf < 0.02$. The largest offset occurs at $x/c = 0.31$ (●), which approximately corresponds to the mean angle of attack and the highest pitching velocity of the sinusoidal motion. This relation will be evaluated in more detail in the next section. For very small separations, $\Delta tf < 0.005$, the results are affected by random scatter. This can be explained by the diminishing signal-to-noise ratio of the DIT peak already discussed in Fig. 3.22. In summary, the current test case yields a non-zero DIT measurement lag error. It can be minimized when choosing separations in the range of $\Delta tf = 0.005 \dots 0.02$, but it cannot be eliminated. This motivates the discussion of different pitching frequencies, k , since it is known from Sec. 4.1 that DIT converges to the “true” IRT results for static cases with $k = 0$.

3.1.6 Discussion of pitch frequency and pitch amplitude effects

The DIT transition positions for different pitching frequencies between $k = 0.005$ (0.25 Hz) and $k = 0.151$ (8 Hz) are shown in Fig. 3.25. The mean and amplitude of the motion, $\alpha = 4^\circ \pm 6^\circ$, and the DIT separation of $\Delta tf = 0.01$ were kept constant. Expectedly the hysteresis between the up- and downstroke increases with increasing k , which includes both aerodynamic and measurement-related lag effects. The transition detection towards the rearward reversal point is better when reducing the pitch frequency, this is caused by an increasing signal-to-noise ratio for slower transition motions.

The influence of the DIT separation Δtf on the DIT measurement lag, see Fig. 3.26, is very similar to the reference case in Fig. 3.24. The optimal separation between about $\Delta tf = 0.005$ and $\Delta tf = 0.02$ is independent of k , it is bounded by large scatter at smaller Δtf and an increasing measurement lag at higher Δtf . Smaller pitch frequencies generally yield a smaller

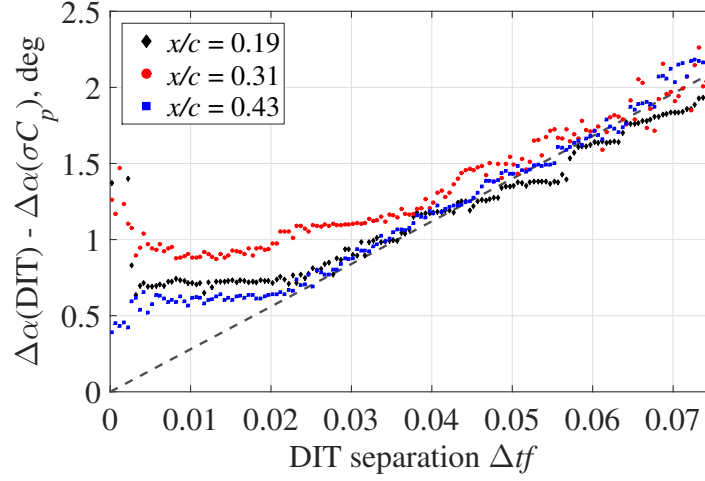


Figure 3.24: Differences between DIT and σC_p hysteresis as function of the DIT phase separation Δtf , $\alpha = 4^\circ \pm 7^\circ$ at $k = 0.075$.

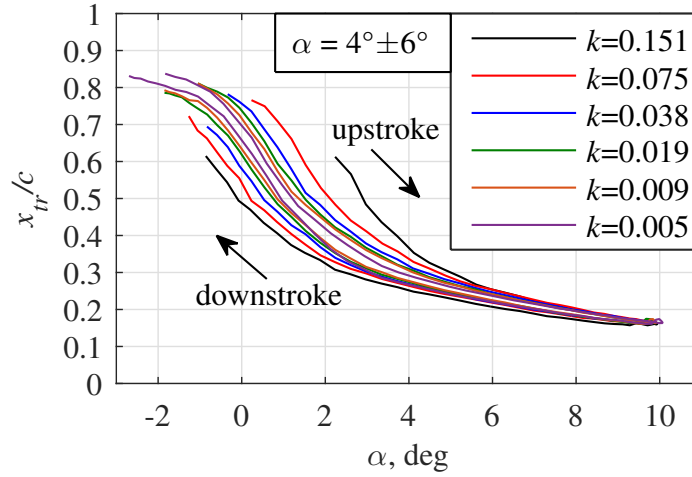


Figure 3.25: DIT transition results, variation of the pitch frequency k for $\alpha = 4^\circ \pm 6^\circ$.

irreducible measurement lag, see the trend marked by a black arrow in Fig. 3.26. This trend is shown by all k -values except for $k=0.151$. It is noted that the uncertainty in the data is partly introduced by the scatter of the σC_p -hysteresis, which was subtracted from the DIT results.

Fig. 3.27 shows the DIT transition results for pitch motions with a constant mean angle of $\bar{\alpha}=4^\circ$ and a constant frequency of $k=0.075$, but a varying amplitude between $\hat{\alpha}=3^\circ$ and $\hat{\alpha}=8^\circ$. The amplitude defines the extent of the transition motion but also its speed and hysteresis, with larger $\hat{\alpha}$ resulting in larger lags. This is due to the effect of $\hat{\alpha}$ on the pitch velocity, which can be derived from the formulation of the angle of attack in Eq. 3.1, yielding

$$\frac{d\alpha}{dt} = 2\pi f \hat{\alpha} \cdot \sin(2\pi tf) . \quad (3.4)$$

A more comprehensive overview is therefore achieved by varying both pitch frequency and amplitude. The results are then evaluated as a function of the pitch velocity.

The hysteresis $\Delta\alpha$ is studied at $x/c=0.31$, which is close to the transition position of the mean angle $\bar{\alpha}=4^\circ$ (see Fig. 3.12) and which is equipped with a pressure tap. This means that the DIT-to- σC_p comparison can be conducted for the entire parameter range of Tab. 3.1. The

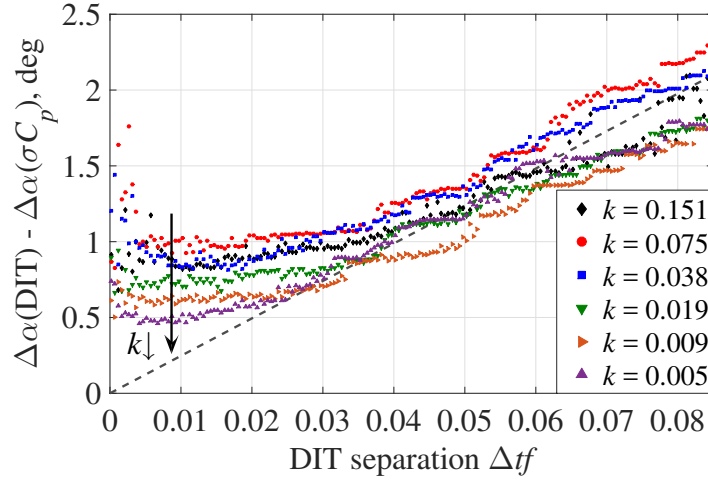


Figure 3.26: Differences between DIT and σC_p hysteresis at $x/c = 0.31$ as function of the DIT phase separation Δt_f , $\alpha = 4^\circ \pm 6^\circ$.

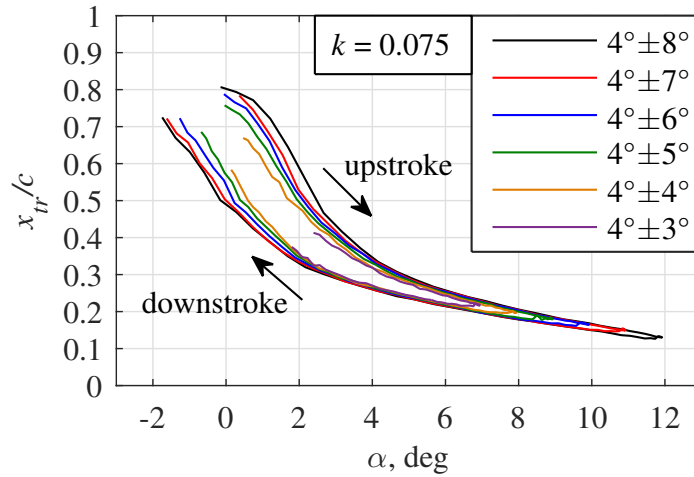


Figure 3.27: DIT transition results, variation of the pitch amplitude $\hat{\alpha}$ for $\bar{\alpha} = 4^\circ$ and $k = 0.075$.

pitch velocity is calculated by averaging the two values for $d\alpha/dt$ at which the transition crosses $x/c = 0.31$ during the up- and downstroke. Both values are close to the mean pitch angle and, therefore, close to the maximum velocity value of $2\pi f \hat{\alpha}$ after Eq. 3.4.

The individual hysteresis of both techniques is shown as filled symbols in Fig. 3.28 (top). The colored symbols belong to DIT and the gray symbols belong to σC_p . Two data points with the same filled marker symbols have the same frequency k but a different amplitude $\hat{\alpha}$. The pitching velocity is apparently the correct scaling parameter, at least for a given transition location. This is evident regarding the clear trend and the low scatter of the DIT data points. The σC_p -reference always has a smaller hysteresis than DIT, and $\Delta\alpha$ decreases with $d\alpha/dt$ roughly linearly towards zero, which is expected for the true aerodynamic hysteresis. The behavior of DIT is easier to understand when subtracting the respective σC_p -values. The result is shown in Fig. 3.28 (bottom), representing the additional DIT measurement lag. For pitch velocities between 15 deg/s and 200 deg/s this error is scattered between 0.6° and 1.1 deg/s with a slightly rising trend. For pitch velocities smaller than 15 deg/s a steep decrease towards zero lag can be seen, which is the expected result when approaching steady conditions.

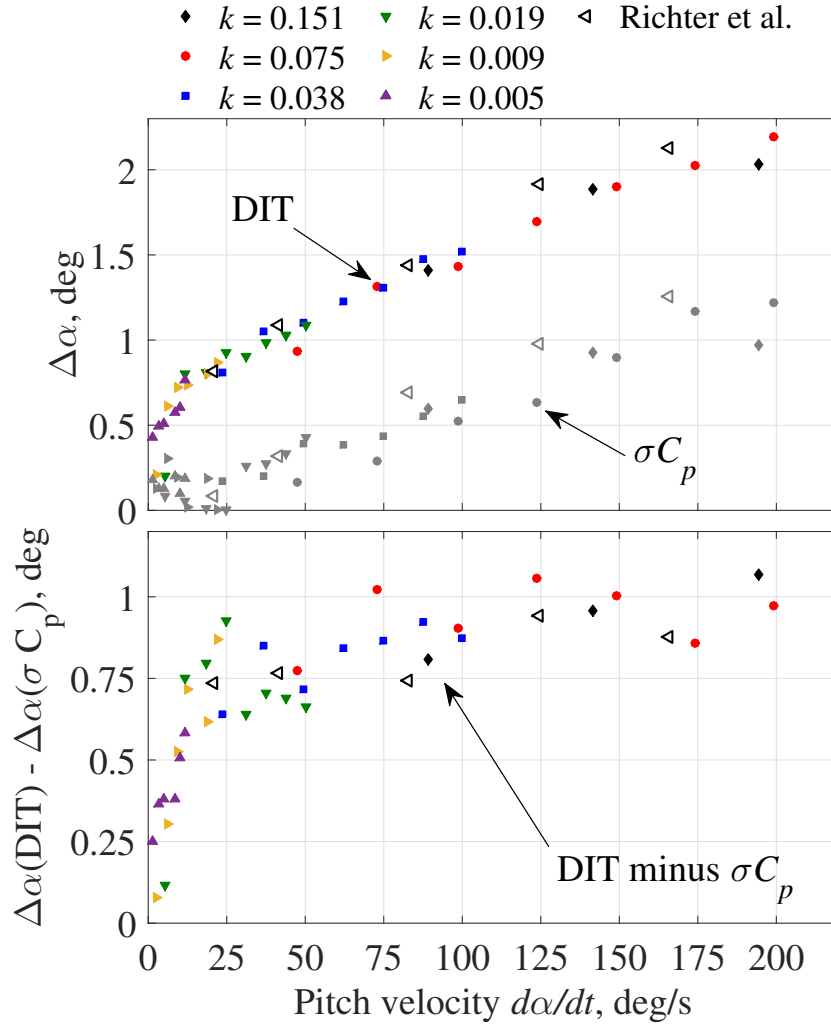


Figure 3.28: Transition hysteresis of DIT and σC_p at $x/c = 0.31$ (top) and difference between both (bottom) as function of the pitch velocity. The unfilled triangles (\triangleleft) is data taken from Richter et al. [35].

The unfilled triangular symbols (\triangleleft) in Fig. 3.28 is data taken from Richter et al. [35] (to be discussed in the current Sec. 3.2), who studied the same airfoil model at $M=0.3$, $Re=1.8 \cdot 10^6$, and reduced frequencies between $k=0.01$ and $k=0.08$. The data agrees well with the current results despite the different freestream conditions. Richter et al. applied a linear fit to the DIT data points and concluded that there is an offset at the zero frequency $k=0$, which contradicts lag-free static infrared measurements. The current Fig. 3.28 shows that Richter et al.'s smallest pitch rate of 20 deg/s is too large to capture the behavior towards $k \rightarrow 0$ correctly, but the current data closes this gap towards static behavior.

3.2 Validation of DIT for airfoil measurements

The pitching airfoil model introduced in the preceding section, Sec. 3.1, was also investigated in the transonic wind tunnel Göttingen (TWG) as part of the DLR project “STELAR”. Compared to the 1MG, the TWG provides a larger Mach- and Reynolds-range, temperature regulation, and adaptive wall segments to reduce the wind tunnel interference. The TWG studies primarily aimed at providing high-quality reference data on dynamic stall phenomena, for example see Refs. [88, 6, 7], but also targeted unsteady boundary layer transition, see Refs. [34, 35]. The BL transition data of the IR images (DIT method) and the pressure taps (σC_p method) was complemented by hot-film sensors, which is a well-established technique to measure the local skin friction at high response frequencies. The data is particularly suitable to compare the three different techniques, and to validate the novel DIT approach. The TWG infrared setup was adapted to the small access windows of a closed test section and to oblique viewing angles, which requires additional image post-processing.

3.2.1 Test setup for airfoil measurements in the TWG

The experiments used the same two-dimensional full-scale model of the rotor blade airfoil “DSA-9A” as in Sec. 3.1. The carbon-fiber composite model has a chord, c , of 0.3 m, a span of 0.997 m, and a maximum thickness of 9% chord. The model was mounted in the 1 m × 1 m adaptive-wall test section of the TWG, see Fig. 3.29 (left). The picture was taken viewing in downstream direction, and the airfoil’s span is horizontal, with a vertical wake rake visible in the background. Pitch oscillations were driven by drive shafts attached at the quarter-chord position and through the tunnel’s side walls. The adaptive test section has a flexible ceiling and floor which were statically adapted based on the airfoil’s mean angle of attack, minimizing the interference velocities at the wall as described in Ref. [231]. Hydraulic motors, located outside the test section, drove the model from both sides.

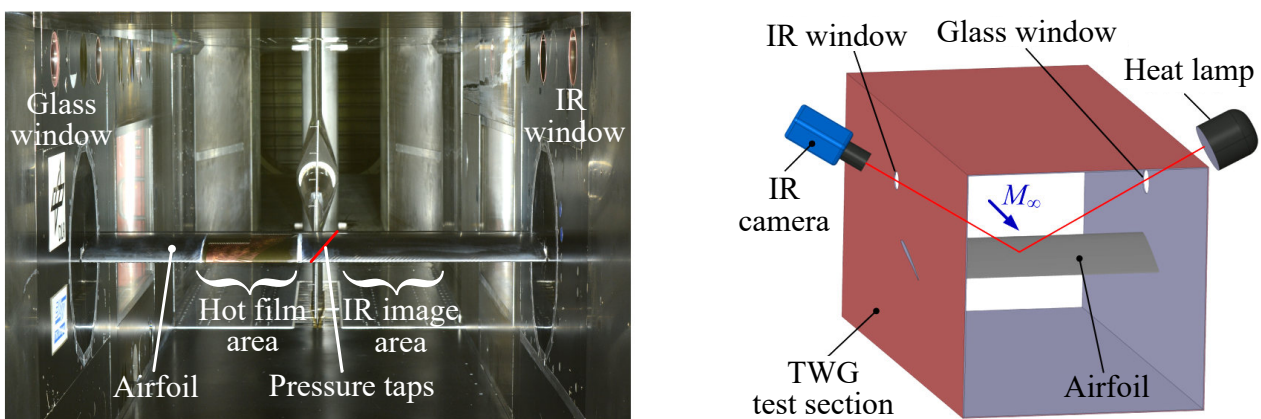


Figure 3.29: Airfoil model in the closed test section of the TWG (left, viewing in downstream direction), sketch of the DIT setup (right, viewing in upstream direction), adapted from Ref. [35].

The central part of the model was equipped with 50 Kulite[®] fast-response pressure sensors as described in Sec. 3.1.1. The pressure data was recorded with a fixed phase-lock of 1024 samples per pitch period and over a total of 160 periods per test point.

In addition, two SenFlex[®] hot-film sensor arrays by TAO Systems [215] were installed next to the pressure transducers and on the starboard side of the model. A total of 61 sensors were distributed over two polyimide sheets on both upper and lower surfaces of the model. The film material was nickel, and the rectangular flow-sensing area of each sensor covered 1.4 mm in spanwise direction and 0.1 mm in streamwise direction. The array layout, the arrangement of the sheets, and the electrical integration were designed to minimize the disturbance of the measurements and the airfoil flow in general. For example, the sensors were placed on a line with an inclination of 15° to the main flow direction to minimize the passage of a sensor's thermal wake over the successive sensors. The upper-surface sheet was wrapped around the model's leading edge and contained 36 sensors between $x/c=0.70$ on the upper side and $x/c=0.05$ on the lower side. The sensor spacing increases from $\Delta x/c=0.01$ around the leading edge to $\Delta x/c=0.05$ towards the trailing edge. The hot-film sheets add no thickness to the model, since they were glued into corresponding recesses cut into the surface. Fig. 3.30 compares the distributions of Kulite[®] sensors (left) and hot-film sensors (right) along the model's surface.

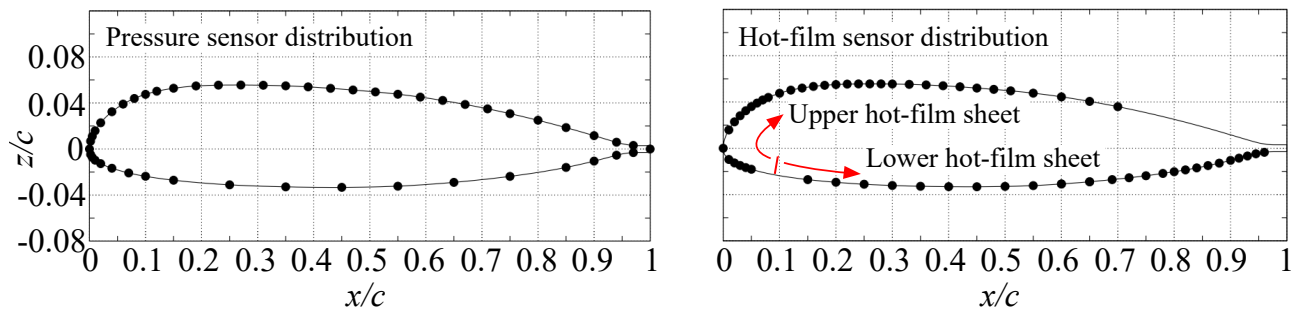


Figure 3.30: Distribution of Kulite[®] sensors (left) and hot-film sensors (right) on the DSA-9A model, the z -axis is enlarged to improve visibility, adapted from Ref. [35].

The hot films were operated in constant-temperature mode with an overheat ratio of 1.3. A quantitative calibration of the shear stress was neglected, since it is very complicated in unsteady flows, and quantitative values are not required to distinguish between a laminar, transitional, or turbulent state of the boundary layer. The signals of the hot films were sampled at a rate of about 135 kHz over 80 pitch cycles, and synchronized with the pressure measurements and the infrared camera. More details on the electrical setup of the hot films are given in Refs. [34, 35].

A sketch of the infrared setup used for DIT measurements is given in Fig. 3.29 (right). The images were taken with the high-speed FLIR[®] SC7750-L camera, combined to a 50 mm focal length-lens with an aperture of $f_{\#} = 2.0$. The camera was installed outside of the test section, observing a part of the airfoil's suction side through a circular germanium window translucent in the long-wave IR range. A halogen spotlight with an electrical power of 2 kW was installed on the opposite side of the test section, providing radiative heating through a standard glass window. The heating increases the model's surface temperature by about $\Delta T = 3$ K, which is small in comparison to the 1MG study in Sec. 3.1.1, due to the limited accessibility of the closed test section in the current campaign. The IR region of interest was located in the central part of the airfoil and on the port side of the pressure transducers, also see Fig. 3.29 (left). The active area of the camera sensor was reduced from 640×512 pixel to 640×310 pixel for an increased image acquisition frequency of 190 Hz. The image exposure

3.2. Validation of DIT for airfoil measurements

time was set to 100 μs . In contrast to the 1MG tests, the temperature levels were calibrated for clarification reasons and are stated in “kelvin” rather than “counts”, even though the DIT method is not dependent on absolute levels.

parameter	unit	value(s)
freestream Mach number, M_∞	-	0.30
chord-based Reynolds number, Re	-	$1.8 \cdot 10^6$
mean pitch angle and amplitude, $\bar{\alpha} \pm \hat{\alpha}$	deg	$3^\circ \pm 3^\circ$ and $5^\circ \pm 6^\circ$
pitch frequency, f	Hz	4.4 and 6.6
reduced frequency, $k = \pi fc / V_\infty$	-	0.040 and 0.060
number of IR images per test point	-	3800
surface heating $T_w - T_\infty$	K	~ 3

Table 3.3: TWG experimental parameters for DIT measurements.

The experimental conditions for the transition measurements are summarized in Tab. 3.3. It is noted that a fixed Reynolds-to-Mach ratio of 6 million was kept constant throughout the entire test campaign. For the current Mach number of 0.3, this was achieved by lowering the wind tunnel’s static pressure to about 90% of the atmospheric pressure. The ratio between the IR camera frequency, 190 Hz, and the airfoil’s pitching frequencies, 4.4 Hz and 6.6 Hz, is odd. Therefore, and due to the large number of images acquired, the pitch phase of the images are randomly but evenly distributed over the entire pitch phase.

3.2.2 Processing of the TWG transition data

Hot films

A general introduction into the hot film measurement technique for BL transition measurements is given in Sec. 2.2.1. The current hot-film array was connected to a multi-channel bridge amplifier keeping the sensors at a constant overheat ratio of 1.3, which corresponds to a sensor temperature of about 50 K above flow temperature. Fig. 3.31 (left) shows a sample sensor voltage signal U_{HF} as a function of the pitch phase tf , with the maximum pitch angle reached at a phase of $tf = 0.5$, and the minimum pitch angle at $tf = 0$ and $tf = 1$. The corresponding sensor is located at $x/c = 0.7$ on the airfoil’s suction side, and the signal was phase-averaged.

The Reynolds analogy for convective heat transfer, Eq. 3.2, is applicable and predicts that the required heating power for a constant sensor surface temperature increases with an increasing skin friction coefficient, C_f . Consequently, the sensor voltage changes between two levels. The high level during $0.39 \leq tf \leq 0.67$ indicates a turbulent boundary layer, and the transition is upstream of the sensor position due to the high angle of attack. Vice versa, the low voltage level for $tf < 0.35$ and $tf > 0.69$ corresponds to a laminar boundary layer at small angles of attack. The gradual drift of the sensor signal during the laminar or turbulent periods is due to the changing velocity in the external flow.

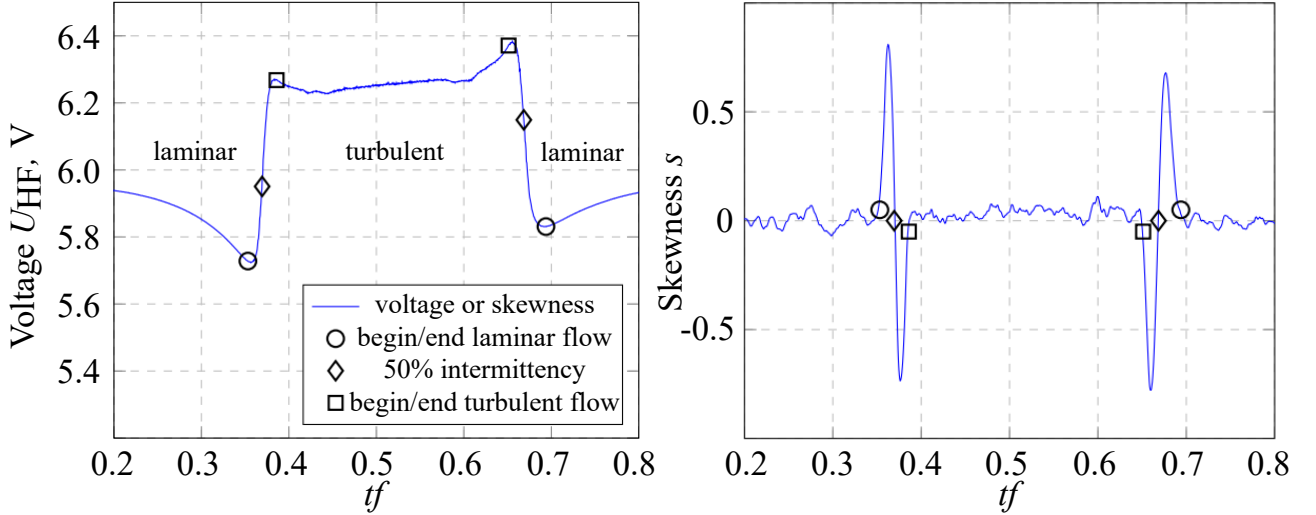


Figure 3.31: Phase-averaged hot-film voltage signal (left) and corresponding skewness (right), sensor located at $x/c = 0.7$ on the suction side, Ref. [34].

The high acquisition frequency of the hot-film signals, U_{HF} , allows to further investigate the short periods of transitional flow. Since the data was sampled over $N = 80$ pitch cycles, the following statistics apply at any given pitch phase, tf :

$$\bar{U}_{HF} = \frac{1}{N} \sum_{i=1}^N U_{HF,i} \quad \text{phase-average} \quad (3.5)$$

$$\sigma U_{HF} = \sqrt{\frac{1}{N-1} \sum_{i=1}^N (U_{HF,i} - \bar{U}_{HF})^2} \quad \text{standard deviation} \quad (3.6)$$

$$s = \frac{1}{N-1} \sum_{i=1}^N \left(\frac{U_{HF,i} - \bar{U}_{HF}}{\sigma U_{HF}} \right)^3 \quad \text{skewness} \quad (3.7)$$

The standard deviation, σU_{HF} (not shown), is strongly increased during transitional periods. The signal's skewness, s , is shown in Fig. 3.31 (right). It has a characteristic double-peak structure when, for example, changing from laminar to turbulent BL states during $0.35 \leq tf \leq 0.39$. In the first half of the transition process, $0.35 \leq tf \leq 0.37$, the skewness is positive due to a generally laminar flow interrupted by an increasing number of turbulent spots. In the second half of the transition, $0.37 \leq tf \leq 0.39$, the flow is predominantly turbulent with a decreasing number of laminar spots, yielding a negative skewness. The point of 50% intermittence, in which laminar and turbulent states occur with the same probability, has zero skewness. During the relaminarization, $0.65 \leq tf \leq 0.69$, the process is reversed, yielding a negative-positive double-peak structure. Detecting the zero-crossing skewness yields an automatable and physics-based criterion to identify begin of transition, 50% intermittence, and end of transition. This is shown by the circular (○), diamond (◇), and rectangular (□) markers in Fig. 3.31 (right). The method is an improvement over a manual analysis of hot-film data, as conducted in earlier publications by Lee and Basu [131] or Richter et al. [177].

Pressure sensors

The applied σC_p -method was introduced in Sec. 2.2.2. As already shown in Fig. 3.8 for the DSA-9A airfoil under steady inflow conditions, the changes of the skin friction are much easier to identify than the transition-related changes of the pressure distribution, which are small in comparison to the surface curvature-related pressure changes.

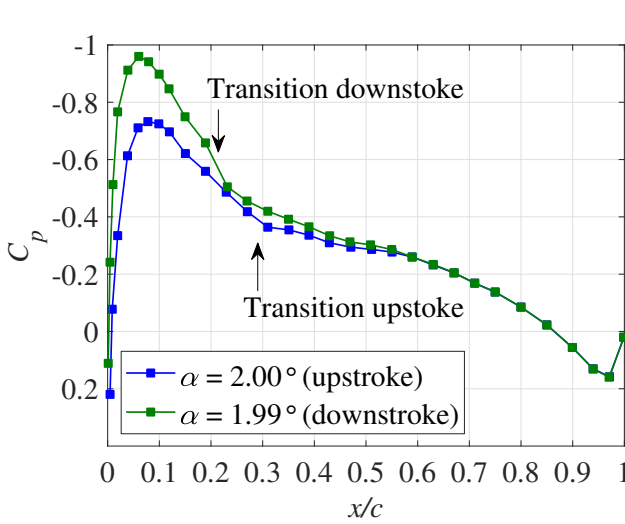


Figure 3.32: C_p -distributions (upper side), $\alpha = 5^\circ \pm 6^\circ$, $k = 0.060$, adapted from Ref. [34].

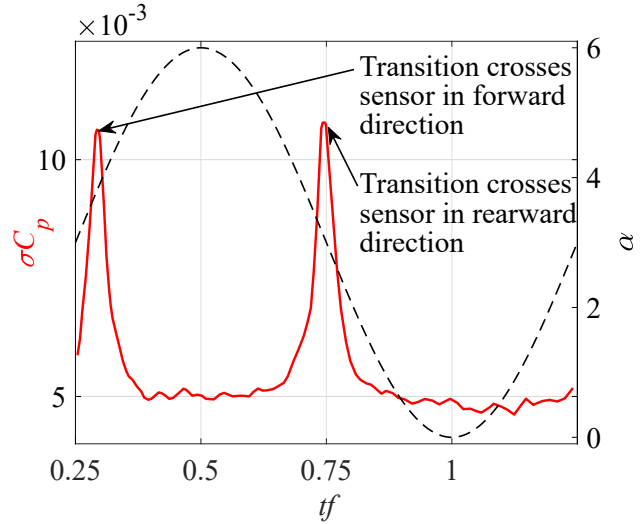


Figure 3.33: σC_p over the pitch phase tf , $x/c = 0.19$, $\alpha = 3^\circ \pm 3^\circ$, $k = 0.040$ [34].

This can be seen in Fig. 3.32 by means of the phase-averaged pressure distributions on the airfoil's upper side for $\alpha \approx 2^\circ$ during the upstroke (■) and downstroke (■) of a pitch oscillation. The hysteresis is apparent by means of a lower suction peak and, consequently, a smaller lift coefficient during the upstroke. The identified transition positions, see the black arrow markers, cause small kinks in C_p due to the local thickening of the boundary layer, which can be easily overlooked in the overall pressure distributions, and which are hard to identify using automated post-processing.

The standard deviation of the pressure signal, σC_p , at $x/c=0.19$ as a function of the pitch phase, tf , and evaluated over 160 pitch cycles is shown in Fig. 3.33 (—). The noise floor of the signal is about $\sigma C_p = 5 \cdot 10^{-3}$, but this level is topped by two distinct peaks exceeding $\sigma C_p = 10 \cdot 10^{-3}$. The peaks correspond to the transition region crossing the sensor in forward motion during the upstroke ($tf \approx 0.29$) and in rearward motion during the downstroke ($tf \approx 0.75$). It is noted that the distribution is void of other “strong” flow features such as shock waves or flow separation.

The calculation of σC_p at a constant pitch phase is particularly easy in the current case, since the data was sampled in phase-lock to the airfoil's pitch motion at 1024 points per cycle. The σC_p -method does not require a very high temporal resolution of the pressure signals, as long as the underlying periodicity of the pitch and transition motions are properly captured. This is in contrast to BL transition measurements by surface microphones, which have a broader spectral range extending to higher frequencies in comparison to the current sub-surface pressure transducer. The microphones not only allow differentiation between laminar, transitional, and turbulent states of a boundary layer based on the overall sound pressure level in an appropriately chosen frequency band [161, 172, 219], but also provide

additional information on the evolution of the transition mode, for example by means of tracking the Tollmien-Schlichting frequencies [73]. This level of detail is inaccessible to the σC_p -criterion.

Infrared images

An instantaneous thermal image acquired during the TWG investigation is shown in Fig. 3.34 (left), viewing the model's suction side with flow from left to right. The airfoil's leading edge, trailing edge, and the hot-film sensors in operation are easily visible. The evaluated region of interest is framed by a yellow line, it is limited by the circular germanium window frame obstructing the view in the lower right corner. The differential temperature in Fig 3.34 (right) was calculated by subtracting two IR images, $\alpha_2 - \alpha_1$, taken at $\alpha_2 = 5.3^\circ$ and $\alpha_1 = 4.7^\circ$. The airfoil's leading/trailing edges and the hot-film sensors are still visible, since their position slightly shifted due to the model's pitch change. In addition, the motion of the transition region towards the leading edge becomes visible by means of a blue stripe aligned in spanwise direction, indicating a more efficient heat convection due to the larger C_f . Hence, the temperature difference is negative, with minimum values around -0.2 K. The differential images also reveal random image-to-image sensor noise with a standard deviation of about 0.08 K.

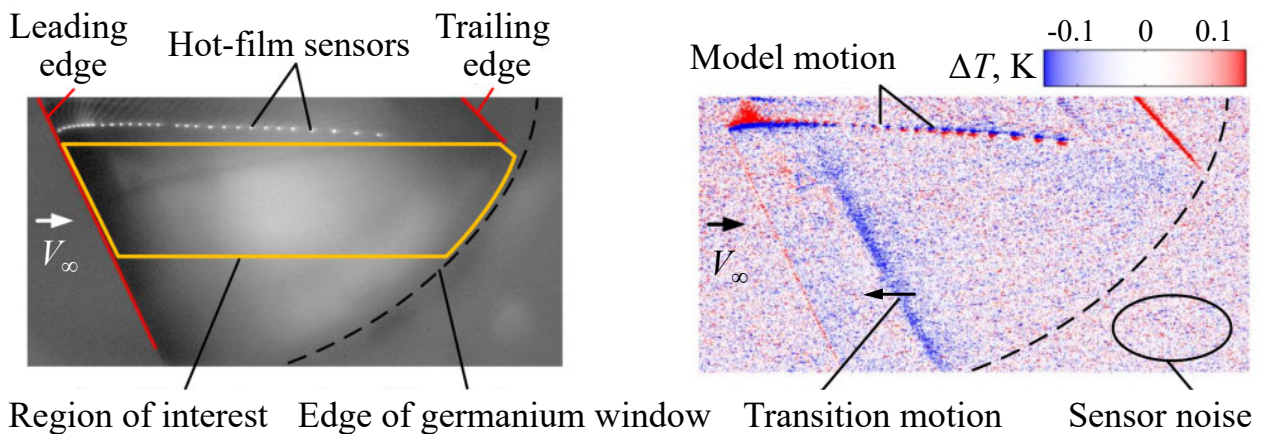


Figure 3.34: Infrared images of the suction side (left) and differential image for $\Delta\alpha = 5.3^\circ - 4.7^\circ$ (right), Ref. [34].

The differential images were dewarped and scaled in a two-step approach using MATLAB image processing tools, and the result is shown Fig. 3.35 (left). In a first step, the leading and trailing edges of the model were identified in the raw IR images through an automated algorithm. The airfoil's upper surface was then mapped to an orthogonal projection. However, this procedure assumes a flat surface and neglects the curvature of the airfoil. An additional error is introduced, since the identified optical edges of the model deviate from the leading and trailing edge as a consequence of an oblique viewing angle. Therefore, a second refinement step was applied, using the clearly identifiable hot-film sensors as reference points. The mapped x -coordinates of the sensors were then compared to the known "true" coordinates for multiple IR images with different α . This allows the formulation of an empirical correction of the dewarped images' streamwise axis as a linear function of both x and α . The remaining

3.2. Validation of DIT for airfoil measurements

error of the hot-film x -coordinates is bounded by $\Delta x/c = \pm 0.006$. This value can be interpreted as an error estimate for the overall dewarping process, and it was observed to predominantly originate in random errors during the automated leading/trailing edge identification. The optical resolution of the dewarped images in chordwise direction is below $\Delta x/c = 0.005$ (0.5% chord) and, thus, much finer than the hot-film and pressure transducer distributions, particularly regarding the sparse instrumentation towards the trailing edge.

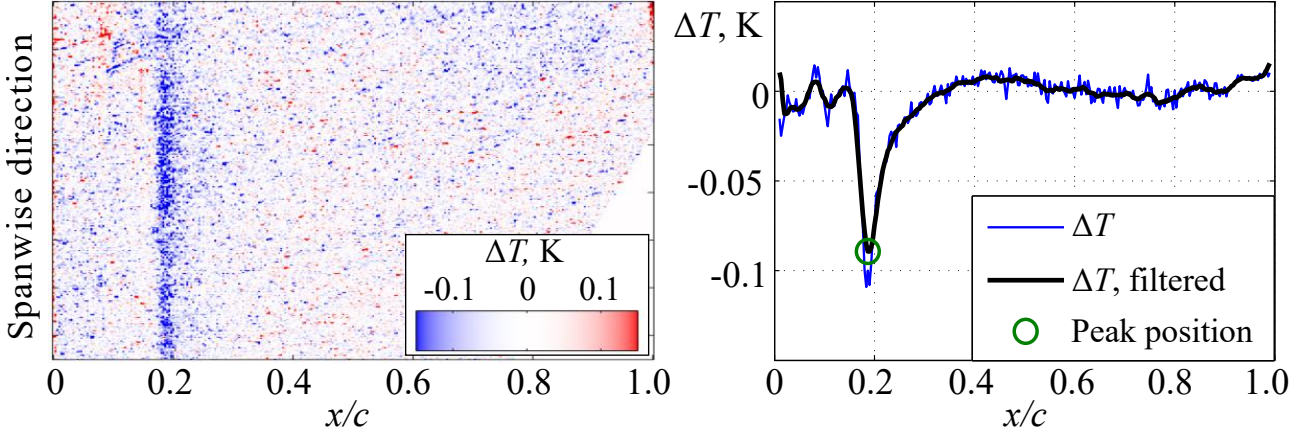


Figure 3.35: Dewarped and scaled differential image (left), spanwise-averaged ΔT -signal, Ref. [34].

An integration in y -direction reduces random sensor noise and provides the spanwise-averaged differential intensity distribution as a function of x/c , see the blue line (—) in Fig. 3.35 (right). The prominent negative peak at $x/c \approx 0.2$ is the transition motion in the upstream direction. The peak-to-noise ratio is about 9 to 1 in this example, but it varies with the transition position and the DIT image separation, as discussed earlier in Fig. 3.22. Remaining small-scale noise was dampened using a sliding-average filter, see the black line (—) in Fig. 3.35 (right). Following the same approach as outlined in Sec. 3.1, the position of the ΔT -peak (○) was identified as the transition position at the average angle of attack, $(\alpha_2 + \alpha_1)/2$.

The analysis was conducted for the entire IR image series of the test cases stated in Tab. 3.3. Depending on the model's pitch frequency, f , the differential image was calculated between every image for $f = 6.6$ Hz, or every other image for $f = 4.4$ Hz. The fixed camera frequency of 190 Hz yields image phase separations of $\Delta t_f = 0.035$ and $\Delta t_f = 0.046$, respectively. Compared to the systematic 1MG study with the same rotor blade model, see Fig. 3.24 and corresponding discussions, the separations are expected to produce valid results. The current choices for Δt_f are larger than the optimum around $\Delta t_f = 0.020$ but conservative, meaning that a slightly increased measurement hysteresis is accepted for a good signal-to-noise ratio.

Fig. 3.36 shows the identified transition positions x_{tr} (●) for the test case with sinusoidal pitch oscillations, $\alpha = 3^\circ \pm 3^\circ$ at $f = 4.4$ Hz, as a function of the phase, t_f . The data represents 88 consecutive cycles, and it is evenly scattered over the entire phase, since the IR camera was not synchronized to the pitch motion drive. The transition moves towards the leading edge at $x = 0$ when the pitch angle increases, and vice versa. In large parts of the cycle, the scatter of the distribution is small and within the estimated dewarping error.

A false and inconsistent behavior is found close to the minimum and maximum pitch angles, see the gray-shaded areas in Fig. 3.36. This is partly due to the DIT signal approaching

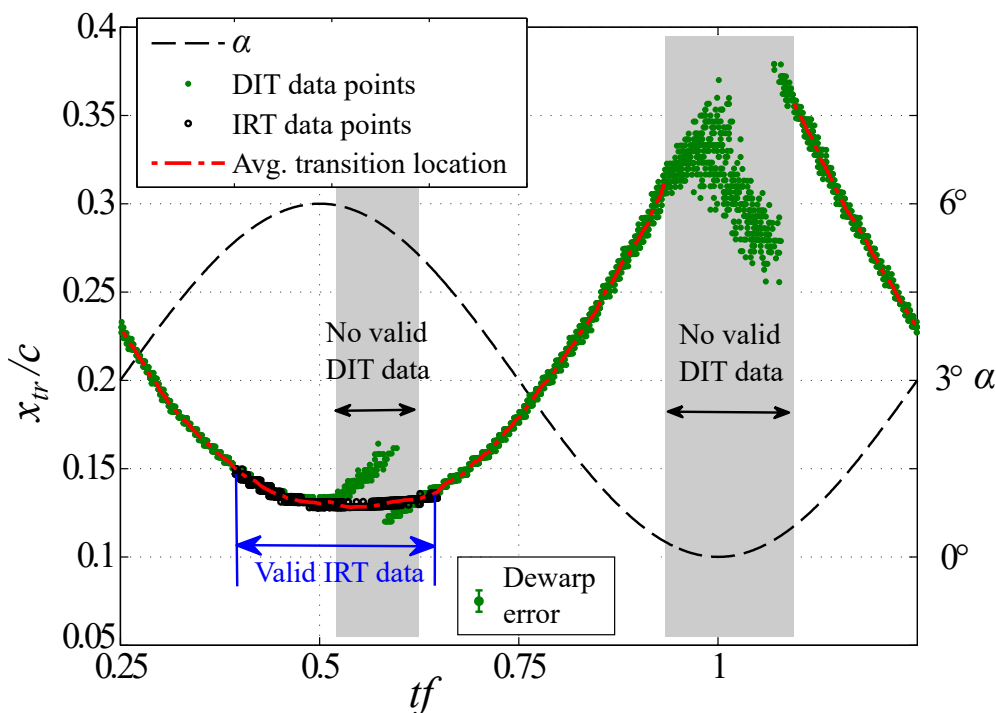


Figure 3.36: DIT transition locations, suction side, for sinusoidal pitch oscillations with $\alpha = 3^\circ \pm 3^\circ$ and $k = 0.040$ ($f = 4.4$ Hz), Ref. [34].

zero when the transition motion reverses. Surprisingly, the corresponding scatter of the DIT data points is not entirely random. The detected peak positions abruptly switch back and forth between two distinct x_{tr} -positions, and the loci of both the forward and the rearward transition motions do not merge in a steady curvature. This behavior is similar to the 1MG tests but even more pronounced. It is again connected to a coexistence of both negative and positive ΔT -peaks from the forward and rearward transition motions, also see Fig. 3.23. A later aerothermal simulation in Sec. 3.3 will show that this behavior results from the limited thermal responsiveness of the model's surface. The erroneous data in the gray boxes was removed from the evaluation of each test point. The DIT data gap at the forward reverse point, about $0.5 \leq tf \leq 0.6$, was padded with a "standard" infrared thermography analysis (IRT). This means that the transition line was identified as temperature steps in individual images, which assumes quasi-steady aerodynamics, and only works for a very slow transition motion. Therefore, the procedure cannot be generalized. The resulting IRT data of the current case, see the black circular symbols (\bullet) in Fig. 3.36, steadily fills up the DIT data. In a last step, the valid data points were phase-averaged in 150 equidistant tf -bins, providing the DIT result shown as a red dashed line (---).

3.2.3 Influence of surface heating

The effect of cooled or heated walls on the temperature and velocity profiles of a boundary layer has been tackled by multiple studies, for example in the context of aircraft drag reduction [126, 173] or non-adiabatic wall effects during high-speed aerodynamic testing [171], particularly in cryogenic facilities [66]. The latter publication by Costantini et al. investigates the boundary layer on the suction side of the laminar-type supercritical "LV2F" airfoil con-

sidering both experimental and numerical data. It was shown that increasing the surface temperature, T_w , over the flow's adiabatic recovery temperature, T_r , decreases the extent of laminar flow and vice versa. However, this effect depends on the BL's stability situation. The thermal condition has a large impact when the transition occurs in a region with zero or negative (favorable) pressure gradient. For example, a shift of $\Delta x_{tr}/c = 0.11$ towards the leading edge was observed when raising the wall temperature from 2.1% to 7.7% above adiabatic temperature, see Fig. 13 in [66] for $Re = 13 \cdot 10^6$. A much smaller or even non-existent temperature influence was observed when the transition is in an area of a positive (adverse) pressure gradient, see Fig. 15 in [66] for $Re = 7.5 \cdot 10^6$, or when the transition results from a laminar separation bubble. In summary, the overheat ratio for DIT measurements should be selected as small as possible on the basis of the differential images' signal-to-noise ratio, and its influence on the flow should be monitored by other measurement techniques if possible.

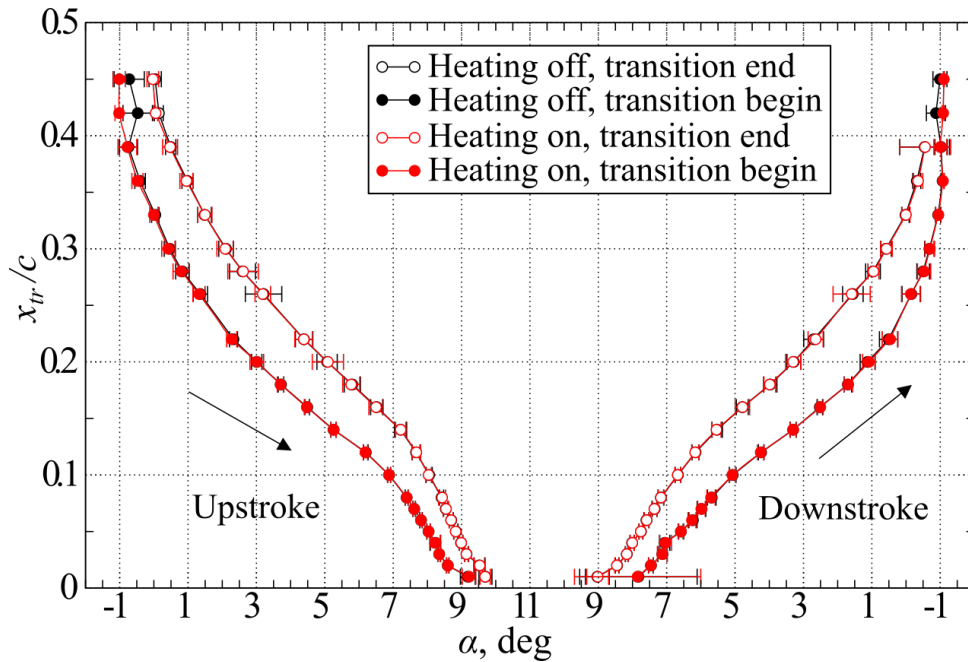


Figure 3.37: Effect of the radiative heating on the transition begin and end, hot-film data, pitch motion with $\alpha = 5^\circ \pm 6^\circ$ and $k = 0.060$, Ref. [34].

The radiative heating applied in the current tests increases the surface temperature by about $\Delta T_w = 3 \text{ K}$, corresponding to a 1%-increase over the adiabatic temperature, and the transition process is primarily driven by a positive pressure gradient [34]. Hence, a rather small influence of the heating is expected, which is supported by Fig 3.37 for a sinusoidal pitch motion with $\alpha = 5^\circ \pm 6^\circ$ at $k = 0.060$ or $f = 6.6 \text{ Hz}$. The begin and end of the transitional region measured by hot-film sensors is shown as function the airfoil's angle of attack, α , which was split between upstroke (left half) and downstroke (right half) to improve visibility. Except for two outliers in the upper left corner, the transition positions with and without heating (— and —) are nearly coincidental, with deviations smaller than the cycle-to-cycle standard deviations represented by error bars. Valid hot-film transition data could only be extracted up to $x_{tr}/c = 0.45$ in this case. An analysis of the σC_p -data further downstream for $0.45 \leq x_{tr}/c \leq 0.55$ (not shown here, see [35] for details) indicates that the heating slightly reduces the laminar flow length by up to $0.02 c$. By tendency, this complies to the expected effect of an increased surface temperature in an area of a small pressure gradient.

3.2.4 Comparison of the different measurement techniques

A comparison between the transition results of hot-film analysis (HF), pressure transducer analysis (σC_p), and differential infrared thermography (DIT) for a sinusoidal pitching motion with $\alpha = 5^\circ \pm 6^\circ$ and $k = 0.060$ ($f = 6.6$ Hz) is shown in Fig. 3.38.

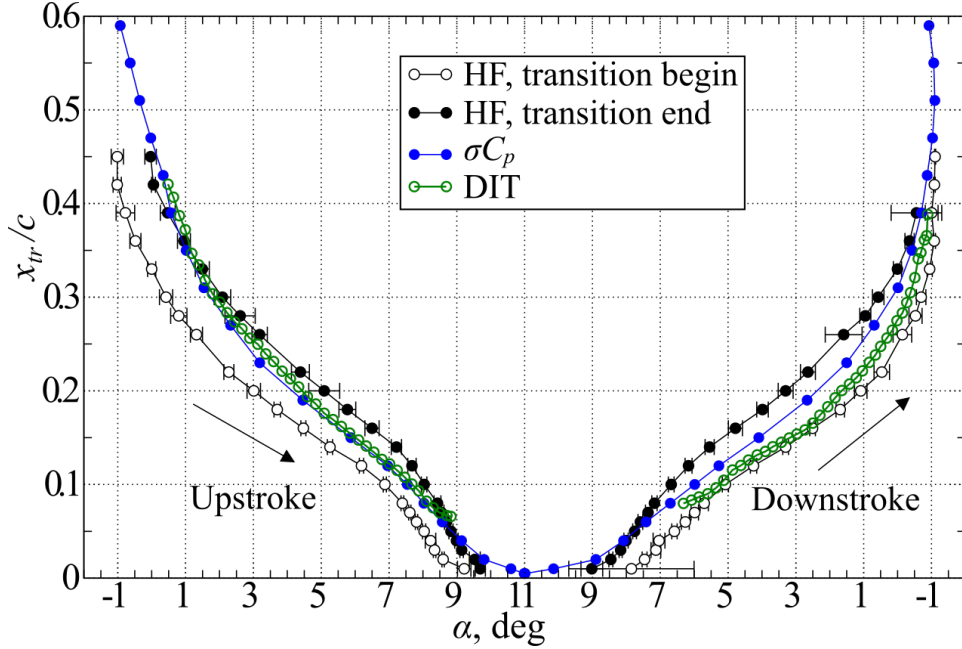


Figure 3.38: Transition begin/end for hot-films (HF), transition position for pressure transducers (σC_p) and infrared images (DIT), pitch motion with $\alpha = 5^\circ \pm 6^\circ$ and $k = 0.060$, Ref. [34].

Up- and downstroke were unfolded over the angle of attack, showing the expected trend in which x_{tr} moves towards the leading edge for increasing α , and vice versa. The HF data is considered the reference for the other two techniques, as it is well-proven and divides between transition onset (o) and transition end (●). The resulting vertical split is the length of transition region, which decreases for an increasing angle of attack, covering about $0.10 c$ at $\alpha = 0^\circ$ and $0.02 c$ at $\alpha = 9^\circ$. A more detailed analysis is provided in Ref. [34], showing that the transition length strongly depends on the local flow conditions, with values exceeding $0.4 c$ on the airfoil's lower side due to its flat pressure distribution.

The single-valued results for σC_p (●) and DIT (○) in Fig. 3.38 generally agree well with the hot films over large parts of the pitch cycle, and mostly lie within the corresponding transition region. Beginning on the left side of the figure with the pitch upstroke, $-1^\circ \leq \alpha \leq 2^\circ$, the data of σC_p and DIT is almost coincidental but located close to the HF transition end. A careful evaluation of steady-state infrared images, also see Fig. 2.3 in Sec. 2.2.1, shows that the hot-film carrier foil triggers premature BL transition in this α -range, which is presumably related to a non-conformal foil application and small changes in the airfoil's contour. In the central part of the upstroke, $2^\circ \leq \alpha \leq 8^\circ$, the DIT data is mostly on top of the σC_p transition positions, and approximately in the center between HF transition begin and end, which is the expected result confirming the validity of DIT. In the central part of Fig. 3.38, $\alpha \approx 11^\circ$, no DIT data is available due to the incorrect double-peak signal at the motion reversal discussed in Fig. 3.36. During the downstroke, the σC_p transition position is again centered between HF transition begin and end, whereas the DIT data is notably delayed towards higher α for the

same x_{tr} -location, indicating a larger hysteresis.

It is assumed that the main reason for this discrepancy lies in the additional thermal hysteresis of the technique, which can be studied in better detail in Fig. 3.39. It uses the same x_{tr} -data for σC_p and DIT as in Fig. 3.38, but shows both upstroke (unfilled symbols: \circ , \circ) and downstroke (filled symbols: \bullet , \bullet) on a common α -axis. Hence, the horizontal difference $\Delta\alpha$ is the hysteresis at a given transition position x_{tr} , which corresponds to the evaluation of the 1MG experiment in Sec. 3.1. The HF-data (\circ, \bullet) was reduced to only show the single-valued 50%-intermittency rather than begin and end of transition.

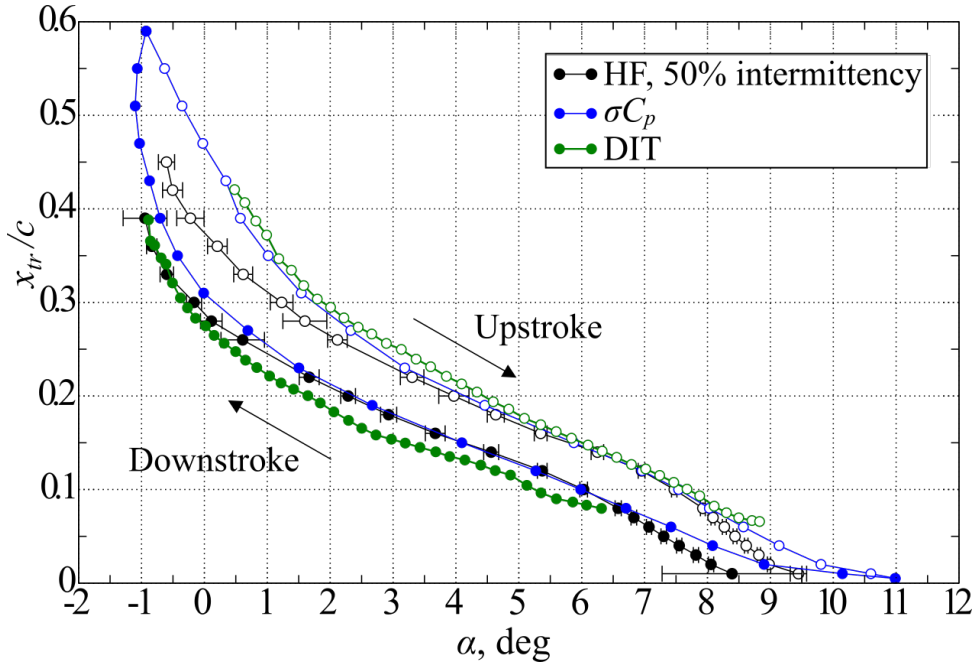


Figure 3.39: Transition position for hot films (HF), pressure transducers (σC_p), and infrared images (DIT), pitch motion with $\alpha = 5^\circ \pm 6^\circ$ and $k = 0.060$, Ref. [34].

Fig. 3.39 confirms the consistent behavior of all three techniques in the central part of the pitch motion, with an additional uncertainty towards the trailing edge (left side, due to premature transition on the HF foil) and close to the leading edge (right side). The maximum hysteresis for σC_p and HF is about $\Delta\alpha = 1.7^\circ$ at $x_{tr} = 0.18$, indicating a significant “true” aerodynamic hysteresis measured by both fast-response techniques. The DIT result has a notably larger split between up- and downstroke, accounting for an additional measurement hysteresis of about $\Delta\alpha = 1.0^\circ$ at $x_{tr} = 0.18$.

The trends and conclusions implied by Figs. 3.38 and 3.39 can be supported by other pitch motions, for example see Fig. 3.40. The mean value and amplitude of the sinusoidal motion was reduced to $\alpha = 3^\circ \pm 3^\circ$ at a constant frequency of $k = 0.060$ ($f = 6.6$ Hz), which decreases the range of the transition motion, and which halves the pitch velocity $d\alpha/dt$. The DIT data gap at the forward reversal of the transition motion, that is, at the right end of Fig. 3.40, was padded with a “standard” evaluation of individual infrared images (IRT), as explained in Fig. 3.36. The data confirms the good overall agreement between the three transition detection techniques, with an excellent agreement between HF (\circ, \bullet) and σC_p (\circ, \bullet) towards the leading edge, $x_{tr}/c \leq 0.22$. The additional thermal measurement hysteresis of DIT is again apparent by the split between upstroke (\circ) and downstroke (\bullet). Richter et al. [35]

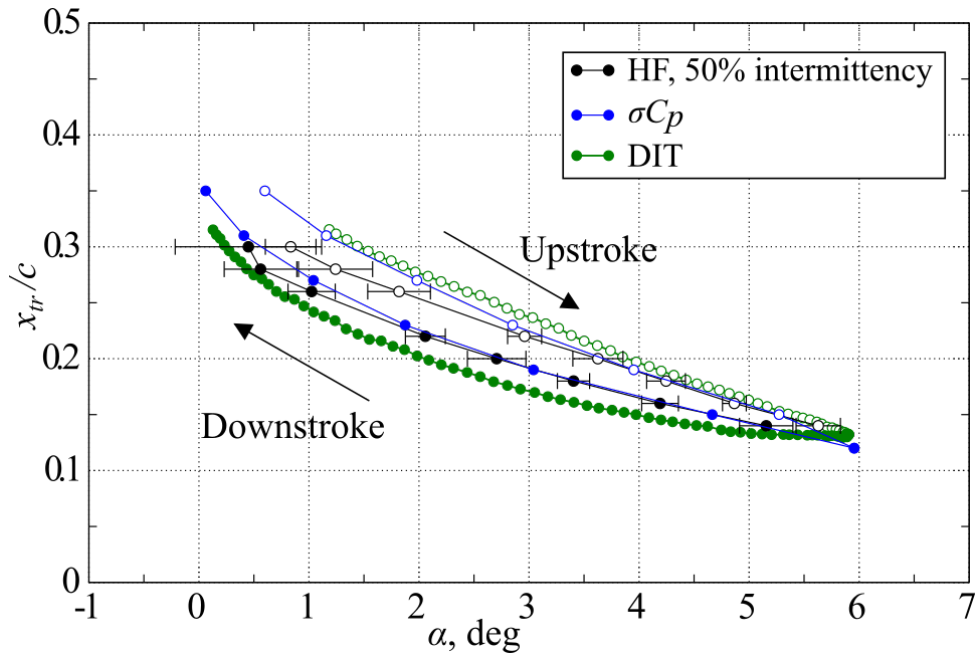


Figure 3.40: Transition position for hot films (HF), pressure transducers (σC_p), and infrared images (DIT), pitch motion with $\alpha = 3^\circ \pm 3^\circ$ and $k = 0.060$, Ref. [34].

discussed several other sinusoidal- and ramp-type motions, adding further indications that the novel DIT approach correctly estimates the 50%-intermittency positions of the reference HF data. The additional DIT thermal hysteresis in the TWG experiments was already shown in Fig. 3.28 (◄) as a function of the pitch rate $d\alpha/dt$. The experiments in the one-meter wind tunnel, 1MG, and the transonic wind tunnel, TWG, agree on similar levels of $\Delta\alpha \approx 1^\circ$ for $d\alpha/dt \geq 50$ deg/s. However, it must be kept in mind that this hysteresis value is specific to the surface material of the current model and the heating technique, which will be shown in the next section.

3.3 Analysis of DIT using a coupled aerothermal simulation

In a next step, the experimental TWG study of the preceding section was further analyzed using a time-resolving numerical simulation of the DIT procedure. Therefore, a 1D finite-volume solver was built to calculate the temperature distribution in a thin layer of the model's surface. Unsteady CFD solutions provide the boundary conditions at the interface to the flow. The analysis not only provides a deeper insight into problems encountered during the experiment, such as the additional measurement hysteresis or the erroneous behavior at the reversal of the transition motion, but also offers some improvements for the DIT method itself. The following sections provide an overview of the entire results published by Gardner et al. [14].

3.3.1 Temperature computation in the surface layer

The surface layer of the model is discretized as shown in Fig. 3.41. A large number of volume cells is stacked in the wall-normal z -direction.

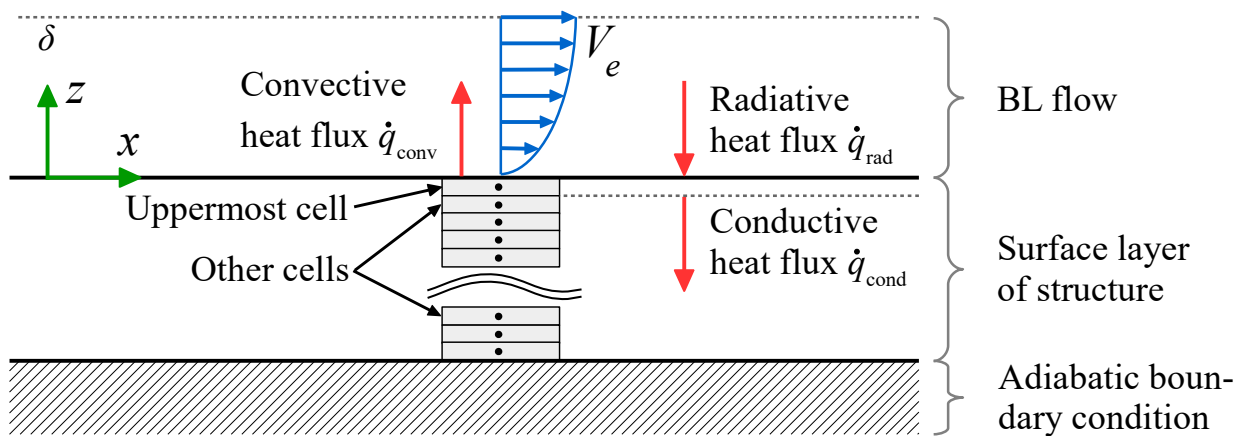


Figure 3.41: Sketch of the numerical scheme for the coupled aero-thermal simulation [14].

The following assumptions are made:

- The thermal properties of the surface layer are homogeneous.
- The surface is heated by an external radiative source, such as a lamp, with a known heat flux.
- The surface does not lose any energy by radiation.
- The airfoil is infinite in the spanwise y -direction.
- The heat flux is only directed in the wall-normal z -direction, but not in the streamwise x -direction.
- The curvature of the surface is neglected for the thermal part of the simulation (but not for the surrounding aerodynamics).
- The lower boundary of the simulated layer is adiabatic (no heat exchange).

These assumptions are a considerable simplification of the physical situation. Nevertheless, all assumptions preserve the qualitative character of the surface temperature response. For example, treating a composite surface material as a homogeneous material will result in incorrect temperature distributions within the wall, but a qualitatively similar response of the surface temperature to flow changes. Under the given assumptions, the differential form of the 1D energy transport equation in z -direction is given by:

$$\frac{\partial T}{\partial t} c_s \rho_s = \frac{\partial \dot{q}}{\partial z}, \quad (3.8)$$

with the surface layer's temperature T , its specific heat capacity c_s , and its density ρ_s . The net heat flux, \dot{q} , of the uppermost cell comprises the convective flux into the flow, \dot{q}_{conv} , the conductive flux into lower cells, \dot{q}_{cond} , and the incoming radiation flux of the heat source, \dot{q}_{rad} :

$$\begin{aligned} \dot{q} &= \dot{q}_{\text{rad}} - \dot{q}_{\text{cond}} - \dot{q}_{\text{conv}}, \quad \text{with:} & (3.9) \\ \dot{q}_{\text{cond}} &= \lambda_{s,v} \frac{\partial T}{\partial z} & \text{(conduction)} \\ \dot{q}_{\text{conv}} &= \frac{1}{2} C_{f,e} c_p \rho_e V_e (T_w - T_r) & \text{(convection)} \\ \dot{q}_{\text{rad}} & & \text{(incoming radiative flux)} \end{aligned}$$

The conductive term depends on the vertical temperature gradient, $\partial T / \partial z$, and the material's thermal conductivity in vertical direction, $\lambda_{s,v}$. The convective term repeats the Reynolds analogy from Eq. 3.2, relating the skin friction coefficient to the surface-to-fluid temperature difference. The effective flow temperature in the BL is given by the recovery temperature, T_r , also known as "adiabatic temperature" or "Eigentemperature". Accounting for a curved airfoil geometry and as argued by van Driest [75], the Reynolds analogy can be formulated with the local conditions of the external flow (index "e") rather than with the freestream conditions. This also holds true for the calculation of T_r :

$$T_r = T_e \left(1 + r_C \frac{\gamma - 1}{2} M_e^2 \right) = T_0 + \underbrace{(r_C - 1) \frac{V_e^2}{2c_p}}_{\Delta T_0 < 0}. \quad (3.10)$$

The recovery factor, $r_C < 1$, indicates that T_r is smaller than the flow's total temperature, T_0 . The recovery factor depends on the fluid's Prandtl number, about 0.71 for air, and the state of the boundary layer. Studies report $r_C \approx 0.82 - 0.85$ for a laminar subsonic BL [75, 142] and $r_C \approx 0.9$ for a turbulent subsonic BL [76, 142]. The numbers are supported by observations and approximations in Schlichting [187], also see Fig. 3.42.

Evaluating Eq. 3.10 for the current TWG case shows that the BL transition results in an increase of $\Delta T_r \approx 0.25 - 0.5$ K. With current IR camera sensitivities well below 0.1 K, it seems feasible to detect this "natural" flow temperature difference of a stationary transition position without additional heating or cooling, even though it will be superimposed by an acceleration or deceleration of the external flow. However, it is very hard to achieve a true flow-to-surface temperature equilibrium in experimental tests [4], and the IR measurement is mostly driven

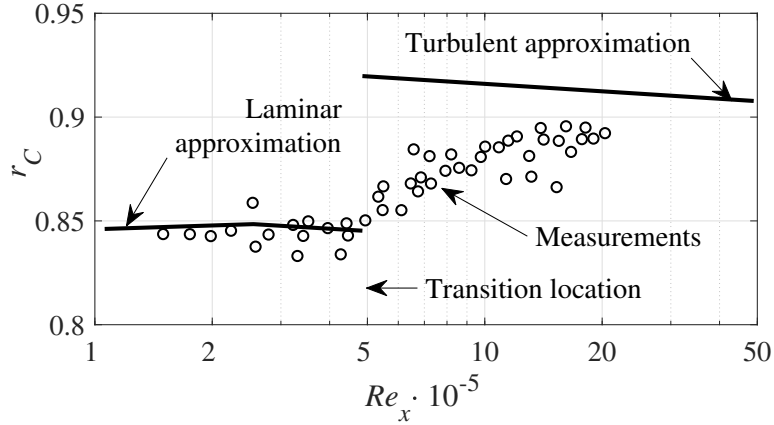


Figure 3.42: Recovery factor of an air flow over a flat plate as a function of the local Reynolds number, approximations for laminar and turbulent regions, adapted from Schlichting [187].

by the convective term and its dependency on C_f [19]. For cases with a moving transition position and the resulting thermal hysteresis, artificial heating or cooling is mandatory for a sufficient signal-to-noise ratio.

The current temperature calculations with active surface heating were carried out assuming a constant $r_C = 0.9$, since the influence of a varying r_C on the simulation is rather small and can be neglected. For all cells below the uppermost surface cell, only the conductive term is considered, with zero convection and radiation. The temperature in the surface layer is then calculated by solving Eq. 3.8 using a first-order finite-difference scheme.

3.3.2 CFD solutions for the skin friction and pressure coefficients

The further analysis considers the TWG reference test point with a sinusoidal pitch motion of $\alpha = 5^\circ \pm 6^\circ$ at a reduced frequency of $k = 0.060$ ($f = 6.6$ Hz), and with $M = 0.3$ and $Re = 1.8 \cdot 10^6$. CFD computations were performed to produce data for the wall skin friction coefficient C_f and the wall pressure coefficient C_p . This synthetic data is used as an input for the coupled computations. Since no skin friction data from the experiment was available, a C_f -distribution as close as possible to the experiment was predicted by a RANS solver. Although the attempt was made to closely reproduce the experimental condition, all of the conclusions of this section are made solely using the CFD results, so any differences will be incidental.

The TAU unstructured flow solver [194] was used on a 2D unstructured hybrid grid generated using the Centaur[®] grid generator. The surface of the airfoil was resolved with cells of maximum size 1% chord, reducing to 0.1% chord at the leading and trailing edges. The boundary layer was resolved with 60 layers, using the guidelines given by Richter et al. [178] and Krumbein et al. [121], and the boundary layer transition position was computed using the 2D e^N transition code LILO [191] coupled with the boundary layer code COCO [190]. The transition position is then fed back to the CFD code where wall nodes are set to be either “laminar” or “turbulent”. This results in a quantized boundary layer transition position which advances in steps, following the topology of the surface grid. This step behavior means that the analysis of the DIT image time separation, Δt , is not as smooth as could be hoped, especially for small time-offsets.

The computations were performed using the Spalart-Allmaras turbulence model [209]

and the boundary layer transition was performed by switching on the turbulence production terms in the boundary layer at the “transition point”, as described in detail in Refs. [121, 122]. The unsteady computations used 1024 time steps per pitch cycle with 800 inner iterations with a 4w multigrid acceleration. A second-order time discretization and a central second-order spatial scheme were applied. The simulation was run for three cycles, of which the last two cycles were periodic. The C_f and C_p data for the last cycle was written by the URANS solver from the surface pressure and vorticity data at each time step, and made available for the subsequent surface temperature code.

Figure 3.43 shows a comparison between the experimental (—) and CFD (—) lift coefficients and the experimental (—) and CFD (—) boundary layer transition positions. The experimental values for x_{tr} were extracted using the σC_p -method as outlined in Sec. 3.2.2, resulting in an estimated error below $\Delta x_{tr}/c = 0.02$ in comparison with hot-film sensors. The CFD is tuned to reproduce the lift and transition position of the experiment knowing that wind tunnel corrections of up to $\Delta\alpha = 1^\circ$ have been used in the TWG wind tunnel. The CFD used a wind tunnel correction of the mean angle so that $\alpha = 4.3^\circ \pm 6^\circ$ is computed rather than $\alpha = 5^\circ \pm 6^\circ$ for the experiments. In both cases the Mach number was $M = 0.3$ and the chord Reynolds number was $Re = 1.8 \times 10^6$. As detailed in the AGARD report 793 [184], the accepted selection method for N -factor is to use the method of Mack [143], combined with a measurement of the turbulence level in the wind tunnel, T_u , yielding

$$N = -8.43 - 2.4 \ln(T_u). \quad (3.11)$$

From turbulence measurements in the TWG wind tunnel, the freestream turbulence level at the $M = 0.3$ -conditions used by [35] is $T_u = 0.05\%$. Thus, the N -factor used in the simulation was $-8.43 - \ln(5 \cdot 10^{-4}) = 9.81 \approx 10$. The comparison between the experiment and CFD is close enough that a qualitative similarity should be achieved, and the experiments can be used to calibrate the simulations. The boundary layer transition position in the CFD result (—) shown in Fig. 3.43 does not move smoothly, since each cell on the airfoil surface is constrained to be either laminar or turbulent, and this leads to steps in the transition position.

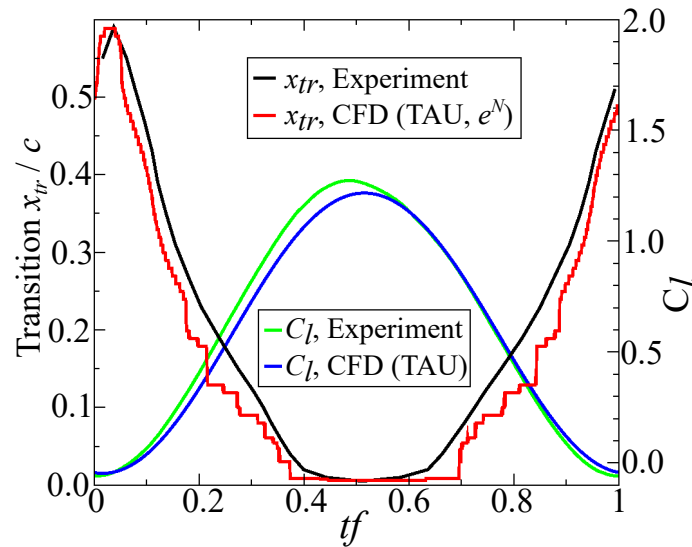


Figure 3.43: Comparison of transition position, x_{tr} , and lift coefficient, C_l , between experiment and CFD.

3.3.3 Coupled computations

The coupled computations were performed by feeding the phase-resolved CFD results for C_p and C_f from the last pitch cycle as a periodic input to the surface layer temperature computation. The settings for the surface computations are shown in Tab. 3.4.

Number of cells in vertical (surface-normal) direction	800
Number of cells in horizontal (chordwise) direction	140
Thickness of the surface layer	5.5 mm
Time step for heat computation	$5 \cdot 10^{-5}$ s
Time step from CFD	$15 \cdot 10^{-5}$ s
Total simulation time	1000 s
Surface layer material	Epoxy
Thermal conductivity (vertical direction), $\lambda_{s,v}$	0.5 W/m/K
Surface heat capacity, c_s	2300 J/kg/K
Surface density, ρ_s	1180 kg/m ³
Lamp heat flux, \dot{q}_{rad}	2000 W/m ²
Freestream static temperature, T_∞	294 K

Table 3.4: Settings for the temperature computation in the surface layer.

The bulk coefficients for epoxy were used. The spatial and time-stepping discretization of the wall was investigated. Figure 3.44 shows the mean temperature of the surface layer, averaged over all cells and within sliding windows larger than the pitching period, as a function of the computation time. The temperature was initiated with the freestream's total temperature, $T_0 \approx 300$ K, and converges to an equilibrium around $T \approx 311.3$ K after about 1000 s or 6600 pitch cycles. Thus, a computation time of 1000 s is used to achieve converged results in all further computations. It is noted that Fig. 3.44 also approximately corresponds to the step response of the airfoil's surface when suddenly switching on the radiative heating in the experiments. The result underlines that a long warm-up time is required before taking the first meaningful infrared images. This was already noted during the initial 1MG tests, and if required, a compensation of residual temperature drift was proposed in Sec. 3.1.4.

The temperature computations were discretized using a time step of $\Delta t = 5 \cdot 10^{-5}$ s. The stepping of the CFD solution is three times coarser, $\Delta t = 15 \cdot 10^{-5}$ s or 1024 points per cycle, and the corresponding aerodynamic input for the thermal simulation was interpolated. A convergence study using steps down to $\Delta t = 1 \cdot 10^{-5}$ s showed that the predicted DIT results are insensitive to the temporal resolution of the thermal calculation, as long as the underlying aerodynamic input is sufficiently resolved. In this context, Eder [77] also studied the thermal solutions for steady aerodynamic conditions without pitch oscillations. It was shown that much larger time steps, for example $\Delta t = 0.03$ s, can be used to speed up the calculation while still maintaining an asymptotic convergence.

Figure 3.45 shows a sample for the instantaneous distributions of C_p , C_f , and T_w on the airfoil's upper surface during the upstroke of the pitch motion. The pressure distribution

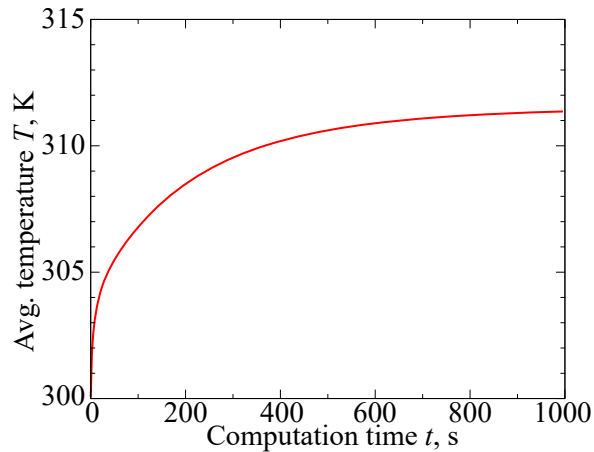


Figure 3.44: Convergence of the average surface layer temperature over the simulated time.

(—), plotted in a reversed y -axis, has a suction peak of $C_p \approx -1.15$ close to the leading edge, before increasing to the static freestream level of $C_p \approx 0$ at the trailing edge. The skin friction coefficient (—) monotonically decreases from the leading edge towards the trailing edge, except for the distinct rise around $x/c=0.15$ connected to the boundary layer transition. The unsteady but time-converged numerical solution for the surface temperature distribution, T_w (—), has no distinct temperature step in the transition region, which is only expected for steady test cases. The temperature is close to the flow's stagnation temperature of 300 K at the leading edge and increases to about 307 K in the central part of the airfoil. The rapid temperature rise near the trailing edge is due to the low heat transfer in the thickening and decelerating boundary layer, which is starting to approach stall.

Figure 3.46 shows DIT differential temperature distributions calculated for the same instant and using an image separation of $\Delta t_f = 0.035$, or 3.5% of the pitch cycle. This value corresponds the experimental image processing, see Sec. 3.2.2, and the IR camera's acquisition frequency of 190 Hz with an image spacing of 5.3 ms. The simulated DIT signal (—) for the chosen grid resolution of 800 cells along the 5.5 mm surface layer (cell height 6.9 μm) shows a clear and prominent peak marking the transition position, with a negative sign due its forward motion during the upstroke. The other lines in Fig. 3.46 were taken from a grid convergence study, indicating only a very small difference between 800 cells (—) and 400 cells (—). Hence, the chosen resolution of 800 cells is sufficient to discretize the heat flux. Cell counts below 400 significantly alter the DIT signal, and the DIT peak decreases since the local surface temperature T_w is no longer captured by the large thickness of the cells.

The aerothermal simulation of the DIT method is not intended to exactly reproduce the experimental results due its assumptions and simplifications, however, a qualitative agreement is still expected. Fig. 3.47 shows the DIT signals for $\alpha = 3.25^\circ \uparrow$ during the upstroke. The transition-related negative peak is visible in both simulation (—) and experiment (—), and both peaks have similar values in the range of -0.05 K to -0.06 K. The simulated peak shape is similar to the experimental shape on the left side, towards the leading edge, but considerably broader on the right side, towards the trailing edge. Also, the peak positions do not match, which is partly a consequence of the aerodynamic input data and not connected to the thermal simulation, see Fig. 3.43. During the upstroke and at $x_{tr}/c = 0.2$, TAU predicts the transition position about $\Delta x_{tr}/c = 0.05$ further upstream of the experiment. When increasing

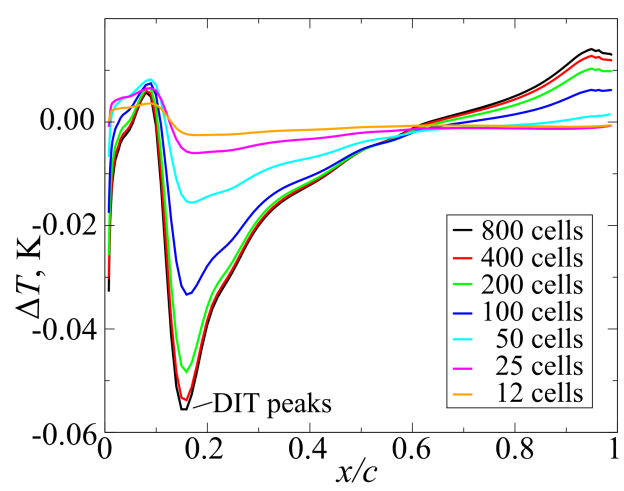
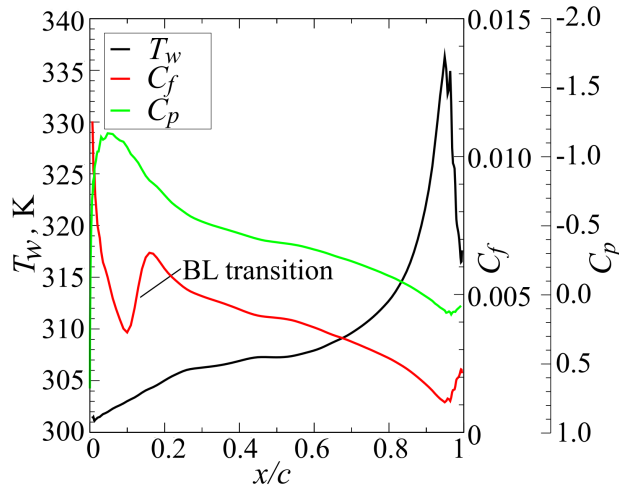


Figure 3.45: Sample for computed pressure, skin friction, and temperature distributions. **Figure 3.46:** Sample for the computed DIT signal for several grid resolutions.

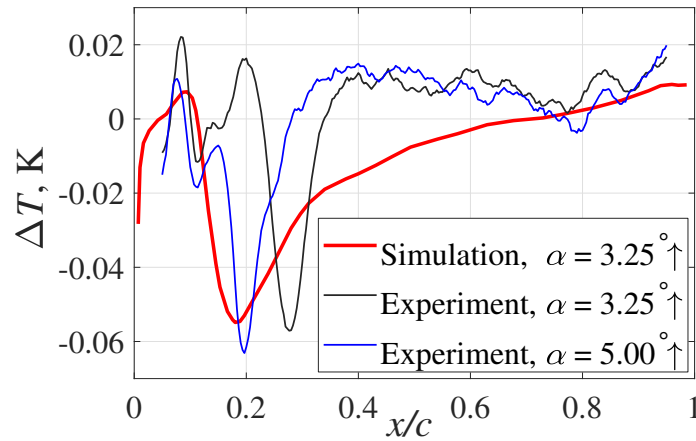


Figure 3.47: Comparison between simulated and experimentally measured DIT signals.

the experimental angle of attack to $\alpha = 5^\circ$, see (—) in Fig. 3.47, a good agreement with the simulation at $\alpha = 3.25^\circ$ is achieved in both magnitude and position of the DIT peak.

3.3.4 Review of the DIT principle and finite temperature delay

Boundary layer transition causes a sudden increase in the skin friction, associated with a change in the surface heat transfer. This is shown by the simulated C_f -distributions in Fig. 3.48, with the transition region moving upstream during the upstroke of the pitch motion from time t_1 (—) to time t_2 (—). The negative peak in the corresponding (time-wise) differential signal $\Delta C_f = C_f(t_2) - C_f(t_1)$ (—) can easily be detected. The simulation supports the basic DIT concept outlined in Sec. 3.1.3. The peak position of ΔC_f coincides with the transition position, $x_{tr}/c = 0.45$, of the intermediate time $t = (t_1 + t_2)/2$ (—). This transition position was identified by the maximum spatial gradient of the skin friction, $\partial C_f/\partial x$, which also represents the point of 50% intermittency close to the center of the transition region.

Figure 3.49 shows the consensus between the nominal transition position given by TAU's first turbulent cell (—, 50% intermittency is not available in TAU), the peak in the spatial gradient of C_f (—), and the peak of the temporal difference ΔC_f over the entire pitch cycle.

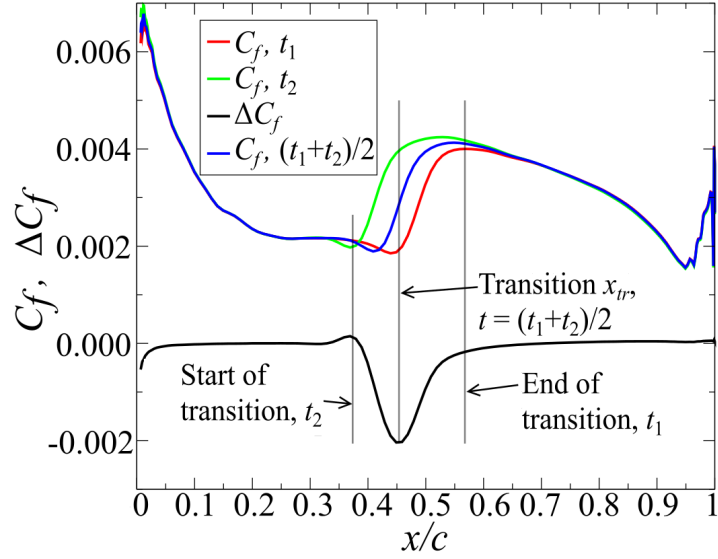


Figure 3.48: Simulated skin friction distributions of the airfoil's upper surface during the upstroke of the pitch motion, for three different times t_1 , t_2 , and $(t_1 + t_2)/2$ [14].

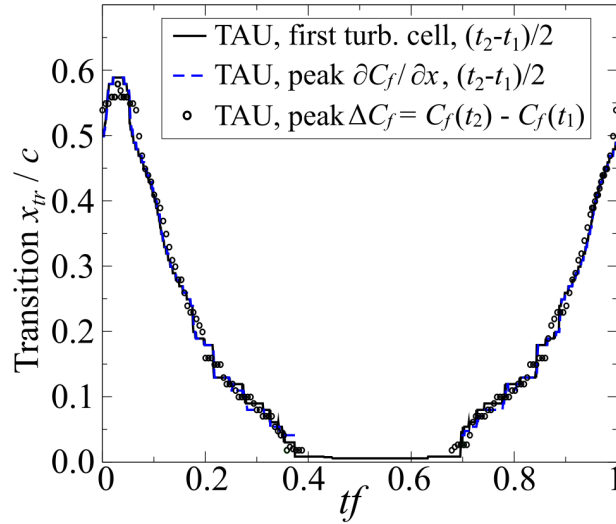


Figure 3.49: Nominal transition position in TAU compared to the peak positions in C_f [14].

The duality between the spatial gradient and the temporal difference in skin friction is not a coincidence, but can be easily understood by the following simplification: Assuming that the shape of the skin friction distribution is constant in the transition region, and that the entire distribution shifts in x -direction due to the changing pitch angle, the following relation applies:

$$\frac{\partial C_f}{\partial t} = \frac{\partial C_f}{\partial x} \frac{\partial x}{\partial t}. \quad (3.12)$$

Hence, if the entire C_f -distribution moves with a common group velocity $\partial x / \partial t$, there is a linear relation between the spatial and temporal gradients of C_f . The peak of $\partial C_f / \partial x$, representing the transition position x_{tr} , is mirrored by a peak in $\partial C_f / \partial t$, in this case approximated at $(t_1 + t_2)/2$ by the finite central difference calculated between t_1 and t_2 .

The original concept of DIT introduced by Raffel and Merz [167] proposed that the

transition begin at t_2 and the transition end at t_1 , as marked by the left and right vertical lines in Fig. 3.48, can be identified by means of the start and end of the differential peak ΔC_f . The idea is correct, however, it was discarded in later publications for practical reasons. The shoulders of the differential peak are broad, and particularly the right shoulder continues on small but non-zero levels downstream of the transition end. A non-zero threshold level must be introduced to identify start and end of the ΔC_f -peak, also depending on the noise level in the measurement. This arbitrary threshold level strongly affects the results, and makes the procedure rather unreliable.

The skin friction distribution, C_f , reflects to the “true” transition position including inviscid and viscous aerodynamic effects, introduced as (i) and (ii) in Tab. 3.2. The temperature distribution as seen by an infrared camera is subject to further effects. An additional thermal hysteresis, (iii) in Tab. 3.2, and pitch-related changes of the external flow velocity affect the DIT measurement. The current simulation enables to differentiate between skin friction and temperature, as shown in Fig. 3.50. The values for ΔC_f (dashed lines) and ΔT (solid lines) were compared at four different times on the upstroke ($\alpha = -0.6^\circ \uparrow$ and $\alpha = 5.9^\circ \uparrow$, left) or downstroke ($\alpha = 1.4^\circ \downarrow$ and $\alpha = -1.6^\circ \downarrow$, right). The extent of the laminar flow decreases during the upstroke, resulting in positive skin friction increments, ΔC_f , and vice versa. Since an increased C_f results in an increased cooling of the radiation-heated surface and vice versa, the peaks of ΔC_p and ΔT have opposite signs.

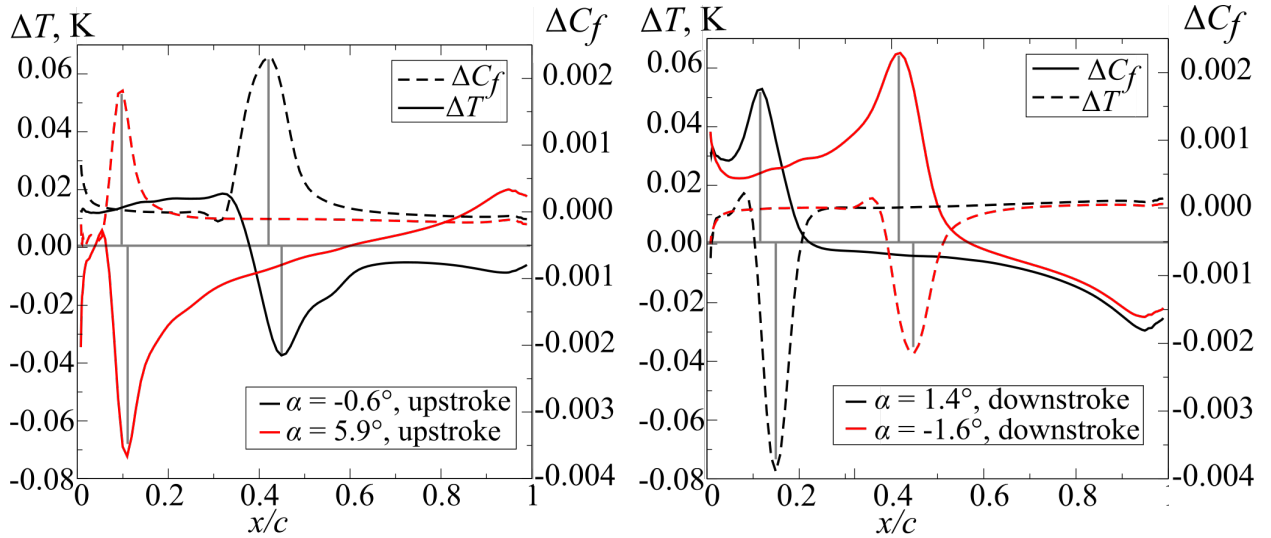


Figure 3.50: Comparison of the differential signals for temperature and skin friction during the upstroke (left) and downstroke (right), phase increment $\Delta t_f = 0.035$ (5.3 ms) [14].

Figure 3.50 also shows that the temperature peak always lags the skin friction peak, meaning that it is shifted towards the trailing edge during the upstroke and towards the leading edge during the downstroke. This is the additional thermal hysteresis effect (iii) as expected from the limited thermal responsiveness of the surface material.

The ΔT -peaks have a different shape than the ΔC_f -peaks, with a sharp and steep edge in the direction of travel and a long tail in the opposite direction. With changing angle of attack, the position of the stagnation point at the leading edge is shifted significantly, resulting in a change of the wetted length of the airfoil by about $\Delta x/c = 0.1$. Additionally, the Mach number and the local density of the flow over the airfoil change as a function of α . The result

is that all positions on the airfoil have a sinusoidal temperature change superimposed onto the transition-related differences, and this also affects the simulated DIT signals. The width of the ΔT -peak increases with an increasing length of the transition region, but similar to Fig. 3.48, the start and end of the transition region cannot be extracted reliably as a feature of the ΔT -distribution.

Figure 3.51 shows the transition results of the simulated DIT process over the entire pitch cycle as a function of the pitch phase tf . The DIT data points (\times) were identified using a conditional peak search, only accepting ΔT -minima on the downstroke (transition moves forward) and ΔT -maxima on the upstroke (transition moves rearward). The DIT simulation result is compared to its input data, given by the position of TAU's first turbulent cell (—) in equivalency to the steepest C_f -increase. Input and output data have a similar shape but the DIT result is systematically delayed towards higher phases tf , underlining the thermal hysteresis. The delay is about 1.5 ms and rather uniform over the entire cycle, even though this is hard to analyze since the input data jumps between TAU cells in staircase-like steps.

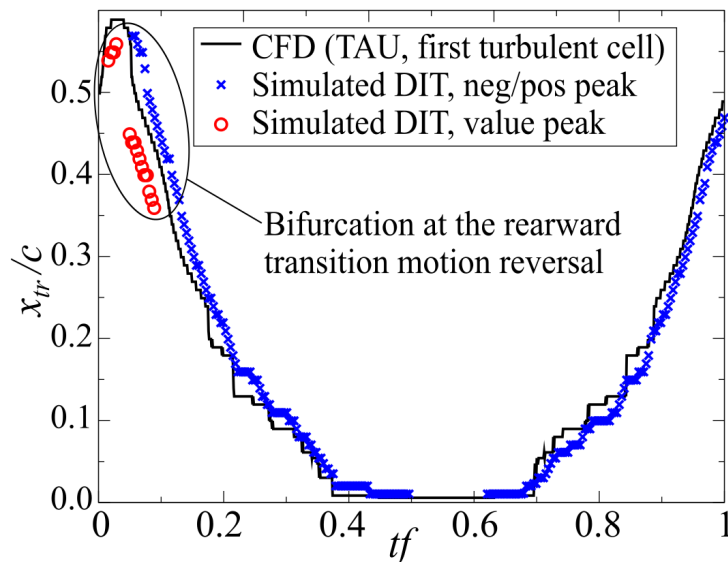


Figure 3.51: Transition results of the simulated DIT process in comparison to the CFD transition input data [14].

The DIT data was re-evaluated using a second approach. The median was subtracted from the ΔT -distributions to account for large-scale offsets unrelated to the transition peak, before identifying the peak position regardless its negative or positive sign. This method was also applied in the TWG experiments, and it is more generalizable, since it does not rely on a priori knowledge of the BL transition's motion direction. This second method generally identifies the same peaks as the first approach, but a systematic difference was observed close to the minimum pitch angle between $0 \leq tf \leq 0.1$, see Fig. 3.51. The first approach (\times) is restricted to negative ΔT -peaks on the upstroke, whereas the second approach (\circ) finds more prominent but positive ΔT -peaks which should be restricted to the downstroke, and which are positioned closer to the leading edge. The result is a bifurcation of the transition positions, and a similar phenomenon was observed in the 1MG experiments (see Fig. 3.21, bottom) and the TWG experiments (see Fig. 3.36).

3.3.5 Reversal of the transition motion

The aerothermal simulation helps to understand the erroneous bifurcation at the motion reversal of pitch-oscillating test cases, since it enables a comparison between the “true” transition position input and the corresponding DIT output. Figure 3.52 shows the simulated DIT results for pitch phases between $tf = -0.013$ and $tf = 0.036$. The solid lines represent the differential temperature signal, and as expected, the peak switches from a positive sign during the downstroke to a negative sign during the upstroke. At the moment of minimum pitch angle ($tf = 0, \alpha = -1^\circ$, —), the transition movement in its rearward reversal point is zero, but a strong peak in ΔT is still visible. This is contrary to the simplified and temperature lag-free DIT idea as originally proposed in Ref. [167], which predicts $\Delta T = 0$.

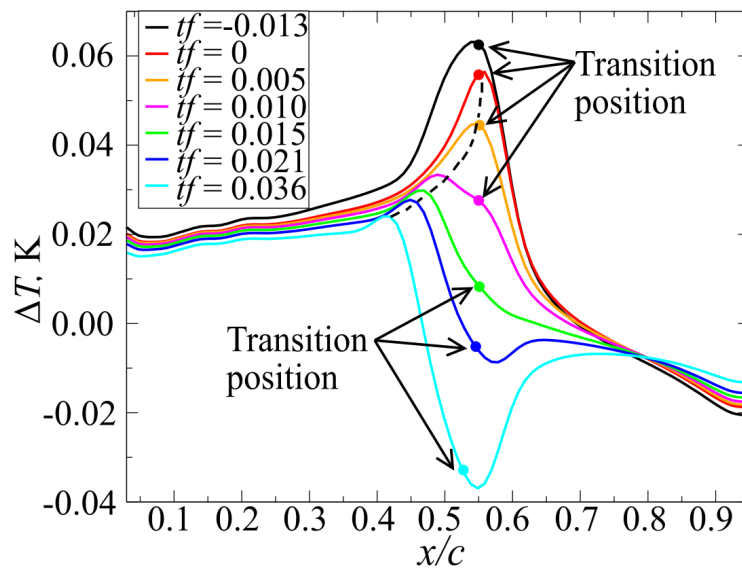


Figure 3.52: Behavior of the differential temperature signal (solid lines) and “true” transition position (dots) during the pitch motion reversal (phase $tf = 0$) at minimum angle of attack.

After this time, the positive peak in ΔT rapidly reduces, and the new negative peak connected to the beginning upstream motion of the transition position is superimposed on the old ΔT -distribution. During this process, the old positive peak is pushed towards the leading edge as seen by the locus (—), even though the transition is almost stationary. Between $tf = 0.010$ (—) and $tf = 0.021$ (—), a double-peaked, “S”-shaped structure appears, which is similar to the experimental observation at the forward transition reversal shown in Fig. 3.23. If the maximum peak value is detected regardless of its sign, the DIT algorithm will randomly switch between both peaks, particularly in the presence of random measurement noise. A comparison to the “true” transition positions shows that neither positive nor negative peak position is correct, and the erroneous bifurcated data should be removed from the result, as for example demonstrated in the TWG post-processing shown in Fig. 3.36.

3.3.6 Simulated effect of DIT image separation

The DIT image separation Δtf chosen to calculate the differential temperature signal ΔT affects the quality of the results, as discussed in Sec. 3.1.5 by means of the experimental 1MG parameter study. A smaller Δtf causes a smaller measurement-related temperature delay (see

Fig. 3.24) but also a smaller signal strength (see Fig. 3.22) and, thus, a decreasing signal-to-noise ratio. This effect is reproduced by the current thermal simulation, as shown in Fig. 3.53. The instantaneous transition position is $x_{tr}/c = 0.42$ (—) during the pitch upstroke, and the ΔT -signal was calculated for six different separations between $\Delta t = 1.8$ ms ($\Delta tf = 0.012$, —) and $\Delta t = 11$ ms ($\Delta tf = 0.073$, —). The DIT peak is always downstream of the “true” transition position due to the added measurement-related delay (hysteresis). With decreasing separation time, the prominence and detectability of the negative DIT peak decreases, but also the artificial measurement delay is reduced. The first effect is obvious, since the cooling of the advancing turbulent boundary layer has less time to act on the model’s surface. The second effect is non-intuitive, it is caused by a combination of the following two aspects:

- Smaller temperature differences occur more quickly after a flow change, and, thus, a smaller temperature difference is inherently less lagged.
- In addition to the fast transition motion, the surface temperature is affected by the flow history, for example, including pitch-related changes of the external flow (note the rise and motion of the positive signal left of the transition peak). These parasitic changes will distort the DIT peaks over time.

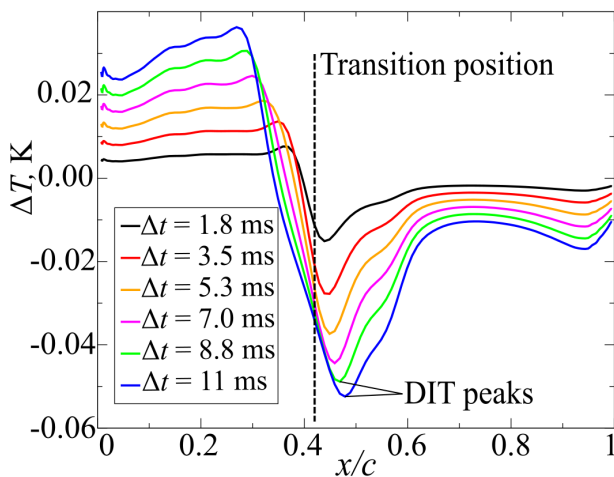


Figure 3.53: Differential temperature signal for different image separation distances.

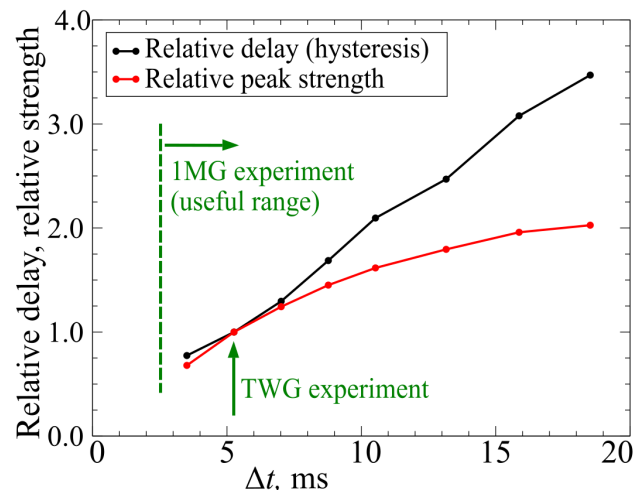


Figure 3.54: Influence of the DIT separation on the measurement delay and signal strength.

The quantitative results of the aerothermal simulation and the experiments were less comparable as could be hoped, in terms of both the ΔT -peak shape and the amount of hysteresis. Nevertheless, it is still expected that the simulation correctly predicts the qualitative influence of the separation Δtf , see Fig. 3.54. The parasitic measurement delay and the peak signal strength are shown over the separation time Δt . The results are normalized with reference to the values at $\Delta t = 5.3$ ms, corresponding to the TWG experiment with successive IR images taken at a camera frequency of 190 Hz. The simulation predicts a linearly decreasing measurement delay (—) with decreasing separation. This result mirrors the linear trend in the experiment, see Fig. 3.24, and an extrapolation of both simulation and experimental curves approximately crosses the origin indicating zero measurement lag for zero separation.

However, the experiment has a practical lower separation limit due to a decreasing peak signal-to-noise limit and increasing data scatter, whereas the simulation only accounts for the decreasing peak signal (—) while disregarding image sensor noise. The sensor noise will be specific to the camera as given by its noise-equivalent temperature difference (NETD), but the simulation supports the finding that the separation should be chosen as small as possible while still producing clear differential signals.

3.3.7 Simulated effect of material selection

From the energy transport equation, Eqs. 3.8 and 3.9, it is expected that the temperature of the surface, T_w , will quickly respond to aerodynamic changes if the wall material has a low thermal conductivity, λ_v , and a low heat capacity per volume unit, $c_s\rho_s$. The current experiments mostly use IR images of raw CFRP surfaces, and omitting an extra surface treatment is an advantage particularly in ad-hoc measurements or full-scale experiments. However, the thermal simulation was used to explore the potential of other surface materials. The heating time curves (Fig. 3.44) and the grid resolution requirement (Fig. 3.46) indicate that not the entire model shell thickness of 5.5 mm undergoes the high-frequency periodic temperature variations. A closer analysis shows that only about 500 μm are affected by the transition-related changes, with larger variations restricted to the first 100 μm to 200 μm . This suggests that thin foil sheets or spray-on coatings can improve the signal-to-noise ratio. Dull black paint is often used to minimize the reflectivity and maximize the emissivity of a surface under IR investigation, which is particularly required for low-emission metal models, e.g. see Refs. [40, 85]. A favorable insulating effect of the paint is also frequently mentioned [67, 130]. With a view to a dynamic detection of the BL transition, Simon et al. [206] measured the peak-to-peak temperature signals on a flat plate as a response to heat pulses. They noted that radiatively heated polymer foils with a low thermal capacity can be advantageous over resistively heated aluminum sheets with a large thermal capacity. Hence, the current DIT simulation was conducted with a variety of different surface materials as listed in Tab. 3.5. Materials 3 to 7 are machinable and could reasonably be used for wind tunnel models, either as a full material, or as a surface covering with a foil or contact sheet. Materials 1 and 2, cork and expanded polystyrene foam, have been included for their superior thermal insulation, but it is questionable whether they can be used as smooth aerodynamic surfaces, and whether the bulk material properties in Tab. 3.5 are valid in very thin sheets.

The material selection can affect both the differential temperature peak, ΔT , and the thermal measurement delay. Both quantities were determined in accordance to the preceding section and Figs. 3.53 and 3.54. The results in Fig. 3.55 were referenced to the baseline material 7 (epoxy), which approximates the TWG model and its CFRP shell.

The effect of the different materials 2 to 7 on the parasitic measurement delay is not significant, with deviations bounded by $\pm 10\%$, see Fig. 3.55 (top). Only the polystyrene foam 1 indicates a notable reduction of about 50%. In contrast, the DIT signal strength shown in Fig. 3.55 (bottom, note the logarithmic y -scaling) clearly benefits from favorable thermal properties of the surface material. For the relevant materials 3 to 6, the signal strength is increased by a factor between 1.3 and 3.0 compared to the epoxy baseline. This means that an insulating coating can be beneficial even for CFRP models, and a larger signal-to-noise distance can be used to compensate smaller image integration times, noisier IR image sensors,

number	material	$\lambda_v, \text{W/m/K}$	$c_s, \text{J/kg/K}$	$\rho_s, \text{kg/m}^3$
1	expanded polystyrene	0.05	1300	20
2	cork	0.05	1900	250
3	polystyrene	0.1	1300	1100
4	Mylar [®]	0.15	1400	1100
5	Plexiglass [®]	0.2	1500	1200
6	polyethylene	0.3	2300	1200
7 (ref.)	epoxy	0.5	2300	1180
8	Pyrex [®] glass	0.6	2800	2200

Table 3.5: Different surface materials and thermal properties, epoxy reference material printed in bold letters.

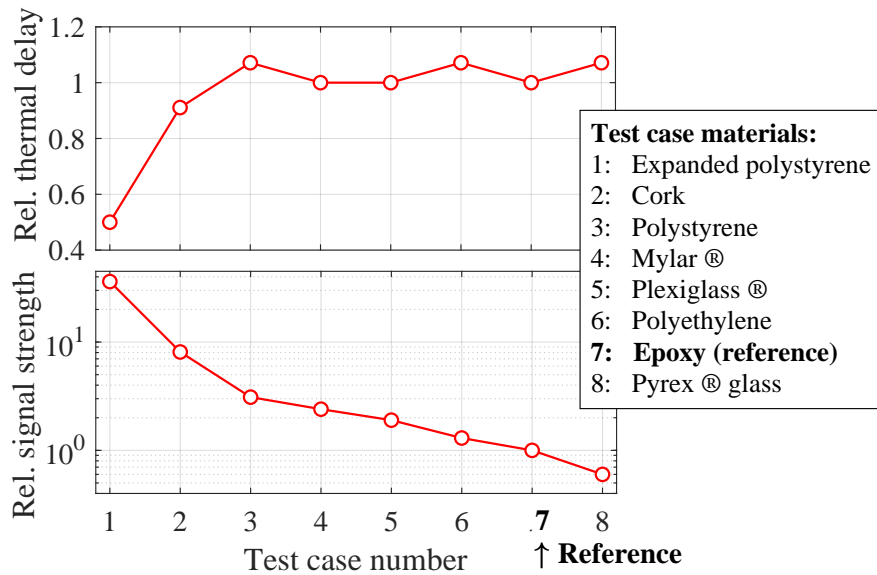


Figure 3.55: DIT measurement delay (top) and DIT signal strength (bottom) for different surface materials [14].

or a lower surface heating power. However, no further studies were conducted in the frame of the current work.

3.4 Application to small-scale rotor experiments

Differential infrared thermography (DIT) was applied to a four-bladed medium-scaled model rotor with a diameter of 1.3 m, operated at the rotor test stand Göttingen (RTG). The facility enables cost-efficient experiments with a good optical access for techniques such as DIT, particle image velocimetry (PIV), or stereo pattern recognition (SPR) for blade deformation measurements. A sinusoidal blade pitch motion resulting in an unsteady boundary layer transition position can be prescribed through a swashplate similar to helicopter main rotors. In terms of aerodynamics, the rotor transition measurement is interesting due to the radial variation of the blade's inflow conditions and due to the blade's twist. In terms of the test setup, the relative motion between the spinning blade surfaces and the IR camera is challenging and requires additional considerations.

The first transition measurement at the RTG was conducted by Schwermer et al. [199] and Raffel et al. [168] in 2014/2015, demonstrating the feasibility of DIT in rotating frames as shown in Fig. 3.56. The following section summarizes a second campaign published by Weiss et al. [30] in 2020, benefiting from an improved setup and a better understanding of the DIT principle.

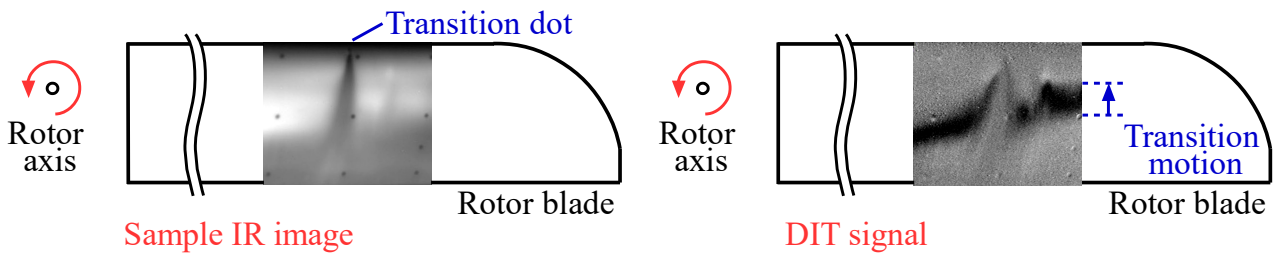
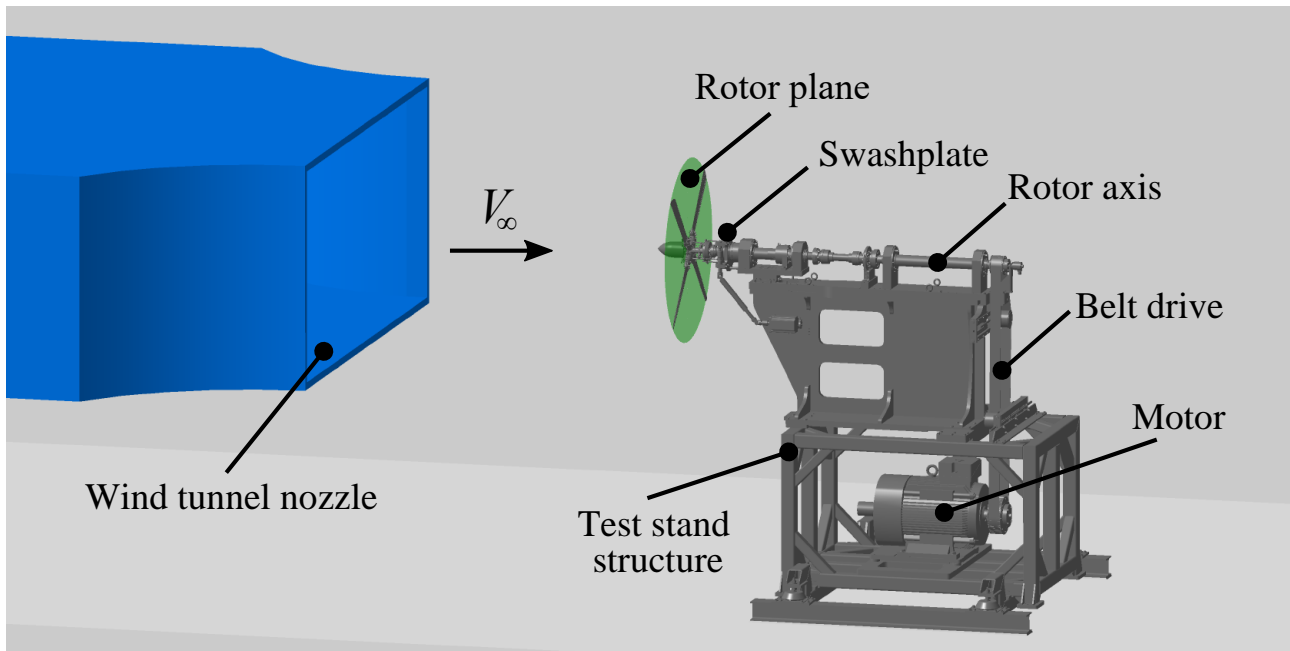


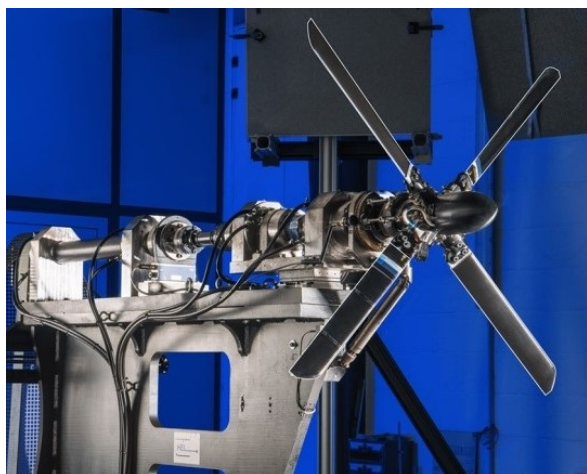
Figure 3.56: Sample IR image (left) and DIT signal (right) at the RTG, sketch made with results adapted from Raffel et al [168].

3.4.1 Rotor test stand Göttingen (RTG) and test cases

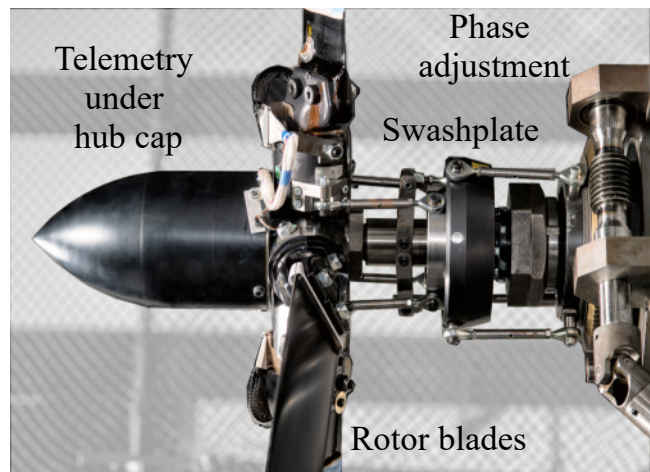
The RTG has a horizontal rotor axis which is belt-driven by an electric motor, see Figs. 3.57(a) and 3.57(b). It was designed for two- or four-bladed rotors with a diameter of $D = 1.3$ m and features a high level of instrumentation for scientific measurement campaigns, such as a six-component piezoelectric balance, a torque meter, a rotation angle encoder with 1000 pulses per revolution, ambient air data sensors, etc. A telemetry system with a sampling frequency of 106 kHz was installed in the rotor hub. It enables the use of instrumented rotor blades which can, for example, be equipped with blade pitch angle sensors, strain gauges, temperature sensors, or Kulite[®] transducers connected to surface pressure taps. The RTG was set up in the test section of an Eiffel-type wind tunnel. The tunnel's nozzle has a rectangular shape with about $2.6 D$ (3.4 m) in width and $1.2 D$ (1.6 m) in height. It provides a slow axial inflow up to 5 m/s into the rotor plane, which corresponds to climb conditions in terms of helicopter main rotor aerodynamics. Here, the Eiffel tunnel is used to push the rotor wake through exit windows further downstream, and to prevent recirculation within the test chamber. The chamber itself is large, about $10.3 D \times 6.6 D \times 5.5 D$ (length \times width \times height), and it enables a convenient installation of camera equipment and optics.



(a) Sketch of the RTG in its wind tunnel environment [12].



(b) Four-bladed rotor configuration.



(c) Detail of the rotor head.

Figure 3.57: The rotor test stand Göttingen (RTG).

The rotor head is equipped with a swashplate which adjusts the collective and cyclic setting of the rotor blades via pitch links, see Fig. 3.57(c). The resulting sinusoidal motion of the blade pitch angle, Θ , over the azimuth is defined in accordance to the airfoil's pitch angle, α , as used in the preceding sections,

$$\Theta(t) = \bar{\Theta} - \hat{\Theta} \cdot \cos(2\pi tf). \quad (3.13)$$

It is noted that Θ refers to the geometric pitch angle between the blade's chord line and the rotor plane. The aerodynamic angle of attack is smaller due to the induced flow through the rotor plane. The usually stationary part of the swashplate can be slowly rotated around the rotor axis through a worm drive, see the "phase adjustment" on the right side of Fig. 3.57(c), similar to a helicopter turning along its vertical yaw axis. Hence, the local phase tf of the blade pitch as seen by a stationary observer can be adjusted, and the entire blade motion

3.4. Application to small-scale rotor experiments

cycle can be swept through a fixed camera field of view. More details about the test stand are given by Schwermer et al. [200]. The RTG facility was initially designed to investigate the dynamic stall-phenomenon [113, 198, 3], but it has also been frequently used to develop or adapt measurement techniques focusing on rotor flows. For example and in addition to DIT, this covers temperature-sensitive paint [232, 233] or advanced schlieren imaging [12, 13].

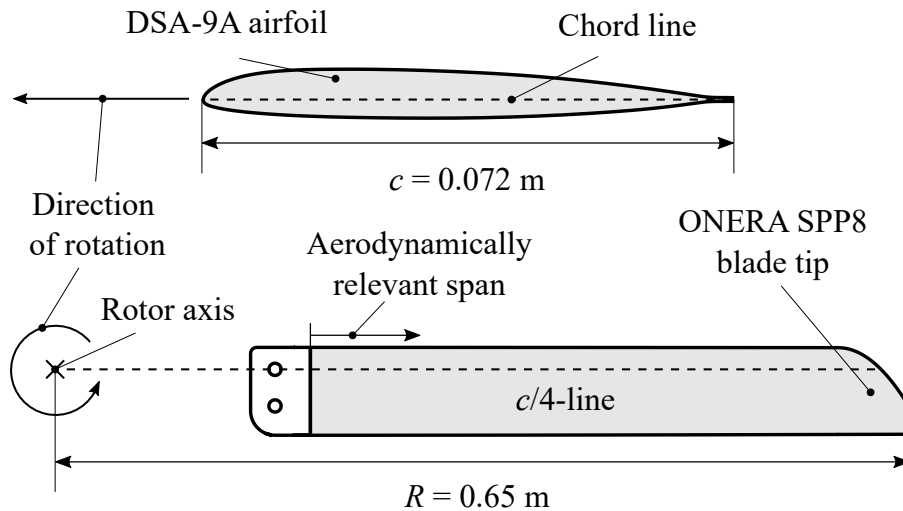


Figure 3.58: Airfoil (top) and planform (bottom) of the RTG rotor blades, different scales in both sketches, adapted from Wolf et al. [3] and Braukmann et al. [12].

The current evaluation considers a rotor with four blades and the “DSA-9A” airfoil as also used in the 1MG and TWG tests in Secs. 3.1 and 3.2. The chord length, c , is 0.072 m, and the thickness-to-chord ratio is 9% . The aerodynamic section of the blade spans between $r/R = 0.25$ and $r/R = 1$, yielding an aspect ratio of 6.8 , see Fig. 3.58. The blades feature a negative twist of -9.3° and a parabolic tip planform after the “ONERA SPP8” geometry [162] without anhedral. One of the blades is equipped with surface pressure taps and miniaturized Kulite[®] sensors of type “LQ-062” to evaluate the unsteady surface pressure at $r/R = 0.53$ and $r/R = 0.77$. Even though the taps have an influence on the BL transition process, this instrumented blade was targeted in all DIT measurements for a comparison to the pressure-based σC_p -method. Table 3.6 gives an overview of the RTG test conditions.

3.4.2 Infrared camera and image de-rotation

The RTG test used the FLIR[®] X8500sc high-speed infrared camera [83], see Fig. 3.59, with a strained layer superlattice (SLS) image sensor operating in the long-wave IR band ($7.5 \mu\text{m} - 10.5 \mu\text{m}$). The camera was provided by NASA under the NASA-DLR agreement on “experimental optical methods applied to rotorcraft”. Compared to the MCT camera of the preceding sections, the newer SLS technology enables a higher resolution (1280×1024 pixel versus 640×512 pixel) at a higher acquisition frequency (180 Hz versus 110 Hz at full frame). Even though the nominal noise-equivalent temperature difference is similar (40 mK versus 35 mK), it was found that under real-life conditions, the SLS images are of higher quality due to a better uniformity and stability of the calibration. The camera was equipped with a 50 mm focal length-lens.

Applying DIT to rotating blades instead of pitching airfoils results in additional problems

parameter	unit	value or range
rotor frequency, f or f_{rotor}	Hz	23.6
red. frequency, $k_{75} = c/(2r_{75})$	-	0.074
mean pitch (collective), $\bar{\Theta}_{75}$	deg	static: 2.1 . . . 17.1, with cyclic input: 9.0
pitch amplitude (cyclic), $\hat{\Theta}$	deg	5.9
blade Mach number, M_{75}	-	0.21
chord Reynolds number, Re_{75}	-	$3.2 \cdot 10^5$
rotor-axial inflow, V_{∞}	m/s	4.9
IR images per test point	-	static: 16, cyclic: 2×1000 (t_1, t_2)

Table 3.6: Variation of RTG experimental parameters, the index “75” refers to $r/R = 0.75$, default values printed in bold letters.

connected to the fast relative motion between the wetted surface and the non-rotating IR camera. This particularly holds true for rotors or propellers in aircraft applications, whose rotational frequency is large in comparison to, for example, wind turbines. To the author’s knowledge, no infrared camera placement within the rotating frame has yet been realized to avoid the relative motion. Hub-mounted rotating cameras have been demonstrated for blade deflection measurements, see Refs. [49, 50, 224]. This approach requires a miniaturized camera size, a high tolerance towards centrifugal forces, and a high resolution to perform image dewarping under oblique viewing angles. These criteria can currently only be met by cameras operating in the visible light spectrum, but not by high-speed IR cameras.

However, the relative motion can be compensated by optical tracking devices, such as prism-based derotators [235] or rotating mirrors [166]. Mirrors are a good choice for long-wave infrared optics, since a large number of suitable surface materials or coatings are available, including polished metal surfaces. Raffel and Heineck [166] discussed several optical layouts, and the “off-axis geometry” shown in Fig. 3.60 is particularly useful in the current rotor experiments since the camera and mirror do not block the rotor plane.

The camera’s field of view follows the rotating blade for all radii if the mirror axis intersects the rotor axis at the hub including an angle β , and the frequencies of mirror and rotor are related by:

$$f_{\text{mirror}} = \frac{1}{2} f_{\text{rotor}} \cos^{-1} \beta. \quad (3.14)$$

The special case of $\beta=0$ yields the “on-axis” geometry, in which the both rotational axes are collinear, and the mirror frequency is half the rotor frequency. In practice, β should be as large as necessary so that the mirror does not obstruct the rotor’s inflow, but as small as possible, since $\beta \rightarrow 90^\circ$ requires an infinite mirror speed and width. Additionally, the periodicity between mirror and rotor must be considered. For example, $\beta = \arccos 3/4 \approx 41.4^\circ$ results in $f_{\text{mirror}} = 2/3 f_{\text{rotor}}$. This means that repetitive images of the blade at the same azimuth angle and with the same viewing geometry can be taken every third revolution of the rotor, corresponding to every second revolution of the mirror. This choice is a good compromise



Figure 3.59: FLIR® X8500sc SLS high-speed IR camera [83].

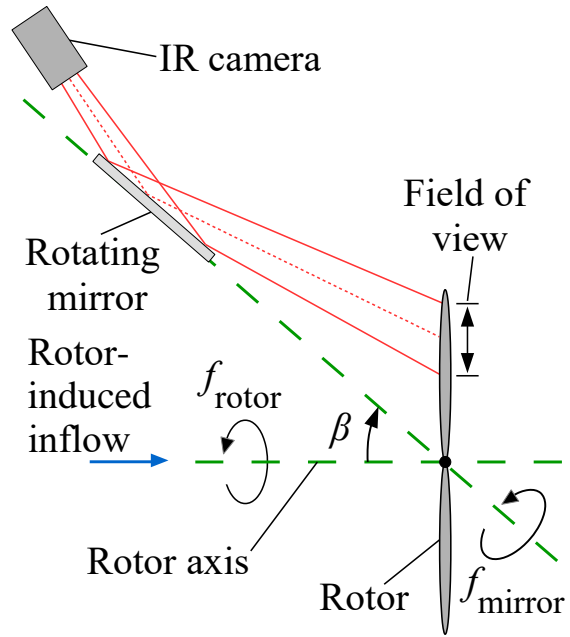


Figure 3.60: Infrared image derotation in off-axis geometry [167].

between the different requirements, and it was also chosen in the current experiment.

The rotating mirror design was optimized in several iterations, Fig. 3.61 shows the final version as used in the RTG. It is driven by a brushless “Maxon EC-i 52” motor-encoder-unit, which is tethered to the RTG encoder following the rotor motion. The 2/3-frequency ratio is achieved through the gear ratio of the belt drive and through a software-selectable divider ratio between both encoders. The mirror itself is 500 mm wide, as required by the flat viewing angle. Even though the IR reflectivity of the polished aluminum base material is good, a front surface mirror on a glass substrate can be added due to its superior evenness. An on-axis laser pointer greatly helps to adjust the mirror’s orientation with respect to the rotor plane center after Fig. 3.60.

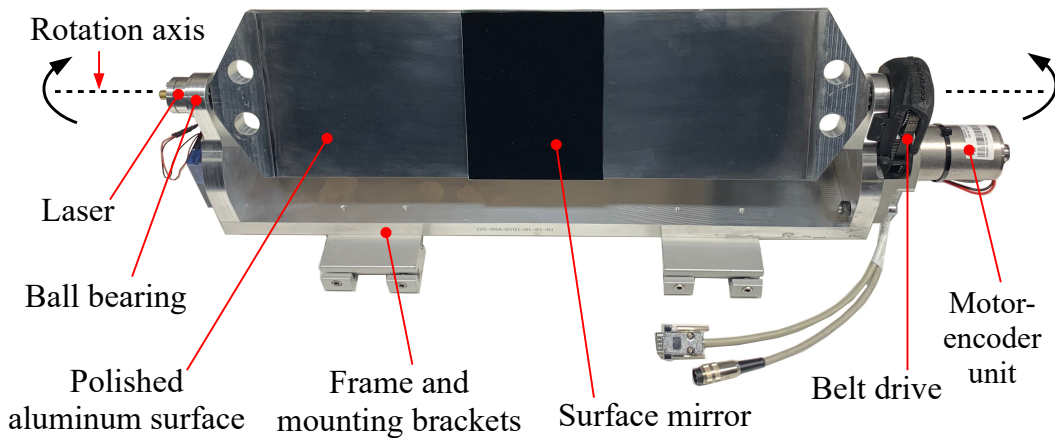


Figure 3.61: DLR-developed rotating mirror for DIT applications.

Figure 3.62 shows the timing of the infrared image acquisition, with the rotor blades turning counter-clockwise when viewed in downstream direction. In static test conditions with zero cyclic pitch input, individual images for standard infrared thermography (IRT)

were taken when the instrumented rotor blade points vertically upwards. The exposure time was set to only $57 \mu\text{s}$, but sixteen images were averaged to increase the signal-to-noise ratio. The image size covers the blade-radial region between $0.46 R$ and $1 R$ with a resolution of about 2 pixel/mm, or 144 pixel along the blade's chord. The images were aligned in the radial-chordwise coordinate system using fiducial markers and DLR's software package "ToPas" [118], accounting for rotation and translation as in Weiss et al. [232].

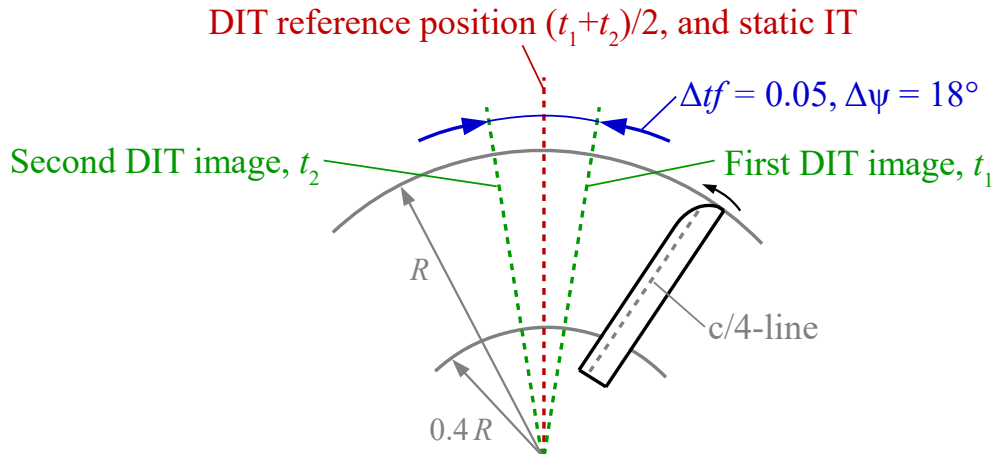


Figure 3.62: Infrared image acquisition for RTG measurements, sketch of the upper part of the rotor plane viewing in downstream direction, adapted from Ref. [30].

Differential infrared thermography (DIT) was applied in pitch-oscillating cases with cyclic input. The required pair of successive images was acquired at t_1 and t_2 during a single rotor revolution to eliminate temperature drift and cycle-to-cycle variations. The individual images were taken symmetrically before and after the vertical reference position at $(t_1 + t_2)/2$. The phase separation is $\Delta t_f = 0.05$, or $\Delta \Psi = 18^\circ$ in terms of the azimuth angle. The minimum separation was limited by the camera's pixel clock, with an image acquisition frequency increased from 180 Hz to 476 Hz by cropping the full-frame image size to approximately match the rotor blade shape. The mirror tracks the blade motion in the camera images, and the exposure time was increased to $150 \mu\text{s}$ for a better signal-to-noise ratio in individual images.

The rotor blades were radiatively heated by an array of lamps mounted above the infrared camera, projecting a heat flux of about $400 - 500 \text{ W/m}^2$ in the rotor plane.

3.4.3 Numerical TAU-RBT simulation

The experiments were accompanied by flow simulations using the DLR TAU code [194] coupled to the "rotor blade transition" (RBT) toolbox developed by Heister [101]. RBT is a framework which approximately predicts the BL transition in blade sections, based on the local flow situation (inflow, chordwise flow, crossflow) and several empirical criteria, also see Fig. 1.6. In contrast to the RBT method, both highly resolved and partially scale-resolving simulations have shown the potential of a very detailed transition modeling, as reported by Coder [64] or Vieira et al. [223] for the NASA PSP rotor. Nevertheless, the computational costs of such investigations are still too high for industry-relevant computations. In the current case, a very coarse grid and the approximate RBT tool is used, which results in much

lower computational costs. The calculations were performed on the SuperMUC cluster of the Leibniz Supercomputing Center, with an effort of about 10 000 CPU h for static-pitch test cases and about 20 000 CPU h for pitch-oscillating test cases.

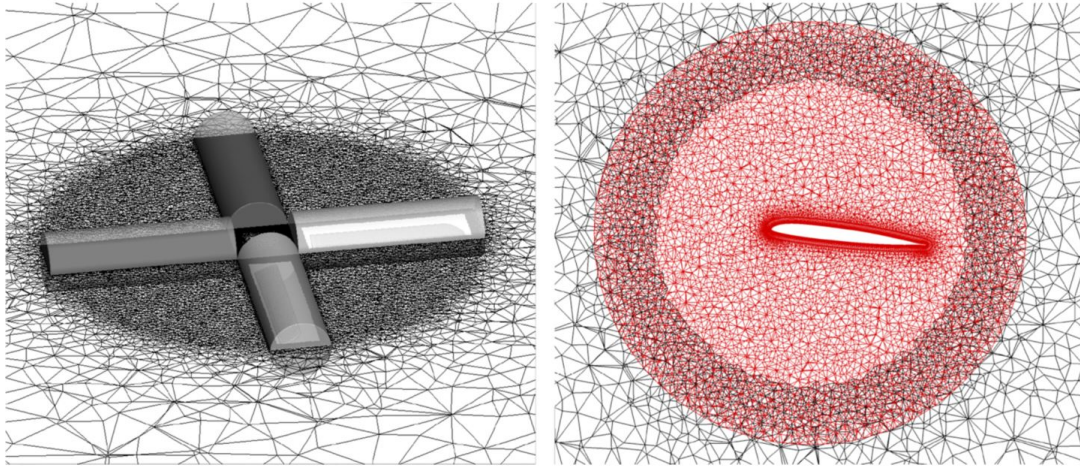


Figure 3.63: Chimera setup of the RTG rotor (left), grid section at $r/R = 0.77$ (right), Ref. [30].

TAU solves the compressible and unsteady RANS equations on an unstructured finite-volume grid. The current hybrid mesh, see Fig. 3.63, consists of hexahedral grids around the blades and tetrahedral elements in the far field. The far field is a full cylinder with a height of $200 R$ and a radius of $100 R$. Both grids were integrated using the chimera technique, also referred to as overset technique. Each blade mesh contains $1.5 \cdot 10^6$ points resulting in a total mesh size of $7.7 \cdot 10^6$ nodes. The BL discretization is about 30 points in wall-normal direction with a first wall spacing set to keep $y^+ < 1$. The mesh was chosen in accordance to the convergence requirements of the RBT tool [101].

A single blade revolution was discretized into time steps corresponding to 1° azimuth. This setting yielded the same results as computations with a finer stepping of 0.1° . The turbulence is modeled using the two-equation $k - \omega$ SST eddy viscosity model according to Menter [148].

The RBT toolbox is capable of detecting BL transition due to five different mechanisms, including the baseline Tollmien-Schlichting (TS) transition as implemented by Arnal et al. [37], also known as the “Arnal-Habiballah-Delcourt” (AHD) criterion. In preceding computations of a two-bladed RTG configuration, Kaufmann et al. [114] included all types of transition mechanisms. It was shown that the predictions were only acceptable if TS transition is modeled exclusively, but in this case, the RBT results were superior to Langtry-Menter approaches. Therefore, the current simulations also only include the TS/AHD criterion.

The AHD criterion was evaluated at 48 sectional cuts along the rotor radius on both suction and pressure sides. The predicted transition begin is used to control the turbulence model. The transition process or intermittency region is not modeled, and point transition is assumed. To compute the local turbulence level required as an input for the AHD criterion, the local flow velocity and the turbulent kinetic energy is extracted in a user-defined distance upstream of the local stagnation point. The turbulent kinetic energy at the far field boundary has to be set in order to align with the experimental turbulence level of the axial inflow. Therefore, the “sustaining turbulence concept” by Spalart and Rumsey [211] is locally implemented up to one rotor radius upstream of the rotor plane. The far field boundary conditions were

adjusted iteratively to match an inflow turbulence level of 0.09% at $r/R=0.77$ as deduced by Weiss et al. [233].

3.4.4 Static pitch angle and intermittency

The infrared result for a test condition with a static pitch angle of $\Theta_{75} = 10^\circ$ and a rotor frequency of $f = 23.6$ Hz is shown in Fig. 3.64, with the flow from bottom to top. The dark areas towards the trailing edge correspond to a stronger convective cooling within the turbulent boundary layer. The turbulent wedge at $r/R = 0.49$ (left, inboard) results from a transition dot placed close to the leading edge. The pressure tap rows at $r/R = 0.53$ and $r/R = 0.77$ also cause premature BL transition. The black circular dots are silver-paint fiducial markers, which were sanded down and do not affect the boundary layer. The chordwise temperature distribution was evaluated at several radial stations (+) after the method of Ashill [39] and similar to the current 1MG data, see Fig. 3.9. The result is the begin and the end of the transition region, x_{begin} and x_{end} (thin red lines, —), and the position of 50% intermittency, x_{tr} (thick red line, —). The former sections mainly concentrated on x_{tr} , but for a comparison to the current RBT simulations, the finite length of the transition region is relevant. The single-valued “transition point” provided by the AHD criterion represents the onset of Tollmien-Schlichting waves and, therefore, compares better with x_{begin} .

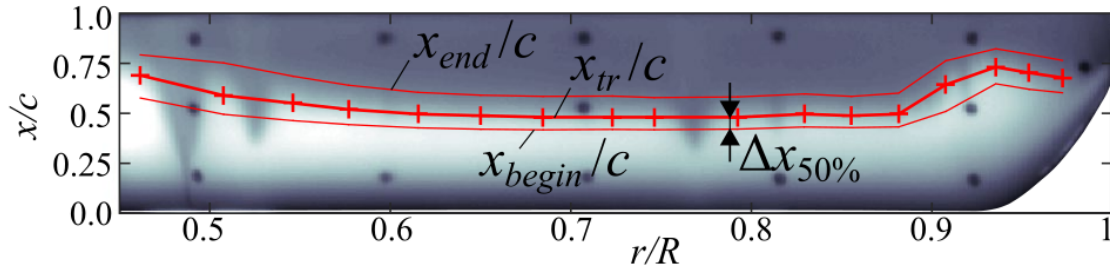


Figure 3.64: Average IR image for static transition position, $f = 23.6$ Hz, $\Theta_{75} = 10.0^\circ$ [30].

The intermittency length is known to increase with a decreasing adverse pressure gradient, see Walker and Gostelow [227]. The DSA-9A airfoil has a weak suction-sided pressure gradient, $\partial C_p / \partial x$, at about $x/c = 0.6$. This can be seen from the 2D MSES predictions of C_p in Fig. 3.8 (neglecting additional Reynolds- and 3D-effects), and the 3D MSES predictions of the BL shape factor in a previous RTG rotor test reported by Weiss et al. [233]. The distance between transition onset and 50% intermittency,

$$\Delta x_{50\%} = \frac{x_{tr} - x_{begin}}{c} \approx \frac{x_{end} - x_{begin}}{2c}, \quad (3.15)$$

is shown in Fig. 3.65 as a function of the transition location and for the current static-pitch data (—). A curve fit was applied to the $\Delta x_{50\%}$ -data (---) which serves as a possible offset to be added to the CFD transition begin.

Figure 3.65 also includes data extracted from the TWG airfoil tests in Sec. 3.3 and Richter et al. [34], showing that the overall trend is continued for pitch-oscillating test cases during both upstroke (●) and downstroke (○).

Figure 3.66 (top) compares the measured and calculated transition results for two steady test cases with collective pitch angles of $\Theta_{75} = 9^\circ$ and $\Theta_{75} = 14^\circ$. The transition lines mirror the

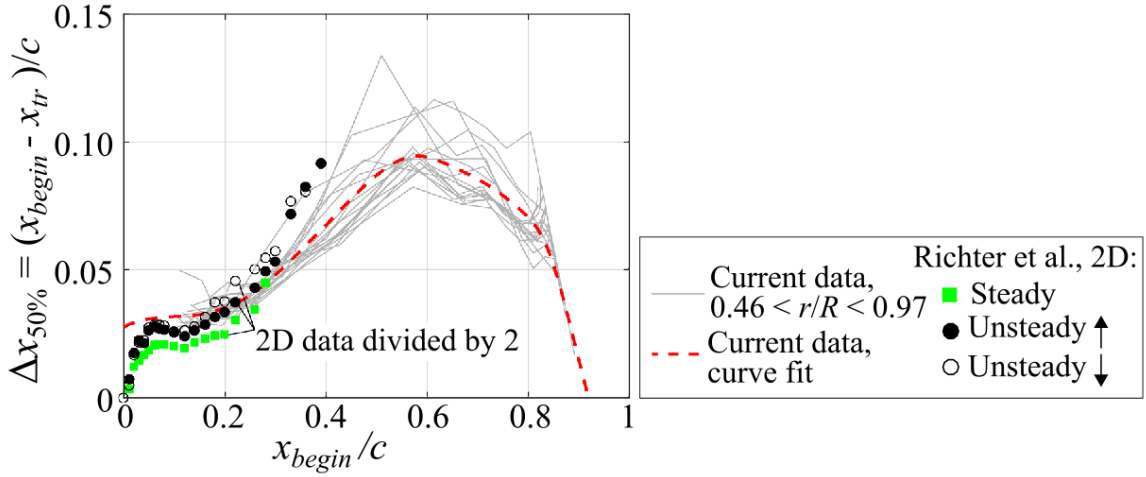


Figure 3.65: Distance between transition begin and 50% intermittency as a function of the transition location, including TWG airfoil data from Richter et al. [34].

predicted lift coefficients, see Fig. 3.66 (bottom). A large C_l causes a strong adverse pressure gradient resulting in a transition close to the leading edge, and vice versa. This not only explains the effect of the pitch angle variation, but also the radial distribution at a given angle. For example, the bulge between $0.9 \leq r/R \leq 0.95$ is caused by the local influence of the blade tip vortex, which reduces the lift and, consequently, pushes the transition towards the trailing edge.

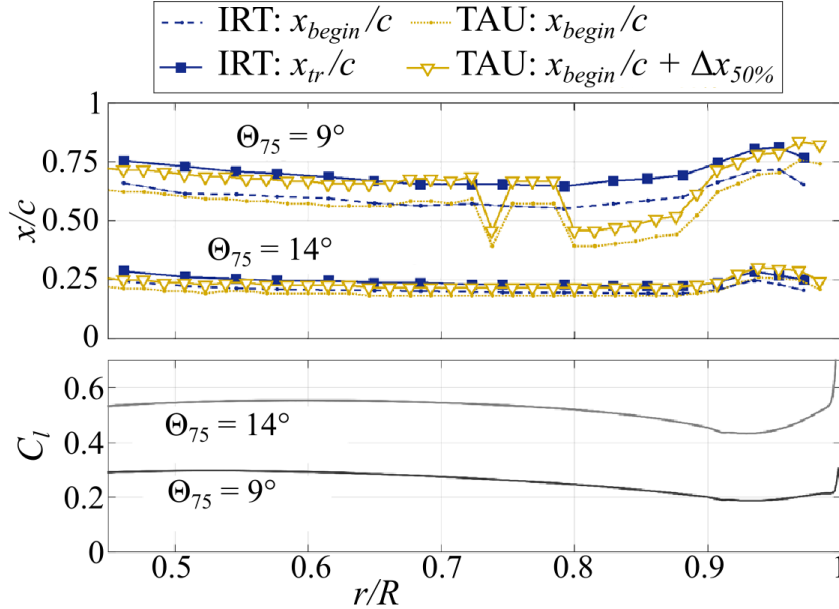


Figure 3.66: Steady transition positions (top) and corresponding C_l -distributions (bottom) for collective pitch angles $\Theta_{75} = 9^\circ$ and $\Theta_{75} = 14^\circ$ [30].

For $\Theta_{75} = 14^\circ$, the measured and predicted positions for transition begin and 50% intermittency agree well, but the intermittency length is small, and all four lines are very close to $x/c = 0.25$. For $\Theta_{75} = 9^\circ$, a notable split between transition begin (dashed lines) and 50% intermittency (solid lines) is observed. The experimental x_{begin} is correctly predicted by the TAU calculations for radii $r/R < 0.72$ and $r/R > 0.90$. Consequently, also the measured value

for x_{tr}/c and its numerical substitute $x_{begin}/c + \Delta x_{50\%}$, featuring the empirical intermittency offset correction $\Delta x_{50\%}$ after Fig. 3.65, agree well. In the radial range of $0.72 \leq r/R \leq 0.9$, the numerical prediction switches abruptly to transition positions located about $\Delta x/c \approx 0.21$ further upstream. This behavior is considered as an error, since neither the experimental transition locations nor the numerical lift data show comparable effects. It is noted that in this streamwise range of the airfoil, the transition position is very sensitive to small pitch changes, see Weiss et al. [233] and Fig. 3.12. Hence, the case at $\Theta_{75} = 9^\circ$ exemplifies that the transition is challenging to predict here, which also matches the observations by Kaufmann et al. [114] regarding a TAU simulation of a two-bladed RTG configuration.

3.4.5 Pitch-oscillating test cases with cyclic input

The next step considers a test case with a rotor frequency of $f = 23.6$ Hz and a cyclic pitch input by tilting the swashplate, resulting in a sinusoidal pitch oscillation with $\Theta_{75} = 9.0^\circ \pm 5.9^\circ$. This case was chosen since it covers a wide range of transition positions, but it is well below the static and dynamic stall limits (static stall occurs at about $\Theta_{75} = 23.5^\circ$ for this flow condition). Figure 3.67 shows two sample differential temperature distributions ΔT . In both cases, the underlying images at t_1 and t_2 were chosen so that the mean pitch angle at $(t_1 + t_2)/2$ equals $\Theta_{75} = 11.5^\circ$. The left image corresponds to the pitch upstroke, and the yellow-orange (positive) region represents the transition moving upstream towards the leading edge, resulting in an increased convective heat transfer within the turbulent BL region. Vice versa, the right image corresponds to the pitch downstroke, with the blue (negative) region showing the transition's motion towards the trailing edge. The blue band is notably thinner than the yellow-orange band since the transition motion in this area is smaller for same pitch difference.

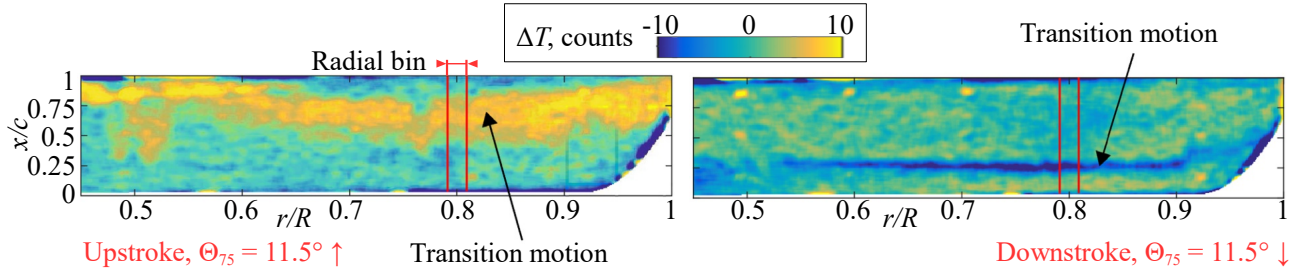


Figure 3.67: Differential temperature distributions for $\Theta_{75} = 11.5^\circ$ during the upstroke (left) and downstroke (right) for a cyclic-pitch case with $\Theta_{75} = 9^\circ \pm 5.9^\circ$ and $f = 23.6$ Hz [30].

It is noted that Weiss et al. [30] define the DIT signal as

$$\Delta T = (T(t_1) - \bar{T}_1) - (T(t_2) - \bar{T}_2), \quad (3.16)$$

which includes two differences from the ΔT -definition applied in the preceding sections. First, the tare images \bar{T}_1 and \bar{T}_2 are subtracted from their respective instantaneous images $T(t_1)$ and $T(t_2)$. The tare images \bar{T}_1 and \bar{T}_2 are defined as the mean temperature distributions in the two azimuthal measurement positions, $\Delta\Psi = 9^\circ$ before and after the vertical as in Fig. 3.62, and averaged over all pitch phases tf of the entire cycle. This removes systematic azimuthal differences unrelated to the unsteady aerodynamics, for example resulting from an inhomogeneous heating of the rotor plane. Second, the later net image at t_2 is subtracted

3.4. Application to small-scale rotor experiments

from the earlier net image at t_1 , which inverts the sign of the differential signal ΔT compared to earlier sections, without any further impact on the DIT evaluation.

The further analysis must consider the spanwise variation of the transition position, hence, the field of view is subdivided into several radial bins in which x_{tr} is considered to be constant. The red vertical lines in Fig. 3.67 show a bin sized $\Delta r = 10$ mm and centered at $r/R = 0.8$. The individual DIT images were averaged along the bin's span, and the chordwise peak position, x_{tr} , is identified by its negative or positive ΔT -peak. Figure 3.68 (left) shows the result (\bullet) as a function of the phase tf . The sinusoidal pitch cycle with a maximum angle at $tf = 0.5$ is shown in the background ($-$) for reference. The measured DIT transition position varies over the pitch cycle between about $0.2 \leq x/c \leq 0.8$, and the general behavior agrees well with the static IRT data (\blacksquare) except for a shift towards later phases (to the right), which represents the hysteresis of the pitch-oscillation case. The quality of the RTG result appears to be on a similar level as the proof-of-concept 1MG test, for example compare Fig. 3.17. This also includes erroneous data at the pitch motion reversal, as seen by the bifurcation at $tf = 0.5$. Other outliers in Fig. 3.68 (left) were filtered out, based on a maximum allowable distance of $\Delta x_{tr}/c = 0.4$ to the static reference, and based on a minimum acceptable peak value of $|\Delta T_p| = 5$ counts.

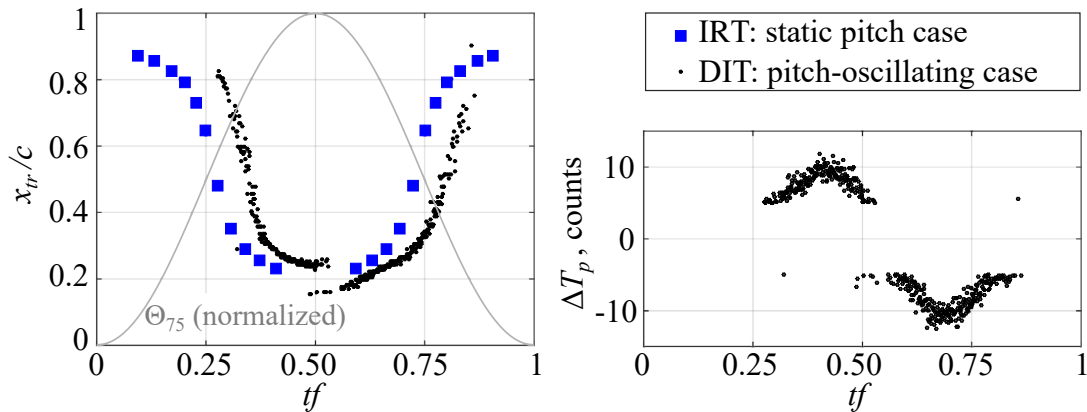


Figure 3.68: Transition position (left) and DIT signal peak (right) at $r/R = 0.8$ for a pitch-oscillating test case with $\Theta_{75} = 9.0^\circ \pm 5.9^\circ$ and $f = 23.6$ Hz, including static transition positions.

The analysis can now be carried out for seventeen radial positions covering the entire field of view, and an overall DIT “transition map” in a polar coordinate system was created to visualize the rotor plane, see Fig. 3.69 (left).

The minimum phase and, thus, the minimum pitch angle is at the top, with the phase increasing in counter-clockwise direction. The raw transition positions of the previous evaluation step were phase-averaged within 50 phase bins, each bin covering 2% of the pitch cycle. The results at the valid data points (\bullet) were used to generate the background contour plot for the measured local transition position, alternating towards the trailing edge (yellow colors) or the leading edge (blue colors). Missing data was interpolated (\times). The interpolated areas are quite large, but mostly located close to the pitch motion reversal, where the transition location is almost stationary. Hence, the resulting map is considered valid. This is underlined by a comparison to the simulated TAU-RBT data in Fig. 3.68 (right), using the same color contour levels, and applying the offset correction $\Delta x_{50\%}$ to the predicted transition begin. Overall, the agreement is remarkable. Both results are not symmetric to the

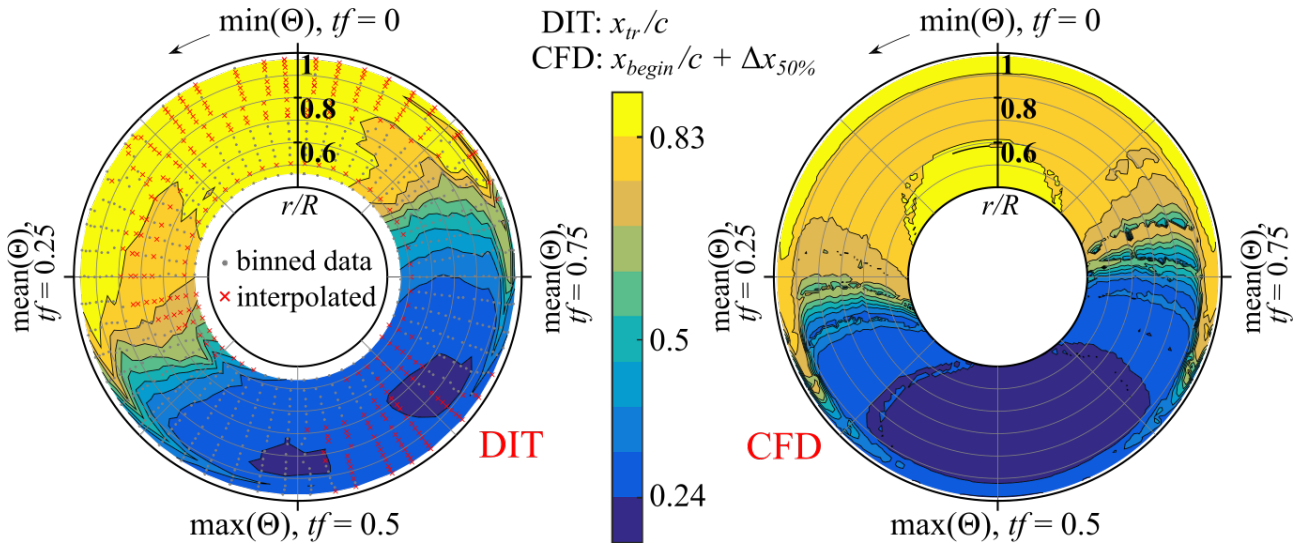


Figure 3.69: Transition map, experimental DIT result (left) and TAU-RBT simulation result (right) or a pitch-oscillating test case with $\Theta_{75} = 9.0^\circ \pm 5.9^\circ$ and $f = 23.6$ Hz [30].

vertical, but slightly rotated in counter-clockwise direction due to the hysteresis, and this tilt is larger in case of DIT. Comparing the yellow-to-blue gradient on the left and the blue-to-yellow gradient on the right, both DIT and CFD indicate a similar three-dimensionality of the transition line as seen by the curvature of the contour isolines. This particularly covers the delayed transition in the blade tip area, see the yellow streaks at $r/R > 0.85$, which was also noted in the static results and connected to the smaller local lift coefficient. The CFD solution predicts a faster transition motion than the DIT result, which can be seen by a tighter isoline spacing.

A more focused view on the remaining uncertainties is given in Fig. 3.70. The transition position was extracted from the map at $r/R = 0.75$, comparing the up- and downstroke for DIT and CFD. Data from the surface pressure taps analyzed via σC_p was added, but it is only available at two chordwise positions ($x/c = 0.31$ and $x/c = 0.62$) and slightly further outboard ($r/R = 0.77$).

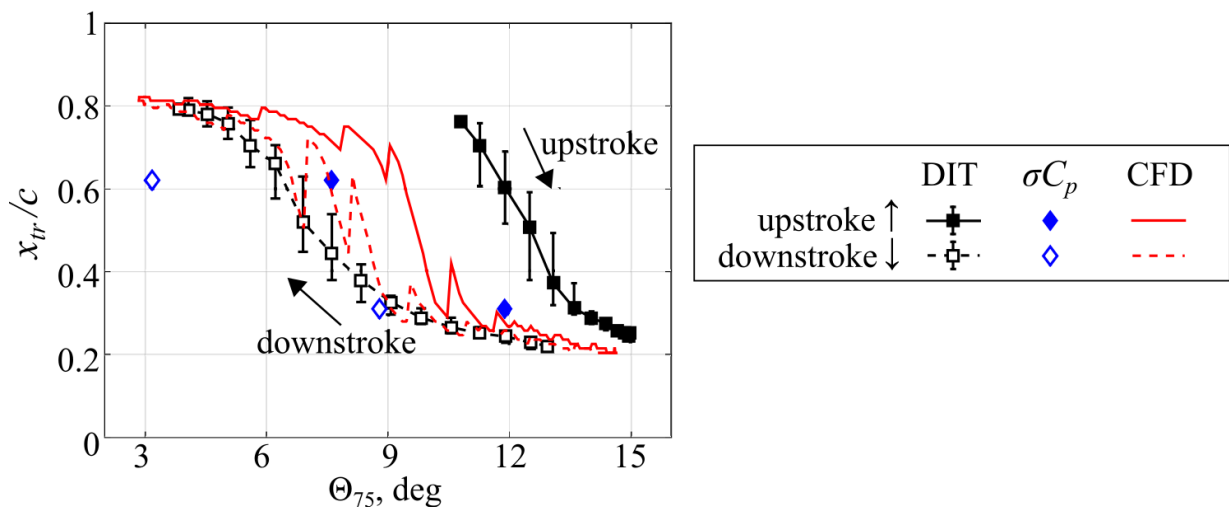


Figure 3.70: Transition positions, DIT and CFD results at $r/R = 0.75$ and σC_p result at $r/R = 0.77$, pitch-oscillating test case with $\Theta_{75} = 9.0^\circ \pm 5.9^\circ$ and $f = 23.6$ Hz [30].

3.4. Application to small-scale rotor experiments

In general, the DIT and CFD data in Fig. 3.70 cover the same transition range and agree well during the downstroke (compare – – and – –), but the DIT data is delayed during the upstroke (compare — and —). The vertical DIT error bars correspond to the scatter of individual results within the phase/pitch-binned data, indicating an increased uncertainty in regions with a fast transition motion. This is also reflected by spikes in the CFD data, at which the transition randomly alternates between different positions. The σC_p -method ($\blacklozenge, \blacklozenge$) measures an earlier transition in comparison to both CFD and DIT. The reason is unknown, but a premature transition onset is probably promoted by the surface disturbance created by the pressure taps. In general, the data scatter in Fig. 3.70 underlines the uncertainties and difficulties of determining the BL transition on a rotor.

The data in Fig. 3.70 is used to estimate the approximate hysteresis of all three methods. In agreement with Sec. 3.3, the hysteresis is defined as the pitch difference $\Delta\Theta$ between up- and downstroke at a given transition position (in Fig. 3.70: horizontal split at $x_{tr}/c=0.31$ and $x_{tr}/c=0.62$). The result is summarized in Tab. 3.7.

x_{tr}/c	$\Delta\Theta, \text{CFD}$	$\Delta\Theta, \sigma C_p$	$\Delta\Theta, \text{DIT}$	pitch velocity
0.31	1.5°	3.1°	4.0°	831°/s
0.62	2.3°	4.4°	5.3°	501°/s

Table 3.7: Hysteresis of the transition position extracted from Fig. 3.70, and corresponding pitch velocity.

Following the argumentation of the preceding sections, σC_p is taken as a reference for the “true” aerodynamic hysteresis. The DIT result yields a larger hysteresis, which is expected due to the additional measurement hysteresis introduced by the thermal mass and the finite responsiveness of the rotor blade surface, also see (iii) in Tab. 3.2. In contrast to this, the CFD simulation underpredicts the measured σC_p -hysteresis. A probable explanation is that the CFD correctly captures the aerodynamic hysteresis of the pressure distribution and the resulting lift, see (i) in Tab. 3.2, but it fails to model the additional finite responsiveness of the boundary layer in reaction to the pressure distribution, see (ii) in Tab. 3.2, since the RBT tool is tuned to quasi-steady input data. It is noted that the current pitch velocities with a maximum of 831°/s by far exceed the pitch velocities of the 1MG and TWG tests, with a maximum of about 200°/s as shown in Fig. 3.28. Hence, the detection of unsteady BL transition is particularly challenging.

3.5 Application to large-scale rotor experiments in forward flight conditions

In a next step, the differential infrared thermography (DIT) was applied to a large-scale rotor operated in forward flight conditions. Supported by the DLR-NASA agreement on “experimental optical methods applied to rotorcraft”, the tests were conducted in the United States under the leadership of NASA scientists, whereas the DLR was responsible for the development of data evaluation methods. The following section is based on the results published by Overmeyer et al. [32], Heineck et al. [31], Gardner et al. [18], and Jain [109].

3.5.1 Experimental setup

The experiments were conducted in the NASA Langley “14- by 22-Foot Subsonic Tunnel” [90] providing an edgewise inflow into the rotor plane. The facility is a large closed-return atmospheric wind tunnel constructed in 1970 with a view to vertical/short take-off and landing aircraft.

The rotor is electrically driven by the “General Rotor Model System” (GRMS), which is enclosed in a helicopter-inspired fuselage shell and held by a sting support, see Fig. 3.71 (left). The GRMS is equipped with a fully articulated rotor system connected to a force balance. The rotor blade design is termed the “PSP” geometry after its initial application in tests with pressure sensitive paint, see Watkins et al. [229] or Wong et al. [237].

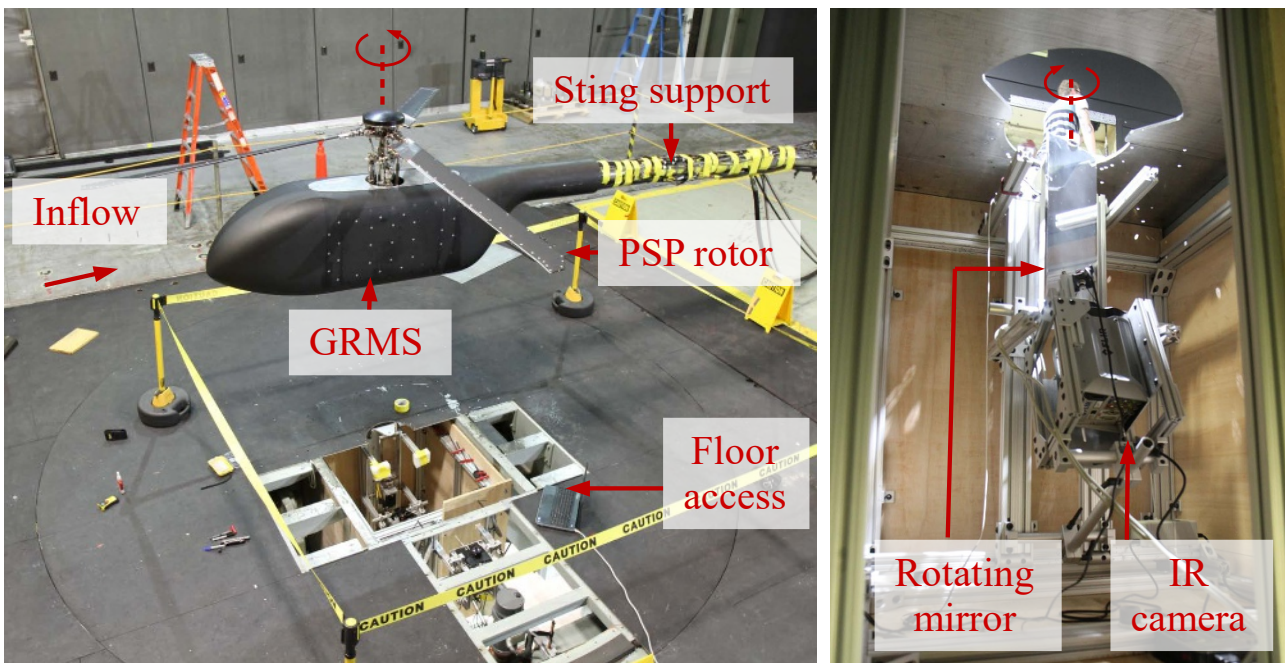


Figure 3.71: GRMS setup in the Langley 14- by 22-Foot Subsonic tunnel (left), IR camera setup below the tunnel’s floor and aimed at the lower side of the rotor, adapted from Heineck et al. [31].

The PSP blades have a radius of 67 in (1.70 m), a chord of 5.45 in (0.138 m), and a planform as shown in Fig. 3.72. Three “RC-series” rotorcraft airfoil geometries [154] were distributed and blended along the span of the blades, with a decreasing relative thickness from 12% at

3.5. Application to large-scale rotor experiments in forward flight conditions

the root to 8% at the tip, and with a linear twist of -14° . The rotor blades were constructed from a mix of carbon- and glass-fiber materials, and covered with Imron 2.1 flat black paint. The surface roughness was measured to $R_z < 0.8 \mu\text{m}$.

The current experiments use a three-bladed rotor hub, which is in contrast to former BL transition measurements on a four-bladed version of the PSP rotor in steady hover conditions [160]. The rotor shaft angle was tilted in “nose-down” direction to $\alpha = -3^\circ$ simulating forward flight. For each test condition, the rotor was trimmed to zero 1/rev flapping to minimize the shaft bending loads. The result is a sinusoidal 1/rev blade pitch motion similar but not identical to a free flight trim, which requires zero rotor head moments. Figure 3.73 shows the trimmed pitch angles for a test case with an advance ratio of $\mu = 0.3$ and a medium thrust setting with a blade loading of $C_T/\sigma_r = 0.10$. Small differences between blade 1 (—), blade 2 (—), and blade 3 (—) are visible but can be neglected. The black line (—) is the single trim solution of the Rotorcraft Comprehensive Analysis System (RCAS), which will be used in a later simulation of the test condition. Additional aerodynamic parameters of the tests are summarized in Tab. 3.8.

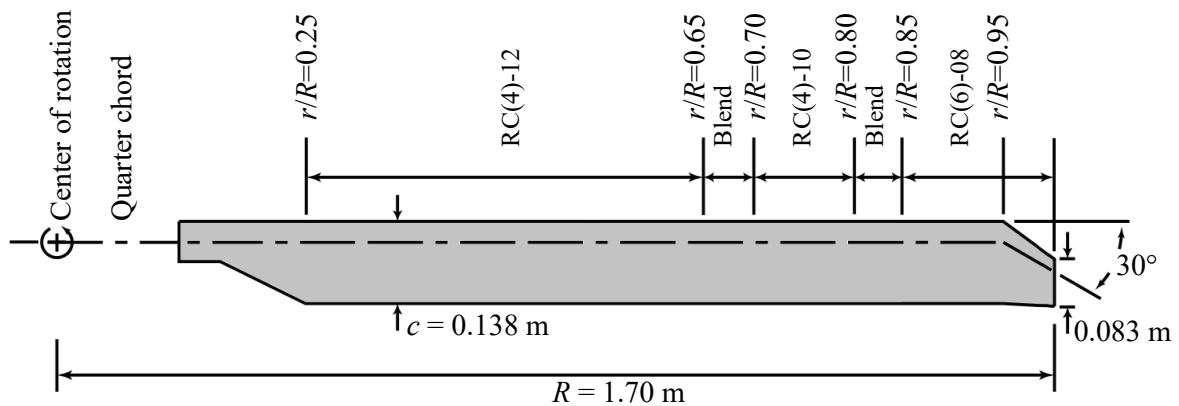


Figure 3.72: PSP rotor blade geometry, adapted from [237].

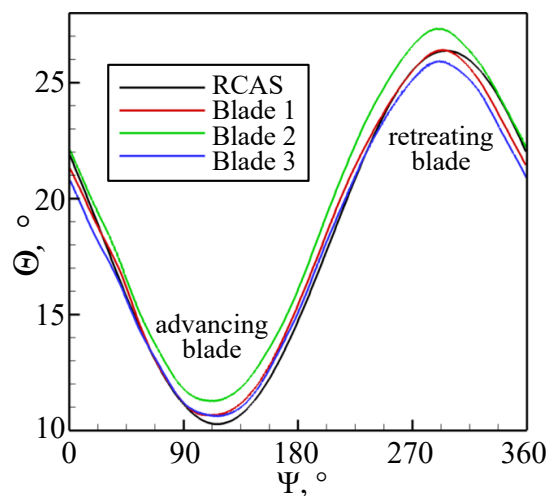


Figure 3.73: Rotor trim for advance ratio $\mu = 0.3$ and thrust setting $C_T/\sigma_r = 0.10$.

Infrared images were taken on both lower and upper side of the rotor plane in two separate measurement campaigns. The later test campaign on the upper side includes several

“lessons learned” regarding the experimental setup and the evaluation technique. A rotating mirror was installed below or above the rotor plane, with a rotational axis approximately collinear to the rotor shaft. In this “on-axis” layout, the mirror spins at half the rotor frequency to track the blade in the camera image (see Sec. 3.4.2 for further details). Fig. 3.71 (right) shows the lower-sided camera installation in the mezzanine below the wind tunnel floor, with the camera looking through a cutout in the floor panels.

parameter	unit	value or range
rotor frequency, f	Hz	18.2
red. frequency, $k_{75} = c/(2r_{75})$	-	0.054
blade loading, C_T/σ_r	-	0.08, 0.10 , 0.12
blade Mach number, M_{75}	-	0.42
chord Reynolds number, Re_{75}	-	1.23 · 10⁶
edgewise inflow, V_x	m/s	58.25
advance ratio, $\mu = V_x/V_{tip}$	-	0.3
inflow temperature, T_∞	K	304

Table 3.8: Experimental parameters, the index “75” refers to $r/R = 0.75$, default values printed in bold letters.

Both campaigns used high-speed IR cameras with strained layer superlattice sensors (FLIR[®] X6900sc for the lower side, FLIR[®] X8500sc for the upper side) and image integration times of $\Delta t = 200 \mu\text{s}$, corresponding to an azimuthal range of $\Delta\Psi = 1.3^\circ$. During DIT processing, differential images were calculated by subtracting two IR images from the same revolution with an azimuthal spacing of $\Delta\Psi = 16.5^\circ$ (lower side³) or $\Delta\Psi = 15.0^\circ$ (upper side). Similar to the RTG processing, the IR images had to be registered before subtraction on the basis of fiducial markers, since an imperfect rotor-mirror alignment and the lead/lag blade motion caused shifts of several pixel. The image resolution is about 90 pixel (lower side) or 200 pixel (upper side) along the blade chord.

3.5.2 Periodic heating and cooling due to edgewise inflow

A rotor in a forward flight condition is subject to an edgewise inflow into the rotor plane. The superposition with the blades’ rotational motion increases the recovery temperature on the advancing side and reduces the recovery temperature on the retreating side, which results in a periodic heating and cooling of the blade surfaces. This effect can be modeled using the heat flux relations in Eq. 3.9. For a constant inflow temperature and density, the convective heat transfer to the blade is proportional to the local inflow velocity, V_∞ , and the difference between the flow’s recovery temperature and the wall temperature, $T_r - T_w$, yielding

$$\dot{q}_{\text{conv}} \propto V_\infty (T_r - T_w) . \quad (3.17)$$

³The original publication, Ref. [32], used a separation of $\Delta\Psi = 23.0^\circ$. For the current work, the data was re-evaluated with $\Delta\Psi = 16.5^\circ$, which is the closest choice to the later upper-sided results with $\Delta\Psi = 15.0^\circ$. As argued in Sec. 3.1.5, a smaller separation leads to a lower signal-to-noise ratio but a smaller hysteresis.

3.5. Application to large-scale rotor experiments in forward flight conditions

The flow's recovery temperature itself is a function of V_∞^2 , since reformulating the corresponding Eq. 3.10 yields

$$T_r = T_\infty + r_C \frac{\gamma - 1}{2\gamma R_s} V_\infty^2. \quad (3.18)$$

The local inflow velocity depends on both the radial and azimuthal position in the rotor plane, r/R and Ψ , and the advance ratio, μ , with

$$\begin{aligned} V_\infty &= \sqrt{\left(\frac{r}{R} V_{tip} + V_x \sin \Psi\right)^2 + (V_x \cos \Psi)^2} \\ &= V_{tip} \sqrt{\left(\frac{r}{R} + \mu \sin \Psi\right)^2 + (\mu \cos \Psi)^2}. \end{aligned} \quad (3.19)$$

Evaluating Eqs. 3.18 and 3.19 for the inflow conditions of the PSP rotor experiment and a recovery factor of $r_C = 0.9$ yields the T_r -distribution shown in Fig. 3.74(a). The edgewise inflow is from the left, the rotor turns in counter-clockwise direction, and the advancing side is in the upper half. The maximum recovery temperature at the blade tip is about 32 K larger than the freestream temperature, and the temperature variation over the azimuth has a peak-to-peak split of about 23 K. These inflow-induced temperature differences render an external radiative heating unnecessary or even counterproductive, but also require to adapt the DIT evaluation scheme. The equilibrium temperature, T_{eq} , was calculated for each radius r/R . T_{eq} is defined as the surface temperature resulting in zero net heat flux over the entire revolution, it is close to but slightly larger than the average surface temperature. Multiplying the inflow velocity with the recovery-to-equilibrium temperature difference yields $V_\infty(T_r - T_{eq})$, representing the local convective flow-to-blade heat transfer after Eq. 3.17. The result in Fig. 3.74(b) expectedly shows that the periodic switch between heating (red colors) and cooling (blue colors) increases towards the blade tip.

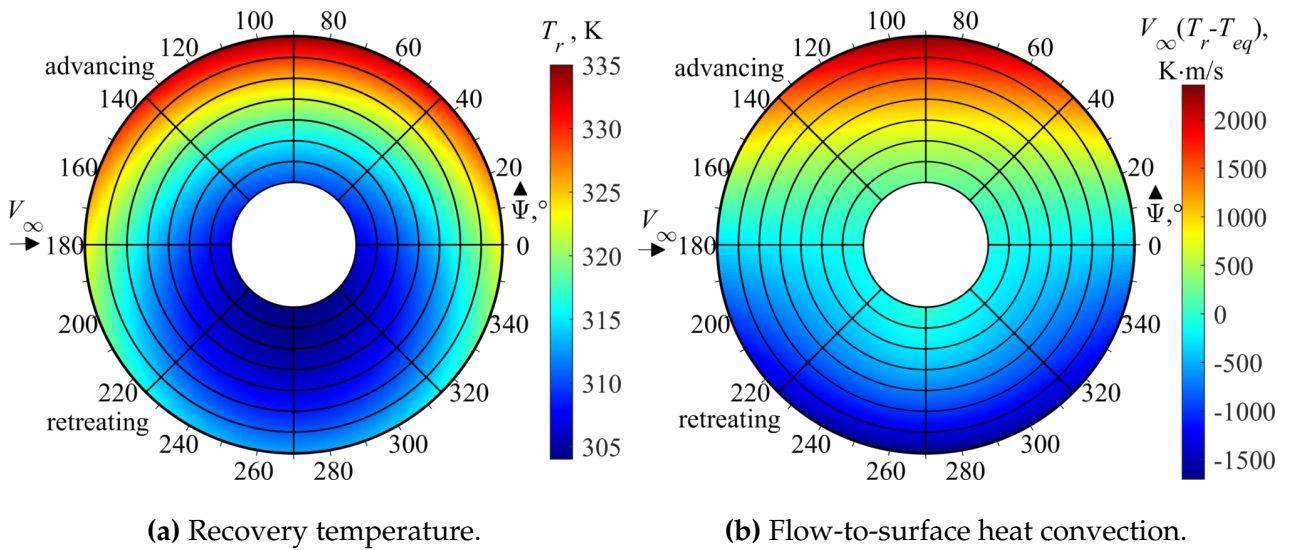


Figure 3.74: Temperature and heat transfer maps for the NASA PSP rotor in reference test conditions. The radial grid lines correspond to $r/R = 0.3, 0.4, \dots, 1.0$.

The implications of the periodic recovery temperature variation and the resulting DIT processing are now discussed by means of the earlier experiments for the lower side of the blades. Fig. 3.75 shows a differential image on the retreating blade side, corresponding to an azimuth angle of $\Psi = 270^\circ$ ($C_T/\sigma_r = 0.08$, $\mu = 0.3$). The data was averaged over three individual rotor revolutions. The blade tip is at the right, and the flow is top to bottom. The overall green-bluish coloring indicates the decreasing surface temperature due to the cooling effect of the surrounding flow. The average difference is only about 3 counts and at the limit of the camera sensitivity. The blade planform and the fiducial markers are visible due to slight errors during the image dewarping process. Due to the large pitch angle of the retreating blade, the BL flow on the lower surface is fully laminar. This can be seen by the absence of any flow structures except from two turbulent wedges, which result from artificial transition dots placed at $r/R = 0.90$ and $r/R = 0.97$, and which span the entire chord length of the blade. From left to right, the triangular wedge shapes have a red-to-blue color gradient resulting from a yaw motion of the flow. At the nominal average azimuth of $\Psi = 270^\circ$, the inflow is perpendicular to the leading edge. However, the differential image was calculated from the IR images at $\Psi_1 = 270^\circ - 8.25^\circ$ and $\Psi_2 = 270^\circ + 8.25^\circ$. The superposition of edgewise flow and rotational motion results in a slightly yawed inflow pointing in inboard direction (at Ψ_1) or outboard direction (at Ψ_2), respectively. Hence, the more effective cooling within the turbulent wedge region, compared to the otherwise laminar flow, is relocated from an inboard position (red color) to an outboard position (dark blue color), creating a two-tone footprint in the differential image.

The effect of a yawed inflow on the turbulent wedges is obvious when comparing Fig. 3.75 to Fig. 3.76. Fig. 3.76 corresponds to a mean azimuth of $\Psi = 300^\circ$, and the local inflow yaw angle at $r/R = 0.9$ is $\beta \approx 13.2^\circ$ as calculated from the advance ratio and the rotor speed. This β -angle is indicated by two black arrows in the upper right corner, whose direction matches well with the yawed alignment of the trailing turbulent wedges.

Fig. 3.77 is a DIT result at $\Psi = 90^\circ$. In general, the orange-reddish coloring indicates a rising surface temperature due to an above-equilibrium recovery temperature on the advancing side. The coloring is not homogeneous but reveals flow structures. A green-bluish pocket of laminar flow is visible at about $r/R = 0.85 - 0.90$, indicating a less effective convective heat transfer compared to the turbulent regions elsewhere. For $r/R < 0.8$, the blade's small pitch angle results in a BL transition close to the leading edge of the lower surface, which is visible as a spanwise dark-red line. The interpretation of the DIT result must be adapted in forward flight conditions. For a constant temperature-inflow discussed in earlier sections, only the transition motion itself appears as a thin spanwise band, but the differential signal of persistently laminar or turbulent regions is close to zero (for example, see Fig. 3.67). In the current case of an increasing recovery temperature, also the turbulent area downstream of the transition region is heated more effectively compared to laminar regions. Hence, the appearance and interpretation of differential images (DIT) in forward flight conditions is quite similar to "standard" infrared thermography (IRT) in steady-state flow conditions.

One of the PSP blades was additionally coated with an electrically conductive paint acting as a surface heating, with a maximum heat flux of up to about 1.3 kW/m^2 . The system worked well for BL transition measurements in hover conditions [160], but it was found to be partly counterproductive in forward flight conditions. Moderately raising the wall temperature will increase the flow's cooling flux on the retreating side, but decrease the flow's heating flux

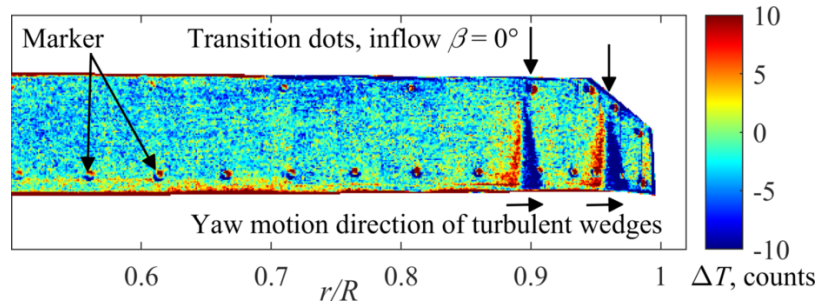


Figure 3.75: DIT result, lower side, $C_T/\sigma_\tau = 0.08$, $\Psi = 270^\circ$ (retreating blade), $\mu = 0.3$.

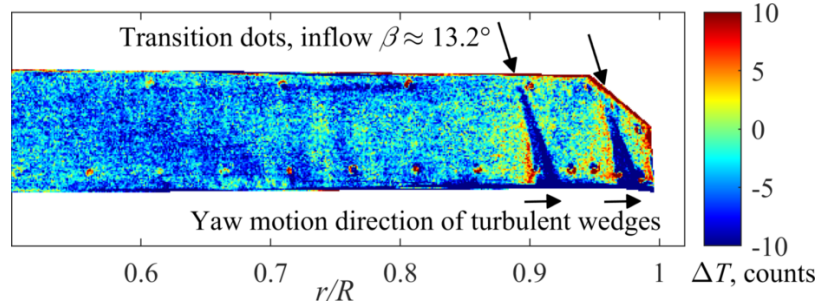


Figure 3.76: DIT result, lower side, $C_T/\sigma_\tau = 0.08$, $\Psi = 300^\circ$ (retreating blade), $\mu = 0.3$.

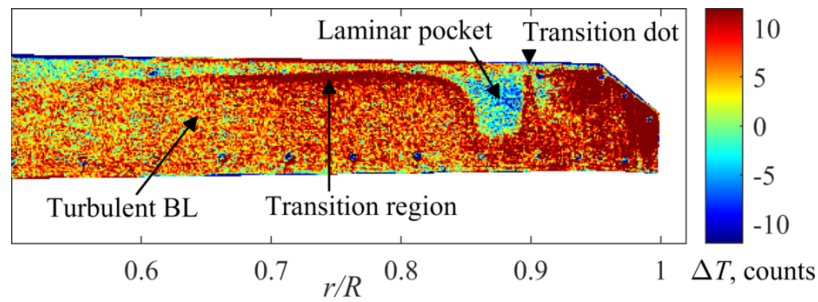


Figure 3.77: DIT result, lower side, $C_T/\sigma_\tau = 0.08$, $\Psi = 90^\circ$ (advancing blade), $\mu = 0.3$.

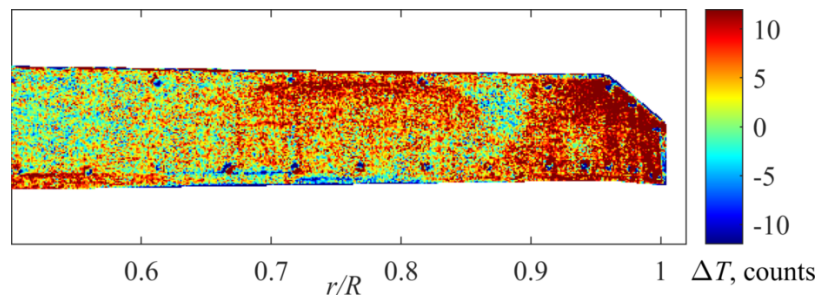


Figure 3.78: Same as above (Fig. 3.77), but with additional surface heating.

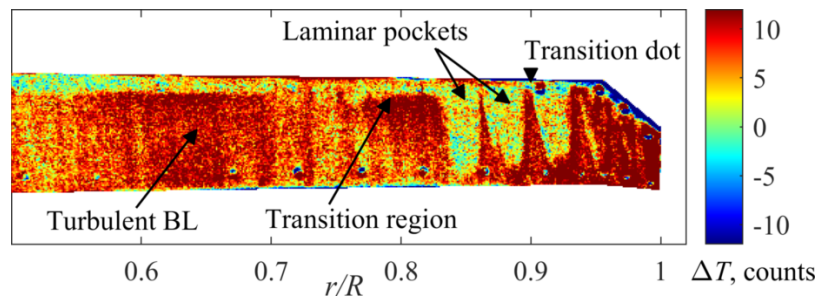


Figure 3.79: DIT result, lower side, $C_T/\sigma_\tau = 0.12$, $\Psi = 90^\circ$ (advancing blade), $\mu = 0.3$.

on the advancing side. Hence, the surface-heated DIT image at $\Psi = 90^\circ$, see Fig. 3.78, shows similar structures with a much lower contrast compared to the unheated blade in Fig. 3.77. In principle, it should be possible to further increase the surface temperature well above the flow's maximum recovery temperature, so that the blade is cooled over the entire rotor plane. However, this is likely to affect the aerodynamics of the boundary layer, and will require transferring a large amount of power to the blade.

Figure 3.79 shows the DIT result at $\Psi = 90^\circ$ with an unheated blade and a higher thrust level of $C_T/\sigma_r = 0.12$. Compared to $C_T/\sigma_r = 0.08$ in Fig. 3.77, the collective pitch angle of the blades was increased, which expectedly leads to a growth of the laminar pockets close to the blade tip. A new turbulent wedge appears at $r/R = 0.85$, which is not connected to an artificial transition dot but probably to a surface defect at the leading edge.

3.5.3 Measurements on the upper side of the rotor plane

The DIT results on the lower side of the NASA PSP rotor discussed in the previous section proved that the periodic blade heating and cooling in forward flight conditions can be used to study boundary layer structures using the DIT method. However, the comparably low data quality prevents an in-depth analysis of the transition map. Hence, a second test campaign was conducted with the following changes:

- A larger number of revolutions (250 versus 3) was acquired to increase the signal-to-noise ratio of the phase-averaged DIT images.
- The optical resolution was increased from 90 pixel to 200 pixel along the chord line. This makes the alignment of raw images before subtraction more precise, and finer flow structures can be identified. Increasing the resolution reduced the radial extent of the viewing field from about $0.50 \leq r/R \leq 1$ to $0.75 \leq r/R \leq 1$.
- Helicopter airfoils have a comparably flat lower surface, hence, the BL transition rapidly jumps between leading and trailing edges over small pitch angle changes. Investigating the upper surface is more insightful due to the slower transition motion, but required to install the camera and rotating mirror at the ceiling of the Langley wind tunnel.
- The camera and rotating mirror were mounted on a belt-driven turntable for a convenient scanning of the entire rotor plane. The camera looked through a germanium window in the tunnel's ceiling. The optical path was folded using a second fixed mirror to reduce the overall size. More details on the optical setup can be found in Heineck et al. [100].
- The experiments were accompanied by a reduced-order aerothermal simulation as in Sec. 3.3, and a high-fidelity CFD simulation by Jain [109].

Figure 3.80 gives a deeper insight into the periodic heating and cooling of the blade surface as a function of the azimuth angle Ψ . The solid black line (—) is the predicted flow-to-surface heat convection after Eqs. 3.17–3.19, and as extracted at $r/R = 0.8$ from Fig. 3.74(b).

The signal is similar but not identical to a sine function, and it is expected to be closely followed by the temporal gradient of the IR-measured upper surface temperature. This

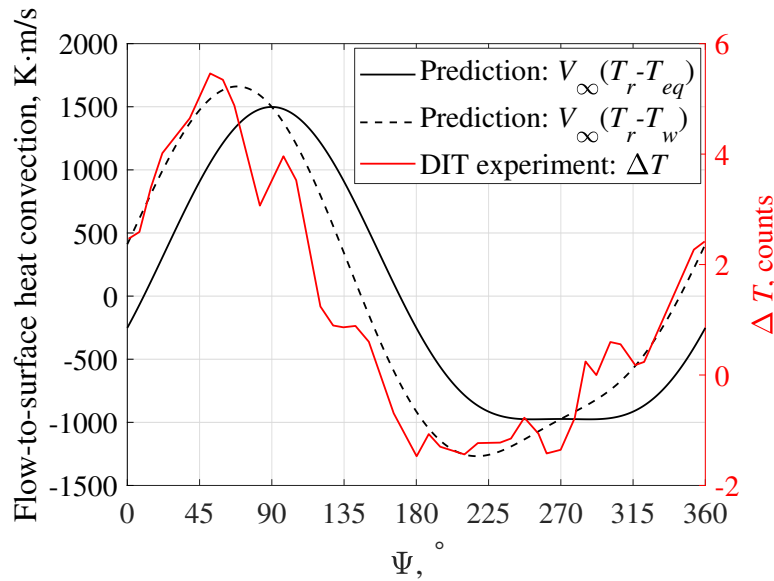


Figure 3.80: Predicted flow-to-surface heat convection at $r/R = 0.8$ (black lines) and corresponding DIT signal (red line) averaged between $0.2 \leq x/c \leq 0.8$.

gradient is represented by the DIT signal, ΔT (—), at $r/R = 0.8$ and averaged in the central part of the blade ($0.2 \leq x/c \leq 0.8$). The IR camera was not calibrated, hence, ΔT is shown in “counts” on the right y -axis, and the comparison is purely qualitative. The overall agreement is reasonable, but the experimental surface temperature gradient (—) leads the predicted heat transfer (—) in phase. This can be explained by the prediction itself. The data in Fig. 3.74(b) is calculated from the difference between the local recovery temperature, T_r , and the constant equilibrium temperature, T_{eq} , as a zeroth-order approximation of the actual wall temperature, T_w . When assuming that a T_w is non-constant but lags behind T_r with a smaller amplitude due to the blade’s thermal inertia, the resulting flow-to-surface convection, $V_\infty(T_r - T_w)$, will indeed lead T_r . This is shown by the second prediction in Fig. 3.80, which assumes a T_w -amplitude of 4 K compared to the T_r -amplitude of about 15 K, and a phase shift of $\Delta\Psi = 90^\circ$ (heating on the advancing side, cooling on the retreating side). As a result, the refined prediction (—) has an excellent qualitative agreement with the experiment (—).

Figure 3.81 shows DIT result images at eight different azimuth angles between $\Psi = 45^\circ$ and $\Psi = 360^\circ$. The advancing blade at $\Psi = 45^\circ, 90^\circ$, and 135° , see Figs. 3.81(a)-(c), results in a characteristic flow pattern similar to the lower-sided result in Fig. 3.77. The increasing recovery temperature raises the blade surface temperature in general, but the heat transfer is less effective in the laminar (bluish) regions close to the leading edge than in the turbulent (reddish) regions further downstream. Several turbulent wedges are visible, which originate from surface defects at the leading edge, since no additional transition dots were applied to the blade’s suction side. Comparing Fig. 3.81(d) at $\Psi = 180^\circ$ to Fig. 3.81(b) at $\Psi = 90^\circ$, a very similar flow pattern is observed in both images, but the blue-red coloring in Fig. 3.81(d) is now inverted due to the beginning flow cooling towards the retreating side, replacing the flow heating on the advancing side.

The differential images partly comprise a pattern of fine and tightly-spaced vertical stripes which is not regarded to be of aerodynamic origin. It is believed that the pattern results from a residual non-uniformity of the IR image sensor, which was not entirely removed by the

camera calibration, and which becomes visible when regarding small intensity differences in DIT processing. An additional flatfield correction was omitted in the post-processing since the necessary information with respect to the boundary-layer transition was unaffected. It is noted that the color range in each individual DIT image was adjusted for a maximum contrast. Looking at the maximum count level, the overall heating effect at $\Psi = 135^\circ$ is smaller than at $\Psi = 45^\circ$ and $\Psi = 90^\circ$, which corresponds to the heat convection signal in Fig. 3.80.

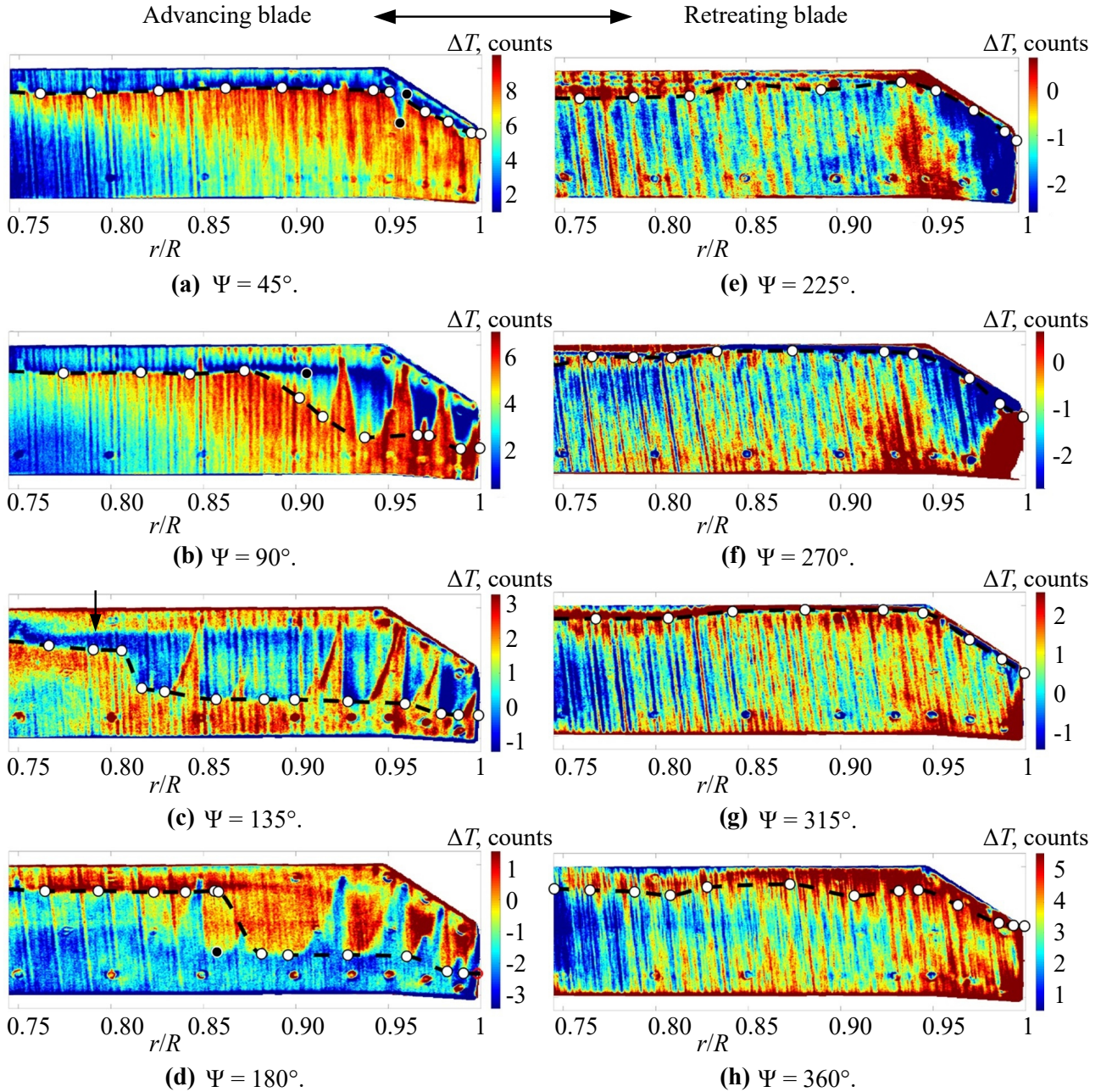


Figure 3.81: Phase-averaged DIT images at azimuth angles $\Psi = 45^\circ, 90^\circ, \dots, 360^\circ$, upper surface of the PSP rotor blade at $C_T/\sigma_r = 0.10$ and $\mu = 0.3$, including valid (o) and invalid (●) transition points and the transition line (—), adapted from Ref. [18].

Fig. 3.81(c) shows a second characteristic spanwise line close to the leading edge (see the black arrow marker), which is connected to the motion of the stagnation area during the pitch step between the original IR images. Hence, the BL transition point was defined at the

maximum ΔT -gradient of the first step seen from the trailing edge. Chordwise slices were extracted and averaged over a spanwise width of 9 pixel (4.5% c). The result, ΔT as a function of x/c , is further smoothed with a sliding window sized 10 pixel (5% c). Between 8 and 23 transition points were extracted along the span, based on a non-automated user evaluation and depending on the geometric complexity of the transition line. Turbulent wedges were ignored for a better comparability with CFD simulations, which assume hydraulically smooth surfaces without defects. A further post-processing step checks the time consistency and plausibility of individual DIT results, separating a few invalid data points (\bullet in Fig. 3.81) from the otherwise valid data (\circ). The spanwise transition line (– –) is a piecewise cubic Hermite-interpolated polynomial. The DIT results on the retreating side of the rotor plane, see Figs. 3.81(e)-(h) for $\Psi = 225^\circ, 270^\circ, 315^\circ$, and 360° , only show a very small variation of the boundary layer state, with transition always being close to the leading edge.

3.5.4 Comparison to numerical simulations

Two different numerical simulations were conducted to accompany the Langley wind tunnel tests. First, DLR’s reduced-order aerothermal approach as described in Sec. 3.3 was used to confirm the DIT principle and its evaluation scheme in forward flight conditions. Second, Jain [109] conducted a high-fidelity simulation within the NASA CFD framework, demonstrating the current state-of-the-art in transition modeling for rotor flows.

Aerothermal simulation

The azimuthal temperature fluctuation of the blade’s upper surface was calculated after Sec. 3.3 and Fig. 3.41 for the current default test conditions with a thrust level of $C_T/\sigma_T=0.10$ and an advance ratio of $\mu=0.30$. The thermal parameter settings are given in Tab. 3.9.

number of cells in vertical (surface-normal) direction	300
total thickness of the surface layer	1.0 mm
time step for heat computation	$5 \cdot 10^{-7}$ s
total simulation time	100 s
surface layer material	epoxy
thermal conductivity (vertical direction), $\lambda_{S,v}$	0.5 W/m/K
surface heat capacity, c_S	2300 J/kg/K
surface density, ρ_S	1180 kg/m ³
freestream static temperature, T_∞	304 K

Table 3.9: Settings for the temperature computation in the surface layer, PSP rotor experiment.

The simulation uses the bulk coefficients of the epoxy matrix material as a simplification for the complex paint-coated carbon- and glass-fiber structure of the PSP blades, in agreement with the earlier TWG simulations (see Tab. 3.4). The rotational/pitch frequency in the current test is larger than in the TWG case, 18.2 Hz versus 6.6 Hz. To adapt to the increased

unsteadiness, the simulation time step was reduced from $5 \cdot 10^{-5}$ s to $5 \cdot 10^{-7}$ s, and the thickness of the simulated surface layer was reduced from 5.5 mm to 1.0 mm.

The time/phase-resolved skin friction coefficient, C_f , is required as an input for the convective heat transfer at the interface between blade and flow, see Eq. 3.9. This input was generated using a combination of the “Rotorcraft Comprehensive Analysis System” (RCAS) [105] and the flow solver “MSES” [74]. RCAS uses a structural model of the PSP blade and the inflow and thrust settings of the test case to calculate the rotor trim, see (—) in Fig. 3.73, which matches the measured pitch angles of the blades well. The predicted aerodynamic angle of attack, α , at $r/R = 0.8$ is shown in Fig. 3.82 (—). Deviations from a smooth sinusoidal shape are, for example, caused by wake interactions as predicted by a prescribed wake model within RCAS [110]. The figure also contains the predicted Mach number (—) and Reynolds number (—) of the blade section.

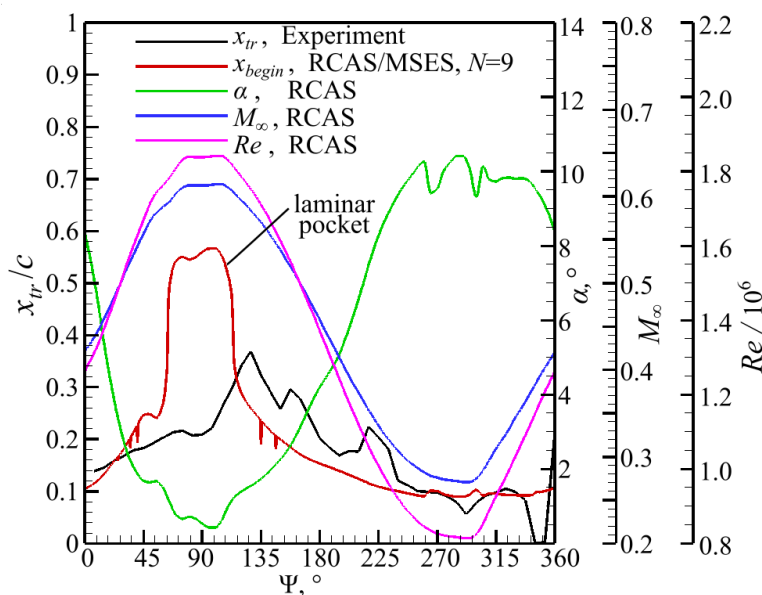


Figure 3.82: RCAS-predicted inflow (α, M, Re), RCAS/MSES-predicted and measured transition positions x_{tr}/c for the trimmed rotor at $r/R = 0.8$ [18].

The RCAS/MSES transition map for the upper surface is shown in Fig. 3.83(a). It is noted that the RCAS computation is inherently three-dimensional, but the flow conditions were extracted at several radial positions and fed into the two-dimensional MSES code and its e^N -based prediction of the Tollmien-Schlichting transition mechanism.

The RCAS/MSES prediction switches between BL transition close to the trailing edge (purple-reddish areas on the advancing side) or close to the leading edge (bluish areas on the retreating side), which is qualitatively similar to the experimental DIT data shown in Fig. 3.83(b). There is a notable phase difference, which is probably caused by the numerical simplifications, for example the stationary and two-dimensional MSES calculation, and the additional measurement-related hysteresis of the DIT approach. Reducing the N -factor in MSES shifts the predicted transition closer to the leading edge (see Ref. [18] for more details), but does not generally improve the agreement with DIT. The extracted transition positions at $r/R=0.8$ are shown in Fig. 3.82, in which the RCAS/MSES result (—) has a distinct pocket of laminar flow around $\Psi=90^\circ$, which is not mirrored by the DIT experiment (—). It is noted that by definition MSES predicts the transition onset, x_{begin} , rather than 50% intermittency, x_{tr} , as

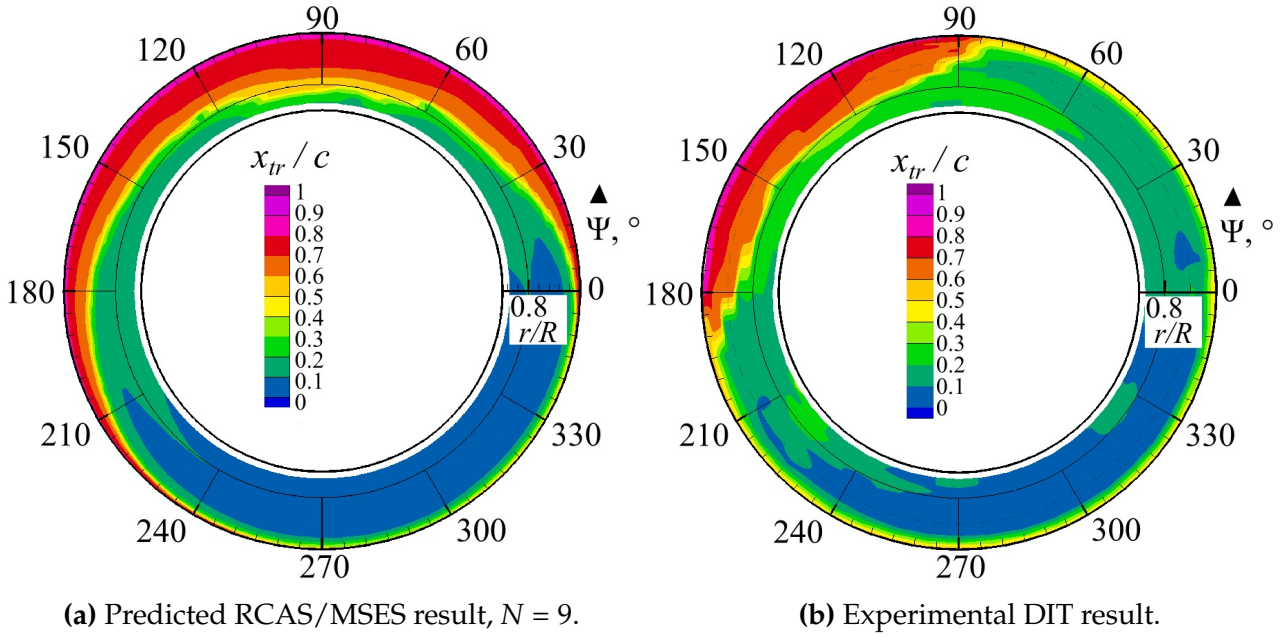


Figure 3.83: Transition map for the upper surface, $C_T/\sigma_r=0.10$ and $\mu = 0.30$ [18].

in the DIT result. Other than that, the agreement is reasonable for this type of reduced-order simulation.

Feeding the aerodynamic RCAS/MSES data into the thermal simulation with the parameters stated in Tab. 3.8 yields the phase-resolved surface temperature, which can be used to predict the differential temperature distributions, ΔT , after applying the DIT procedure. Figure 3.84 compares the predicted results (—) at $r/R = 0.8$ to the corresponding experimental results as a single-pixel line (—) and after applying the sliding-window smoothing (—).

It is noted that the comparison is qualitative, since the IR camera sensitivity was not calibrated and the result is given in counts (left y -axis), whereas the simulation result is in kelvin (right y -axis). Significant and unambiguous ΔT -distributions are observed at $\Psi = 45^\circ$, see Fig. 3.84(a), where the advancing-sided flow heating results in a positive surface temperature gradient. Starting at the trailing edge and moving upstream, the experimental signal (—) rises from about 3 counts at $x/c=1$ to about 8 counts at $x/c=0.2$, which spans the turbulent part of the boundary layer. A fiducial marker causes an interruption at $0.8 \leq x/c \leq 0.9$, its silver-paint surface mirrors the background IR radiation and is in contrast to the surrounding blade temperature. The marker area was masked and excluded from further evaluation. Upstream of $x/c=0.2$, the experimental ΔT -signal sharply drops to much smaller but positive values, indicating the less effective flow heating in the laminar part of the boundary layer. The experimental transition point, x_{tr} (50% intermittence, —), is identified at the first step from the trailing edge, avoiding parasitic temperature differences at the leading edge caused by the motion of the stagnation point. The qualitative agreement with the simulated ΔT -distribution (—) is good, even though the corresponding transition (—) is further downstream at about $x/c=0.25$. This deviation is also present in the RCAS/MSES aerodynamic prediction, see Fig. 3.83 at $\Psi = 45^\circ$, and not connected to the successive thermal simulation. Since MSES provides the transition onset rather than 50% intermittency, the position of x_{begin} (—) is located at the upstream end of the ΔT -step (—) rather than in its center.

The differential temperature signals at an azimuth of $\Psi = 90^\circ$ are shown in Fig. 3.84(b). The

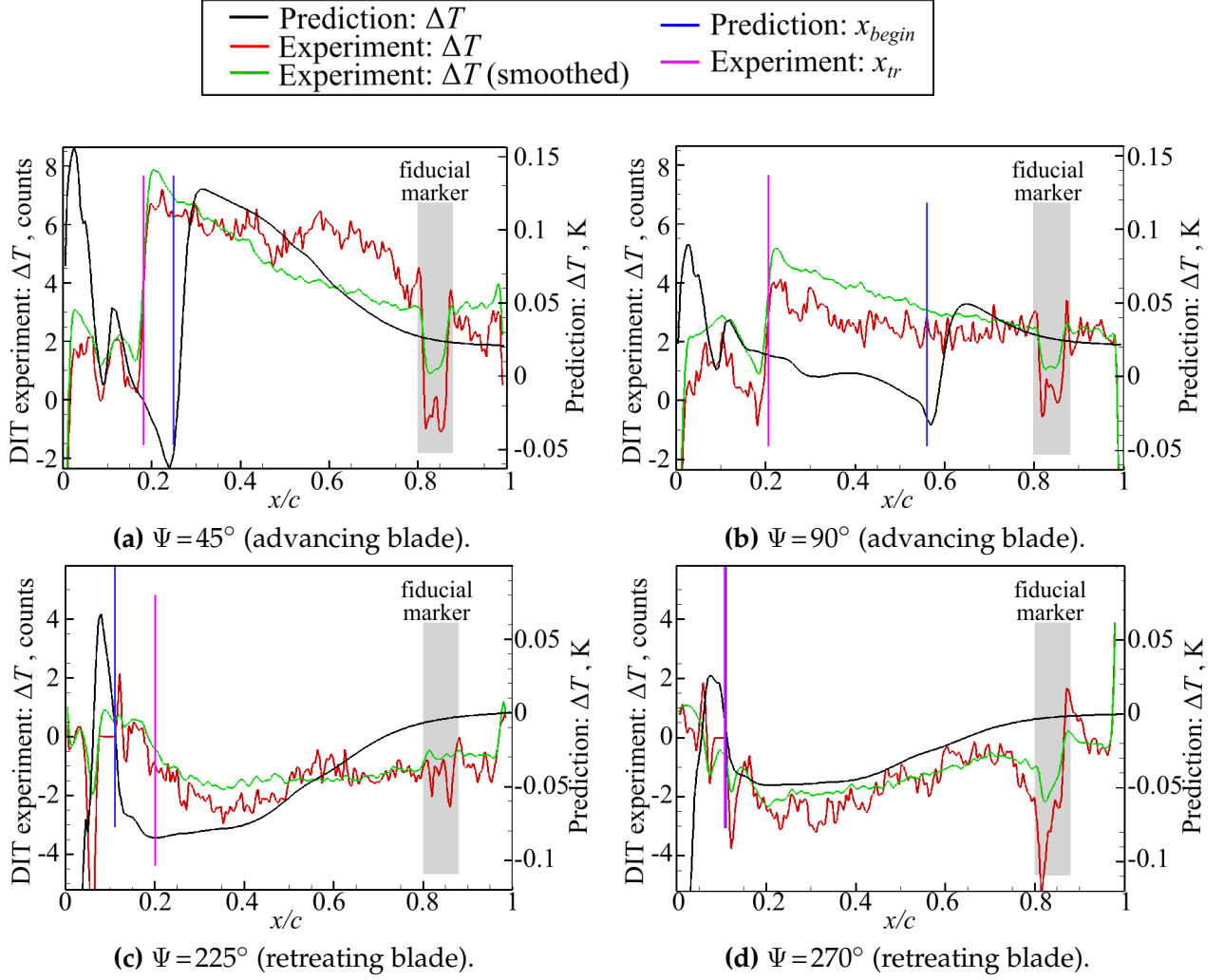


Figure 3.84: Differential temperature distributions and transition positions for the experiment and the aerothermal prediction, $r/R=0.8$, $C_T/\sigma_r=0.10$ and $\mu = 0.30$, adapted from Ref. [18].

signal-to-noise ratio is smaller due to the declining level of flow heating, and the simulated transition position (—) is about $\Delta x/c=0.35$ downstream of the experimental result due to the MSES/RCAS-predicted laminar pocket at $\Psi = 90^\circ$, also compare Fig. 3.82. Other than that, the evaluation of the DIT result is similar to the procedure at $\Psi = 45^\circ$.

Figures 3.84(c) and 3.84(d) correspond to the azimuth angles of $\Psi = 225^\circ$ and $\Psi = 270^\circ$, respectively. Due to the flow's cooling effect on the retreating side of the rotor plane, and seen from the trailing edge in upstream direction, a negative ΔT -value is observed in the turbulent part of the boundary layer. A ΔT -step in positive direction indicates the transition due to the less effective cooling in the laminar region. Again, both experiment and simulation agree that identifying the first ΔT -step from the trailing edge is advisable to neglect strong temperature fluctuations close to the leading edge. As expected from the heating curve in Fig. 3.80, the signal-to-noise ratio on the retreating side is smaller than on the advancing side. It approaches zero when switching from heating to cooling ($\Psi \approx 135^\circ$) and vice versa ($\Psi \approx 315^\circ - 360^\circ$). Additional DIT samples at various azimuth angles can be found in Ref. [18].

In summary, comparing the experimental data to the aerothermal simulation underlines the applicability of DIT in forward flight conditions. This particularly includes the flow's fluctuating recovery temperature, which enables the DIT visualization of laminar and turbulent

areas similar to conventional infrared thermography in steady conditions.

High-fidelity CFD simulations

Jain [109] conducted a state-of-the-art CFD simulation of the wind tunnel test using the “CREATE™ -AV Helios” software framework supporting a multi-mesh multi-solver approach. As in the preceding aerothermal simulation, the reference test case with a thrust level of $C_T/\sigma_r=0.10$ and an advance ratio of $\mu=0.30$ was considered.

The flow around each of the three blades is represented by a structured overset near-body grid containing a total of $17.6 \cdot 10^6$ nodes, see Fig. 3.85 (left) for a sectional view. The overset blade grids not only consider rigid-body motion (rotation, cyclic pitch, etc.) with respect to the RCAS rotor trim solution, but also an elastic deformation after a loose coupling to a computational structural dynamics (CSD) module [164] integrated into RCAS. The flow is simulated by solving the RANS/DDES equations (Reynolds-averaged Navier-Stokes/delayed detached-eddy simulation [210]) via the NASA solver “Overflow”, with the boundary layer region in RANS mode. A freestream turbulence level of $T_u = 0.08\%$ was prescribed at the inflow boundary of the blade grids, based on the qualification of the wind tunnel [153]. Three different combinations of turbulence models and transition predictions were tested:

- **SA-AFT:** The Spalart-Allmaras turbulence model (SA) is combined to the “amplification factor transport” equation (AFT) after Coder and Maughmer [65], which implements the detection of Tollmien-Schlichting instabilities.
- **SST-LM-G:** The Langtry-Menter (LM) transition criterion was formulated for the shear stress transport (SST) turbulence model [128]. The transition prediction is based on empirical correlations to reference test cases, including Tollmien-Schlichting and bypass transition. The LM formulation is only based on local boundary layer properties, hence, it is particularly suitable for a highly parallel execution of production CFD codes. Galileian invariance (G) was ensured for the application to the moving blade surfaces.
- **SST-LM-G-CF:** The Langtry-Menter criterion was extended to also include crossflow (CF) effects [129], which is particularly interesting for rotor flows.

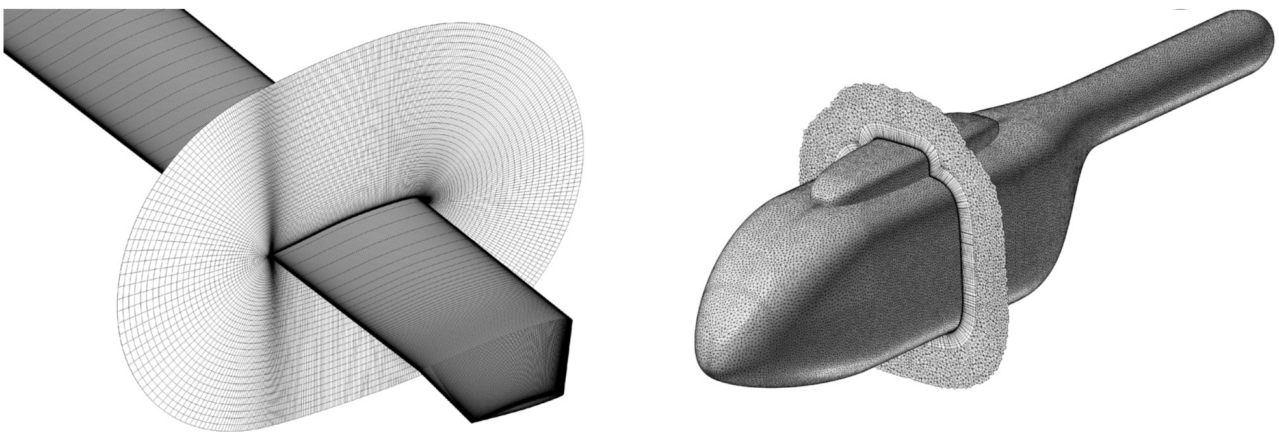


Figure 3.85: Rotor blade grid (left) and fuselage grid (right) for Helios/Overflow simulations, adapted from Ref. [109].

The fuselage grid is unstructured and contains $2.5 \cdot 10^6$ nodes, see Fig. 3.85 (right). The boundary layer of the fuselage was modeled as fully turbulent.

The fuselage and blade grids were embedded into a Cartesian off-body grid with a total of $188 \cdot 10^6$ nodes representing the wind tunnel's test section. The simulation was run over one rotor revolution with a coarse time stepping corresponding to $\Delta\Psi = 1^\circ$, and then over two additional revolutions with $\Delta\Psi = 0.25^\circ$. An extensive description of the flow solver settings and convergence considerations can be found in Ref. [109]. Figure 3.86 shows an instantaneous solution of the wake structure. Due to the forward tilt angle of the rotor plane, $\alpha = -3^\circ$, the vortical structures convect downstream with only few rotor-wake interactions.

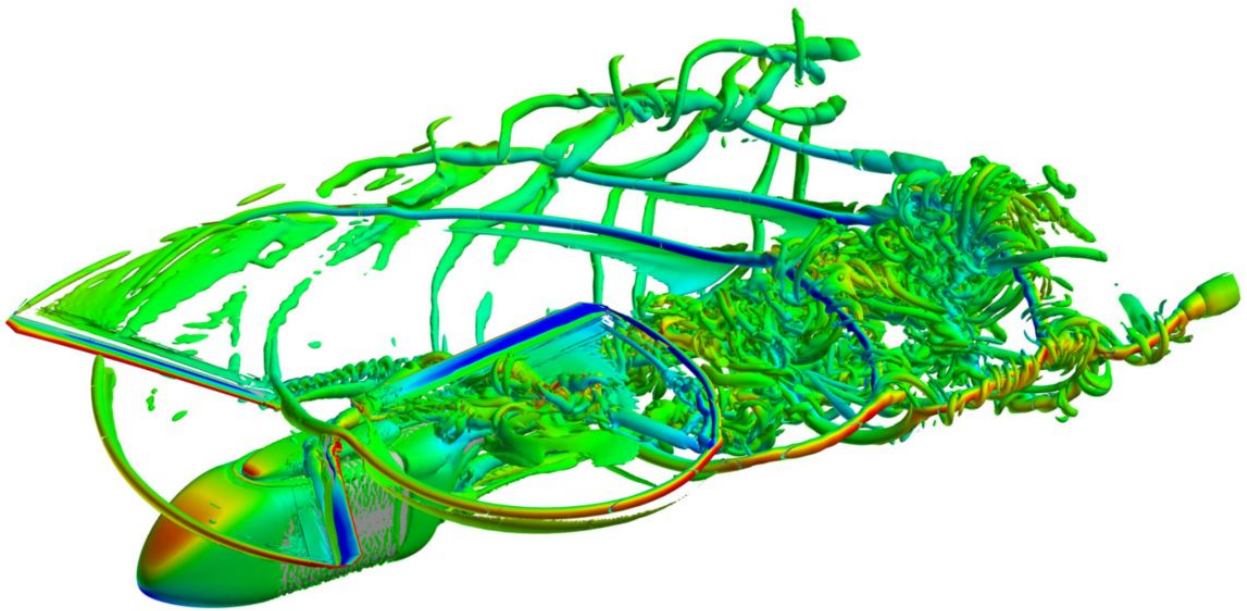


Figure 3.86: Flow of the PSP rotor and fuselage, SST-LM-G-CF computation, isosurfaces of the normalized Q -criterion colored by vertical velocity, adapted from Ref. [109] and repeated from Fig. 1.5.

Figures 3.87(a) to 3.87(c) show the predicted transition maps for the upper side of the rotor plane and for the three different transition models. The experimental DIT result in Fig. 3.87(d) is repeated from the preceding section as a reference. In CFD, the transition position, x_{tr} , was identified as the chordwise location where the local BL turbulence level has grown by an order of magnitude in comparison to the inflow condition. This scheme can be applied to all three models as a robust indicator. The qualitative agreement between DIT and CFD is very good. Remarkably, the simulations faithfully predict the rapid transition motion towards the trailing edge, $90^\circ < \Psi < 120^\circ$, and back towards the leading edge, $180^\circ < \Psi < 210^\circ$. It is noted that the simulation quality is significantly improved over the reduced-order RCAS/MSES approach discussed in Fig. 3.83. The SST-LM-C-CF approach, Fig. 3.87(b), predicts an earlier transition in comparison to SST-LM-G, Fig. 3.87(a), particularly on the advancing side of the rotor plane. This indicates a probable influence of crossflow effects on the transition position, which is supported by the direction of the corresponding surface streamline pattern (not shown, see Ref. [109] for further details). The inclusion of crossflow effects decreases the rotor's predicted lift-over-drag ratio by about 3.1%. However, this was mostly attributed to an earlier transition on the lower side of the rotor plane, with only a small contribution of the

3.5. Application to large-scale rotor experiments in forward flight conditions

upper-sided transition. SA-AFT, Fig. 3.87(c), predicts transition positions roughly between SST-LM-G and SST-LM-G-CF.

As concluding remarks, Jain underlines that the work is one of the first transition model validation studies for a high-speed high-thrust forward flight condition with a large-scale rotor. Future work will focus on a deeper understanding of crossflow effects and a comparison to further well-established transition models.

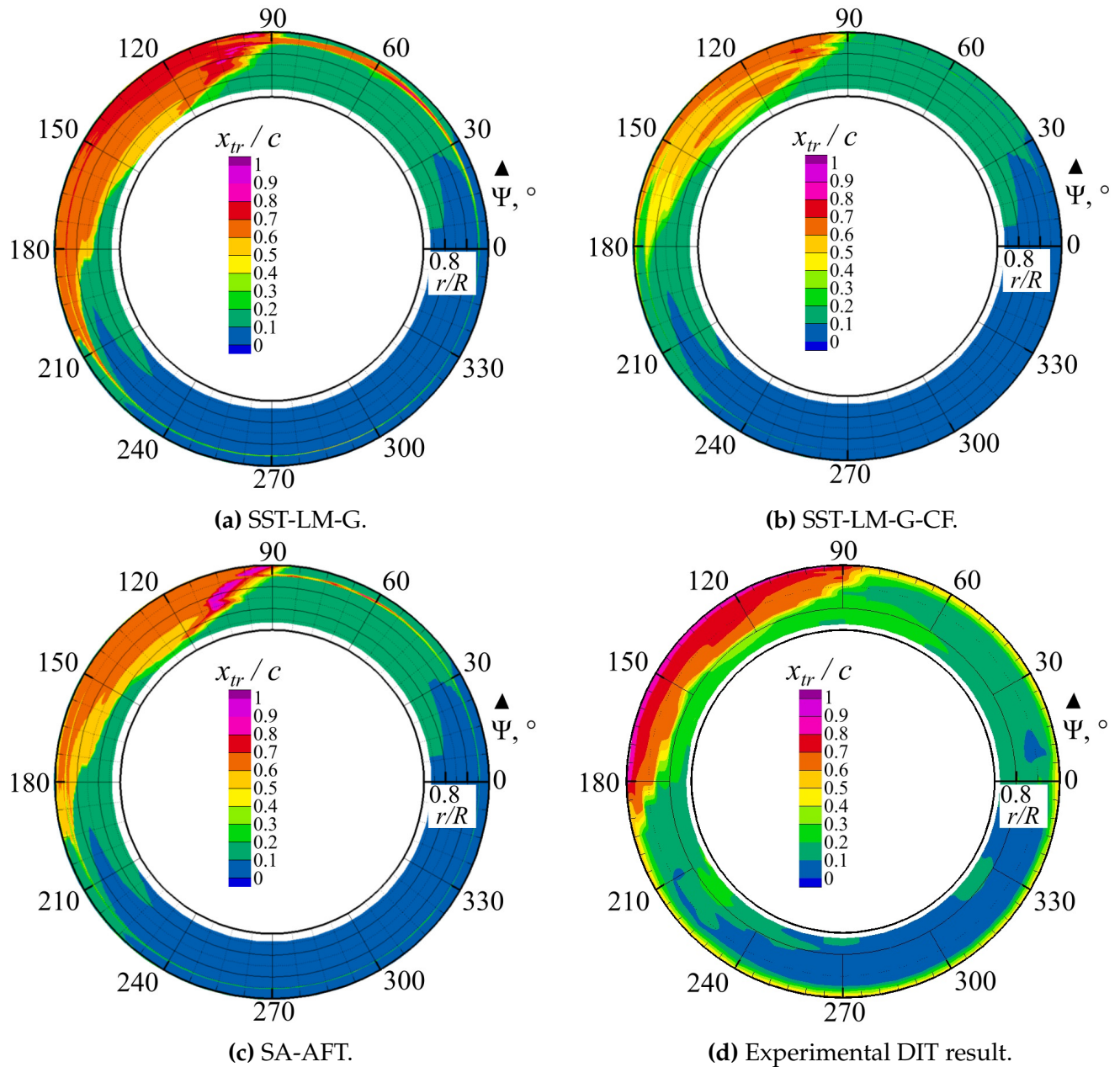


Figure 3.87: CFD and DIT transition maps for the upper surface, $C_T/\sigma_r=0.10$ and $\mu = 0.30$, adapted from Jain [109].

3.6 Application to flight tests

In a final step, the DIT-based methods for boundary layer transition detection were applied during an in-flight test campaign on a full-scale helicopter. The study aims at a proof of concept, and the identified transition is consistent with previous hover measurements and reduced-order numerical predictions. However, the DIT results themselves are not conclusive and require further validation. The main problems are summarized as follows:

- The investigated rotor blade of an Airbus EC135 test helicopter has a comparably short length of laminar BL flow, and the evaluation is further complicated by leading-edge erosion protection.
- The IR images suffer from a low resolution due to large observation distances, and from a low signal-to-noise ratio due to short exposure times and small heating/cooling differences on the advancing and retreating sides of the rotor plane. Hence, the in-flight result quality is inferior to earlier wind-tunnel results.

An improvement is expected with the development of future IR sensor technology and modern low-drag helicopter airfoils. A summary of the current study, also see Gardner et al. [19] and Heineck et al. [31], is given in the following sections.

3.6.1 Experimental setup and test procedure

The in-flight DIT tests were conducted in summer 2018 in the surroundings of the Braunschweig regional airport (ICAO-code: EDVE) using the two DLR research helicopters, see Fig. 3.88 and Tab. 2.2 in Sec. 2.3.2. The MBB/Eurocopter Bo105 served as a camera platform, following the leading Airbus EC135 in formation flight. Both rotorcraft were piloted manually. The Bo105 chase pilot kept a separation distance between 50 m and 100 m, observing the EC135's rotor plane from the top-left direction, see Fig. 3.89. The viewing angle was about 30° to 45° from the vertical top-down direction, and between 270° to 300° in the EC135's rotor plane azimuth. A more perpendicular view on the rotor is preferable to reduce image distortion. This was not possible in formation flight, since the EC135 would have been outside the viewing field of both the Bo105 pilot and the IR camera. The test conditions include hover outside ground effect (OGE) at 4.5 rotor diameter above ground as measured by the helicopter's radar altimeter, and steady forward flight in an altitude of 1700 ft (about 520 m). The forward flight speed was 80 kt ($V_x = 41$ m/s) corresponding to an EC135 advance ratio of $\mu = V_x / V_{tip} = 0.20$, limited by restrictions when flying with an open Bo105 passenger door.

The EC135 main rotor has a diameter of 5.1 m and spins at 6.58 Hz. The four rotor blades are made of a glass fiber composite material [41] and use the DMH3/4 airfoil geometry [112]. The blade planform is shown in Fig. 3.90. The outboard part of the leading edge is protected from erosion damage by a titanium shell, starting at $r/R = 0.59$ ($r = 3000$ mm). The thermal properties of the bare titanium surface are not suitable for IR evaluations. The inboard part of the leading edge is protected up to $x/c = 0.18$ by an optional polyurethane tape of type "3M 8681 HS". The tape surface itself is suitable for IR transition analyses, but its add-on thickness of 0.36 mm and its differing thermal properties must be treated with care. Figure 3.91 shows



Figure 3.88: DLR's Bo105 with infrared camera (foreground) and EC135 (background).



- ① IR camera
- ② Viewfinder
- ③ EC135 helicopter
- ④ Gimbal mount
- ⑤ Open door
- ⑥ Bo105 pilot (M. Barnett)
- ⑦ Camera operator (C. C. Wolf)

Figure 3.89: Infrared camera operation in the Bo105 cabin during formation flight.

a steady-state IRT result of an earlier EC135 ground test run⁴ with a reduced rotor speed of 75% nominal rpm and a non-moving transition position. The end of the add-on tape protection (left side) results in a backward facing step and, thus, in an earlier transition compared to the conformal titanium protection (right side) placed in a recess of the blade surface. On the other hand, the premature transition is still clearly downstream of the tape's edge, and the IR signature of the tape cannot be distinguished from the blade's base material. It is noted that for nominal rpm and higher thrust settings, the transition position difference between tape and titanium protections is much smaller [179].

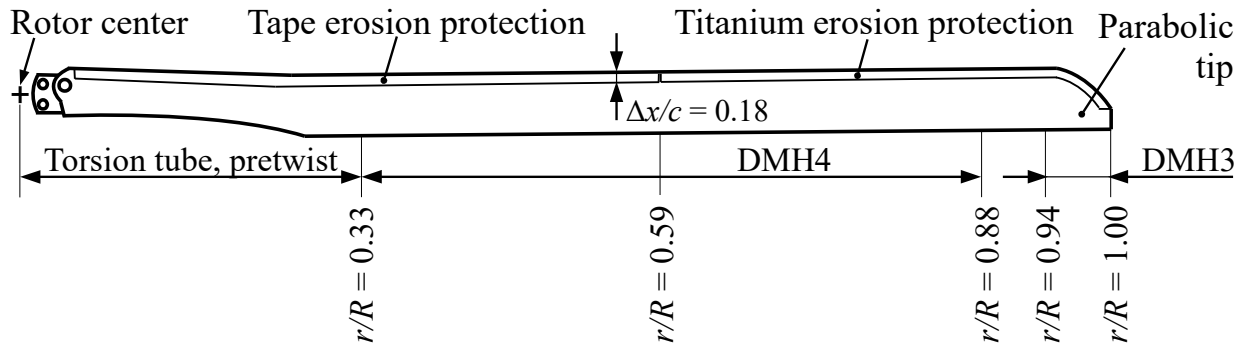


Figure 3.90: Layout of the EC135 rotor blade, including geometry data from [112].

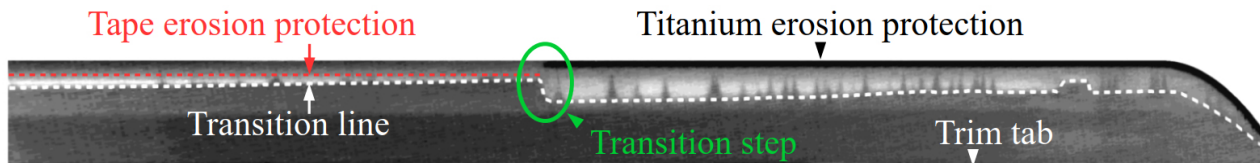


Figure 3.91: IRT result of the EC135 blade for a ground test run with reduced rotor speed (75% nominal rpm, $f = 5$ Hz), adapted from Richter and Schülelein [179].

The IR camera was mounted on a gimbal-joint support structure and placed on the lap of the camera operator, who aimed the viewing axis at the EC135's rotor through the open passenger door. Aiming was assisted by a coaxial viewfinder camera providing a live feed on a small screen, also see Fig. 3.89. The image acquisition and data handling was performed by a second operator on the left side of the passenger compartment.

The experiments used the same FLIR[®] X8500sc SLS camera as already applied in the rotor experiments of Secs. 3.4.1 and 3.5.1, also see Fig. 3.59. The camera operates in the long-wave IR band between wavelengths of 7.5 μm and 10.5 μm . The image size was reduced from 1280 \times 1024 pixel (full frame) to 768 \times 800 pixel for an increased image acquisition frequency of 294 Hz. Image sequences were recorded in bursts comprising 1500 images or 5.1 s, followed by about 10 s required to store the image data on an internal solid-state drive. The camera was paired with a 200 mm focal length-lens, limited by the scarce availability and high costs of IR telescopic lenses.

A mirror-based image de-rotation to counter the motion blur could not be applied in the flight tests. As described in Sec. 3.4.2, the working principle requires the mirror axis to constantly point at the EC135 rotor hub, and to keep a prescribed viewing angle matching

⁴The tests by Richter and Schülelein [179] were conducted before the development of DIT. More details on the experimental campaign is discussed in the "state of research" of the current work, see Sec. 2.1 and Fig. 2.1.

the mirror-to-rotor rpm ratio. In formation flight, these conditions could not be met with the required precision. Hence, the image exposure was reduced from its usual value of about $200\ \mu\text{s}$ to only $50\ \mu\text{s}$. The resulting motion blur is $2.6\% c$ at $r/R=0.75$, at the cost of a reduced image signal-to-noise ratio.

A sample IR image is shown in Fig. 3.92. The field of view covers about one quarter of the entire rotor plane, and successive images within a single rotor revolution are available for DIT processing due to the high image acquisition frequency. The camera operator did not intentionally aim at specific parts of the rotor plane, for example, the advancing or retreating side. A variation of the field of view was rather a consequence of the random relative motion between the two helicopters, and relevant image sequences were later selected in a manual post-processing.

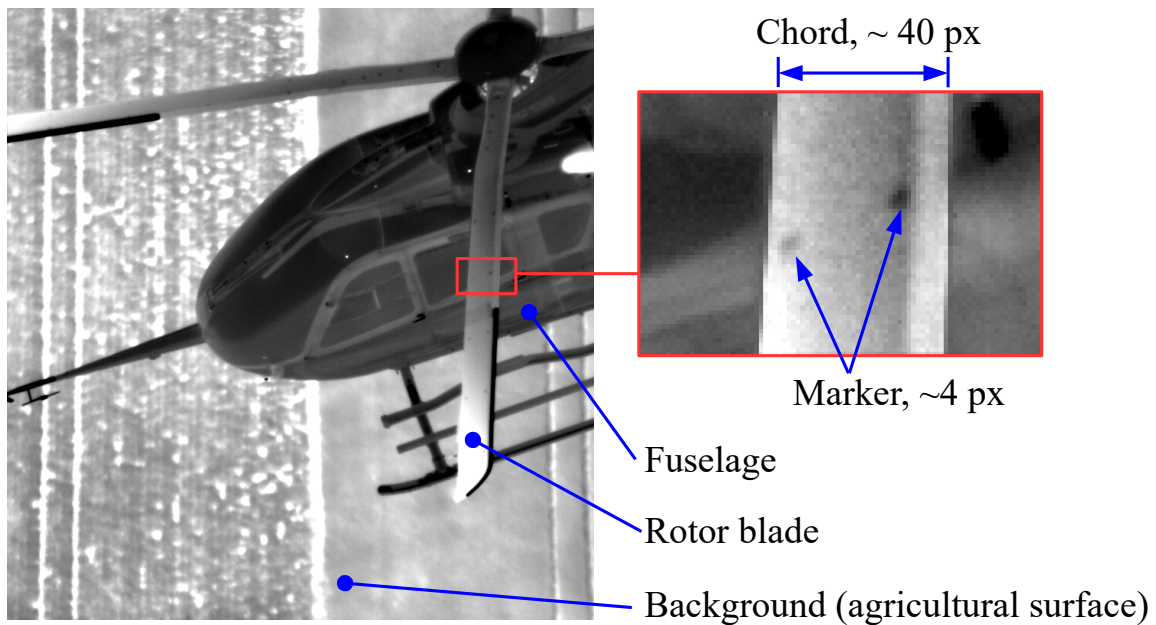


Figure 3.92: Sample IR image of the EC135's rotor plane.

Ten fiducial markers with a diameter of $0.1 c$ were painted on each rotor blade, located at two chordwise positions of $x/c=0.23$ and $x/c=0.83$, and at five radial positions between $r/R = 0.36$ and $r/R = 0.91$. The usual silver-paint color had to be replaced with common black whiteboard ink due to regulatory restrictions. Unfortunately, this strongly reduced the marker contrast in the IR images, see Fig. 3.92 (right), and the volatile ink had to be touched up repeatedly during the test campaign. Additional markers close to the blade root helped to differentiate between individual blades, and the results shown in this section always cover the same rotor blade.

3.6.2 Hover results outside of ground effect

The first part of the tests considered OGE hover conditions with a stationary BL transition position to complement earlier hover tests in ground effect (IGE) [179]. Figure 3.93 shows the blade's IR intensity after application of a 2D projective mapping using the ten known marker positions. The dark-bluish area of the titanium protection reflects the cold sky. The other areas can be interpreted as the blade surface temperature.

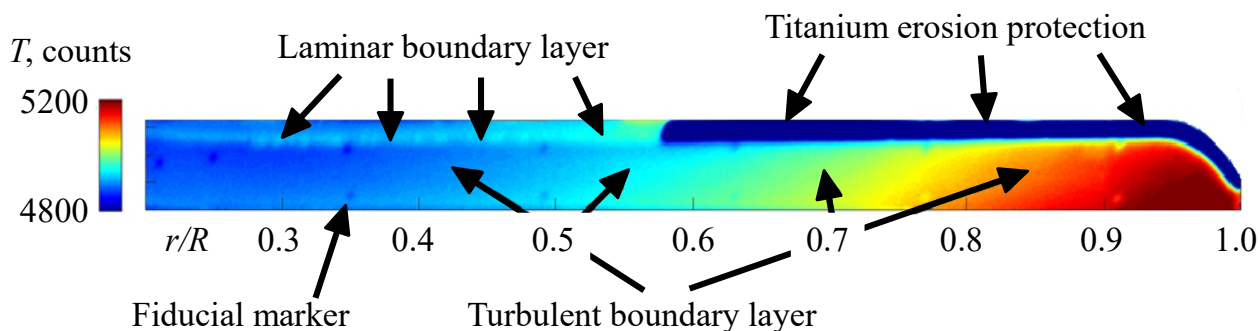


Figure 3.93: Dewarped IR image of the EC135 rotor blade in hover, azimuth $\Psi = 228^\circ$, adapted from Ref. [19].

The most prominent feature is an increasing surface temperature towards the blade tip. This is expected from the relation between the flow's recovery temperature, T_r , and the local inflow velocity, V_∞ . This relation was discussed in Sec. 3.5.2, and restating Eqs. 3.18 and 3.19 for zero forward flight velocity yields

$$T_r = T_\infty + r_C \frac{\gamma - 1}{2\gamma R_s} V_{tip}^2 \left(\frac{r}{R} \right)^2. \quad (3.20)$$

Figure 3.94 shows the predicted recovery temperature (—) for an ambient temperature of $T_\infty = 293$ K, underlining the quadratic relation between T_r and r/R . The measured infrared signal (—) qualitatively matches the prediction and underlines that T_r scales with $(r/R)^2$. The IR camera signal was not calibrated quantitatively, but comparing the left and right ordinates yields a conversion factor of about 30 mK/count.

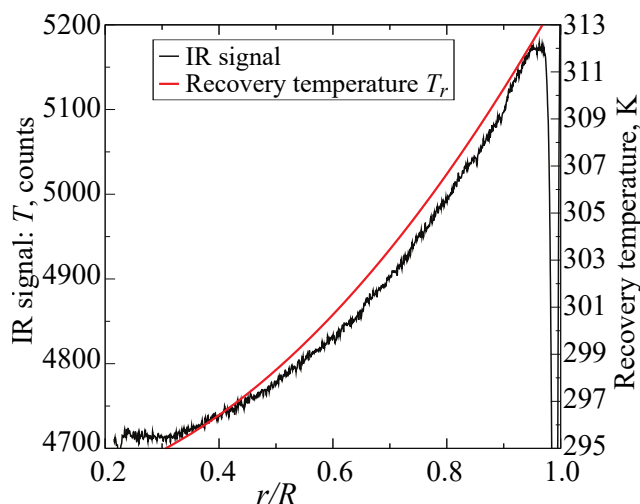


Figure 3.94: Measured temperature distribution along the rotor blade span during hover, and predicted recovery temperature [19].

In addition to the radial temperature variation, Fig. 3.93 also visualizes the boundary layer transition in the inboard part of the blade, $r/R < 0.59$. The blade is heated by sunlight from a cloudless sky, and the laminar part is at a higher temperature due to the less effective convective cooling. The estimated radiative sun flux is about 500 W/m^2 based on the test site and date. Fine structures appear in the laminar region due to turbulent wedges formed

by insect impacts, which shows that the differing IR signal is due to the boundary layer aerodynamics rather than the different materials on the blade and erosion protection tape.

Figure 3.95 (left) shows the chordwise temperature profiles at several radii between $r/R = 0.30$ and $r/R = 0.90$. The radial temperature-increase was eliminated by subtracting the local average temperature in the midchord region. The BL transition position can be identified in areas with a tape-protected leading edge, $0.30 \leq r/R \leq 0.55$, by means of a steep temperature gradient, $\partial T/\partial x < 0$. The corresponding result is shown in Fig. 3.95 (right) as a function of r/R , averaged in bins with a width of $\Delta r/R = 0.05$. The colored solid lines (—, —, —, —) correspond to the results from four consecutive IR images with increasing blade azimuth angle. The identified BL transition position is within $0.17 \leq x_{tr}/c \leq 0.23$, and the scatter of individual lines is supposed to partly originate in the limited spatial resolution of the images. The results are supported by MSES predictions, with a variation of the N -factor between $N = 5$ (—) and $N = 9$ (---) approximately spanning the experimental range. The required angle of attack, α , was provided by an OGE hover solution for the EC135 helicopter using the comprehensive code “CAMRAD”⁵. It is noted that former experiments in hover IGE conditions (▲) are approximately equivalent to the current OGE results, meaning that the reduced thrust requirements in ground effect have no significant impact on the BL transition. A notable transition delay is only observed for a ground run with reduced rpm and thrust (●).

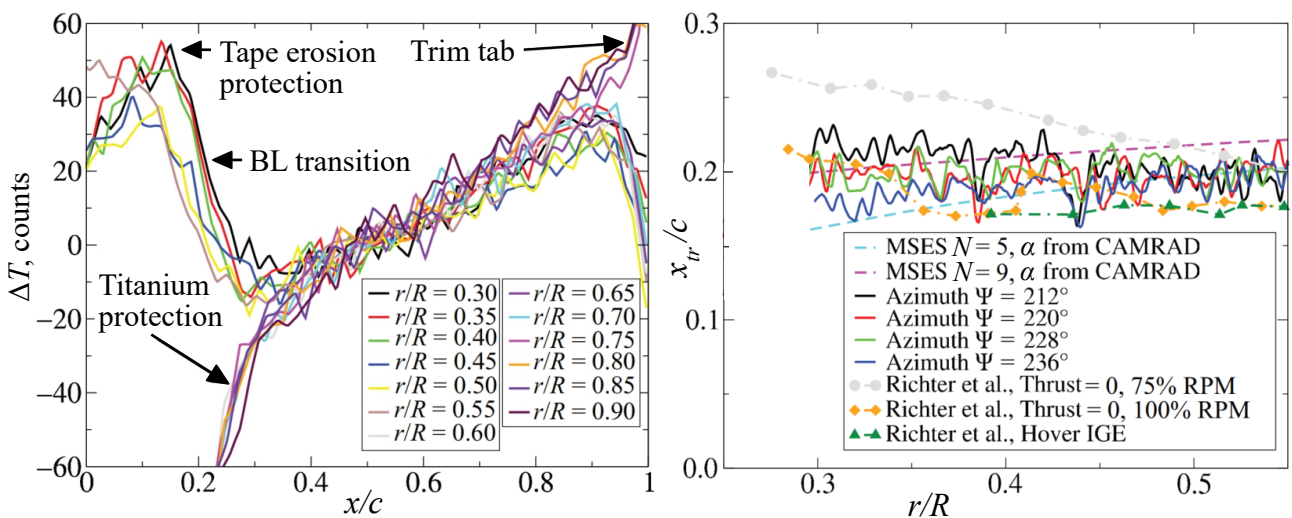


Figure 3.95: EC135 OGE hover results, normalized chordwise temperature profiles at different radii (left), and radial distribution of the transition position (right) [19].

3.6.3 Forward flight results

The forward flight test cases were accompanied by CAMRAD/MSES simulations to support the interpretation of the DIT results. Figure 3.96 shows the predicted inflow conditions in the midspan region, $r/R = 0.5$, as a function of the azimuth angle, Ψ . The radius was chosen since it is close to the radial end of the tape erosion protection at $r/R = 0.59$. The CAMRAD calculations provide a trim solution based on an aeromechanic model of the

⁵CAMRAD is a commercial tool for comprehensive aeromechanical rotorcraft simulations, similar to RCAS used in the previous section. The current CAMRAD solution was provided by Dr. Alexander Klein from Airbus helicopters.

EC135, an estimated gross mass of 2700 kg, and the flight velocity of $V_x = 41$ m/s. The local Mach number (---) varies within a range of about $0.19 < M < 0.44$, with according changes of the Reynolds number (---). The angle of attack (---) deviates from a sinusoidal shape as a result of wake interactions and blade dynamics, and a minimum of about $\alpha = 2^\circ$ is reached on the advancing side close to $\Psi = 90^\circ$. Following the argumentation of the Sec. 3.5.2, the azimuthal inflow variation between advancing and retreating sides of the rotor plane should enable DIT due to a periodic flow heating and cooling. Evaluating Eqs. 3.18 and 3.19 for the test conditions at $r/R = 0.5$ yields a peak-to-peak recovery temperature-difference of $\Delta T_r = 8.3$ K due to a peak-to-peak velocity difference of $\Delta V_\infty = 2 V_x = 82$ m/s. The changes in the blade surface temperatures are expected to be much smaller due to the thermal inertia. Figure 3.97 shows the radial temperature profile for the azimuth angles $\Psi = 0^\circ, 90^\circ, 180^\circ, 270^\circ$. The measurements were taken during an interval of 5 s and normalized to the blade root temperature to account for different viewing angles. The assumption of small azimuthal surface temperature variations is correct, with a larger slope on the advancing side (---) compared to the retreating side (---) being barely visible.

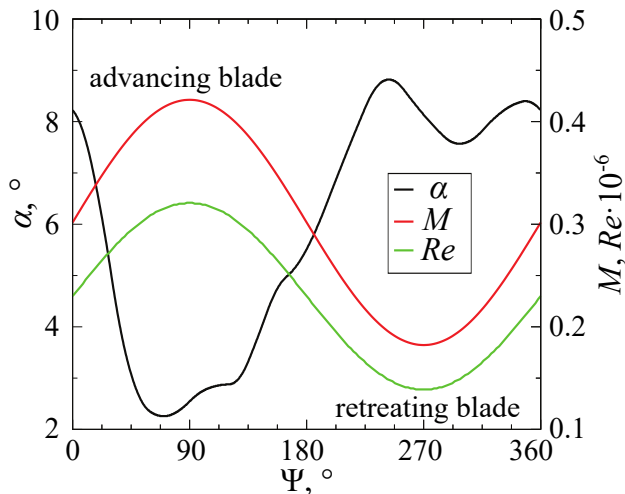


Figure 3.96: Forward flight, CAMRAD prediction of the inflow at $r/R = 0.5$.

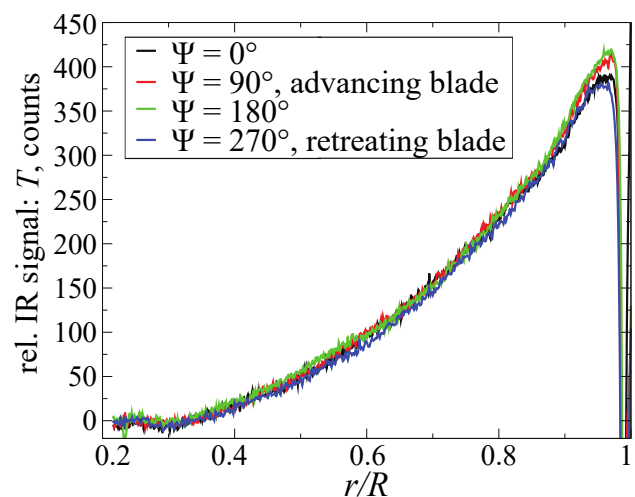


Figure 3.97: Forward flight, measured radial temperature profiles.

Figure 3.98 shows the azimuthal temperature variation at $r/R = 0.5$ taken from IR snapshots of 95 individual rotor revolutions (\bullet , left axis). The scatter is large, but a roughly sinusoidal distribution emerges. The peak-to-peak distance is about 20 counts, which can be approximately converted to 0.7 K using the scales in Fig. 3.94. Expectedly, this is only a fraction of the recovery temperature fluctuation of 8.3 K. Figure 3.98 also contains a prediction of the flow-to-surface heat convection (--- , right axis), represented by $V_\infty(T_r - T_{eq})$ as defined in Eq. 3.17. Comparing this figure to the conditions of the NASA wind tunnel test in forward flight, see Fig. 3.80, yields a much smaller peak-to-peak variation of the heat transfer $V_\infty(T_r - T_{eq})$ in the current case (about 820 K m/s versus 2470 K m/s). This is due to the smaller advance ratio (0.20 versus 0.30) and the smaller average inflow velocity at the chosen radial station (about 105 m/s versus 156 m/s). Therefore, the current DIT is expected to suffer from a low signal-to-noise ratio, even though the rotor speed is also reduced in comparison to the wind tunnel test. It is noted that the blade temperature in Figure 3.98 (\bullet) lags the convective heat transfer (---). Given the small surface temperature changes, an even higher

lag close to $\Delta\Psi = 90^\circ$ was expected (advancing blade=heating, retreating blade=cooling), which is not shown in the data for unknown reasons.

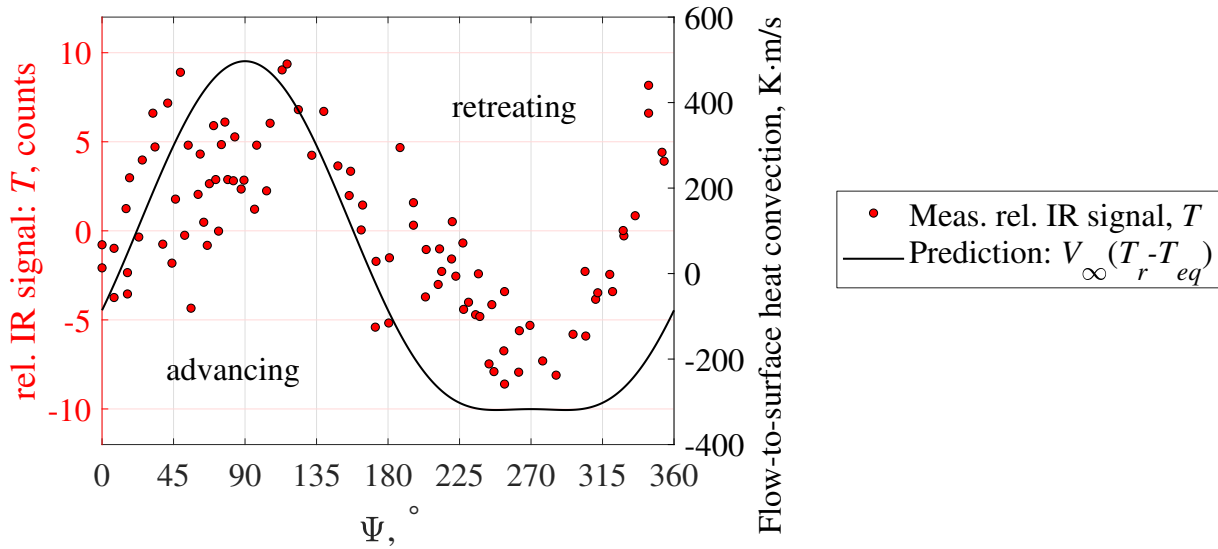


Figure 3.98: EC135 forward flight, measured relative blade temperature (left axis) and predicted flow-to-surface convective heat transfer (right axis) at $r/R=0.5$ as a function of the azimuth angle.

The differential images in the DIT processing were calculated with a separation distance of about $\Delta\Psi = 24^\circ$ or $t/T = 0.07$, corresponding to three images in a series taken at $f = 294$ Hz. This separation is larger than the recommendations implied by earlier wind-tunnel campaigns, for example see Sec. 3.1.5, increasing the signal content at the cost of a larger measurement hysteresis. Figure 3.99 shows sample differential images at azimuth angles of $\Psi = 102^\circ$ (top, $\Psi = 114^\circ$ minus $\Psi = 90^\circ$) and $\Psi = 176^\circ$ (bottom, $\Psi = 188^\circ$ minus $\Psi = 164^\circ$). At $\Psi = 102^\circ$, large parts of the blade show small or no temperature changes, but an area inboard of the titanium protection and close to the leading edge stands out, highlighted by a black box. This feature is barely visible at $\Psi = 176^\circ$.

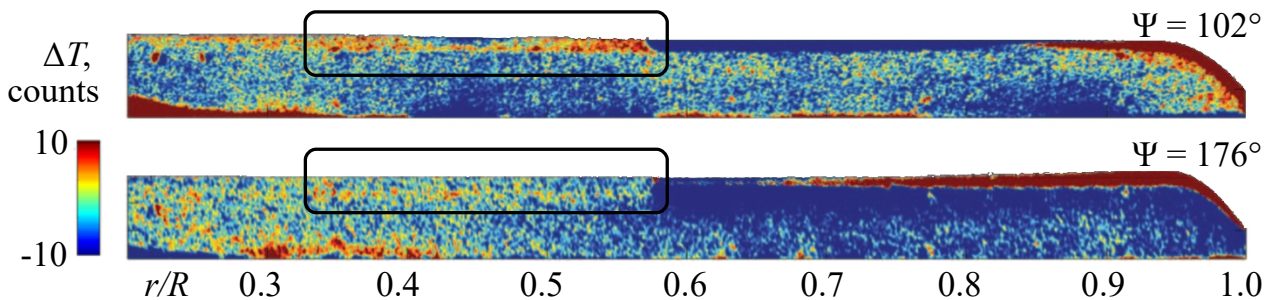


Figure 3.99: DIT images during EC135 forward flight, separation $\Delta\Psi = 24^\circ$, at average azimuth angles $\Psi = 102^\circ$ and $\Psi = 176^\circ$ (advancing blade), adapted from Ref. [19].

Chordwise profiles of the DIT images at $r/R = 0.5$, averaged over $\Delta r/R = 0.05$, are shown in Fig. 3.100. The data for $\Psi = 102^\circ$ (—) visualizes the relevant ΔT -step, which after the evaluation strategy developed during the wind-tunnel tests in Sec. 3.5 (“first positive or negative ΔT -step seen from the trailing edge”) should be assigned to the transition

position, $x_{tr}/c \approx 0.2$. Figure 3.101 shows the BL transition prediction (—) provided by the CAMRAD/MSES toolchain with an N -factor of 5. Indeed, the small local angle of attack on the advancing side results in a laminar pocket stretching up to $x_{tr}/c \approx 0.22$ and centered at $\Psi = 90^\circ$, which supports the experimental result at $\Psi = 102^\circ$. It is noted that MSES considers the “clean” airfoil without tape protection, and applies steady-state prediction algorithms to the unsteady CAMRAD inflow data. Therefore, the simulation can only be seen as a rough estimate for the true EC135 blade aerodynamics. Further experimental data points are included in Fig. 3.101, with dataset 1 (■) covering the entire azimuth over a measurement interval of 5 min, and dataset 2 (●) covering the advancing side during a second short-term interval of 2 s. Experimental data could not be extracted on the retreating side of the rotor plane, and the data on the advancing side has a large scatter bounded by about $\pm 10\%$ of the chord length.

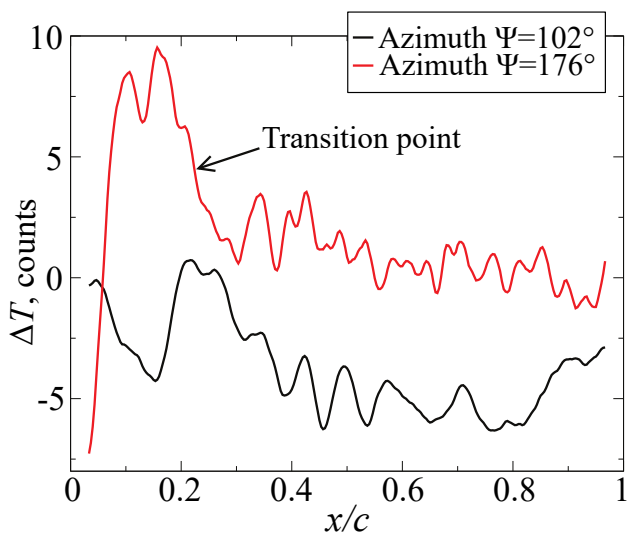


Figure 3.100: DIT results, chordwise profiles of the DIT images in Fig. 3.99 at $r/R = 0.5$.

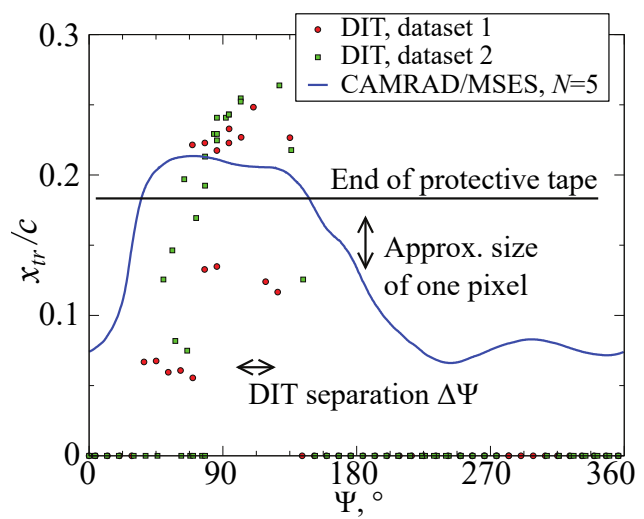


Figure 3.101: CAMRAD/MSES predicted transition positions and DIT results.

The figure also includes the average size of one pixel in the IR images, implying that the data scatter is partly connected to a low resolution, which affects the precision of image dewarping and the later ΔT -step search. In summary, the current formation-flight measurements provide valid IRT data for non-moving BL transition positions and promising DIT results for forward flight conditions, which need further validation and improvements as outlined at the beginning of this section.

3.7 DIT applied to flow separation detection

The DIT field of application is not only restricted to BL transition detection, it can be extended to investigate the dynamic stall-phenomenon. The relevance of dynamic stall in rotor applications was addressed in Sec. 2.3.3. The application of DIT to separated flow regions will be demonstrated by revisiting pitching-airfoil experiments in the 1MG and rotor blades in the RTG, also covered by Refs. [20, 33, 26].

As a side note, the current results only concern dynamic stall on the suction side of an airfoil or a rotor blade resulting from large angles of attack. Infrared thermography is also able to localize laminar separation bubbles (LSB) with turbulent reattachment, observed for steady inflow conditions and small to moderate Reynolds numbers. For example, Wynnychuk and Yarushevych [239] investigated a heated NACA 0018 airfoil at $Re=0.8 \cdot 10^5$ and $Re=1.2 \cdot 10^5$, showing that the fluid “trapped” within the steady LSB yields a very low convective heat transfer and, consequently, a wall temperature spike of several kelvin stretching over a bubble length larger than $0.3 c$. Similar results are found in Refs. [91, 150, 174], but the DIT evaluation strategies for the dynamic stall phenomenon discussed in the following sections are fundamentally different.

3.7.1 Airfoil in static and dynamic stall

In a first step, the infrared stall detection by DIT was tested on the suction side of the DSA-9A airfoil operated in the one-meter wind tunnel Göttingen (1MG). The experimental setup was adopted from the earlier test campaign on BL transition detection, including the pitch test rig, the FLIR[®] SC7750-L high-speed IR camera, and the heat spotlights mounted above the airfoil. A detailed description of the setup is given in Sec. 3.1.1 and will not be repeated here. The inflow velocity of $V_\infty = 50 \text{ m/s}$ ($M = 0.14$, $Re = 1.0 \cdot 10^6$) was also taken over, but the airfoil’s pitch angle was increased up to $\alpha = 28^\circ$ to initiate stall. The DIT results in Fig. 3.102 were calculated by subtracting two successive IR images taken at t_1 and t_2 , with an acquisition frequency of 107 Hz and an exposure time of 200 μs . The region of interest is sized 490×315 pixel and was mapped to the streamwise and spanwise coordinates (x, y) with flow from left to right. The images cover almost the entire chord, $c=0.3 \text{ m}$, and a small spanwise segment in the midspan area of the airfoil model.

Fig. 3.102 (left) was taken at a small angle of attack, $\alpha = 10^\circ$. The flow over the airfoil is fully attached and steady, with almost identical IR images. This results in a uniform near-zero DIT signal, small deviations of only a few counts (green colors) mainly originate in the readout noise of the camera sensor. In contrast, a DIT result for fully separated flow at $\alpha = 28^\circ$ is shown in Fig. 3.102 (right). A random pattern of zones with either heating (red colors) or cooling (blue colors) is observed. The pattern originates in the footprint of large-scale, three-dimensional, probably vortical flow structures within the separated flow region. The unsteady distribution alters the local flow velocity and, hence, the convective heat transfer of the radiation-heated model surface. The spatial structure of the pattern itself cannot be interpreted since it represents the tare signal between the instantaneous flow fields at t_1 and t_2 . During $t_2 - t_1 = 1/107 \text{ Hz} = 93 \text{ ms}$, the external flow covers more than 1.5 chord lengths. Hence, the temporal resolution of the high-speed IR camera is insufficient to track individual flow structures in the separation region. The current evaluation quantifies the unsteadiness of

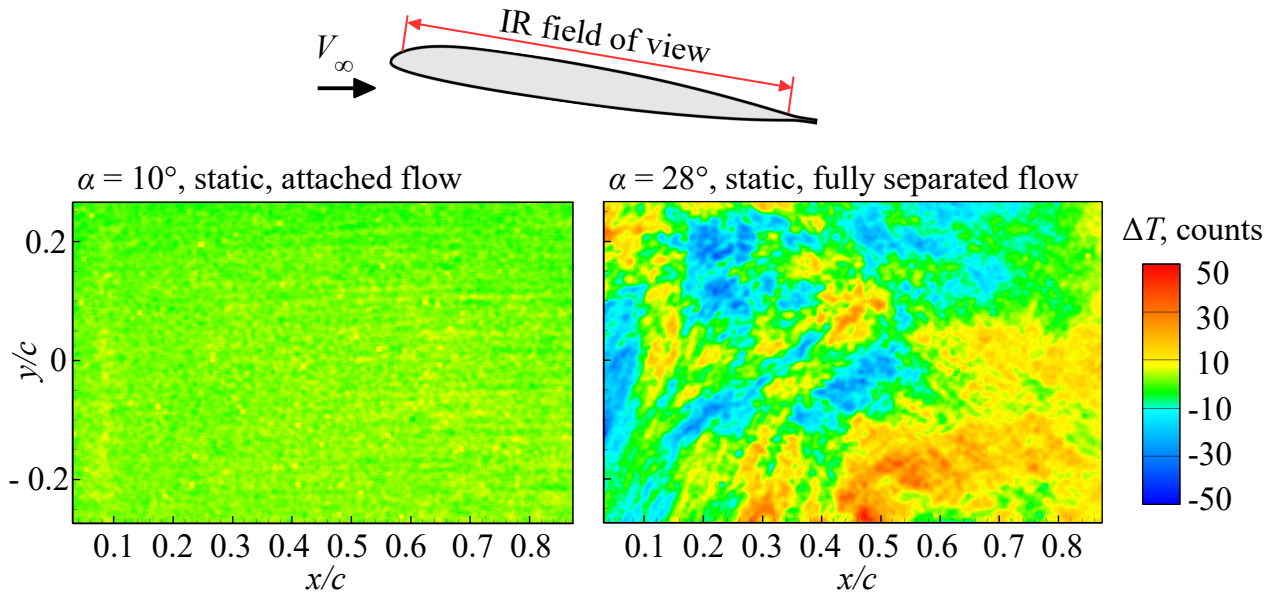


Figure 3.102: Sample DIT images of the airfoil's upper surface for static inflow conditions, attached flow (left, $\alpha = 10^\circ$) and fully stalled flow (right, $\alpha = 28^\circ$) [20].

the DIT signal using its standard deviation, σ_{DIT} , in analogy to the evaluation of the surface pressure signal, σ_{C_p} , as introduced in Sec. 3.2.2. The standard deviation can be calculated either for a spatial window selected in an individual DIT image, or for a DIT time series at a given one-pixel location, or a spatio-temporal combination of both.

Figure 3.103 shows static polar data with a stepping of $\Delta\alpha = 2^\circ$. The coefficients for lift (C_l , —) and pitching moment (C_m , —) were calculated via integration of the data from 50 Kulite[®]-equipped pressure taps as introduced in Fig. 3.1. Static stall is observed between $\alpha = 18^\circ$ and $\alpha = 20^\circ$, as indicated by a sudden collapse of the lift and a negative (nose-down) pitching moment. The increased unsteadiness of the separated flow is also accompanied by a larger standard deviation of the aerodynamic coefficients, shown by vertical error bars.

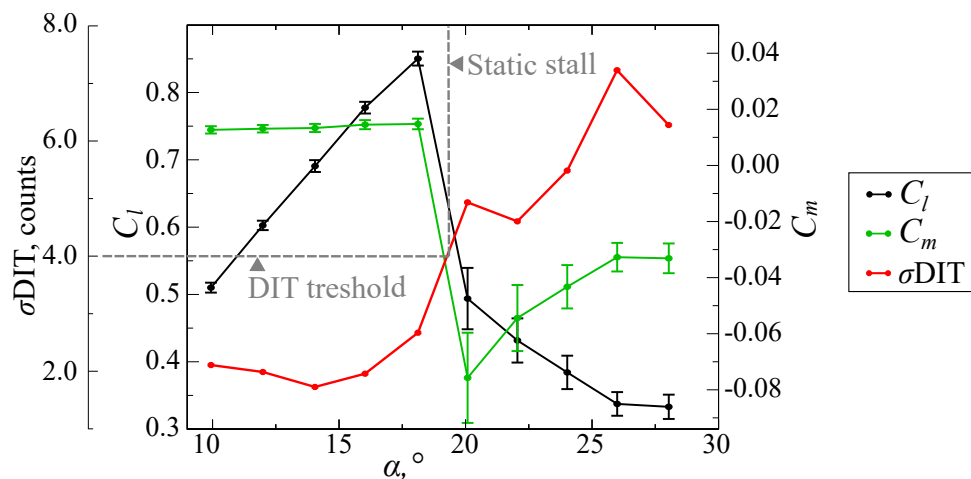


Figure 3.103: Lift and moment polar for the airfoil in static inflow conditions, and standard deviation of the DIT signal, adapted from Ref. [20].

To calculate the DIT standard deviation, the differential images were smoothed using a sliding-average low-pass filter over 3×3 pixel to dampen pixelwise sensor noise while

maintaining larger-scale aerodynamic structures, more details will be given later in this section. The standard deviation was then calculated including all pixel of a smoothed differential image, and averaged over a total of 6000 DIT samples. The resulting σ DIT-value (—) remains at a constant noise floor of about 2.0 counts during attached flow conditions, $\alpha \leq 16^\circ$, and is slightly increased at $\alpha = 18^\circ$ due to a beginning trailing edge separation also seen in a decreasing lift slope. For $\alpha \geq 18^\circ$, the flow is fully stalled, as indicated by large separation-driven σ DIT-values. The DIT stall threshold for this evaluation is around σ DIT = 4 counts.

An extensive analysis was conducted on the basis of a sinusoidal pitch motion with $\alpha = 19^\circ \pm 8^\circ$ and a frequency of $f = 2.5$ Hz ($k = 0.047$), resulting in a dynamic stall test case. Important parameters of this case are shown in Fig. 3.104 as a function of the pitch phase, tf . The pitch angle, α , is shown qualitatively in the background (—). The aerodynamic coefficients, C_l and C_m , were sampled at 8000 points per pitch cycle and phase-averaged over 100 cycles. An in-depth discussion including comparisons to the airfoil's pressure distribution can be found in Ref. [20], with the most important aspects summarized in the following, also see the annotations in Fig. 3.104. The stall process is initiated around $tf = 0.3$, well before reaching the maximum pitch at $tf = 0.5$, with a beginning trailing edge separation and a consequent moment stall. At this point, the lift is still increasing. A dynamic stall vortex is then generated close to the leading edge, yielding an increase of the lift slope and a consecutive C_l -maximum of about 1.2 at $tf = 0.35$, which is larger than the static maximum of about $C_l = 0.9$. The dynamic stall vortex then convects towards the trailing edge, resulting in a characteristic nose-down pitch spike of $C_m = -0.175$, which exceeds the static value by a factor of two. The flow over the airfoil then enters a fully separated state similar to static stall, before reattachment starts at about $tf = 0.75$.

Fig. 3.104 also shows the phase-averaged surface temperature, T (—), calculated from a total of 6000 IR images. Since the pitch frequency and the camera frequency were not synchronized, the images were sorted by phase into 300 bins during the data post-processing. The surface undergoes distinct temperature changes during the pitch cycle, with a peak-to-peak distance of 120 counts (about 1.3 K). The convective heat transfer from the airfoil's surface into the flow is decreased during the fully separated phase, yielding an increasing surface temperature. Fig. 3.104 implies that an IR stall detection is also possible solely based the surface temperature itself, without applying differential methods. However, an unambiguous interpretation of the T -signal (—) requires a fine resolution of the pitch phase, whereas DIT can differentiate between attached and separated flow only using two instantaneous samples as shown in Fig. 3.102.

Figure 3.105 shows the phase-resolved standard deviation of DIT (—). The differential images were calculated from pairs of successive IR images, low-pass filtered, and sorted according to their average pitch phase into the same 300 bins as used in the previous figure. The σ DIT-signal can be divided into a high level (up to 12 counts) during flow separation and reattachment, a medium level during fully separated flow (~ 8 counts), and a low level during attached flow (~ 4 counts). The three regimes compare well with the analysis of C_l and C_m , and a threshold level of e.g. 6 counts correctly identifies begin and end of stall at $tf = 0.3$ and $tf = 0.9$, respectively. It is noted that the attached-flow noise level of 4 counts is twice as large as in the static test case, see Fig. 3.103, supposedly due to cycle-to-cycle variations or camera vibrations in the pitch-oscillating test case. Hence, the threshold level should be adapted to

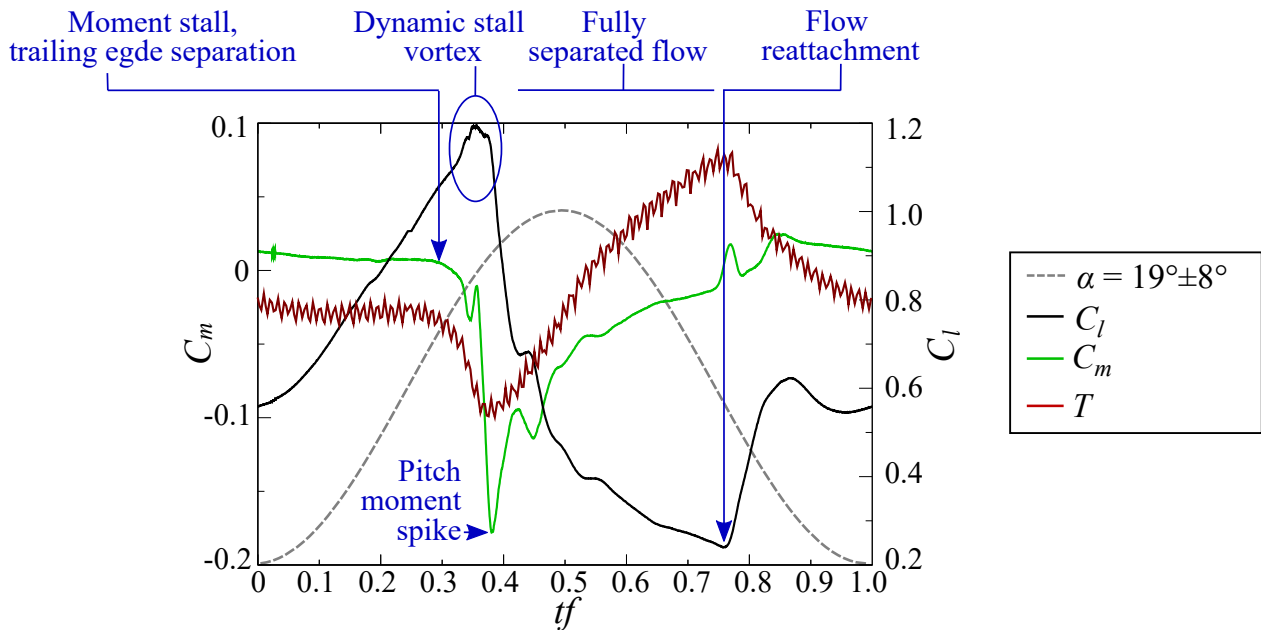


Figure 3.104: Phase-averaged lift and moment coefficients, and phase averaged surface temperature, for a dynamic stall test case with $\alpha = 19^\circ \pm 8^\circ$ and $f = 2.5$ Hz [20].

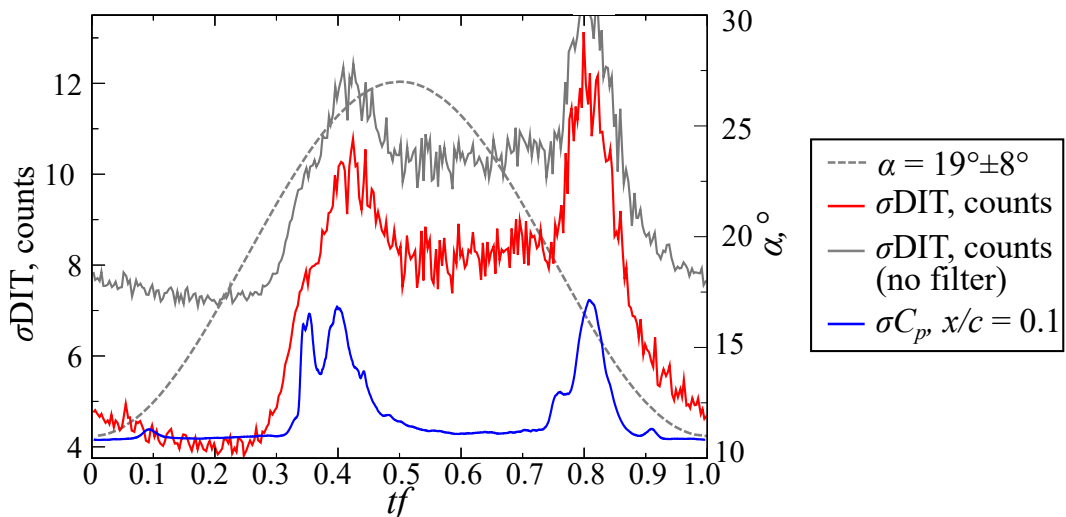


Figure 3.105: Phase-resolved standard deviation of the DIT signal, σ_{DIT} , and the surface pressure signal, σ_{C_p} , at $x/c = 0.1$ for the test case shown in Fig. 3.104 [20].

the specific test case, which will be supported by later results for different pitch frequencies.

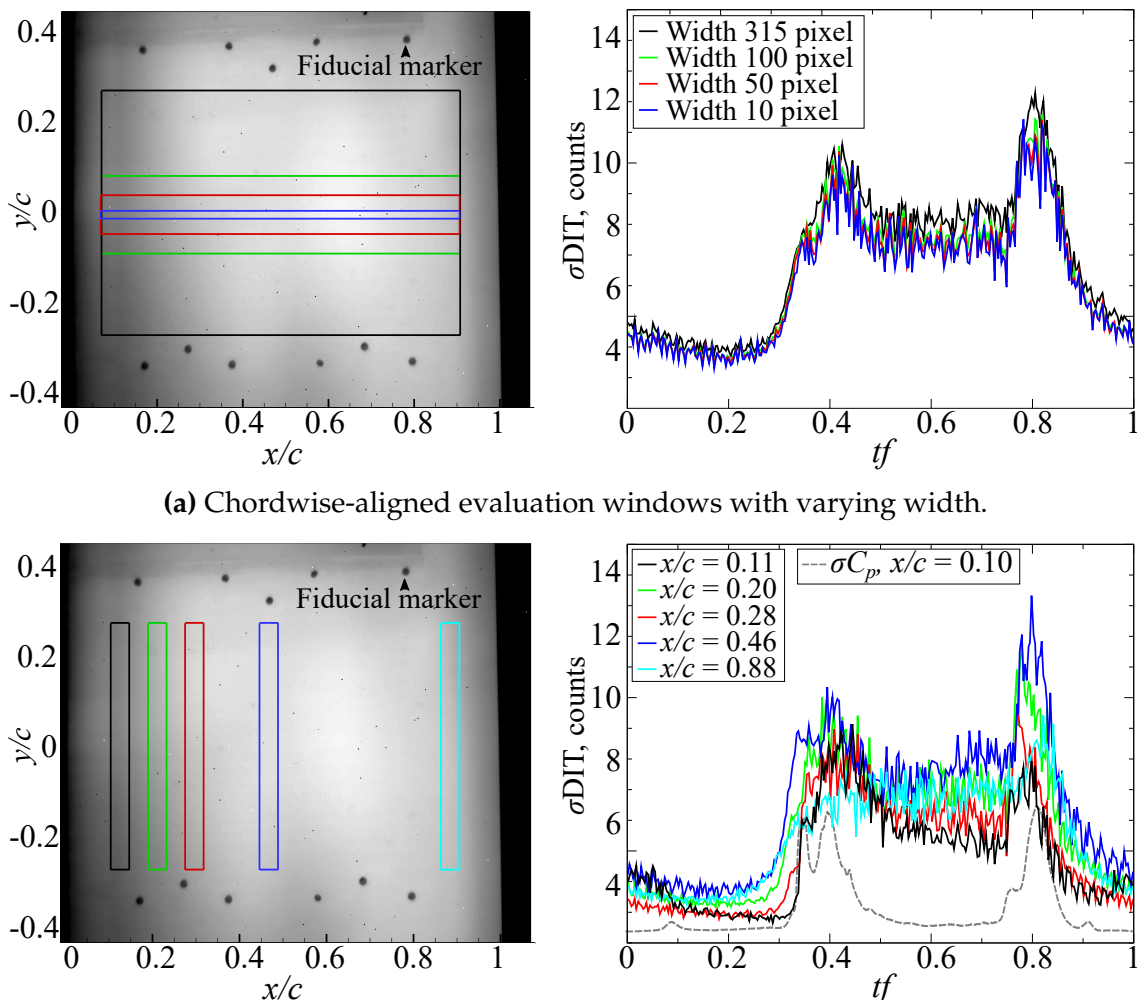
Figure 3.105 also includes a second DIT result (—) which underwent the same processing but skipped the low-pass sliding-average filter in 3×3 pixel windows. The flow features can still be identified, but the noise floor is almost doubled, and the offset between attached and separated flow regimes is decreased. This shows that the filter effectively separates random small-scale camera noise from large-scale aerodynamic structures. Several additional filter strategies were tested in Ref. [20], with no significant further improvement over the current processing.

The filtered σ_{DIT} -signal (—) is strikingly similar to the well-established σ_{C_p} -method, which is shown in Fig. 3.105 for a sample pressure tap position close to the leading edge ($x/c = 0.1$, —). Despite accounting for very different quantities, the spatial variation of the

3.7. DIT applied to flow separation detection

surface temperature distribution versus the cycle-to-cycle variation of the surface pressure signal, both methods characterize the dynamic stall process in a very similar way. The gradients in σC_p at the start and end of stall are higher than seen in σ DIT. This is an effect of the point-wise nature of the pressure tap compared to the large spatial area covered by the IR images, which implies to use smaller sub-windows for a more localized DIT analysis.

The spanwise width of the entire DIT evaluation window is 315 pixel or about $\Delta y = 0.15$ m, limited by silver-paint fiducial marker. In a first step, this width was reduced in three steps to only 10 pixel, see Fig. 3.106(a). The corresponding σ DIT-results are almost identical, even though the smallest width (—) has a slightly noisier signal compared to the largest width (—). Hence, the stall behavior in the central part of the airfoil model is two-dimensional and independent of the covered spanwise range, at least when looking at statistics and not at instantaneous flow structures. On the other hand, smaller window slices enable to detect a three-dimensional behavior if present, which will be shown in the next section by means of a rotor dynamic stall-map.



(a) Chordwise-aligned evaluation windows with varying width.

(b) Spanwise-aligned evaluation windows at different chordwise positions, the σC_p -result is repeated qualitatively from Fig. 3.105.

Figure 3.106: Effect of windowing on the DIT separation analysis [20].

The stall evaluation in Fig. 3.106(b) uses thin spanwise-aligned slots at different chordwise position between $x/c=0.11$ and $x/c=0.88$. In this case, the individual σ DIT-signals show a larger deviation over the pitch phase tf . As expected, the window closest to the leading edge (—) stalls later and reattaches earlier in comparison to windows closer to the trailing edge (— and —) as expected from the airfoil's stall behavior. The better localization of the evaluation windows also yields steeper gradients of σ DIT in the separation and reattachment area. In particular, the stall behavior seen by σ DIT at $x/c = 0.11$ (—) is now in very good agreement with the σC_p -result of the pressure tap at $x/c = 0.10$ (—), which is an improvement over the large DIT window applied in Fig. 3.105. In summary, adapting smaller evaluation windows to the local flow behavior is very useful if the signal-to-noise ratio is sufficient, depending mostly on the image quality and statistics.

In a last step, the frequency of the sinusoidal pitch motion with $\alpha = 19^\circ \pm 8^\circ$ was varied between 1.25 Hz, 2.5 Hz, and 5.0 Hz ($k=0.024, 0.047, 0.094$), see Fig. 3.107. A comparison of the C_l -distributions (—, —, —) shows that both flow separation and flow reattachment are delayed towards higher pitch phases, tf , with increasing pitch frequency, f , indicating a larger hysteresis. Also, the maximum value of C_l increases, which is the expected behavior of the dynamic stall process. The σ DIT-signals (—, —, —) were evaluated for the entire field of view and confirm the increasing hysteresis for an increasing pitch frequency. It is noted that due to the odd camera frequency of 107 Hz, the 6000 IR images taken for each test point are statistically distributed over the entire pitch phase, yielding a constant phase resolution after phase binning despite the different pitch frequencies.

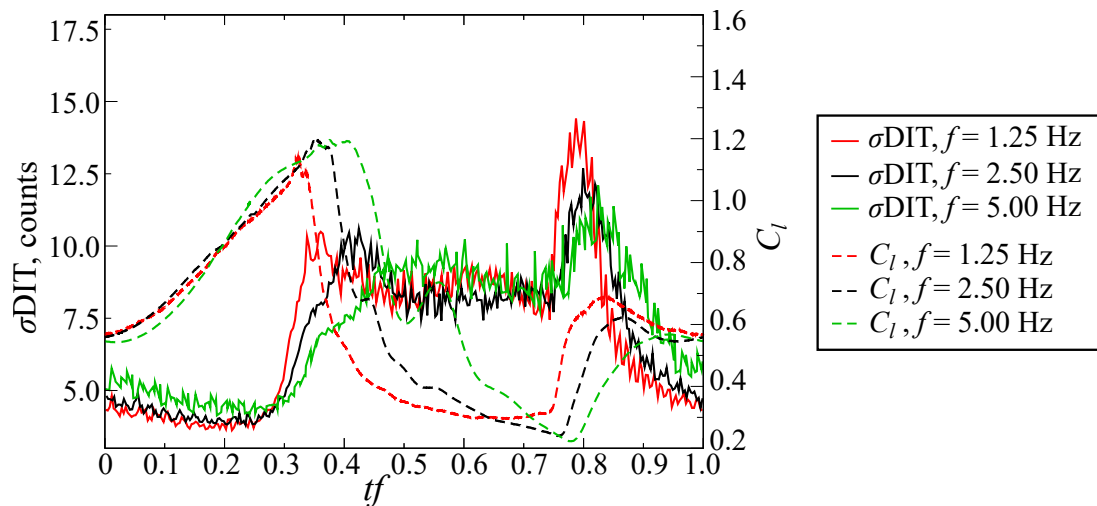


Figure 3.107: Frequency effect on the dynamic stall process as seen by the DIT method [20].

Fig. 3.107 also shows that the DIT peak-to-peak distance by tendency decreases for an increasing pitch frequency. The ratio between the maximum and the minimum of σ DIT is 3.6 for $f = 1.25$ Hz, 3.1 for $f = 2.5$ Hz, and 2.5 for $f = 5.0$ Hz. This behavior is plausible, since the airfoil's temperature fluctuations will approach zero for $f \rightarrow \infty$ due to the finite thermal responsiveness of the material. However, Fig. 3.107 also indicates that stall should still be identifiable when increasing the pitch frequency beyond 5 Hz, motivating the application of DIT stall detection to a model rotor at $f = 23.6$ Hz in the next section.

3.7.2 Small-scale rotor in dynamic stall

The dynamic stall process was visualized via DIT on a model rotor with a diameter of $D = 1.3$ m, operated at the rotor test stand Göttingen (RTG), see Fig. 3.108. The main goal of the test was to demonstrate that DIT is able to produce “stall maps” of the RTG rotor without further preparation or instrumentation of the CFRP rotor blades. The overall test setup is similar to the BL transition campaign as described extensively in Sec. 3.4.1. In contrast to the earlier four-bladed configuration and Fig. 3.108, the current rotor was equipped with only two blades, and the axial wind-tunnel inflow was reduced from $V_\infty = 4.9$ m/s to $V_\infty = 2.4$ m/s.

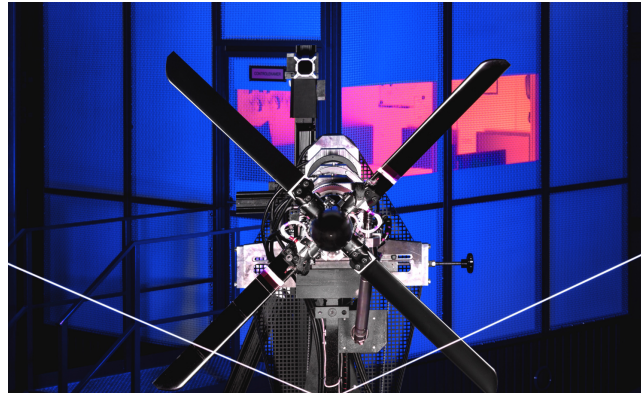


Figure 3.108: Rotor test stand Göttingen viewed in downstream direction, the control room is visible in the background. For the dynamic stall tests, two rotor blades were removed.

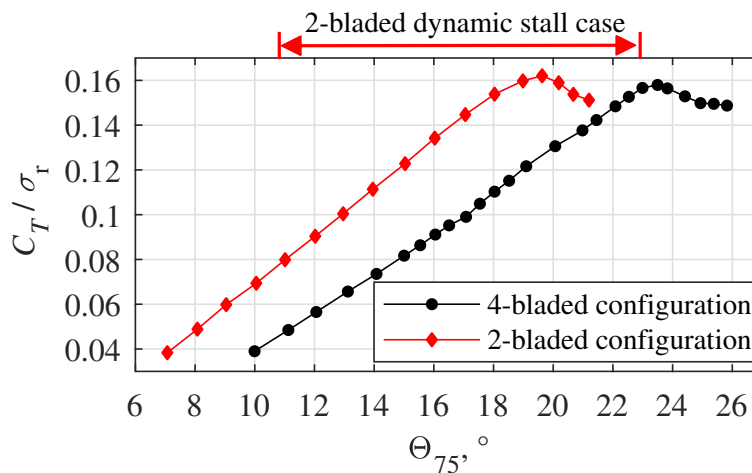


Figure 3.109: Static polar data for the RTG rotor, blade loading C_T / σ_r as function of the blade pitch angle, Θ , for the 4-bladed configuration of Sec. 3.4.1 and the 2-bladed configuration of the current section.

The rotational frequency of 23.6 Hz ($M_{75} = 0.21$, $Re_{75} = 3.2 \cdot 10^5$) and the blade geometry were kept, including the DSA-9A airfoil and the negative twist of -6.9° (also see Fig. 3.58). The reduction of both the blade number and the axial inflow velocity decreases the induced velocity in the rotor plane, which increases the aerodynamic angle of attack for a given geometric blade pitch. This is shown by the polar data in Fig. 3.109. Both lift polars stall at the same blade loading of $C_T / \sigma_r = 0.16$, corresponding to a thrust of about 84 N per blade, but the current 2-bladed configuration (—) has a smaller geometric stall pitch angle of $\Theta_{75} = 19.5^\circ$ compared to $\Theta_{75} = 23.5^\circ$ for the four-bladed configuration (—). A cyclic swashplate setting

with a sinusoidal blade pitch motion of $\Theta_{75} = 16.8^\circ \pm 6.0^\circ$ was selected for the DIT dynamic stall tests, during which the static stall angle is exceeded by $\Delta\Theta = 3.3^\circ$. This case has an average thrust of 73 N per blade, yielding an average blade loading of $C_T/\sigma_r = 0.14$.

The tests used DLR's FLIR[®] SC7750-L high-speed IR camera with a sensor size of 640×512 pixel, see Fig. 3.4 and corresponding description. A rotating mirror after Sec. 3.4.2 was installed, allowing for image exposure times of 200 μ s without motion blur. A sample image is shown in Fig. 3.110 (top). The resolution is about 2.8 pixel/mm yielding 200 pixel along the chord. Similar to earlier studies, several silver-paint fiducial markers were applied to the blade surface, allowing an image alignment to counter random timing jitter, blade lead-lag motion, or vibrations of the optical system before image subtraction. The IR camera was triggered to take one image of the same blade for every rotor revolution, since the statistical σ_{DIT} -evaluation of the flow unsteadiness also works on the basis of cycle-to-cycle deviations instead of differences developing within a single rotor cycle. A total of 1487 IR images was acquired, and the local pitch phase, tf , within the camera's fixed field of view was slowly increased from 0 to 1 during this image series using the RTG's swashplate actuation. After image dewarping, the differential images were then calculated from two successive rotor revolutions, and a sliding average-filter sized 3×3 pixel was applied to separate unsteady aerodynamic features from camera noise as described in the previous section.

A sketch of the rotor blade in the camera's field of view is given in Fig. 3.110 (bottom), with data available over the entire chord and between about $r/R=0.7$ and $r/R=1.0$.

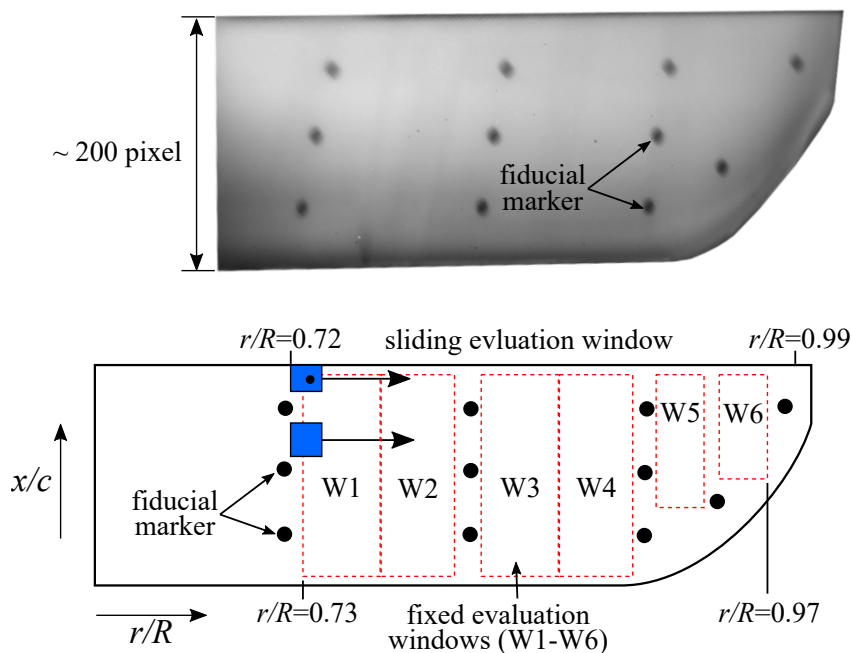


Figure 3.110: Raw IR image (top), sketch of the RTG blade planform and DIT dynamic stall evaluation windows (bottom), adapted from [26].

Six comparably large windows, labeled "W1" to "W6" in Fig. 3.110 (bottom), were selected for an initial analysis. The corresponding standard deviations of the differential temperature, σ_{DIT} , are shown in Fig. 3.111 as a function of the pitch phase, tf . Successive windows are offset by 5 counts. The signals were filtered with a sliding average covering 11 differential images (0.7% of the pitch cycle), creating a similar smoothing effect as the phase-binning in the

previous section. The blade pitch angle (—) is included qualitatively in the background for reference. During the upstroke motion of the pitch cycle, $0 \leq tf \leq 0.5$, all σ_{DIT} -signals agree on a constant noise floor around 5 counts representing attached flow conditions. Increased fluctuation levels indicating dynamic stall begin at the most inboard window (W1) close to the pitch motion reversal, $tf = 0.5$. Stall onset is delayed at larger radii, for example occurring at $tf = 0.6$ in W6. This effect is expected due to the increasing influence of the blade tip vortex, which reduces the effective angle of attack in the tip region, as also seen by a delayed BL transition in the transition maps of Fig. 3.69. Vice versa, flow reattachment starts at the blade tip ($tf = 0.8$ in W6) and is delayed towards the blade root ($tf = 0.9$ in W1). All six evaluation windows show a significant hysteresis with respect to the pitch curve. The current stall behavior is less severe and covers a smaller portion of the entire pitch cycle in comparison to the airfoil test of the previous section, in which dynamic stall was initiated well before the pitch motion reversal, and in which a dynamic stall-vortex caused a notable spikes in both σ_{DIT} and the pitching moment⁶.

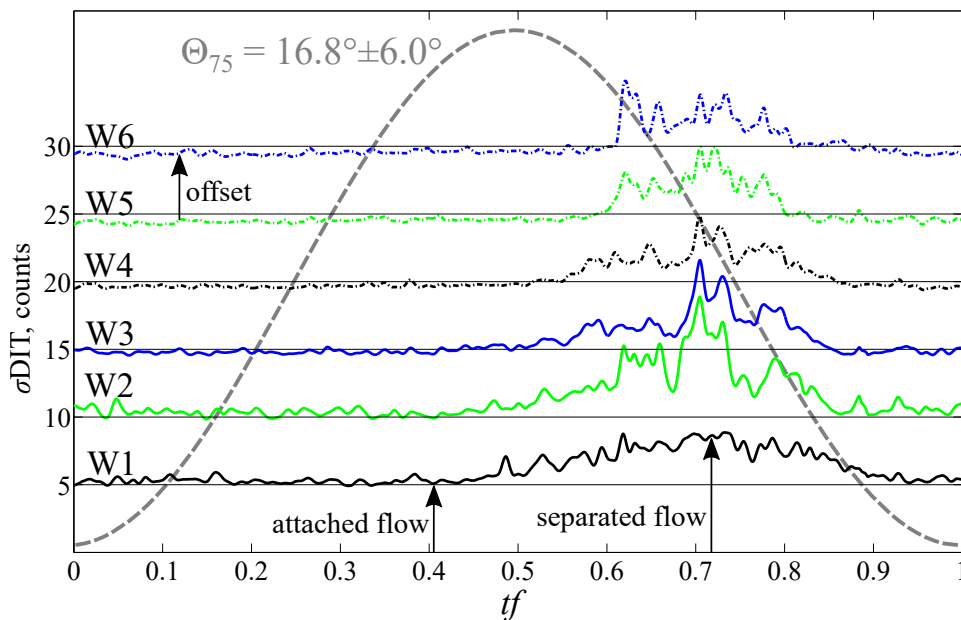


Figure 3.111: DIT standard deviation, σ_{DIT} , in the six fixed interrogation windows W1 to W6 as a function of the pitch phase tf . Successive curves are offset by 5 counts.

The different results of the windows W1 to W6 motivate a closer look at the stall behavior as a function of the radial coordinate. Therefore, a sliding window was defined by combining two rectangular regions as shown in Fig. 3.110 (■). The sliding window can be moved over the entire radial range and avoids the area of fiducial markers. A sample result for an evaluation centered at $r/R = 0.77$ is shown in Fig. 3.112 (—). The σ_{DIT} -signal was normalized so that the minimum is 0 and the maximum is 1. As expected, the smaller evaluation window size yields a higher noise level. The separation-related large values in the second half of the pitch cycle are still clearly visible, but the selection of a threshold value between attached

⁶Using the well-adopted categorization by McCroskey [146] or later refinements e.g. by Mulleners and Raffel [151], the 2D-airfoil test case can be termed “deep stall”. As argued by Schwermer [197], the current RTG rotor test case includes features of both “light stall” and “deep stall” depending on the radial position and the chosen argumentation. Schwermer concluded that a strict categorization is probably not useful for a 3D stall phenomenon.

and separated flow conditions is less obvious. The subsequent analysis uses a value halfway between the minimum and the maximum of σ_{DIT} , or 0.50 in normalized units (- - -). This choice is arbitrary, but it compares rather well to a σ_{C_p} -stall analysis using a surface pressure tap located at the same radial position, $r/R=0.77$, but closer to the leading edge, $x/c=0.31$. It is noted that the corresponding Kulite[®] pressure sensor acquired data over the entire test point, 63 s, and the result (—) is less noisy compared to the infrared signal. The flow separation as identified by σ_{DIT} (■) at least approximately corresponds to high levels of σ_{C_p} , but the overall shape of the fluctuation signal is very different. Even though the DIT result does not allow the identification of begin and end of stall with a precision better than about 5% tf , the agreement was considered to be good enough to calculate the entire dynamic stall map by traversing the center of the sliding window between $r/R=0.72$ and $r/R=0.99$.

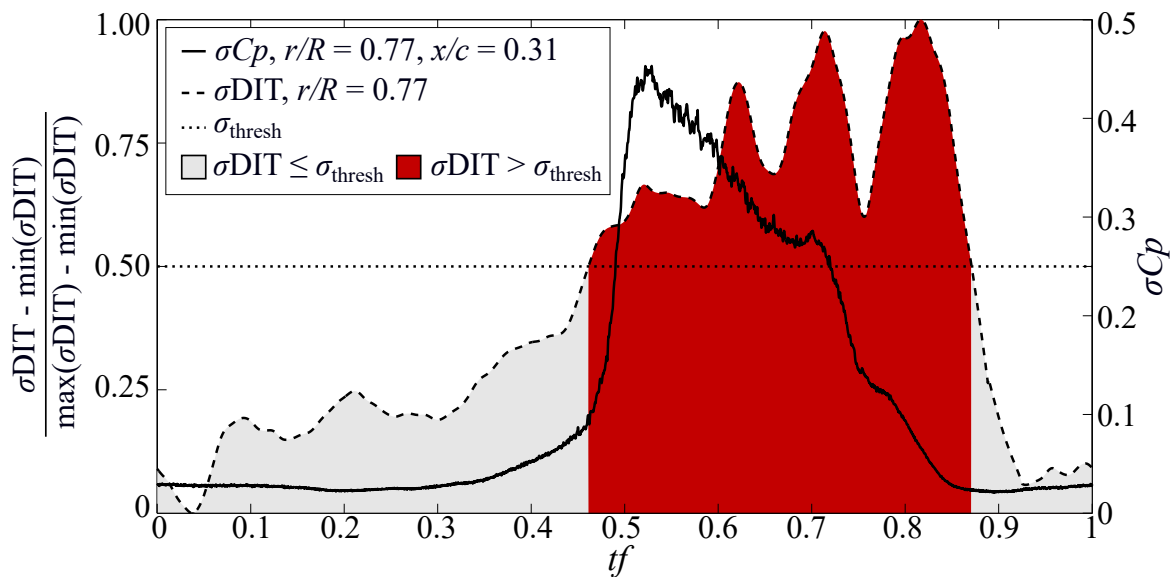


Figure 3.112: Comparison of the σ_{DIT} -signal for the sliding evaluation windows and the σ_{C_p} -signal, both at $r/R=0.77$, adapted from [26].

This stall map is shown in Fig. 3.113. The layout of the figure is the same as the RTG boundary layer transition map in Fig. 3.69. The map confirms the hysteresis of the dynamic stall process, as the center of the separated flow is delayed in relation to the maximum pitch angle at $tf = 0.5$. The stall reduction in the blade tip area due to the presence of the tip vortex is also confirmed by Fig. 3.113. The current result is similar to Schwermer's stall map [197] acquired for the test same case but using a tuft visualization, even though the flow perturbation created by the tufts triggers a slightly earlier flow separation, also in comparison to σ_{C_p} . The jagged and unsteady dividing line between attached flow and separated flow in Fig. 3.113 is considered to result from the DIT data quality and not from aerodynamics. Also, DIT is not able to identify individual structures or phases of the stall process, as for example the occurrence of a dynamic stall vortex as seen in the pressure tap data.

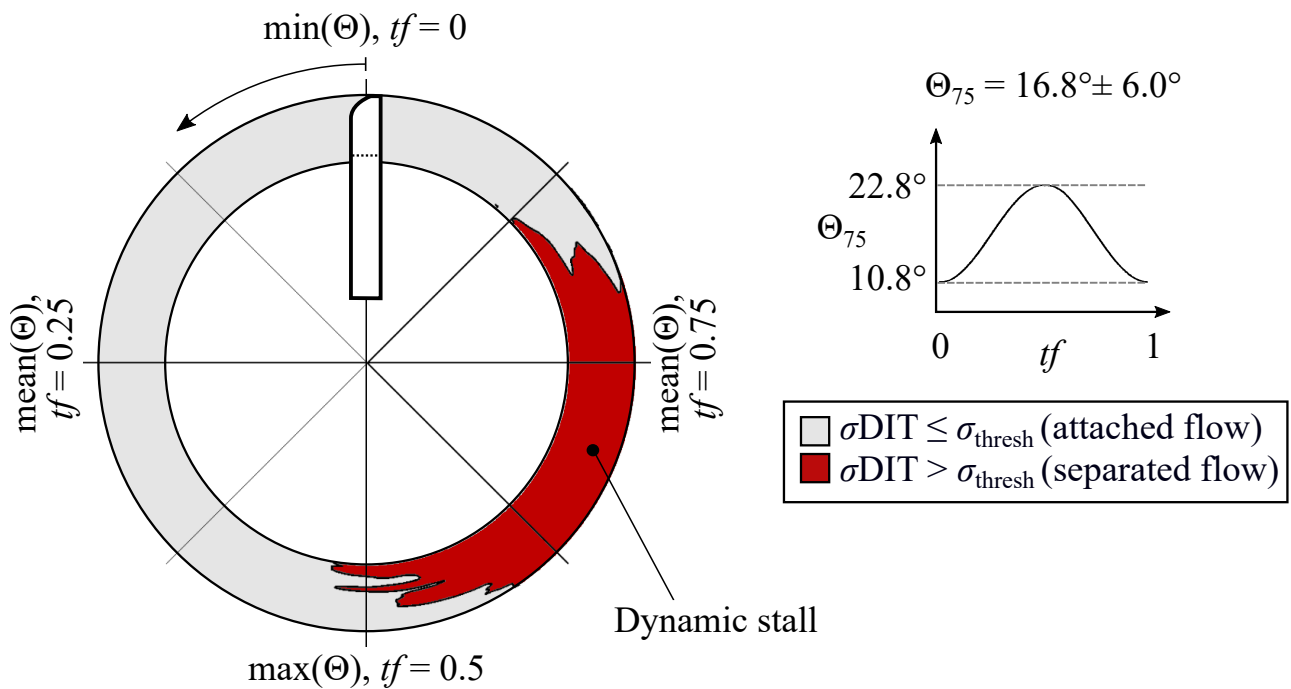


Figure 3.113: Dynamic stall map of the RTG test case, adapted from [26].

4 Conclusions and outlook

The current work presented recent progress in the experimental analysis of unsteady aerodynamic phenomena using optical measurement techniques. A focus was set on the development of differential infrared thermography (DIT) at the “helicopter aerodynamics” department of the Institute of Aerodynamics and Flow Technology at the German Aerospace Center (DLR) Göttingen. DIT is able to quantify the moving position of the laminar-turbulent transition of a boundary layer (BL) using short-exposure infrared images of the wetted surface. The method was demonstrated on multiple scales ranging from laboratory experiments to large-scale wind tunnel tests and flight experiments. The main conclusions and results can be summarized as follows:

- Similar to “standard” infrared thermography, DIT is based on a visualization of the differing convective heat transfer in laminar and turbulent regions of the BL. This requires an insulating surface material and a fluid-to-surface temperature difference, for example, $\Delta T = 5 \text{ K} - 10 \text{ K}$. The difference can be established by surface heating or by flow cooling in laboratory or wind tunnel environments. For a rotor in edgewise flight at a sufficiently large advance ratio, the flow’s recovery temperature difference between the advancing and retreating sides can also be utilized, but the data evaluation must be adapted. Untreated carbon or glass composite surfaces are suitable, which is favorable for many wind tunnel models or full-scale helicopter rotor blades. Additional insulating surface coatings can be applied to increase the signal-to-noise ratio.
- Steady-state infrared thermography evaluations fail in unsteady flow conditions due to the thermal inertia of the surface, which decouples the temperature distribution from the flow field. However, local peaks of the temperature gradient within the uppermost surface layer ($< 1 \text{ mm}$) can still be attributed to the motion of the BL transition position. The underlying DIT principle was confirmed using aerothermal simulations of the surface temperature distribution.
- The gradient-based DIT analysis requires IR images taken with a high time- or phase-resolution and with small image exposure times. The signal-to-noise ratio of current high-speed IR cameras is sufficient for exposure times down to about $50 \mu\text{s} - 200 \mu\text{s}$, which effectively “freeze” the flow situation. Optical tracking devices, for example rotating mirrors, can be used to reduce the motion blur of rotor blades viewed from fixed camera positions.
- The DIT method was successfully applied to pitch-oscillating airfoil tests in a smaller wind tunnel (1MG) and in a large industrial wind tunnel (TWG). Rotor tests were

conducted with the small-scale “RTG” rotor ($D = 1.3$ m) in hover-like conditions and in a laboratory environment, as well as with the large-scale “PSP” rotor ($D = 3.4$ m) in trimmed edgewise flight at an advance ratio of $\mu = 0.3$.

- The DIT results agree well with established transition analyses using fast-response pressure transducers and hot-film sensors. The thermal inertia of the wetted surface introduces an additional, measurement-related lag. For technically relevant airfoil/blade pitch rates of several hundred degrees per second, this lag results in a hysteresis of about 1° to 1.5° between the up- and downstroke of the motion, in addition to the “true” aerodynamic hysteresis.
- Within the demonstrated level of measurement uncertainty, DIT was able to produce space- and phase-resolved “transition maps” with a comparably small effort for the preparation and evaluation of the experiments. This is a decisive advantage over point-wise pressure transducers or hot-film sensors, which require a sensor integration into the rotor blade structure, and a corresponding telemetry system.
- The RTG results agree well with a numerical transition map using the “rotor blade transition toolbox” as an add-on to the DLR TAU code. The tests with the PSP rotor at the Langley Research Center were conducted within the framework of the NASA-DLR agreement on “experimental optical methods applied to rotorcraft”. NASA’s accompanying high-fidelity CFD simulations led to the first experimental-numerical tool validation for BL transition on a large rotor in forward flight.
- DIT was also applied in a helicopter flight test campaign, with DLR’s Bo105 helicopter serving as a camera platform to observe the EC135 main rotor in forward flight. The test must be seen as a proof-of-concept. The flow’s differing recovery temperatures on the advancing and retreating sides, acting as a driver of the BL visualization, were confirmed. Also, a transition position close to the leading edge was observed over parts of the rotor plane. The laminar flow length is comparably small due to surface steps caused by the erosion protection covering the blade’s leading edge. An in-depth analysis of the DIT results is difficult due to large observation distances, oblique viewing angles, and the resulting low spatial resolution of the infrared images.
- The development of DIT can be transferred to other fields of application in addition to a moving BL transition position. For example, it was shown that the differential image-principle can also be applied to (quasi)-steady inflow conditions during pitch angle sweeps. Even though standard infrared thermography is an established method, DIT offers the advantage of a very unambiguous result well-suited for an automatization of the post-processing. Furthermore, it was shown that differential infrared images can clearly detect the dynamic stall process, which is also relevant for helicopter rotor flows.
- DIT proved to be a very useful and relevant addition to the family of optical measurement techniques applicable to rotor aerodynamics, for example, including background-oriented schlieren visualization, particle image velocimetry, optical deformation measurements, etc.

Even though the DIT principle itself has reached a high level of maturity over the last few years, several trends and improvements are envisioned for the future.

The increasing performance of infrared image sensor technology in terms of image resolution and signal-to-noise ratio is monitored closely, opening new opportunities particularly for the result quality during flight tests. Also, a systematic study of new helicopter rotor blade designs with a possibly larger laminar flow length and a better conformal integration of erosion protection is encouraged. An alternative to flight tests could be given by full-scale whirl tower tests as conducted by helicopter manufacturers, and as demonstrated in the current blade deformation study. However, the possibility to investigate unsteady aerodynamics on whirl towers is limited by the lack of an edgewise inflow, and by the maximum allowable rotor head moment limiting a cyclic pitch input.

The DIT data acquired during the NASA PSP rotor tests, and the subsequent validation of CFD transition prediction, will hopefully result in a better simulation fidelity, and trigger further investigations. An application of the DIT method to steady-state transition measurements for hover prediction workshops is planned for mid-2022.

Recently, several research groups including the “experimental methods”-department at DLR Göttingen demonstrated progress in the application of unsteady temperature- or pressure-sensitive paint, which also covered a measurement campaign at the RTG test stand. In comparison to DIT, the higher experimental effort comprising the application and excitation of the sensitive paint is rewarded by a higher result quality, which is predominantly connected to the higher performance of visible-light image sensors over infrared image sensors. Analysis techniques for image time series of unsteady aerodynamic phenomena can partly be shared between both measurement approaches.

5 References

5.1 Reviewed journal publications (first authorship)

- [1] C. C. Wolf, A. Weiss, C. Schwarz, J. N. Braukmann, S. Koch, and M. Raffel, "Wake Unsteadiness and Tip Vortex System of Full-Scale Helicopters in Ground Effect," *Journal of the American Helicopter Society*, vol. 67, no. 1, 2022. DOI: [10.4050/JAHS.67.012010](https://doi.org/10.4050/JAHS.67.012010).
- [2] C. C. Wolf, A. D. Gardner, and M. Raffel, "Infrared Thermography for Boundary Layer Transition Measurements," *Measurement Science and Technology*, vol. 31, no. 11, 2020. DOI: [10.1088/1361-6501/aba070](https://doi.org/10.1088/1361-6501/aba070).
- [3] C. C. Wolf, J. N. Braukmann, W. Stauber, T. Schwermer, and M. Raffel, "The Tip Vortex System of a Four-Bladed Rotor in Dynamic Stall Conditions," *Journal of the American Helicopter Society*, vol. 64, no. 2, 2019. DOI: [10.4050/JAHS.64.022005](https://doi.org/10.4050/JAHS.64.022005).
- [4] C. C. Wolf, C. Mertens, A. D. Gardner, C. Dollinger, and A. Fischer, "Optimization of Differential Infrared Thermography for Unsteady Boundary Layer Transition Measurement," *Experiments in Fluids*, vol. 60, no. 1, 2019. DOI: [10.1007/s00348-018-2667-0](https://doi.org/10.1007/s00348-018-2667-0).
- [5] C. C. Wolf, C. Schwarz, K. Kaufmann, A. Gardner, D. Michaelis, J. Bosbach, D. Schanz, and A. Schröder, "Experimental Study of Secondary Vortex Structures in a Rotor Wake," *Experiments in Fluids*, vol. 60, no. 11, 2019. DOI: [10.1007/s00348-019-2807-1](https://doi.org/10.1007/s00348-019-2807-1).
- [6] C. C. Wolf, A. D. Gardner, C. B. Merz, and S. Opitz, "Influence of a Back-Flow Flap on the Dynamic Stall Flow Topology," *CEAS Aeronautical Journal*, vol. 9, no. 1, 2018. DOI: [10.1007/s13272-017-0274-z](https://doi.org/10.1007/s13272-017-0274-z).
- [7] C. C. Wolf, C. B. Merz, K. Richter, and M. Raffel, "Tip-Vortex Dynamics of a Pitching Rotor Blade Tip Model," *AIAA Journal*, vol. 54, no. 10, 2016. DOI: [10.2514/1.J054656](https://doi.org/10.2514/1.J054656).
- [8] C. C. Wolf, A. D. Gardner, B. Ewers, and M. Raffel, "Starting Process of a Pulsed Jet as Seen by Schlieren Measurements," *AIAA Journal*, vol. 52, no. 8, 2014. DOI: [10.2514/1.J053198](https://doi.org/10.2514/1.J053198).

5.2 Conference publications (first authorship)

- [9] C. C. Wolf, J. N. Braukmann, A. Bauknecht, and M. Raffel, "Elastic Main Rotor Blade Motions on Whirl Tower - Optical Measurement Technique," in *Deutscher Luft- und Raumfahrtkongress*, Friedrichshafen, Germany, Sep. 2018.

5.3 Reviewed journal publications (co-authorship)

- [10] A. Bauknecht, B. Ewers, C. C. Wolf, F. Leopold, J. Yin, and M. Raffel, "Three-Dimensional Reconstruction of Helicopter Blade-Tip Vortices Using a Multi-Camera BOS System," *Experiments in Fluids*, vol. 56, no. 1, 2015. DOI: [10.1007/s00348-014-1866-6](https://doi.org/10.1007/s00348-014-1866-6).
- [11] J. N. Braukmann, A. Bauknecht, C. C. Wolf, and M. Raffel, "Towards Density Reconstruction of Helicopter Blade Tip Vortices from High-Speed Background Oriented Schlieren Data," in *New Results in Numerical and Experimental Fluid Mechanics XI*, Springer International Publishing, 2018, pp. 375–385. DOI: [10.1007/978-3-319-64519-3_34](https://doi.org/10.1007/978-3-319-64519-3_34).
- [12] J. N. Braukmann, A. Goerttler, C. C. Wolf, C. Schwarz, and M. Raffel, "Combining Simultaneous Density and Velocity Measurements of Rotor Blade Tip Vortices under Cyclic Pitch Conditions," vol. 62, 2021. DOI: [10.1007/s00348-021-03281-w](https://doi.org/10.1007/s00348-021-03281-w).
- [13] J. N. Braukmann, C. C. Wolf, A. Goerttler, and M. Raffel, "Blade Tip Vortex System of a Rotor with Cyclic Pitch," *AIAA Journal*, vol. 58, no. 7, 2020. DOI: [10.2514/1.J058678](https://doi.org/10.2514/1.J058678).
- [14] A. D. Gardner, C. Eder, C. C. Wolf, and M. Raffel, "Analysis of Differential Infrared Thermography for Boundary Layer Transition Detection," *Experiments in Fluids*, vol. 58, no. 9, 2017. DOI: [10.1007/s00348-017-2405-z](https://doi.org/10.1007/s00348-017-2405-z).
- [15] A. D. Gardner, C. B. Merz, and C. C. Wolf, "Effect of Sweep on a Pitching Finite Wing," *Journal of the American Helicopter Society*, vol. 64, no. 3, 2019. DOI: [10.4050/JAHS.64.032007](https://doi.org/10.4050/JAHS.64.032007).
- [16] A. D. Gardner, S. Opitz, C. C. Wolf, and C. B. Merz, "Reduction of Dynamic Stall using a Back-Flow Flap," *CEAS Aeronautical Journal*, vol. 8, no. 2, 2017. DOI: [10.1007/s13272-017-0237-4](https://doi.org/10.1007/s13272-017-0237-4).
- [17] A. D. Gardner, M. Raffel, J. N. Schwarz C. Braukmann, and C. C. Wolf, "Reference-Free Digital Shadowgraphy Using a Moving BOS Background," *Experiments in Fluids*, vol. 61, no. 2, 2020. DOI: [10.1007/s00348-019-2865-4](https://doi.org/10.1007/s00348-019-2865-4).
- [18] A. D. Gardner, A. Weiss, J. T. Heineck, A. D. Overmeyer, H. R. Spooner, R. K. Jain, C. C. Wolf, and M. Raffel, "Boundary layer transition measured by DIT on the PSP rotor in forward flight," *Journal of the American Helicopter Society*, vol. 66, no. 2, 2021. DOI: [10.4050/JAHS.66.022008](https://doi.org/10.4050/JAHS.66.022008).
- [19] A. D. Gardner, C. C. Wolf, J. T. Heineck, M. Barnett, and M. Raffel, "Helicopter Rotor Boundary Layer Transition Measurement in Forward Flight Using an Infrared Camera," *Journal of the American Helicopter Society*, vol. 65, no. 1, 2020. DOI: [10.4050/JAHS.65.012002](https://doi.org/10.4050/JAHS.65.012002).
- [20] A. D. Gardner, C. C. Wolf, and M. Raffel, "A New Method of Dynamic and Static Stall Detection Using Infrared Thermography," *Experiments in Fluids*, vol. 57, no. 9, 2016. DOI: [10.1007/s00348-016-2235-4](https://doi.org/10.1007/s00348-016-2235-4).
- [21] A. D. Gardner, C. C. Wolf, and M. Raffel, "Review of Measurement Techniques for Unsteady Helicopter Rotor Flows," *Progress in Aerospace Sciences*, vol. 111, 2019. DOI: [10.1016/j.paerosci.2019.100566](https://doi.org/10.1016/j.paerosci.2019.100566).

- [22] A. Goerttler, J. N. Braukmann, C. C. Wolf, A. D. Gardner, and M. Raffel, "Blade Tip-Vortices of a Four-Bladed Rotor with Axial Inflow," *Journal of the American Helicopter Society*, vol. 65, no. 4, 2020. DOI: [10.4050/JAHS.65.042002](https://doi.org/10.4050/JAHS.65.042002).
- [23] K. Kaufmann, C. C. Wolf, C. B. Merz, and A. D. Gardner, "Numerical Investigation of Blade-Tip-Vortex Dynamics," *CEAS Aeronautical Journal*, vol. 9, no. 1, 2018. DOI: [10.1007/s13272-018-0287-2](https://doi.org/10.1007/s13272-018-0287-2).
- [24] C. Mertens, C. C. Wolf, A. D. Gardner, F. F. J. Schrijer, and B. W. van Oudheusden, "Advanced Infrared Thermography Data Analysis for Unsteady Boundary Layer Transition Detection," *Measurement Science and Technology*, vol. 31, no. 1, 2020. DOI: [10.1088/1361-6501/ab3ae2](https://doi.org/10.1088/1361-6501/ab3ae2).
- [25] C. B. Merz, C. C. Wolf, K. Richter, K. Kaufmann, A. Mielke, and M. Raffel, "Spanwise Differences in Static and Dynamic Stall on a Pitching Rotor Blade Tip Model," *Journal of the American Helicopter Society*, vol. 62, no. 1, 2017. DOI: [10.4050/JAHS.62.012002](https://doi.org/10.4050/JAHS.62.012002).
- [26] M. Raffel, A. D. Gardner, T. Schwermer, C. B. Merz, A. Weiss, J. N. Braukmann, and C. C. Wolf, "Rotating Blade Stall Maps Measured by Differential Infrared Thermography," *AIAA Journal*, vol. 55, no. 5, 2017. DOI: [10.2514/1.J055452](https://doi.org/10.2514/1.J055452).
- [27] C. Schwarz, A. Bauknecht, C. C. Wolf, A. Coyle, and M. Raffel, "A Full-Scale Rotor-Wake Investigation of a Free-Flying Helicopter in Ground Effect using BOS and PIV," *Journal of the American Helicopter Society*, vol. 65, no. 3, 2020. DOI: [10.4050/JAHS.65.032007](https://doi.org/10.4050/JAHS.65.032007).
- [28] C. Schwarz, A. Bodling, C. C. Wolf, R. Brinkema, M. Potsdam, and A. D. Gardner, "Development of Secondary Vortex Structures in Rotor Wakes," *Experiments in Fluids*, vol. 63, no. 1, 2022. DOI: [10.1007/s00348-021-03348-8](https://doi.org/10.1007/s00348-021-03348-8).
- [29] H. Stadler, A. Bauknecht, S. Siegrist, R. Flesch, C. C. Wolf, N. van Hinsberg, and M. Jacobs, "Background-Oriented Schlieren Imaging of Flow around a Circular Cylinder at Low Mach Numbers," *Experiments in Fluids*, vol. 58, no. 9, 2017. DOI: [10.1007/s00348-017-2398-7](https://doi.org/10.1007/s00348-017-2398-7).
- [30] A. Weiss, C. C. Wolf, K. Kaufmann, J. N. Braukmann, J. T. Heineck, and M. Raffel, "Unsteady Boundary-Layer Transition Measurements and Computations on a Rotating Blade Under Cyclic Pitch Conditions," *Experiments in Fluids*, vol. 61, no. 2, 2020. DOI: [10.1007/s00348-020-2899-7](https://doi.org/10.1007/s00348-020-2899-7).

5.4 Conference publications (co-authorship)

- [31] J. T. Heineck, A. D. Overmeyer, C. C. Wolf, and M. Raffel, "Boundary Layer Transition Visualization of a Helicopter Blade in Forward Flight using Thermography," in *18th International Symposium on Flow Visualization (ISFV18)*, Zurich, Switzerland, Jun. 2018.
- [32] A. Overmeyer, J. T. Heineck, and C. C. Wolf, "Unstead Boundary Layer Transition Measurements on a Rotor in Forward Flight," in *74th Annual Forum of the Vertical Flight Society*, Phoenix, AZ, USA, May 2018.

- [33] M. Raffel, A. D. Gardner, T. Schwermer, C. B. Merz, A. Weiss, J. B. Braukmann, C. C. Wolf, and B. Ewers, "Differential Infrared Thermography (DIT) for Dynamic Stall Detection," in *18th International Symposium on Applications of Laser Techniques to Fluid Mechanics*, Lisbon, Portugal, Jul. 2016.
- [34] K. Richter, S. Koch, A. Goerttler, B. Lütke, C. C. Wolf, and A. Benkel, "Unsteady Boundary Layer Transition on the DSA-9A Rotor Blade Airfoil," in *41st European Rotorcraft Forum*, Munich, Germany, Sep. 2015.
- [35] K. Richter, C. C. Wolf, A. D. Gardner, and C. B. Merz, "Detection of Unsteady Boundary Layer Transition Using Three Experimental Methods," in *AIAA SciTech 2016*, San Diego, CA, USA, Jan. 2016. DOI: [10.2514/6.2016-1072](https://doi.org/10.2514/6.2016-1072).

5.5 Publications by other authors

- [36] A. I. Abrego, L. Meyn, A. W. Burner, and D. A. Barrows, "Summary of Full-Scale Blade Displacement Measurements of the UH-60A Airloads Rotor," in *AHS Technical Meeting on Aeromechanics Design for Vertical Lift*, San Francisco, CA, USA, Jan. 2016.
- [37] D. Arnal, M. Habiballah, and E. Coustols, "Théorie de l'instabilité laminaire et critères de transition en écoulement bi et tridimensionnel (Laminar Instability Theory and Transition Criteria in Two- and Three-Dimensional Flow)," *La Recherche Aéronautique*, vol. 2, 1984.
- [38] K. Asai, H. Kanda, T. Kunimasu, T. Liu, and J. P. Sullivan, "Boundary-Layer Transition Detection in a Cryogenic Wind Tunnel Using Luminescent Paint," *Journal of Aircraft*, vol. 34, no. 1, 1997. DOI: [10.2514/2.2132](https://doi.org/10.2514/2.2132).
- [39] P. R. Ashill, C. J. Betts, and I. M. Gaudet, "A Wind Tunnel Study of Transitional Flows on a Swept Panel Wing at High Subsonic Speeds," in *CEAS 2nd European Forum on Laminar Flow Technology*, Bordeaux, France, Jun. 1996.
- [40] T. Astarita and G. M. Carlomagno, *Infrared Thermography for Thermo-Fluid-Dynamics*. Springer Verlag, 2013. DOI: [10.1007/978-3-642-29508-9](https://doi.org/10.1007/978-3-642-29508-9).
- [41] H. Bansemir and K. Pfeifer, "The Damage Tolerant Design of the EC135 Bearingless Main Rotor," in *24th European Rotorcraft Forum*, Marseille, France, Sep. 1998.
- [42] A. Bauknecht, C. B. Merz, and M. Raffel, "Airborne Visualization of Helicopter Blade Tip Vortices," *Journal of Visualization*, vol. 20, 2017. DOI: [10.1007/s12650-016-0389-z](https://doi.org/10.1007/s12650-016-0389-z).
- [43] A. Bauknecht, C. B. Merz, M. Raffel, A. Landolt, and A. H. Meier, "Blade-Tip Vortex Detection in Maneuvering Flight Using the Background-Oriented Schlieren Technique," *Journal of Aircraft*, vol. 51, no. 6, 2014. DOI: [10.2514/1.C032672](https://doi.org/10.2514/1.C032672).
- [44] A. Bauknecht, M. Raffel, and B. Grebing, "Airborne Acquisition of Blade Tip Displacements and Vortices on a Coaxial Helicopter," *AIAA Journal*, vol. 55, no. 5, 2018. DOI: [10.2514/1.C034647](https://doi.org/10.2514/1.C034647).
- [45] P. Beaumier and R. Houdeville, "3D Laminar-Turbulent Boundary Layer Calculations on Helicopter Rotors in Forward Flight: Application to Drag Prediction," in *21st European Rotorcraft Forum*, St. Petersburg, Russia, Sep. 1995.
- [46] P. Beaumier, J. Zibi, and M. Costes, "CFD Drag and Power Prediction for a Rotor in Hover or Forward Flight. Formulation and First Applications," *Journal of the American Helicopter Society*, vol. 42, no. 4, 1997. DOI: [10.4050/JAHS.42.327](https://doi.org/10.4050/JAHS.42.327).
- [47] T. Beeby, J. Ackermann, C. M. Langel, R. Chow, C. P. Van Dam, and T. Raffius, "A Quantitative Investigation of Surface Roughness Effects on Airfoil Boundary Layer Transition Using Infrared Thermography," in *54th AIAA Aerospace Sciences Meeting*, San Diego, CA, USA, Jan. 2016. DOI: [10.2514/6.2016-2066](https://doi.org/10.2514/6.2016-2066).
- [48] B. J. Bellhouse and D. L. Schultz, "Determination of Mean and Dynamic Skin Friction, Separation and Transition in Low-Speed Flow with a Thin-Film Heated Element," *Journal of Fluid Mechanics*, vol. 24, no. 2, 1966. DOI: [10.1017/S0022112066000715](https://doi.org/10.1017/S0022112066000715).

- [49] F. Boden, B. Stasicki, and K. Ludwikowski, "Optical Rotor-Blade Deformation Measurements using a Rotating Camera," in *European Test and Telemetry Conference*, Nuremberg, Germany, Jun. 2018. DOI: [10.5162/etct2018/7.4](https://doi.org/10.5162/etct2018/7.4).
- [50] F. Boden, B. Stasicki, M. Szypuła, P. Ružička, Z. Tvrđik, and K. Ludwikowski, "In-Flight Measurements of Propeller Blade Deformation on a VUT100 Cobra Aeroplane using a Co-Rotating Camera System," *Measurement Science and Technology*, vol. 27, no. 7, 2016. DOI: [10.1088/0957-0233/27/7/074013](https://doi.org/10.1088/0957-0233/27/7/074013).
- [51] A. V. Boiko, A. V. Ivanov, V. I. Borodulin, and D. A. Mischenko, "Quantification Technique of Transition to Turbulence in Boundary Layers using Infrared Thermography," *International Journal of Heat and Mass Transfer*, vol. 183, 2022. DOI: [10.1016/j.ijheatmasstransfer.2021.122065](https://doi.org/10.1016/j.ijheatmasstransfer.2021.122065).
- [52] H. Bolnot, S. Le Dizès, and T. Leweke, "Pairing Instability in Helical Vortices," in *Research Topics in Wind Energy*, Springer, 2014, pp. 23–28. DOI: [10.1007/978-3-642-54696-9_4](https://doi.org/10.1007/978-3-642-54696-9_4).
- [53] V. I. Borodulin, A. V. Ivanov, and Y. S. Kachanov, "Swept-Wing Boundary-Layer Transition at Various External Perturbations: Scenarios, Criteria, and Problems of Prediction," *Physics of Fluids*, vol. 29, 2017. DOI: [10.1063/1.4999952](https://doi.org/10.1063/1.4999952).
- [54] W. G. Bousman, "A Qualitative Examination of Dynamic Stall from Flight Test Data," *Journal of the American Helicopter Society*, vol. 43, no. 4, 1998. DOI: [10.4050/JAHS.43.279](https://doi.org/10.4050/JAHS.43.279).
- [55] M. Braune and S. Koch, "Application of Hot-Film Anemometry to Resolve the Unsteady Boundary Layer Transition of a Laminar Airfoil Experiencing Limit Cycle Oscillations," *Experiments in Fluids*, vol. 61, no. 2, 2020. DOI: [10.1007/s00348-020-2907-y](https://doi.org/10.1007/s00348-020-2907-y).
- [56] Brincken, Bernd, *Eurocopter X³ at the ILA Berlin 2012*, Wikimedia Commons, URL: https://commons.wikimedia.org/wiki/File:Ila12_X3_0600_b1.jpg (Accessed: 2022-01-08), 2012.
- [57] H. H. Bruun, *Hot-Wire Anemometry: Principles and Signal Analysis*. Oxford University Press, 1995.
- [58] G. Carlomagno, L. de Luca, G. Buresti, and G. Lombardi, "Boundary Layer Diagnostics by Means of an Infrared Scanning Radiometer," *Proceedings of the SPIE, Applications of Infrared Technology*, vol. 918, 1988. DOI: [10.1117/12.945598](https://doi.org/10.1117/12.945598).
- [59] G. M. Carlomagno and G. Cardone, "Infrared Thermography for Convective Heat Transfer Measurements," *Experiments in Fluids*, vol. 49, no. 6, 2010. DOI: [10.1007/s00348-010-0912-2](https://doi.org/10.1007/s00348-010-0912-2).
- [60] N. M. Chaderjian, "Navier-Stokes Simulation of UH-60A Rotor/Wake Interaction Using Adaptive Mesh Refinement," in *73rd Annual Forum of the American Helicopter Society*, Fort Worth, TX, USA, May 2017.
- [61] M. S. Chandrasekhara and M. C. Wilder, "Heat-Flux Gauge Studies of Compressible Dynamic Stall," *AIAA Journal*, vol. 41, no. 5, 2003. DOI: [10.2514/2.2019](https://doi.org/10.2514/2.2019).
- [62] R. T. N. Chen, "A Survey of Nonuniform Inflow Models for Rotorcraft Flight Dynamics and Control Applications," NASA TM 102219, 1989.

- [63] X. Chen, Z. X. Bi, J. Gong, D. P. Yao, and S. Wen, "Optical Skin Friction Measurement using Shear-Sensitive Liquid-Crystal Coatings," *Journal of Experiments in Fluid Mechanics*, vol. 26, no. 6, 2012.
- [64] J. G. Coder, "OVERFLOW Rotor Simulations Using Advanced Turbulence and Transition Modeling," in *55th AIAA Aerospace Sciences Meeting*, Grapevine, TX, USA, Jan. 2017. DOI: [10.2514/6.2017-1432](https://doi.org/10.2514/6.2017-1432).
- [65] J. G. Coder and M. D. Maughmer, "Computational Fluid Dynamics Compatible Transition Modeling Using an Amplification Factor Transport Equation," *AIAA Journal*, vol. 52, no. 11, 2014. DOI: [10.2514/1.J052905](https://doi.org/10.2514/1.J052905).
- [66] M. Costantini, U. Fey, U. Henne, and C. Klein, "Nonadiabatic Surface Effects on Transition Measurements Using Temperature-Sensitive Paints," *AIAA Journal*, vol. 53, no. 5, 2015. DOI: [10.2514/1.J053155](https://doi.org/10.2514/1.J053155).
- [67] B. K. Crawford, G. T. Duncan Jr., D. E. West, and W. S. Saric, "Laminar-Turbulent Boundary Layer Transition Imaging Using IR Thermography," *Optics and Photonics*, vol. 3, no. 3, 2013. DOI: [10.4236/opj.2013.33038](https://doi.org/10.4236/opj.2013.33038).
- [68] B. K. Crawford, G. T. Duncan Jr., D. E. West, and W. S. Saric, "Robust, Automated Processing of IR Thermography for Quantitative Boundary-Layer Transition Measurements," *Experiments in Fluids*, vol. 56, no. 7, 2015. DOI: [10.1007/s00348-015-2011-x](https://doi.org/10.1007/s00348-015-2011-x).
- [69] H. C. Curtiss Jr., M. Sun, W. F. Putman, and E. J. Hanker Jr., "Rotor Aerodynamics in Ground Effect At Low Advance Ratios," *Journal of the American Helicopter Society*, vol. 29, no. 1, 1984. DOI: [10.4050/JAHS.29.48](https://doi.org/10.4050/JAHS.29.48).
- [70] E. Dick and S. Kubacki, "Transition Models for Turbomachinery Boundary Layer Flows: A Review," *International Journal of Turbomachinery, Propulsion and Power*, vol. 2, no. 2, 2017. DOI: [10.3390/ijtp2020004](https://doi.org/10.3390/ijtp2020004).
- [71] O. Dieterich, D. Roth, and M. Priems, "Elastic Main Rotor Blade Motions on Whirl Tower - Comparison of Measurements and Analysis," in *Deutscher Luft- und Raumfahrtkongress*, Friedrichshafen, Germany, Sep. 2018.
- [72] M. Dietz and O. Dieterich, "Towards Increased Industrial Application of Rotor Aeroelastic CFD," in *35th European Rotorcraft Forum*, Hamburg, Germany, Sep. 2009.
- [73] M. Døssing, "High Frequency Microphone Measurements for Transition Detection on Airfoils," Danmarks Tekniske Universitet, Risø Nationallaboratoriet for Bæredygtig Energi, Risoe-R No. 1645(EN), 2008.
- [74] M. Drela, "Newton Solution of Coupled Viscous/Inviscid Multielement Airfoil Flows," in *AIAA 21st Fluid Dynamics, Plasma Dynamics and Lasers Conference*, Seattle, WA, USA, Jun. 1990. DOI: [10.2514/6.1990-1470](https://doi.org/10.2514/6.1990-1470).
- [75] E. R. van Driest, "Problem of Aerodynamic Heating," *Aeronautical Engineering Review*, vol. 15, no. 10, 1956.
- [76] J. P. Dussauge, R. W. Smith, A. J. Smits, H. Fernholz, P. J. Finley, and E. F. Spina, "Turbulent Boundary Layers in Subsonic and Supersonic Flow," AGARD-AG-335, 1996.

- [77] C. Eder, "Analyse der Differenzinfrarotthermographie (Analysis of the Differential Infrared Thermography)," M.S. thesis, Bundeswehr University Munich, 2016.
- [78] T. A. Egolf, N. Hariharan, R. Narducci, and E. Reed, "AIAA Standardized Hover Simulation: Hover Performance Prediction Status and Outstanding Issues," in *AIAA SciTech 2017 Forum*, Grapevine, TX, USA, Jan. 2017. DOI: [10.2514/6.2017-1429](https://doi.org/10.2514/6.2017-1429).
- [79] Federal Aviation Administration, "Rotorcraft Flying Handbook," FAA-H-8083-21, 2000.
- [80] H. Fernandes, C. Ibarra-Castanedo, H. Zhang, and X. Maldague, "IR Thermography for Dynamic Detection of Laminar Turbulent Transition," *Journal of Nondestructive Evaluation*, vol. 34, 2015. DOI: [10.1007/s10921-015-0303-y](https://doi.org/10.1007/s10921-015-0303-y).
- [81] U. Fey and Y. Egami, "Transition Detection by Temperature-Sensitive Paint," in *Springer Handbook of Experimental Fluid Mechanics*, Springer Verlag, 2007, pp. 537–552.
- [82] FLIR[®] Systems, Inc., *FLIR SC7000 Series*, URL: https://www.flirmedia.com/MMC/THG/Brochures/RND_017/RND_017_US.pdf (Accessed: 2022-01-08), Data Sheet RND_017_US, 2014.
- [83] FLIR[®] Systems, Inc., *FLIR X8500sc SLS*, URL: https://www.flirmedia.com/MMC/THG/Brochures/RND_099/RND_099_US.pdf (Accessed: 2022-01-08), Data Sheet RND_099_US, 2017.
- [84] Y. Gao, Q. Zhu, and L. Wang, "Measurement of Unsteady Transition on a Pitching Airfoil using Dynamic Pressure Sensors," *Journal of Mechanical Science and Technology*, vol. 30, no. 10, 2016.
- [85] T. J. Garbeff and J. Baerny, "A Qualitative Investigation of Selected Infrared Flow Visualization Image Processing Techniques," in *AIAA Aviation 2019 Forum*, Dallas, TX, USA, Jun. 2019. DOI: [10.2514/6.2019-2907](https://doi.org/10.2514/6.2019-2907).
- [86] A. D. Gardner and K. Richter, "Boundary Layer Transition Determination for Periodic and Static Flows using Phase-Averaged Pressure Data," *Experiments in Fluids*, vol. 56, no. 6, 2015. DOI: [10.1007/s00348-015-1992-9](https://doi.org/10.1007/s00348-015-1992-9).
- [87] A. D. Gardner and K. Richter, "Transition Determination on a Periodic Pitching Airfoil Using Phase Averaging of Pressure Data," in *New Results in Numerical and Experimental Fluid Mechanics X*, Springer International Publishing, 2016, pp. 291–301. DOI: [10.1007/978-3-319-27279-5_26](https://doi.org/10.1007/978-3-319-27279-5_26).
- [88] A. D. Gardner and K. Richter, "Effect of the Model-Sidewall Connection for a Dynamic Stall Airfoil Experiment," *Journal of Aircraft*, vol. 57, no. 1, 2020. DOI: [10.2514/1.C035613](https://doi.org/10.2514/1.C035613).
- [89] E. Gartenberg and R. E. Wright, "Boundary-Layer Transition Detection with Infrared Imaging Emphasizing Cryogenic Applications," *AIAA Journal*, vol. 32, no. 9, 1994. DOI: [10.2514/3.12186](https://doi.org/10.2514/3.12186).
- [90] G. L. Gentry Jr., P. F. Quinto, G. M. Gatlin, and Z. T. Applin, "The Langley 14- by 22-Foot Subsonic Tunnel: Description, Flow Characteristics, and Guide for Users," NASA TP 3008, 1990.

- [91] F. Ghorbanishohrat and D. A. Johnson, "Evaluating Airfoil Behaviour such as Laminar Separation Bubbles with Visualization and IR Thermography Methods," *Journal of Physics: Conference Series*, vol. 1037, 2018. DOI: [10.1088/1742-6596/1037/5/052037](https://doi.org/10.1088/1742-6596/1037/5/052037).
- [92] A. Goerttler, A. D. Gardner, and K. Richter, "Unsteady Boundary Layer Transition Detection by Automated Analysis of Hot Film Data," in *New Results in Numerical and Experimental Fluid Mechanics XI*, Springer International Publishing, 2017, pp. 387–396. DOI: [10.1007/978-3-319-64519-3_35](https://doi.org/10.1007/978-3-319-64519-3_35).
- [93] C. P. Goynes, R. J. Stalker, and A. Paull, "Skin-Friction Measurements in High-Enthalpy Hypersonic Boundary Layers," *Journal of Fluid Mechanics*, vol. 485, 2003. DOI: [10.1017/S0022112003003975](https://doi.org/10.1017/S0022112003003975).
- [94] M. Grawunder, R. Reiß, and C. Breitsamter, "Thermographic Transition Detection for Low-Speed Wind-Tunnel Experiments," *AIAA Journal*, vol. 54, no. 6, 2016. DOI: [10.2514/1.J054490](https://doi.org/10.2514/1.J054490).
- [95] R. M. Hall, C. J. Obara, D. L. Carraway, C. B. Johnson, R. E. Wright Jr., and P. F. Covell, "Comparisons of Boundary-Layer Transition Measurement Techniques at Supersonic Mach Numbers," *AIAA Journal*, vol. 29, no. 6, 1990. DOI: [10.2514/3.10669](https://doi.org/10.2514/3.10669).
- [96] U. Hartmann and J. R. Seume, "Combining ART and FBP for Improved Fidelity of Tomographic BOS," *Measurement Science and Technology*, vol. 27, no. 9, 2016. DOI: [10.1088/0957-0233/27/9/097001](https://doi.org/10.1088/0957-0233/27/9/097001).
- [97] J. S. Hayden, "The Effect of the Ground on Helicopter Hovering Power Required," in *32nd Annual National Forum of the American Helicopter Society*, Washington, DC, USA, May 1976.
- [98] A. Hebler, "Experimental Assessment of the Flutter Stability of a Laminar Airfoil in Transonic Flow," in *17th International Forum on Aeroelasticity and Structural Dynamics*, Como, Italy, Jun. 2017.
- [99] J. T. Heineck, D. W. Banks, N. T. Smith, E. T. Schairer, P. S. Bean, and T. Robillos, "Background-Oriented Schlieren Imaging of Supersonic Aircraft in Flight," *AIAA Journal*, vol. 59, no. 1, 2021. DOI: [10.2514/1.J059495](https://doi.org/10.2514/1.J059495).
- [100] J. T. Heineck, A. Overmeyer, H. R. Spooner, A. Gardner, A. Weiss, and M. Raffel, "Transition Measurements of Upper and Lower Rotor Blade Surfaces in Forward Flight," in *AIAA Aviation 2020 Forum*, Virtual, Jun. 2020. DOI: [10.2514/6.2020-3103](https://doi.org/10.2514/6.2020-3103).
- [101] C. C. Heister, "A Method for Approximate Prediction of Laminar-Turbulent Transition on Helicopter Rotors," *Journal of the American Helicopter Society*, vol. 63, no. 3, 2018. DOI: [10.4050/JAHS.63.032008](https://doi.org/10.4050/JAHS.63.032008).
- [102] C. C. Heister, "Methodik zur näherungsweise Vorhersage des laminar-turbulenten Umschlags an Hubschrauberrotoren," Ph.D. dissertation, Universität Stuttgart, 2018.
- [103] S. von Hoesslin, J. Gruendmayer, A. Zeisberger, M. S. Sommer, J. Klimesch, S. Behre, H. Brandies, and C. J. Kähler, "Visualization of Laminar–Turbulent Transition on Rotating Turbine Blades," *Experiments in Fluids*, vol. 61, 2020. DOI: [10.1007/s00348-020-02985-9](https://doi.org/10.1007/s00348-020-02985-9).

- [104] S. von Hoesslin, M. Stadlbauer, J. Gruendmayer, and C. J. Kähler, "Temperature Decline Thermography for Laminar-Turbulent Transition Detection in Aerodynamics," *Experiments in Fluids*, vol. 58, 2017. DOI: [10.1007/s00348-017-2411-1](https://doi.org/10.1007/s00348-017-2411-1).
- [105] S. Hossein, M. Hasbun, J. Y. Hong, H. Yeo, and R. A. Ormiston, "Overview of RCAS Capabilities, Validations, and Rotorcraft Applications," in *71st Annual Forum of the American Helicopter Society*, Virginia Beach, VA, USA, May 2015.
- [106] T. Ikami, K. Fujita, H. Nagai, and D. Yorita, "Measurement of Boundary Layer Transition on Oscillating Airfoil using cntTSP in Low-Speed Wind Tunnel," *Measurement Science and Technology*, vol. 32, no. 7, 2021. DOI: [10.1088/1361-6501/abe2be](https://doi.org/10.1088/1361-6501/abe2be).
- [107] T. Ikami, K. Fujita, H. Nagai, and D. Yorita, "Response Evaluation of cntTSP for Detection of Dynamic Boundary Layer Transition in Low-Speed Wind Tunnel," in *AIAA SciTech 2020 Forum*, Virtual, Jan. 2021. DOI: [10.2514/6.2021-0329](https://doi.org/10.2514/6.2021-0329).
- [108] J. L. van Ingen, "The e^N Method for Transition Prediction. Historical Review of Work at TU Delft," in *AIAA 38th Fluid Dynamics Conference*, Seattle, WA, USA, Jun. 2008. DOI: [10.2514/6.2008-3830](https://doi.org/10.2514/6.2008-3830).
- [109] R. Jain, "CFD Turbulence Transition Models Validation for Rotors in Unsteady Axial and Forward-flight Conditions using CREATETM-AV Helios," in *77th Annual Forum of the Vertical Flight Society*, Virtual, May 2021.
- [110] R. K. Jain, H. Yeo, J. C. Ho, and M. Bhagwat, "An Assessment of RCAS Performance Prediction for Conventional and Advanced Rotor Configurations," *Journal of the American Helicopter Society*, vol. 61, no. 4, 2016. DOI: [10.4050/JAHS.61.042005](https://doi.org/10.4050/JAHS.61.042005).
- [111] L. A. Joseph, A. Borgoltz, and W. Devenport, "Infrared Thermography for Detection of Laminar-Turbulent Transition in Low-Speed Wind Tunnel Testing," *Experiments in Fluids*, vol. 57, 2016. DOI: [10.1007/s00348-016-2162-4](https://doi.org/10.1007/s00348-016-2162-4).
- [112] K. Kampa, B. Enenkl, G. Polz, and G. Roth, "Aeromechanic Aspects in the Design of the EC135," *Journal of the American Helicopter Society*, vol. 44, no. 2, 1999. DOI: [10.4050/JAHS.44.83](https://doi.org/10.4050/JAHS.44.83).
- [113] K. Kaufmann, M. M. Müller, and A. D. Gardner, "Dynamic Stall Computations of Double-Swept Rotor Blades," in *New Results in Numerical and Experimental Fluid Mechanics XII*, Springer International Publishing, 2020, pp. 351–361. DOI: [10.1007/978-3-030-25253-3_34](https://doi.org/10.1007/978-3-030-25253-3_34).
- [114] K. Kaufmann, P. Ströer, F. Richez, C. Lienard, P. Gardarein, N. Krimmelbein, and A. D. Gardner, "Validation of Boundary-Layer-Transition Computations for a Rotor with Axial Inflow," in *75th Annual Forum of the Vertical Flight Society*, Philadelphia, PA, USA, May 2019.
- [115] P. Khayatzadeh and S. Nadarajah, "Laminar-Turbulent Flow Simulation for Wind Turbine Profiles using the γ - $Re_{\theta t}$ Transition Model," *Wind Energy*, vol. 17, no. 6, 2013. DOI: [10.1002/we.1606](https://doi.org/10.1002/we.1606).
- [116] K. Kindler, E. Goldhahn, F. Leopold, and M. Raffel, "Recent Developments in Background Oriented Schlieren Methods for Rotor Blade Tip Vortex Measurements," *Experiments in Fluids*, vol. 43, 2007. DOI: [10.1007/s00348-007-0328-9](https://doi.org/10.1007/s00348-007-0328-9).

- [117] K. Kindler, K. Mulleners, H. Richard, B. G. van der Wall, and M. Raffel, "Aperiodicity in the Near Field of Full-Scale Rotor Blade Tip Vortices," *Experiments in Fluids*, vol. 50, no. 6, 2011. DOI: [10.1007/s00348-010-1016-8](https://doi.org/10.1007/s00348-010-1016-8).
- [118] C. Klein, R. H. Engler, U. Henne, and W. E. Sachs, "Application of Pressure-Sensitive Paint for Determination of the Pressure Field and Calculation of the Forces and Moments of Models in a Wind Tunnel," *Experiments in Fluids*, vol. 39, no. 2, 2005. DOI: [10.1007/s00348-005-1010-8](https://doi.org/10.1007/s00348-005-1010-8).
- [119] C. Klein and U. Henne, "Combination of Temperature Sensitive Paint and Carbon Nanotubes for Transition Detection," in *53rd AIAA Aerospace Sciences Meeting*, Kissimmee, FL, USA, Jan. 2015. DOI: [10.2514/6.2015-1558](https://doi.org/10.2514/6.2015-1558).
- [120] N. M. Komerath, M. J. Smith, and C. Tung, "A Review of Rotor Wake Physics and Modeling," *Journal of the American Helicopter Society*, vol. 56, no. 2, 2011. DOI: [10.4050/JAHS.56.022006](https://doi.org/10.4050/JAHS.56.022006).
- [121] A. Krumbein, N. Krimmelbein, and G. Schrauf, "Automatic Transition Prediction in Hybrid Flow Solver, Part 1: Methodology and Sensitivities," *Journal of Aircraft*, vol. 46, no. 4, 2009. DOI: [10.2514/1.39736](https://doi.org/10.2514/1.39736).
- [122] A. Krumbein, N. Krimmelbein, and G. Schrauf, "Automatic Transition Prediction in Hybrid Flow Solver, Part 2: Practical Application," *Journal of Aircraft*, vol. 46, no. 4, 2009. DOI: [10.2514/1.39738](https://doi.org/10.2514/1.39738).
- [123] R. M. Kufeld, E. A. Romander, and M. Dominguez, "Data Quality Analysis of the UH-60A Airloads Program Flight Test Data - Volume 1," NASA TM-2019-220014, 2019.
- [124] A. Kus, S. Schneider, M. Hollands, R. Rammer, O. Dieterich, and M. Priems, "GRC1: An Advanced Five-Bladed Bearingless Main Rotor Dynamics and Acoustics from Draft to Flight Test," in *74th Annual Forum of the American Helicopter Society*, Phoenix, AZ, USA, May 2018.
- [125] B. M. Kutz, M. Keßler, and E. Krämer, "Experimental and Numerical Examination of a Helicopter Hovering in Ground Effect," *CEAS Aeronautical Journal*, vol. 4, no. 4, 2013. DOI: [10.1007/s13272-013-0084-x](https://doi.org/10.1007/s13272-013-0084-x).
- [126] D. B. Landrum and J. M. Macha, "Influence of a Heated Leading Edge on Boundary Layer Growth, Stability, and Transition," in *AIAA 19th Fluid Dynamics, Plasma Dynamics and Laser Dynamics Conference*, Honolulu, HI, USA, Jun. 1987. DOI: [10.2514/6.1987-1259](https://doi.org/10.2514/6.1987-1259).
- [127] W. Lang, A. D. Gardner, S. Mariappan, C. Klein, and M. Raffel, "Boundary-Layer Transition on a Rotor Blade Measured by Temperature-Sensitive Paint, Thermal Imaging and Image Derotation," *Experiments in Fluids*, vol. 56, 2015. DOI: [10.1007/s00348-015-1988-5](https://doi.org/10.1007/s00348-015-1988-5).
- [128] R. B. Langtry and F. R. Menter, "Correlation-Based Transition Modeling for Unstructured Parallelized Computational Fluid Dynamics Codes," *AIAA Journal*, vol. 47, no. 12, 2009. DOI: [10.2514/1.42362](https://doi.org/10.2514/1.42362).
- [129] R. B. Langtry, K. Sengupta, D. T. Yeh, and A. J. Dorgan, "Extending the Local Correlation based Transition Model for Crossflow Effects," in *AIAA 45th Fluid Dynamics Conference*, Dallas, TX, USA, Jun. 2015. DOI: [10.2514/6.2015-2474](https://doi.org/10.2514/6.2015-2474).

- [130] Y. Le Sant, M. Marchand, P. Millan, and J. Fontaine, "An Overview of Infrared Thermography Techniques used in Large Wind Tunnels," *Aerospace Science and Technology*, vol. 6, no. 5, 2002. DOI: [10.1016/S1270-9638\(02\)01172-0](https://doi.org/10.1016/S1270-9638(02)01172-0).
- [131] T. Lee and S. Basu, "Measurement of Unsteady Boundary Layer Developed on an Oscillating Airfoil Using Multiple Hot-Film Sensors," *Experiments in Fluids*, vol. 25, no. 2, 1998. DOI: [10.1007/s003480050214](https://doi.org/10.1007/s003480050214).
- [132] T. Lee and P. Gerontakos, "Investigation of Flow Over an Oscillating Airfoil," *Journal of Fluid Mechanics*, vol. 512, 2004. DOI: [10.1017/S0022112004009851](https://doi.org/10.1017/S0022112004009851).
- [133] J. G. Leishman, *Principles of Helicopter Aerodynamics*. Cambridge University Press, 2006.
- [134] F. Leopold, "The Application of the Colored Background Oriented Schlieren Technique (CBOS) to Free-Flight and In-Flight Measurements," in *22nd International Congress on Instrumentation in Aerospace Simulation Facilities*, Pacific Grove, CA, USA, Jun. 2007. DOI: [10.1109/ICIASF.2007.4380894](https://doi.org/10.1109/ICIASF.2007.4380894).
- [135] J. Letzgus, M. Keßler, and E. Krämer, "Simulation of Dynamic Stall on an Elastic Rotor in High-Speed Turn Flight," *Journal of the American Helicopter Society*, vol. 65, no. 2, 2020. DOI: [10.4050/jahs.65.022002](https://doi.org/10.4050/jahs.65.022002).
- [136] Z. Li, B. Wen, X. Dong, Z. Peng, Y. Qu, and W. Zhang, "Aerodynamic and Aeroelastic Characteristics of Flexible Wind Turbine Blades under Periodic Unsteady Inflows," *Journal of Wind Engineering and Industrial Aerodynamics*, vol. 197, 2020. DOI: [10.1016/j.jweia.2019.104057](https://doi.org/10.1016/j.jweia.2019.104057).
- [137] H. W. Liepmann and G. T. Skinner, "Shearing-Stress Measurements by Use of a Heated Element," NACA TN 3268, 1954.
- [138] T. Liu, J. P. Sullivan, K. Asai, C. Klein, and Y. Egami, *Pressure and Temperature Sensitive Paints*, 2nd ed. Springer Verlag, 2021. DOI: [10.1007/978-3-030-68056-5](https://doi.org/10.1007/978-3-030-68056-5).
- [139] X. Liu and W. Rodi, "Experiments on Transitional Boundary Layers with Wake-Induced Unsteadiness," *Journal of Fluid Mechanics*, vol. 231, 1991. DOI: [10.1017/S0022112091003385](https://doi.org/10.1017/S0022112091003385).
- [140] P. F. Lorber and F. O. Carta, "Unsteady Transition Measurements on a Pitching Three-Dimensional Wing," in *The Fifth Symposium on Numerical and Physical Aspects of Aerodynamic Flows*, Long Beach, CA, USA, Jan. 1992.
- [141] L. de Luca, G. M. Carlomagno, and G. Buresti, "Boundary Layer Diagnostics by Means of an Infrared Scanning Radiometer," *Experiments in Fluids*, vol. 9, 1990. DOI: [10.1007/BF00187411](https://doi.org/10.1007/BF00187411).
- [142] D. Mabey, "A Summary of Effects of Heat Transfer on Aerodynamics and Possible Implications for Wind Tunnel Tests," in *29th Aerospace Sciences Meeting*, Reno, NV, USA, Jan. 1991. DOI: [10.2514/6.1991-401](https://doi.org/10.2514/6.1991-401).
- [143] L. M. Mack, "Transition and Laminar Instability," JPL Publication 77-15, 1977.
- [144] H. Mai and A. Hebler, "Aeroelasticity of a Laminar Wing," in *15th International Forum on Aeroelasticity and Structural Dynamics*, Paris, France, Jun. 2011.
- [145] R. E. Mayle, "The Role of Laminar-Turbulent Transition in Gas Turbine Engines," *Journal of Turbomachinery*, vol. 113, no. 4, 1991. DOI: [10.1115/1.2929110](https://doi.org/10.1115/1.2929110).

- [146] W. J. McCroskey, "The Phenomenon of Dynamic Stall," NASA TM 81264, 1981.
- [147] D. J. Mee, "Boundary-Layer Transition Measurements in Hypervelocity Flows in a Shock Tunnel," *AIAA Journal*, vol. 40, no. 8, 2002. DOI: [10.2514/2.1851](https://doi.org/10.2514/2.1851).
- [148] F. R. Menter, "Two-Equation Eddy-Viscosity Turbulence Models for Engineering Applications," *AIAA Journal*, vol. 32, no. 8, 1994. DOI: [10.2514/3.12149](https://doi.org/10.2514/3.12149).
- [149] J. A. Miller and A. A. Fejer, "Transition Phenomena in Oscillating Boundary-Layer Flows," *Journal of Fluid Mechanics*, vol. 18, no. 3, 1964. DOI: [10.1017/S0022112064000325](https://doi.org/10.1017/S0022112064000325).
- [150] S. Montelpare and R. Ricci, "A Thermographic Method to Evaluate the Local Boundary Layer Separation Phenomena on Aerodynamic Bodies Operating at Low Reynolds Number," *International Journal of Thermal Sciences*, vol. 43, no. 3, 2004. DOI: [10.1016/j.ijthermalsci.2003.07.006](https://doi.org/10.1016/j.ijthermalsci.2003.07.006).
- [151] K. Mulleners and M. Raffel, "The Onset of Dynamic Stall Revisited," *Experiments in Fluids*, vol. 52, no. 3, 2012. DOI: [10.1007/s00348-011-1118-y](https://doi.org/10.1007/s00348-011-1118-y).
- [152] NASA LARC (unknown photographer), *Sikorsky HNS-1 (YR-4B)*, Public Domain via Wikimedia Commons, URL: [https://commons.wikimedia.org/wiki/File:Sikorsky_HNS-1_\(YR-4B\)_-_GPN-2000-001729.jpg](https://commons.wikimedia.org/wiki/File:Sikorsky_HNS-1_(YR-4B)_-_GPN-2000-001729.jpg) (Accessed: 2022-01-08), NASA Photo ID GPN-2000-001729, 1944.
- [153] D. H. Neuhart and C. B. McGinley, "Free-Stream Turbulence Intensity in the Langley 14- by 22-Foot Subsonic Tunnel," NASA TP 2004-213247, 2004.
- [154] K. W. Noonan, "Aerodynamic Characteristics of a Rotorcraft Airfoil Designed for the Tip Region of a Main Rotor Blade," NASA TM 4264, 1991.
- [155] Nugent, Pat, *A Soviet Ka-32 Helicopter passes over the Airfield during Airshow Canada '89*, Public Domain via Wikimedia Commons, URL: <https://commons.wikimedia.org/wiki/File:Ka-32-SovietUnion-1989.jpg> (Accessed: 2022-01-08), 1989.
- [156] D. Nürnberger and H. Greza, "Numerical Investigation of Unsteady Transitional Flows in Turbomachinery Components Based on a RANS Approach," *Flow, Turbulence and Combustion*, vol. 69, 2002. DOI: [10.1023/A:1027307211377](https://doi.org/10.1023/A:1027307211377).
- [157] H. J. Obremski and A. A. Fejer, "Transition in Oscillating Boundary Layer Flows," *Journal of Fluid Mechanics*, vol. 29, no. 1, 1967. DOI: [10.1017/S0022112067000655](https://doi.org/10.1017/S0022112067000655).
- [158] M. M. Opoka and H. P. Hodson, "Experimental Investigation of Unsteady Transition Processes on High-Lift T106A Turbine Blades," *Journal of Propulsion and Power*, vol. 24, no. 3, 2008. DOI: [10.2514/1.31947](https://doi.org/10.2514/1.31947).
- [159] U. Orth, "Unsteady Boundary-Layer Transition in Flow Periodically Disturbed by Wakes," *Journal of Turbomachinery*, vol. 115, no. 4, 1993. DOI: [10.1115/1.2929306](https://doi.org/10.1115/1.2929306).
- [160] A. D. Overmeyer and P. B. Martin, "Measured Boundary Layer Transition and Rotor Hover Performance at Model Scale," in *55th AIAA Aerospace Sciences Meeting*, Grapevine, TX, USA, Jan. 2017. DOI: [10.2514/6.2017-1872](https://doi.org/10.2514/6.2017-1872).
- [161] Ö. S. Özçakmak, N. N. Sørensen, H. A. Madsen, and J. N. Sørensen, "Laminar-Turbulent Transition Detection on Airfoils by High-Frequency Microphone Measurements," *Wind Energy*, vol. 22, no. 10, 2019. DOI: [10.1002/we.2361](https://doi.org/10.1002/we.2361).

- [162] J. J. Philippe, "Définition et évaluation de nouvelles extrémités de pales de rotors d'hélicoptère (Definition and Evaluation of New Helicopter Rotor Blades Extremities)," ONERA-TAP-92-179, 1992.
- [163] A. V. Popov, R. M. Botez, and M. Labib, "Transition Point Detection from the Surface Pressure Distribution for Controller Design," *Journal of Aircraft*, vol. 45, no. 1, 2008. DOI: [10.2514/1.31488](https://doi.org/10.2514/1.31488).
- [164] M. Potsdam, H. Yeo, and W. Johnson, "Rotor Airloads Prediction Using Loose Aerodynamic/Structural Coupling," *Journal of Aircraft*, vol. 43, no. 3, 2006. DOI: [10.2514/1.14006](https://doi.org/10.2514/1.14006).
- [165] A. Quast, "Detection of Transition by Infrared Images," *Technical Soaring*, vol. 30, no. 1-2, 2006.
- [166] M. Raffel and J. T. Heineck, "Mirror-Based Image Derotation for Aerodynamic Rotor Measurements," *AIAA Journal*, vol. 52, no. 6, 2014. DOI: [10.2514/1.J052836](https://doi.org/10.2514/1.J052836).
- [167] M. Raffel and C. B. Merz, "Differential Infrared Thermography for Unsteady Boundary-Layer Transition Measurements," *AIAA Journal*, vol. 52, no. 9, 2014. DOI: [10.2514/1.J053235](https://doi.org/10.2514/1.J053235).
- [168] M. Raffel, C. B. Merz, T. Schwermer, and K. Richter, "Differential Infrared Thermography for Boundary Layer Transition Detection on Pitching Rotor Blade Model," *Experiments in Fluids*, vol. 56, 2015. DOI: [10.1007/s00348-015-1905-y](https://doi.org/10.1007/s00348-015-1905-y).
- [169] M. Raffel, H. Richard, J. Agocs, D. Otter, H. Mattner, and U. Göhmann, "Experimental Aspects of PIV applied to a Bo 105 Helicopter in Hover-Flight Condition," in *4th International Symposium on Particle Image Velocimetry*, Göttingen, Germany, Sep. 2001.
- [170] M. Raffel, H. Richard, and G. E. A. Meier, "On the Applicability of Background Oriented Optical Tomography for Large Scale Aerodynamic Investigations," *Experiments in Fluids*, vol. 28, no. 5, 2001. DOI: [10.1007/s003480050408](https://doi.org/10.1007/s003480050408).
- [171] S. Raghunathan and D. Mitchell, "Computed Effects of Heat Transfer on the Transonic Flow over an Aerofoil," *AIAA Journal*, vol. 33, no. 11, 1995. DOI: [10.2514/3.12956](https://doi.org/10.2514/3.12956).
- [172] T. Reichstein, A. Schaffarczyk, C. Dollinger, N. Balaesque, E. Schülein, C. Jauch, and A. Fischer, "Investigation of Laminar-Turbulent Transition on a Rotating Wind-Turbine Blade of Multimegawatt Class with Thermography and Microphone Array," *Energies*, vol. 22, 2019. DOI: [10.3390/en12112102](https://doi.org/10.3390/en12112102).
- [173] E. Reshotko, "Drag Reduction by Cooling in Hydrogen-Fueled Aircraft," *Journal of Aircraft*, vol. 16, 1979. DOI: [10.2514/3.58571](https://doi.org/10.2514/3.58571).
- [174] R. Ricci, S. Montelpare, and E. Renzi, "Study of Mechanical Disturbances Effects on the Laminar Separation Bubble by means of Infrared Thermography," *International Journal of Thermal Sciences*, vol. 50, no. 11, 2011. DOI: [10.1016/j.ijthermalsci.2011.05.013](https://doi.org/10.1016/j.ijthermalsci.2011.05.013).
- [175] H. Richard and M. Raffel, "Principle and Applications of the Background Oriented Schlieren (BOS) Method," *Measurement Science and Technology*, vol. 12, no. 9, 2001. DOI: [10.1088/0957-0233/12/9/325](https://doi.org/10.1088/0957-0233/12/9/325).

- [176] F. Richez, A. Nazarians, and C. Lienard, "Assessment of Laminar-Turbulent Transition Modeling Methods for the Prediction of Helicopter Rotor Performance," in *43rd European Rotorcraft Forum*, Milan, Italy, Sep. 2017.
- [177] K. Richter, S. Koch, A. D. Gardner, H. Mai, A. Klein, and C. H. Rohardt, "Experimental Investigation of Unsteady Transition on a Pitching Rotor Blade Airfoil," *Journal of the American Helicopter Society*, vol. 59, no. 1, 2014. DOI: [10.4050/JAHS.59.012001](https://doi.org/10.4050/JAHS.59.012001).
- [178] K. Richter, A. Le Pape, T. Knopp, M. Costes, V. Gleize, and A. D. Gardner, "Improved Two-Dimensional Dynamic Stall Prediction with Structured and Hybrid Numerical Methods," *Journal of the American Helicopter Society*, vol. 56, no. 4, 2011. DOI: [10.4050/JAHS.56.042007](https://doi.org/10.4050/JAHS.56.042007).
- [179] K. Richter and E. Schülein, "Boundary-Layer Transition Measurements on Hovering Helicopter Rotors by Infrared Thermography," *Experiments in Fluids*, vol. 55, 2014. DOI: [10.1007/s00348-014-1755-z](https://doi.org/10.1007/s00348-014-1755-z).
- [180] K. Richter, E. Schülein, B. Ewers, J. Raddatz, and A. Klein, "Boundary Layer Transition Characteristics of a Full-Scale Helicopter Rotor in Hover," in *72nd Annual Forum of the American Helicopter Society*, West Palm Beach, FL, USA, May 2016.
- [181] L. S. Roberts, M. V. Finnis, K. Knowles, and N. J. Lawson, "Forcing Boundary-Layer Transition on an Inverted Airfoil in Ground Effect," *Journal of Aircraft*, vol. 54, no. 6, 2017. DOI: [10.2514/1.C034304](https://doi.org/10.2514/1.C034304).
- [182] J. Romblad, D. Ohno, W. Würz, and E. Krämer, "Laminar to Turbulent Transition at Unsteady Inflow Conditions: Wind Tunnel Measurements at Oscillating Inflow Angle," in *New Results in Numerical and Experimental Fluid Mechanics XII*, Springer International Publishing, 2020, pp. 254–264. DOI: [10.1007/978-3-030-25253-3_25](https://doi.org/10.1007/978-3-030-25253-3_25).
- [183] W. S. Saric, H. L. Reed, and E. B. White, "Stability and Transition of Three-Dimensional Boundary Layers," *Annual Review of Fluid Mechanics*, vol. 35, no. 1, 2003. DOI: [10.1146/annurev.fluid.35.101101.161045](https://doi.org/10.1146/annurev.fluid.35.101101.161045).
- [184] W. S. Saric et al., "Progress in Transition Modelling," AGARD-R-793, 1994.
- [185] A. P. Schaffarczyk, D. Schwab, and M. Breuer, "Experimental Detection of Laminar-Turbulent Transition on a Rotating Wind Turbine Blade in the Free Atmosphere," *Wind Energy*, vol. 20, no. 2, 2017. DOI: [10.1002/we.2001](https://doi.org/10.1002/we.2001).
- [186] J. A. Schetz, "Direct Measurement of Skin Friction in Complex Flows," in *48th AIAA Aerospace Sciences Meeting*, Orlando, FL, USA, Jan. 2010. DOI: [10.2514/6.2010-44](https://doi.org/10.2514/6.2010-44).
- [187] H. Schlichting and K. Gersten, *Boundary-Layer Theory*, 8th ed. Springer Verlag, 2010. DOI: [10.1007/978-3-642-85829-1](https://doi.org/10.1007/978-3-642-85829-1).
- [188] O. Schneider, B. G. van der Wall, and K. Pengel, "HART II Blade Motion Measured by Stereo Pattern Recognition (SPR)," in *59th Annual Forum of the American Helicopter Society*, Phoenix, AZ, USA, May 2003.
- [189] M. T. Schobeiri, K. Read, and J. Lewalle, "Effect of Unsteady Wake Passing Frequency on Boundary Layer Transition, Experimental Investigation, and Wavelet Analysis," *Journal of Fluids Engineering*, vol. 125, no. 2, 2003. DOI: [10.1115/1.1537253](https://doi.org/10.1115/1.1537253).

- [190] G. Schrauf, "COCO: A Program to Compute Velocity and Temperature Profiles for Local and Nonlocal Stability Analysis of Compressible, Conical Boundary Layers with Suction," ZARM Technik Report, 1998.
- [191] G. Schrauf, "LILO 2.1 User's Guide and Tutorial," GSSC Technical Report, 2006.
- [192] S. J. Schreck, W. E. Faller, and H. E. Helin, "Pitch Rate and Reynolds Number Effects on Unsteady Boundary-Layer Transition and Separation," *Journal of Aircraft*, vol. 35, no. 1, 1998. DOI: [10.2514/2.2258](https://doi.org/10.2514/2.2258).
- [193] E. Schülein, "Experimental Investigation of Laminar Flow Control on a Supersonic Swept Wing by Suction," in *AIAA 4th Flow Control Conference*, Seattle, WA, USA, Jun. 2008. DOI: [10.2514/6.2008-4208](https://doi.org/10.2514/6.2008-4208).
- [194] D. Schwamborn, A. D. Gardner, H. von Geyr, A. Krumbein, H. Lüdeke, and A. Stürmer, "Development of the TAU-Code for Aerospace Applications," in *50th NAL International Conference on Aerospace Science and Technology*, Bangalore, India, Jun. 2008.
- [195] C. Schwarz, A. Bauknecht, S. Mailänder, and M. Raffel, "Wake Characterization of a Free-Flying Model Helicopter in Ground Effect," *Journal of the American Helicopter Society*, vol. 64, no. 1, 2019. DOI: [10.4050/jahs.64.012010](https://doi.org/10.4050/jahs.64.012010).
- [196] T. Schwarz and K. Pahlke, "Generation of an Advanced Helicopter Experimental Aerodynamic Data Base for CFD Validation - The European GOAHEAD Project," *Aerospace Science and Technology*, vol. 19, no. 1, 2012. DOI: [10.1016/j.ast.2011.09.007](https://doi.org/10.1016/j.ast.2011.09.007).
- [197] T. Schwermer, "Experimentelle Untersuchung des dynamischen Strömungsabrisses an einem Rotor mit axialer Zuströmung," Ph.D. dissertation, Leibniz University of Hannover, 2018.
- [198] T. Schwermer, A. D. Gardner, and M. Raffel, "A Novel Experiment to Understand the Dynamic Stall Phenomenon in Rotor Axial Flight," *Journal of the American Helicopter Society*, vol. 64, no. 1, 2019. DOI: [10.4050/JAHS.64.012004](https://doi.org/10.4050/JAHS.64.012004).
- [199] T. Schwermer, C. B. Merz, K. Richter, D. Frieling, and M. Raffel, "Differential Infrared Thermography for Transition Detection on Rotor Blades," in *17th International Symposium on Applications of Laser Techniques to Fluid Mechanics*, Lisbon, Portugal, Jul. 2014.
- [200] T. Schwermer, K. Richter, and M. Raffel, "Development of a Rotor Test Facility for the Investigation of Dynamic Stall," in *New Results in Numerical and Experimental Fluid Mechanics X*, Springer International Publishing, 2016, pp. 663–673. DOI: [10.1007/978-3-319-27279-5_58](https://doi.org/10.1007/978-3-319-27279-5_58).
- [201] Y. Sémézis and P. Beaumier, "Détermination de l'état de la couche limite sur des sections de pale d'hélicoptère à l'aide de films chauds," Technical Report ONERA TAP-95-065, 1995.
- [202] C. Sheng, "Role of Transition Modeling in Rotor Hover Predictions," *Journal of Aircraft*, vol. 55, no. 1, 2018. DOI: [10.2514/1.C034137](https://doi.org/10.2514/1.C034137).
- [203] P. F. Sheridan and W. Wiesner, "Aerodynamics of Helicopter Flight Near the Ground," in *33rd Annual National Forum of the American Helicopter Society*, Washington, DC, USA, May 1977.

- [204] I. I. Sikorsky, *The Story of the Winged-S - An Autobiography*. Barajima Books (english e-book edition, originally published in 1944 by Dodd, Mead & Company), 2020.
- [205] M. J. Silva and R. Riser, "CH-47D Tandem Rotor Outwash Survey," in *67th Annual Forum of the American Helicopter Society*, Virginia Beach, VA, USA, May 2011.
- [206] B. Simon, A. Filius, C. Tropea, and S. Grundmann, "IR Thermography for Dynamic Detection of Laminar Turbulent Transition," *Experiments in Fluids*, vol. 57, 2016. DOI: [10.1007/s00348-016-2178-9](https://doi.org/10.1007/s00348-016-2178-9).
- [207] M. J. Smith, A. D. Gardner, R. Jain, D. Peters, and F. Richez, "Rotating Wing Dynamic Stall: State of the Art and Future Directions," in *76th Annual Forum of the Vertical Flight Society*, Virtual, May 2020.
- [208] M. J. Smith, A. R. Jones, F. Ayancik, K. Mulleners, and J. W. Naughton, "An Assessment of the State-of-the-Art from the 2019 ARO Dynamic Stall Workshop," in *AIAA Aviation 2020 Forum*, Virtual, Jun. 2020. DOI: [10.2514/6.2020-2697](https://doi.org/10.2514/6.2020-2697).
- [209] P. Spalart and S. Allmaras, "A One-Equation Turbulence Model for Aerodynamic Flows," in *30th Aerospace Sciences Meeting and Exhibit*, Reno, NV, USA, Jan. 1992. DOI: [10.2514/6.1992-439](https://doi.org/10.2514/6.1992-439).
- [210] P. R. Spalart, S. Deck, M. L. Shur, K. D. Squires, M. K. Strelets, and A. Travin, "A New Version of Detached-Eddy Simulation, Resistant to Ambiguous Grid Densities," *Theoretical and Computational Fluid Dynamics*, vol. 20, no. 3, 2006. DOI: [10.1007/s00162-006-0015-0](https://doi.org/10.1007/s00162-006-0015-0).
- [211] P. R. Spalart and C. L. Rumsey, "Effective Inflow Conditions for Turbulence Models in Aerodynamic Calculations," *AIAA Journal*, vol. 45, no. 10, 2007. DOI: [10.2514/1.29373](https://doi.org/10.2514/1.29373).
- [212] M. Sugiura, V. Tanabe, H. Sugawara, N. Matayoshi, and H. Ishii, "Numerical Simulations and Measurements of the Helicopter Wake in Ground Effect," *Journal of Aircraft*, vol. 54, no. 1, 2017. DOI: [10.2514/1.C033665](https://doi.org/10.2514/1.C033665).
- [213] B. Sun, B. Ma, P. Wang, J. Luo, J. Deng, and C. Gao, "High Sensitive Flexible Hot-Film Sensor for Measurement of Unsteady Boundary Layer Flow," *Smart Materials and Structures*, vol. 29, no. 3, 2020. DOI: [10.1088/1361-665X/ab6ba8](https://doi.org/10.1088/1361-665X/ab6ba8).
- [214] M. Szewczyk, R. Smusz, K. de Groot, J. Meyer, A. Kucaba-Pietal, and P. Rzucidlo, "In-Flight Investigations of the Unsteady Behaviour of the Boundary Layer with Infrared Thermography," *Measurement Science and Technology*, vol. 28, no. 4, 2017. DOI: [10.1088/1361-6501/aa529c](https://doi.org/10.1088/1361-6501/aa529c).
- [215] *Tao of Systems Integration, Inc.* URL: <https://www.taosystem.com> (Accessed: 2022-01-08), Hampton, VA, USA.
- [216] S. A. Teagar, K. J. Biehl, L. J. Garodz, J. J. Tymczyszczym, and D. C. Burnham, "Flight Test Investigation of Rotorcraft Wake Vortices in Forward Flight," Federal Aviation Administration, report DOT/FAA/CT-94/117, 1996.
- [217] T. Theodorsen, "General Theory of Aerodynamic Instability and the Mechanism of Flutter," NACA report TR 496, 1949.

- [218] R. Thiessen and E. Schülein, "Infrared Thermography and DIT of Quadcopter Rotor Blades Using Laser Heating," in *15th International Workshop on Advanced Infrared Technology and Applications*, Florence, Italy, Sep. 2019. DOI: [10.3390/proceedings2019027031](https://doi.org/10.3390/proceedings2019027031).
- [219] N. Troldborg, C. Bak, H. Aagaard Madsen, and W. R. Skrzypinski, "DANAERO MW: Final Report," DTU Wind Energy E No. 0027(EN), 2013.
- [220] C. Tropea, A. L. Yarin, and J. F. Foss, Eds., *Springer Handbook of Experimental Fluid Mechanics*, 1st ed. Springer Verlag, 2007. DOI: [10.1007/978-3-540-30299-5](https://doi.org/10.1007/978-3-540-30299-5).
- [221] E. A. Truckenbrodt, "Grenzschichtströmung an festen Wänden," in *Fluidmechanik Band 2*, 4th ed. Springer Verlag, 2008, ch. 6.3, pp. 283–361. DOI: [10.1007/978-3-540-79024-2](https://doi.org/10.1007/978-3-540-79024-2).
- [222] H. R. Velkoff, D. A. Blaser, and K. M. Jones, "Boundary-Layer Discontinuity on a Helicopter Rotor Blade in Hovering," *Journal of Aircraft*, vol. 8, no. 2, 1971. DOI: [10.2514/3.44236](https://doi.org/10.2514/3.44236).
- [223] B. A. Vieira, M. P. Kinzel, and M. D. Maughmer, "CFD Hover Predictions Including Boundary-Layer Transition," in *55th AIAA Aerospace Sciences Meeting*, Grapevine, TX, USA, Jan. 2017. DOI: [10.2514/6.2017-1665](https://doi.org/10.2514/6.2017-1665).
- [224] A. E. Voigt, J. C. Dauer, and K. F., "Measurement of Blade Deflection of an Unmanned Intermeshing Rotor Helicopter," in *43rd European Rotorcraft Forum*, Milan, Italy, Sep. 2017.
- [225] A. J. Wadcock, L. A. Ewing, E. Solis, M. Potsdam, and G. Rajagopalan, "Rotorcraft Downwash Flow Field Study to Understand the Aerodynamics of Helicopter Brownout," in *AHS Southwest Region Technical Specialists Meeting*, Dallas, TX, USA, Oct. 2008.
- [226] C. E. Waddle, J. T. Bolan, C. L. Dobbins, Z. M. Hall, and M. A. McDaniel, "Visualization and Analysis of Boundary Layer Transitions using Infrared Thermography," *Proceedings SPIE, Thermosense: Thermal Infrared Applications XL*, vol. 10661, 2018. DOI: [10.1117/12.2304426](https://doi.org/10.1117/12.2304426).
- [227] G. J. Walker and J. P. Gostelow, "Effects of Adverse Pressure Gradients on the Nature and Length of Boundary Layer Transition," *Journal of Turbomachinery*, vol. 112, no. 2, 1990. DOI: [10.1115/1.2927633](https://doi.org/10.1115/1.2927633).
- [228] B. van der Wall, *Grundlagen der Hubschrauber-Aerodynamik*. Springer Verlag, 2015, pp. 364–367.
- [229] A. N. Watkins, B. D. Leighty, W. E. Lipford, K. Z. Goodman, J. Crafton, and J. W. Gregory, "Measuring Surface Pressures on Rotor Blades Using Pressure-Sensitive Paint," *AIAA Journal*, vol. 54, no. 1, 2016. DOI: [10.2514/1.J054191](https://doi.org/10.2514/1.J054191).
- [230] B. Wei, Y. Gao, L. Wang, and D. Li, "Analysis of Flow Transition and Separation on Oscillating Airfoil by Pressure Signature," *Journal of Mechanical Science and Technology*, vol. 33, no. 1, 2019.
- [231] P. Weiand, S. Michelis, and A. D. Gardner, "Numerical Simulation of an Adaptive Wall in a Virtual Transonic Wind Tunnel," *AIAA Journal*, vol. 55, no. 9, 2017. DOI: [10.2514/1.J055481](https://doi.org/10.2514/1.J055481).

- [232] A. Weiss, A. D. Gardner, C. Klein, and M. Raffel, "Boundary-Layer Transition Measurements on Mach-Scaled Helicopter Rotor Blades in Climb," *CEAS Aeronautical Journal*, vol. 8, no. 4, 2017. DOI: [10.1007/s13272-017-0263-2](https://doi.org/10.1007/s13272-017-0263-2).
- [233] A. Weiss, A. D. Gardner, T. Schwermer, C. Klein, and M. Raffel, "On the Effect of Rotational Forces on Rotor Blade Boundary-Layer Transition," *AIAA Journal*, vol. 57, no. 1, 2019. DOI: [10.2514/1.J057036](https://doi.org/10.2514/1.J057036).
- [234] A. Weiss, R. Geisler, M. M. Müller, C. Klein, U. Henne, J. N. Braukmann, and J. Letzgus, "Dynamic-Stall Measurements using Time-Resolved Pressure-Sensitive Paint on Double-Swept Rotor Blades," *Experiments in Fluids*, vol. 63, 2022. DOI: [10.1007/s00348-021-03366-6](https://doi.org/10.1007/s00348-021-03366-6).
- [235] T. Wollmann, E. Koch, J. Lich, M. Vater, R. Kuschmierz, C. Schnabel, J. Czarske, A. Filippatos, and M. Gude, "Motion Blur Suppression by Using an Optical Derotator for Deformation Measurement of Rotating Components," in *Nondestructive Characterization and Monitoring of Advanced Materials, Aerospace, Civil Infrastructure, and Transportation XIV*, SPIE, 2020, pp. 183–191. DOI: [10.1117/12.2556153](https://doi.org/10.1117/12.2556153).
- [236] O. D. Wong and P. E. Tanner, "Photogrammetric Measurements of an EH-60L Brownout Cloud," *Journal of the American Helicopter Society*, vol. 61, no. 1, 2016. DOI: [10.4050/JAHS.61.012003](https://doi.org/10.4050/JAHS.61.012003).
- [237] O. D. Wong, A. N. Watkins, K. Z. Goodman, J. Crafton, A. Forlines, L. Goss, J. W. Gregory, and T. J. Juliano, "Blade Tip Pressure Measurements Using Pressure-Sensitive Paint," *Journal of the American Helicopter Society*, vol. 63, no. 1, 2018. DOI: [10.4050/JAHS.63.012001](https://doi.org/10.4050/JAHS.63.012001).
- [238] W. Würz and S. Wagner, "Experimental Investigations of Transition Development in Attached Boundary Layers and Laminar Separation Bubbles," in *New Results in Numerical and Experimental Fluid Mechanics*, Springer International Publishing, 1997, pp. 413–420. DOI: [10.1007/978-3-322-86573-1_52](https://doi.org/10.1007/978-3-322-86573-1_52).
- [239] D. W. Wynnchuk and S. Yarusevych, "Characterization of Laminar Separation Bubbles Using Infrared Thermography," *AIAA Journal*, vol. 58, no. 7, 2020. DOI: [10.2514/1.J059160](https://doi.org/10.2514/1.J059160).
- [240] Y. Yokokawa, "Transition Measurement on Metallic Aircraft Model in Typical Low-speed Wind Tunnel," *Transactions of the Japan Society for Aeronautical and Space Sciences*, vol. 48, no. 161, 2005. DOI: [10.2322/tjsass.48.175](https://doi.org/10.2322/tjsass.48.175).
- [241] D. Yorita, J. Lemarechal, C. Klein, K. Fujita, and H. Nagai, "Transition Detection Methods in a Pitch-Sweep Test by means of TSP using Lifetime and Intensity Measurements," in *AIAA SciTech 2020 Forum*, Orlando, FL, USA, Jan. 2020. DOI: [10.2514/6.2020-0296](https://doi.org/10.2514/6.2020-0296).
- [242] D. O. Yu and O. J. Kwon, "Time-Accurate Aeroelastic Simulations of a Wind Turbine in Yaw and Shear Using a Coupled CFD-CSD Method," *Journal of Physics: Conference Series*, vol. 524, 2014. DOI: [10.1088/1742-6596/524/1/012046](https://doi.org/10.1088/1742-6596/524/1/012046).
- [243] D. H. Zhang, Y. T. Chew, and S. H. Winoto, "Investigation of Intermittency Measurement Methods for Transitional Boundary Layer Flows," *Experimental Thermal and Fluid Science*, vol. 12, no. 4, 1996. DOI: [10.1016/0894-1777\(95\)00133-6](https://doi.org/10.1016/0894-1777(95)00133-6).

- [244] G. Zografakis, G. Barakos, and M. Johnson, "Transitional Modelling for Rotorcraft CFD," in *34th European Rotorcraft Forum*, St. Petersburg, Russia, Sep. 2008.
- [245] S. Zuccher and W. S. Saric, "Infrared Thermography Investigations in Transitional Supersonic Boundary Layers," *Experiments in Fluids*, vol. 44, no. 1, 2008. DOI: [10.1007/s00348-007-0384-1](https://doi.org/10.1007/s00348-007-0384-1).

Curriculum Vitae

Dr. Claus Christian Wolf
born on 19 May 1982 in Aachen, Germany
Christian.Wolf@DLR.de

Work experience

- since 05/2013 **Institute of Aerodynamics and Flow Technology,
German Aerospace Center (DLR), Göttingen**
Research Scientist
- Research interests: optical measurement techniques, vortex dynamics, airfoil aerodynamics
- Sub-project manager for DLR projects “FAST-Rescue” and “URBAN-Rescue” and for LuFo projects “ECO-HC2” and “CHARME”
- 07/2008–12/2012 **Institute of Aerospace Systems (ILR), RWTH Aachen University**
PhD Student

Education

- 08/2015 **Laser Safety Officer (Lasersachkunde/Laserfachkunde)**
- 07/2015 **NASA International Project Management Course**
Kennedy Space Center, Cape Canaveral, FL, USA
- 12/2012 **Dissertation (Dr.-Ing.) at RWTH Aachen University:**
“The Subsonic Near-Wake of Bluff Bodies” (*summa cum laude*)
- 01/2008 **Diploma thesis (Dipl.-Ing.) at RWTH Aachen University:**
“Adaptive Parameter Identification in Real-Time” (*with distinction*)
- 10/2002–01/2008 **Student at RWTH Aachen University,**
Mechanical engineering with specialization in aerospace engineering

Awards

2021	Best test & evaluation paper award, 77th Forum of the Vertical Flight Society, Virtual
2019	ERF 2019 Chairman's award for the best paper with a focus on international cooperation, 45th European Rotorcraft Forum, Warsaw, Poland
2019	Best aerodynamic paper award, 75th Forum of the Vertical Flight Society, Philadelphia, PA, USA
2018	Best aerodynamic paper award, 74th Forum of the Vertical Flight Society, Phoenix, AZ, USA
2014	Borchers award, RWTH Aachen University
2008	Claudius Dornier Jr. award, Deutsche Gesellschaft für Luft- und Raumfahrt
2008	Springorum award, RWTH Aachen University

Teaching experience

since 2020	Lecturer "Background Oriented Schlieren Technique", Part of the PIV course at DLR Göttingen and the lecture series "Image Based Measurement Techniques for Fluid Mechanics" at BTU Cottbus
since 2014	Lecturer "Strömungsmechanik II", Leibniz University Hannover
2008–2012	Assistant lecturer "Raumfahrzeugbau I & II", RWTH Aachen University